Precise Measurement of Reactor Antineutrino Oscillation Parameters and Fuel-dependent Variation of Antineutrino Yield and Spectrum

Dongha Lee

Under the supervision of
Professor Soo-Bong Kim

A Dissertation submitted to the Graduate
Faculty of Seoul National University
in partial fulfillment of the requirement
for the Degree of Doctor of Philosophy

Department of Physics and Astronomy
Graduate School of Natural Science
Seoul National University
Seoul, KOREA

February 2019

Abstract

The reactor experiment for neutrino oscillation (RENO) since August 2011 has been extracting electron antineutrino ($\overline{\nu}_e$) data from two identical detectors located near the Yonggwang nuclear reactors in Korea. Using roughly 2,200 live days of data, we observed 850 666 (103 212) reactor $\overline{\nu}_e$ candidate events with 2.0%(4.7)% background in the near (far) detector. A discrepancy of approximately 5 MeV between the measured positron spectra of the reactor $\overline{\nu}_e$ events and the predicted positron spectra of the current reactor $\overline{\nu}_e$ model was observed. A far-to-near ratio measurement was conducted using the spectral and rate information, which gave $\sin^2 2\theta_{13} = 0.0896 \pm 0.0048(\text{stat.}) \pm 0.0047(\text{syst.})$ and $|\Delta m^2_{ee}| = [2.68 \pm 0.12(\text{stat.}) \pm 0.07(\text{syst.})] \times 10^{-3}$ eV^2. On the other hand, we observed from the multiple fuel cycles a fuel-dependent variation in an inverse beta decay (IBD) yield of $(6.15 \pm 0.19) \times 10^{43}$ cm^2/fission for ^{235}U and $(4.18 \pm 0.26) \times 10^{43}$ cm^2/fission for ^{239}Pu, and measured a total average IBD yield per fission of $(5.84 \pm 0.13) \times 10^{43}$ cm^2/fission. This observation rejects the hypothesis of fuel-independent IBD yield or identical fuel-isotope spectra at 6.6 σ. The measured IBD yield per fission for ^{235}U shows the largest deficit relative to a reactor model prediction. Re-evaluation of the ^{235}U IBD yield per fission could solve the reactor antineutrino anomaly. We also report a correlation between the 5 MeV discrepancy in the observed IBD spectrum and ^{235}U reactor fuel isotope fraction.

Contents

List of Figures

List of Tables

Chapter 1

Introduction

1.1 Overview

There has been great progress in the understanding of the neutrinos sector in elementary particle physics in the last two decades. The observations on neutrino oscillations proved that neutrinos have mass. However, neutrinos are still subject of intense research. For instance, the physics of the Standard Model is being modified to determine the three neutrino mass values. The determination of neutrino masses can will take us a step closer to a grand unified theory (GUT). Furthermore, the discovery of neutrino oscillations provides a new window to explore physics at the GUT scale, including flavor dynamics and extra dimensions. Neutrino oscillation is the lepton flavor transformation of a neutrino from one lepton family to another. Neutrino mixing is the oscillation of flavor states of the neutrino and the nonzero neutrino masses, and it provides insights into the modification of the current Standard Model. Neutrino oscillation is a consequence of the neutrino flavor being a linear combination of the mass eigenstate. The currently accepted model describing neutrino mixing is a framework of three flavors(ν_e, ν_μ, ν_τ). This phenomenon is represented by three mixing angles (θ_{12}, θ_{23}, θ_{13}), three mass differences (Δm^2_{21}, Δm^2_{31}, and Δm^2_{32}), and one phase angle (δ_{CP}) [1, 2]. In 1998, the Super-Kamiokande experiment discovered neutrino oscillation and mixing angle θ_{23} [3]. It is interesting to note that angle θ_{23} is close to the maximal value. The solar neutrino oscillation was determined by the SNO collaboration in 2001, and the mixing angle θ_{12} was obtained [4, 5].

The smallest mixing angle θ_{13} was found in the RENO, Daya Bay, and Double Chooz experiments from the disappearance of the electron antineutrino from the reactor [6, 7, 8]. These reactor neutrino experiments could measure θ_{13} without disturbances from matter effects or charge parity (CP) violation. The first measurement of θ_{13} by RENO, which was was based on the rate-only analysis, com-

pared expected and observed reactor neutrino rates [6]. In 2016, we presented a more precise measurement of θ_{13}, and the first measurement of $|\Delta m^2_{ee}|$, a mixture of $|\Delta m^2_{31}|$ and $|\Delta m^2_{32}|$, obtained from energy- and baseline-dependent disappearance of reactor electron antineutrinos with data on 500 live days [9]. Furthermore, in this thesis, we also measure θ_{13} and $|\Delta m^2_{ee}|$ via rate+shape analysis performed with deeper statistical analysis ($\sim$ four times the results of the 500-live-days experiment [9]) and reduced systematic uncertainties. A precise measurement of θ_{13} by a reactor $\overline{\nu}_e$ experiment will help to determine the δ_{CP} phase and mass ordering when combined with the results of accelerator neutrino experiments [10, 11]. In addition, we present a study on antineutrino yield and spectrum with fuel-dependent variation caused by the unprecedented number of reactor antineutrino events($\sim$1M).

1.2 Neutrino Oscillation

A neutrino with flavor α and momentum $\overrightarrow{p}$ is the combination of different mass eigenstates. Mathematically

$$|\nu_\alpha\rangle = \sum_i U^*_{\alpha i} |\nu_i\rangle \tag{1.1}$$

The massive neutrino states are an eigenstate of the Hamiltonian. This implies the evolution of the massive neutrino over time into a plane wave.

$$|\nu_\alpha(t)\rangle = \sum_i U^*_{\alpha i} e^{-iE_i t} |\nu_i\rangle \tag{1.2}$$

inverting equation 1.1, the neutrino flavor states can be expressed in terms of flavor states.

$$|\nu_\alpha(t)\rangle = \sum_{\beta=e,\mu,\tau} U^*_{\alpha i} e^{-iE_i t} U_{\beta i} |\nu_\beta\rangle \tag{1.3}$$

Just as the Cabibbo-Kobayashi-Maskawa (CKM) matrix measures the mixing of quark flavors, the mixing of neutrino lepton flavor states can be related to the mass states through the Pontecorvo-Maki-Nakagawa-Sakata (PMNS) matrix assuming three flavors [12].

$$\begin{aligned} U &= \begin{pmatrix} 1 & 0 & 0 \\ 0 & c_{23} & s_{23} \\ 1 & -s_{23} & c_{23} \end{pmatrix} \begin{pmatrix} c_{13} & 0 & s_{13}e^{i\delta} \\ 0 & 1 & 0 \\ -s_{13}e^{-i\delta} & 0 & c_{13} \end{pmatrix} \begin{pmatrix} c_{12} & s_{12} & 0 \\ -s_{12} & c_{12} & 0 \\ 0 & 0 & 1 \end{pmatrix} \\ &= \begin{pmatrix} c_{12}c_{13} & s_{12}c_{13} & s_{13}e^{-i\delta} \\ -s_{12}c_{23} - c_{12}s_{23}s_{13}e^{i\delta} & c_{12}c_{23} - s_{12}s_{23}s_{13}e^{i\delta} & s_{23}c_{13} \\ s_{12}s_{23} - c_{12}c_{23}s_{13}e^{i\delta} & -c_{12}s_{23} - s_{12}c_{23}s_{13}e^{i\delta} & c_{23}c_{13} \end{pmatrix}, \end{aligned} \tag{1.4}$$

where $c_{ij} = \cos\theta_{ij}$, $s_{ij} = \sin\theta_{ij}$, and δ is a Dirac CP violating phase.

The probability of ν_α with energy E transforming to ν_β ($\nu_{\alpha,\beta} = \nu_{e,\mu,\tau}$) after travelling a distance L in vacuum is

$$P(\nu_\alpha \to \nu_\beta) = \delta_{\alpha\beta} - 2\mathrm{Re}\sum_{j>i} U_{\alpha i}U^*_{\alpha j}U^*_{\beta i}U_{\beta j}\left(1 - \exp\left\{i\Delta m^2_{ji}L\frac{2}{E}\right\}\right), \quad (1.5)$$

where $\Delta m^2_{ji} \equiv m^2_j - m^2_i$ and m_i is the mass of the ith eigenstate.

Various experiments using solar, atmospheric, reactor, and accelerator neutrinos have recorded oscillations among different flavors of neutrinos, providing rich information on the flavor structure of the lepton sector. The current best values of neutrino oscillation parameters with an error of one standard deviation (1σ) are summarized as follows [13]:

$$\begin{aligned}
\sin^2\theta_{23} &= 0.417^{+0.025}_{-0.028} \text{ (normal)} \quad (1.6)\\
&\text{or } 0.421^{+0.033}_{-0.025} \text{ (inverted)}\\
\sin^2\theta_{12} &= 0.307 \pm 0.013\\
\sin^2\theta_{13} &= (2.12 \pm 0.08) \times 10^{-2}\\
\Delta m^2_{32} &= (2.51 \pm 0.05) \times 10^{-3}\text{eV}^2 \text{ (normal)}\\
&\text{or } (2.56 \pm 0.04) \times 10^{-3}\text{eV}^2 \text{ (inverted)}\\
\Delta m^2_{21} &= (7.53 \pm 0.18) \times 10^{-5}\text{eV}^2
\end{aligned}$$

1.3 Reactor Neutrino Experiment

Nuclear reactors have played a crucial role in experimental neutrino physics. The neutrino was discovered by Frederick Reines, Clyde Cowan, and other researchers at the Savannah River Reactor in 1956 [14]. KamLAND observed the disappearance of reactor antineutrinos and neutrino oscillation-induced distortions in the energy spectrum because of the mixing angle θ_{12} [15, 16]. The low energy levels of the reactor neutrino allows the measurement of the latter's mixing angle in short baseline experiment without matter effects or CP violation. The reactor neutrino detector does not need to be large, and the construction of a neutrino beam device is not needed. RENO, Daya Bay and Double-Chooz experiments measured the θ_{13} via rate-only analysis in 2012 [6, 7, 8].

However, past reactor experiments found that using a single detector located $\sim$ less than a 1 km from the reactor was insufficient for observing neutrino disappearance, as summarized in Table 1.1. Early efforts to measure θ_{13} by using reactors, such as the CHOOZ and Palo Verde experiments, encountered the problem of instability of Gd-doped liquid scintillator (LS). Palo Verde struggled with

Experiment	Year	Reactor Power (MW_{th})	Baselines (m)	N_{obs} $/N_{exp}$
ILL [17]	1980-1981	57	8.8	0.96 ± 0.12
Goesgen [18, 19, 20]	1981-1985	2800	37.9	1.02
			45.9	1.05 ± 0.06
			64.7	0.98 ± 0.06
Rovno [21, 22, 23]	1983-1991	1375	18, 25	0.964 ± 0.07
Krasnoyarsk [24]	1987-1994	-	57,231	0.99 ± 0.05
Bugey [25]	1995	2800	15	0.99 ± 0.05
			40	0.99 ± 0.05
			95	0.92 ± 0.14
Chooz [26]	1997	8500	1000	1.01 ± 0.04
Palo Verde [27, 28]	1999	11600	890, 750	1.01 ± 0.10

Table 1.1: Past short-baseline reactor neutrino experiments

the gradual deterioration of Gd-doped LS due to precipitation [29, 30]. The Gd-doped LS in the CHOOZ experiment turned yellow a few months after deployment, which reduced the photo-electron collection efficiency [26, 31]. To avoid these problems, researchers have used new methods to successfully synthesize a Gd-doped LS with good optical properties and long-term stability [32, 33, 34]. To measure the rate and energy spectrum of the $\bar{\nu}_e$s, CHOOZ and Palo Verde used a single detector with ∼1 km baseline. However, such measurements from the single detector are sensitive to systematic issues related to the detector and the reactors. To avoid this problem, current experiments (Daya Bay, Double Chooz, and RENO) are deploying multiple identical detectors at different locations with respect to the reactors, which will allow the calculation of the disappearance of $\bar{\nu}_e$ from the ratio of the observed $\bar{\nu}_e$ rates. Because it is a relative measurement, the far-to-near ratio can significantly reduce the systematic uncertainties from the detector and the reactor. In 2012, three reactor disappearance experiments, Daya Bay [7], Double-Chooz [8], and RENO [6], reported the measurement of θ_{13}. The first measurement of θ_{13} by RENO was based on the rate-only analysis of deficit found [6]. In 2016, the reactor experiment reported a more precise value of θ_{13} and Δm^2_{ee} based on the rate, spectral, and baseline information of reactor neutrino disappearance (rate+shape analysis) for 500 live days. [9] Using shape information of reactor neutrino made it possible to obtain a θ_{13} value with fewer systematic errors than the rate-only analysis. Because the spectral shape of the background is different from that of the reactor neutrino, it is easy to distinguish between the two. In this thesis, more precise values of θ_{13} and Δm^2_{ee} than the

2016 results of RENO are reported with deeper statistical anlysis (∼4 times) and lower systematic uncertainties using rate+shape analysis.

1.3.1 Reactor Neutrino Production

The electron antineutrinos are produced from β-decay of reactor fuels: ^{235}U, ^{238}U, ^{239}Pu and ^{235}Pu. Fig. 1.1 shows the Feynman diagram of the β-decay process. A down quark of neutron transforms into an up quark by weak interaction and emits a W^- boson. The W^- boson decays into an electron and antineutrino.

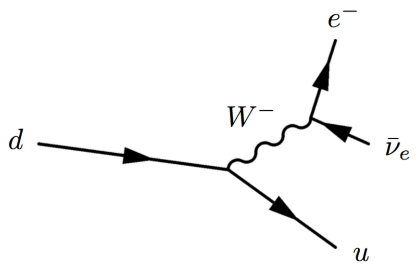

Figure 1.1: Feynman diagram for β-decay of neutron. A neutron decays into a proton, an electron and an electron antineutrino.

Each fission of the four isotopes produces ∼6 an electron antineutrino [35, 36, 37, 38]and releases an average of ∼200 MeV of energy [39]. Based on this information, the neutrino intensity can be estimated to be $\sim 2 \times 10^{20}/(GW_{th} \cdot s)$.

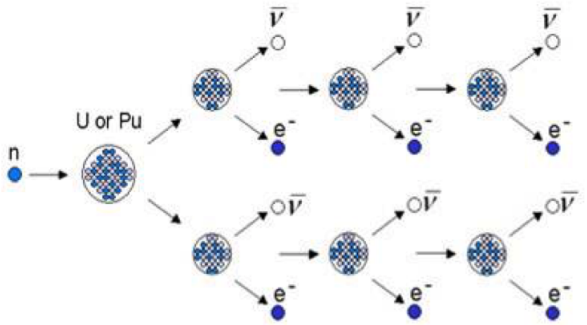

Figure 1.2: Production of neutrino in the fission process of reactor fuel [40].

The reactor antineutrino energy spectrum is a function of the reactor thermal

power and the fission fraction of the four major isotopes. The thermal output varies over time and with reactor status. The fission fraction of the isotopes varies with fuel burnup, as shown on the left side plot of Fig. 1.3. In addition, the reactor antineutrino energy spectrum per fission of four isotopes are different from each other, as shown on the right side of Fig. 1.3 Thus, the expected antineutrino flux and spectrum are calculated by combining these three pieces of information.

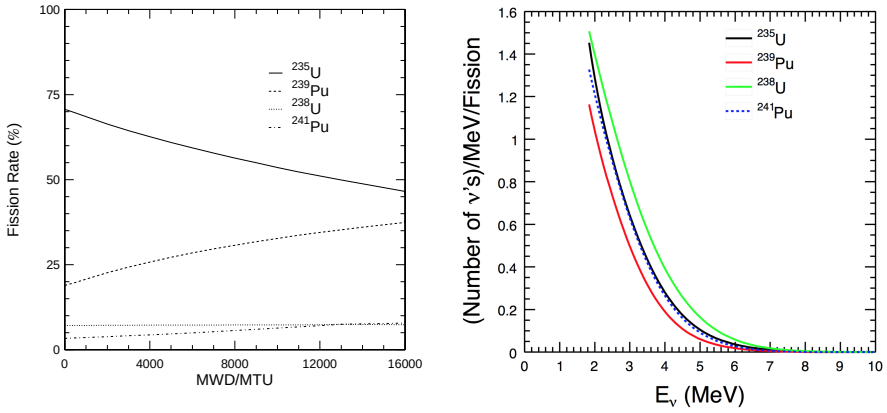

Figure 1.3: The left plot shows evolution of fissile rate of four main isotopes according to burnup. The right plot shows normalized neutrino spectrum from the fission of each isotope [41, 42].

1.3.2 Reactor Neutrino Detection

When an electron antineutrino enters matter, it can be captured by a free proton via inverse neutron decay (IBD)

$$\bar{\nu}_e + p \rightarrow e^+ + n, \tag{1.7}$$

which has an 1.8 MeV antineutrino energy threshold. The resulting neutron is subsequently captured by a proton in the following process:

$$n + p \rightarrow D + \gamma, \tag{1.8}$$

where D is deuterium. The mean time for neutron capture is $\sim$ 200 μs. The incident antineutrino energy is directly related to the energy of the positron by

$$E_{\bar{\nu}_e} = E_{e^+} + (m_n - m_p) + \mathcal{O}(E_{\bar{\nu}_e}/m_n), \tag{1.9}$$

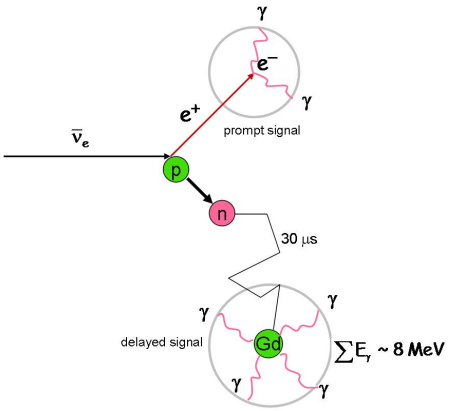

Figure 1.4: An electron antineutrino would be detected by a coincident signal of a prompt positron and a delayed captured neutron. The neutrino energy is directly related to the measured energy of the outgoing positron.

where E_{e^+} is the energy of the positron liberated from the inverse neutron decay and $m_n(m_p)$ is the neutron (proton) mass. The positron deposits its energy and then annihilates, yielding two photons each with 0.511 MeV; thus, the experimentally visible energy is $(E_{e^+} + 0.511$ MeV) with minimum energy at 1.022 MeV. An electron antineutrino event then can be identified by a distinctive signature of a prompt positron signal followed by a photon from the delayed neutron capture.

However, when a neutron is captured by Gd, in which a proton is bound, the capture cross section becomes larger and additional gamma rays are produced to result in a total energy of approximately 8 MeV. The experimental signature for reactor neutrinos is a prompt energy deposit of 1-8 MeV, because of the positron kinetic energy and the annihilated e^+e^- masses, followed an average 26 μs later by 8 MeV energy deposit of gammas from neutron capture on Gd. Exploiting the delayed coincidence is key to controlling backgrounds. Fig. 1.4 shows both prompt and delayed signals produced by a reactor neutrino.

The inverse neutron decay process's cross section takes the form of,

$$\sigma(E_{e^+}) \simeq \frac{2\pi^2\hbar^3}{m_e^5 f \tau_n} p_{e^+} E_{e^+}, \tag{1.10}$$

where p_{e^+} and m_e are the momentum and the mass of the positron, respectively, τ_n is the lifetime of a free neutron, and $f = 1.7152$ is the free neutron decay phase space factor [43].

Fig. 1.5 shows the neutrino flux, IBD cross section, and interaction spectrum

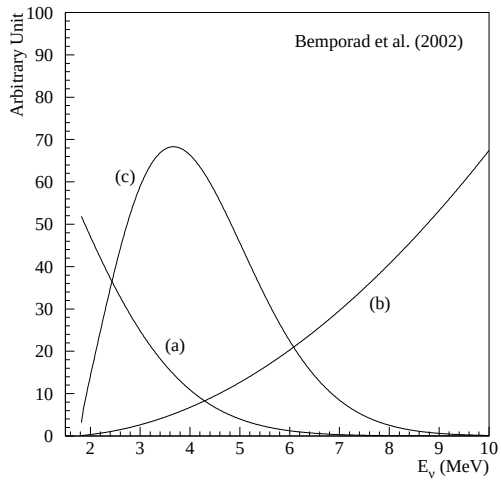

Figure 1.5: Reactor $\bar{\nu}_e$ flux (a), IBD cross section (b), and interaction spectrum at a detector based on such reaction (c) in Ref. [44]. The cut-off at 1.8 MeV is due to the minimum neutrino energy required for IBD process.

at a detector in arbitrary units calculated in Ref. [44]. The most probable neutrino energy interacting at a detector is ~ 3.8 MeV.

1.3.3 Neutrino Oscillation in Reactor Experiments

Because neutrinos from reactors have low energy—of the order of a few MeVs—they cannot produce muons or taus through charged current interaction. Therefore, the only possible reactor experiment are disappearance experiments, which measure the survival probability $P(\bar{\nu}_e \to \bar{\nu}_e)$.

It was shown in Ref. [45] that survival probability did not depend on the CP phase δ. Moreover, because of the low-energy neutrinos and short baseline, matter effects are negligible in reactor experiments [46]. Thus, the neutrino survival probability in vacuum can be used to model the neutrino oscillations in the reactor experiments. Assuming a mass hierarchy of $m_1 < m_2 < m_3$, the expression for the $\bar{\nu}_e$ disappearance probability is written as [47]

$$
\begin{aligned}
P(\bar{\nu}_e \to \bar{\nu}_e) &= 1 - 4\sum_{j>k} |U_{ej}|^2 |U_{ek}|^2 \sin^2\left(\frac{\Delta m^2_{jk} L}{4E}\right) \qquad (1.11)\\
&= 1 - \cos^4\theta_{13}\sin^2 2\theta_{12}\sin^2\left(\frac{\Delta m^2_{21} L}{4E}\right)\\
&- \sin^2 2\theta_{13}\left(\cos^2\theta_{12}\sin^2\left(\frac{\Delta m^2_{31} L}{4E}\right) + \sin^2\theta_{12}\sin^2\left(\frac{\Delta m^2_{32} L}{4E}\right)\right)\\
&\simeq 1 - \cos^4\theta_{13}\sin^2 2\theta_{12}\sin^2\left(\frac{\Delta m^2_{21} L}{4E}\right) - \sin^2 2\theta_{13}\sin^2\left(\frac{\Delta m^2_{ee} L}{4E}\right)
\end{aligned}
$$

where,

$$\Delta m^2_{ee} = \cos^2\theta_{12}\Delta m^2_{31} + \sin^2\theta_{12}\Delta m^2_{32} \qquad (1.12)$$

Equation 1.11 consists of two quadratic components: Δm^2_{21} and Δm^2_{ee}. Fig. 1.6 shows survival probability as a function of baseline L (km). The Δm^2_{21} term is negligible in smaller region. The other term, (Δm^2_{ee}), makes full contribution in this region. The first minimum is located ∼1.5 km away from the reactor. If the far detector is placed at a distance of ∼1.5 km, the value of θ_{13} can be easily measured.

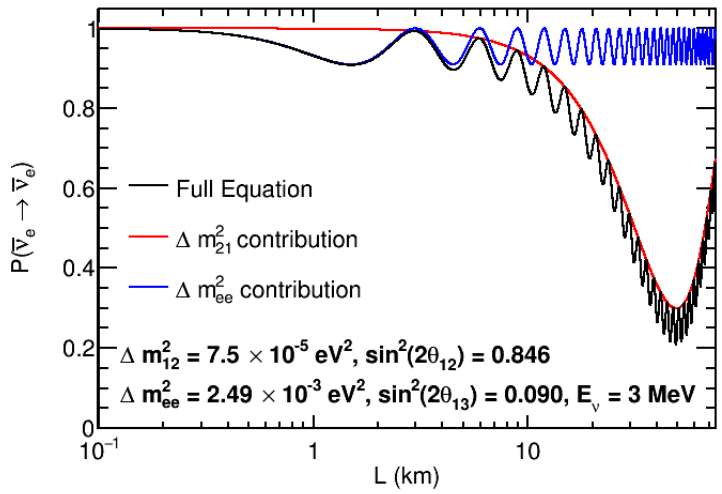

Figure 1.6: Survival probability $P(\bar{\nu}_e \to \bar{\nu}_e)$ vs the distance. The blue line is the Δm^2_{ee} term in Equation 1.11. The red curve represents the Δm^2_{21}. The black line is the sum of the two terms. The first local minimum is located ∼1.5 km away from the reactor core. At this point, contribution of Δm^2_{21} term is negligible.

1.3.4 Determination of Mixing Angle θ_{13}

As shown in Equation 1.11, mixing angle θ_{13} determines the magnitude of survival probability in the smaller region. The measurement of angle θ_{13} enhances our understanding of neutrino oscillation. In addition, the angle θ_{13} can also serve as a guide for determining neutrino mass hierarchy and CP violation in neutrino oscillation. The ordering of the neutrino masses can be directly measured by a reactor experiment with a large θ_{13} value and a ∼50 km baseline, such as the RENO-50 [49] and Jiangmen underground neutrino observatory (JUNO) [50]. The CP phase angle δ_{CP} is always found in the $U_{e3} = \sin\theta_{13}e^{-i\delta_{CP}}$. Therefore, mixing angle θ_{13} plays an important role in the determination of phase angle δ_{CP} [48].

1.3.5 Determination of Mass Squared Difference $|\Delta m^2_{ee}|$

The parameter $|\Delta m^2_{ee}|$ determines the shape of survival probability $\mathrm{P}(\bar{\nu_e} \to \bar{\nu_e})$ because $|\Delta m^2_{ee}|$ is the angular frequency of the trigonometric function in Equation 1.11. The measurement of mass difference $|\Delta m^2_{ee}|$ enables the further understanding of neutrino oscillation and determination of mass hierarchy.

As shown in Equation 1.12, the mass difference $|\Delta m^2_{ee}|$ is the ν_e weighted average of $|\Delta m^2_{31}|$ and $|\Delta m^2_{32}|$. On the other hand, the mass difference $|\Delta m^2_{\mu\mu}|$ is used in the $\mathrm{P}(\nu_\mu \to \nu_e)$ in the accelerator neutrino appearance experiment T2K [48] and MINOS [49].

$$\begin{aligned} \Delta m^2_{\mu\mu} &= \sin^2\theta_{12}\Delta m^2_{31} + \cos^2\theta_{12}\Delta m^2_{32} \\ &\quad + \cos\delta_{CP}\sin\theta_{13}\sin\theta_{12}\tan\theta_{23}\Delta^2_{21} \end{aligned} \tag{1.13}$$

$|\Delta m^2_{\mu\mu}|$ is also the ν_e weighted average of $|\Delta m^2_{31}|$ and $|\Delta m^2_{32}|$, and has a tiny difference because of δ_{CP}, as shown in Equation 1.13. Therefore, measuring Δm^2_{31} and Δm^2_{32} in the reactor experiment is simpler than doing so in the accelerator neutrino experiment.

$|\Delta m^2_{ee}|$ is also shown as following equation.

$$|\Delta m^2_{ee}| = |\Delta m^2_{32}| \pm 5.21 \times 10^{-5}\ \mathrm{eV}^2\ (+\text{: Normal, } -\text{: Inverted}) \tag{1.14}$$

The Equation 1.14 shows the relation between $|\Delta m^2_{ee}|$ and $|\Delta m^2_{32}|$ [47]. If the value of $|\Delta m^2_{ee}|$ is measured within a 3% error margin, the mass hierarchy of the neutrinos can be determined.

Fig. 1.7 shows the probability curve as a function of neutrino energy. The value of $|\Delta m^2_{ee}|$ determines the location of the minimum point of the probability curve. When using spectral information of the reactor neutrino, RENO could

measure $|\Delta m^2_{ee}|$. In this thesis, we will report the first measurement of $|\Delta m^2_{ee}|$ in RENO. Recently, similar measurement results of θ_{13} and $|\Delta m^2_{ee}|$ were reported at the Daya Bay experiment [50].

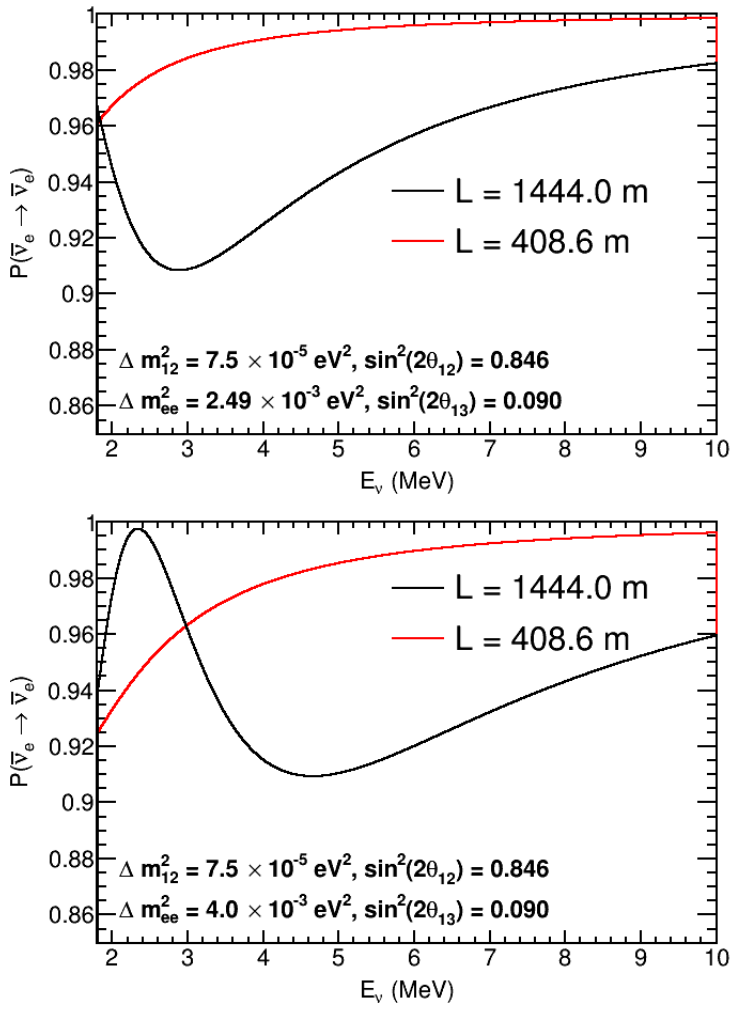

Figure 1.7: Survival probability $P(\bar{\nu_e} \rightarrow \bar{\nu_e})$ vs the energy. The upper (lower) plot shows the probability with $\Delta m^2_{ee} = 2.49 \times 10^{-3} eV^2$ ($\Delta m^2_{ee} = 4.00 \times 10^{-3} eV^2$).

1.4 The RENO Experiment

As mentioned earlier, RENO is a reactor-driven experiment to measure neutrino mixing angle θ_{13} and mass squared difference $|\Delta m^2_{ee}|$. The experiment is being conducted near the Hanbit nuclear power plant in Korea. Suggested in 2005, the experiment obtained a grant of ∼1M US dollars in 2006. The construction of the project began in 2007. The near and far detectors were established in early 2011. Data extraction from the detectors began in August 2011. In early April 2012, the experiment successfully calibrated θ_{13} by observing the deficit of reactor neutrinos [6]. In 2016, the measurement result of θ_{13} and $|\Delta m^2_{ee}|$ from rate and shape analysis was published [9]. As of February 2018, the experiment has collected approximately 2,200 live days of data at a higher accumulated data-taking efficiency than that collected by ∼95%. The subsequent sections are arranged in the following order: Chapter 2 describes experimental arrangement and RENO detectors. Chapter 3 describes the expected flux in and spectrum of the reactor neutrino and Monte Carlo simulation. Chapter 4 describes the reconstruction of event vertex and energy. Chapter 5 elicits the energy calibration of the near and far detectors. Chapter 6 to 9 presents a spectral analysis of 2,200 days of data. Chapter 6 also describes the IBD event selection criteria in, while Chapter 7 estimates the backgrounds. Chapter 8 discusses the systematic uncertainties. Chapter 9 presents a spectral measurement of θ_{13} and $|\Delta m^2_{ee}|$ is presented, and Chapter 10 describes the study on the fuel-dependent variation of antineutrino yield and spectrum . Conclusions and discussions are presented in Chapter 11.

1.5 Fuel-dependent Variation of Antinetrino Yield and Spectrum

A definitive measurement of the smallest neutrino mixing angle θ_{13} was being considered a tremendous success in neutrino physics during the last decade [6, 7]. The measurement was achieved by comparing the observed antineutrino fluxes with detectors placed at two different distances from the reactors. Because reactor antineutrino experiments suffer from large-reactor-related uncertainties of the expected antineutrino flux and energy spectrum [51, 52, 53, 54], it is necessary to have identical detector configurations that cancel out them.

The reactor antineutrino anomaly, which is nothing but the ∼6% deficit of measured antineutrino flux compared to the predicted deficit, is an intriguing mystery in current neutrino physics research that must be understood [52, 53, 54, 55, 56, 35, 36]. There have been numerous attempts to explain this anomaly, which may be caused by incorrect inputs to the fission spectrum conversion, deficiencies in nuclear databases, underestimated uncertainties of the reactor an-

tineutrino model, and the existence of sterile neutrinos [51, 57, 58]. Moreover, all ongoing reactor antineutrino experiments have observed a 5 MeV excess in the IBD prompt spectrum with respect to the expected one [55, 56, 59, 60]. This suggests that the present reactor antineutrino model can be a strong candidate to explain the reactor antineutrino anomaly.

In commercial nuclear reactor power plants, almost all (>99%) $\overline{\nu}_e$'s are produced through thousands of β-decay branches of fission products from ^{235}U, ^{239}Pu, ^{241}Pu, and ^{238}U. The antineutrino flux calculation is based on the inversion of spectra of the β-decay electrons of the thermal fissions, which were measured in 1980s at the ILL [35, 36]. The reactor antineutrino models due to these measurements as inputs have large uncertainties [53, 54]. Therefore, reevaluation of reactor antineutrino model and precise measurements of the neutrino flux and spectrum are essential to understand the reactor antineutrino anomaly.

In Fig. 1.8, as described in sections 1.3.1 and 1.3.2, the reactor antineutrino energy spectrum per fission for the four isotopes are different from each other. On the right side of Fig. 1.8, detected interaction spectrum is the product of neutrino flux and IBD cross section. While the IBD cross section does not dependent on the isotope, reactor neutrino flux is different for the four isotopes. Moreover, the fission fraction of the isotopes varies with fuel burnup. Thus, the observed IBD yield and spectrum depends on the fission fraction or fuel composition of the four isotopes. This cannot occur without the four isotopes having different reactor antineutrino energy spectrum. Therefore, by studying the observed IBD yield and spectrum with fuel composition, we were able to get shed light on the reactor antineutrino model and reactor antineutrino anomaly.

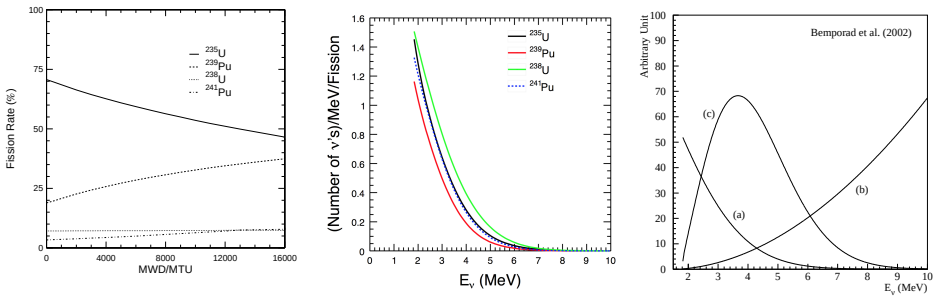

Figure 1.8: The left plot shows the evolution of fissile rate of four main isotopes according to burn up. The middle plot shows normalized neutrino spectrum from the fission of each isotope [41, 42]. In the right plot, (c)interaction spectrum at a detector based on such reaction is a product of (a)Reactor $\bar{\nu}_e$ flux and (b)inverse beta decay cross section.

In this analysis, we concluded that ^{235}U fuel isotope may be the primary contributor to the reactor antineutrino anomaly. Moreover, we report a fuel-dependent variation of the reactor antineutrino flux and spectrum over 1807.9 days of RENO near detector data. We also demonstrate a correlation between the 5 MeV excess and the reactor fuel isotope fraction of ^{235}U.

Chapter 2

Setup of the RENO Experiment

2.1 Overview

The Reactor Experiment for Neutrino Oscillation (RENO) is an experiment to measure the neutrino oscillation mixing angle θ_{13} using electron antineutrino emitted from the Habit nuclear power plant in Yonggwang, Korea. The power plant, which has six reactors producing a total thermal output of 16.4 GWh and the second largest in the world, is an intense source of low-energy antineutrinos suitable for measuring neutrino oscillation parameters.

The RENO has two identical 16 ton liquid scintillator detectors, with one at a near site, at a distance of 294 m from the center of reactor array, and the other at a far site, at a distance of 1384 m away from center of the reactor array. The two detectors are designed identically to cancel out a number of systematic uncertainties by normalizing the neutrino fluxes at the far detector and the near detector.

The RENO detectors have a layered structure similar to those in other reactor neutrino experiments, such as those in the Daya Bay and Double Chooz experiments. The RENO detectors consist of a target, γ-catcher, buffer, and veto, arranged from the center to the outer part of the detector. The photomultiplier tubes (PMTs) for detecting neutrino interaction are located in the buffer layer. A cross-sectional view of one of the RENO detectors is shown in Fig. 2.1

The "target" is a gadolinium (Gd) doped liquid scintillator contained in a transparent cylindrical vessel made of acrylic plastic. An inverse beta decay (IBD) event produces a pair of positron and neutron. The positron loses energy via a scintillating process before it is converted into two gammas by a pair annihilation. The neutron thermalizes, and then captured by the Gd nucleus, producing several

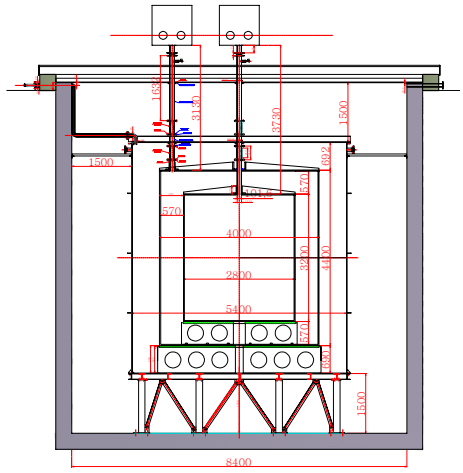

Figure 2.1: Cross-sectional view of one of the RENO detectors. The order of the sections from the centerline are as follows: liquid scintillator filled target, gamma catcher in a transparent acrylic vessel, mineral oil filled buffer in a stainless steel vessel, and water filled veto layer. The PMTs for the inner and outer detectors are mounted on buffer and veto vessels, respectively, and facing inward.

gammas. The gammas produced close to the boundary of the target can escape the target without completely depositing their energy in the scintillator. Not to lose the energy carried by gammas escaping from the target, a "γ-catcher" is employed, which is another liquid scintillator layer surrounding target. Unlike the target, the liquid scintillator in this γ-catcher is not loaded with Gd, because this layer is intended to augment the target in the energy measurement of the gammas emitted in the target. The transparent cylindrical acrylic vessel contains γ-catcher liquid, similar to the that of the target.

The γ-catcher is surrounded by a non-scintillating liquid layer, known as the "buffer". Mineral oil is used as buffer and it is contained in a cylindrical vessel made of stainless steel. The PMTs are mounted on the inner surface of the buffer vessel immersed in the buffer. The buffer acts as a shield against gammas, mostly originating from radioactive isotopes contained in the PMTs, entering the scintillating volume.

The outermost layer of the RENO detector is the "veto", which is a water Cherenkov detector layer. The purpose of the "veto" is to reduce background gammas and neutrons from the surrounding environment (such as rocks, etc.) as well as from background events induced by cosmic muon. The material of the veto container is 40-cm-thick concrete and the top lid is made of stainless steel. The PMTs are mounted on the inner surface of the veto container for detecting Cherenkov light from cosmic muons.

The various design parameters have been determined for optimal performance using detailed simulation. The simulation includes background gammas from the PMTs and surrounding rocks, cosmic muons reaching the detector site, as well as inverse beta decay from the reactor antineutrinos. The details of the detector layers and vessels are summarized in Table 2.1

Detector Component	Outer Diamete (mm)	Outer Height (mm)	Material	Volume (m^3)	Mass (tons)
Target	2750	3150	Gd-loaded LS	18.70	16.08
Target Vessel	2800	3200	Acrylic	0.99	1.18
γ-catcher	3940	4340	LS	33.19	28.55
γ-catcher Vessel	4000	4400	Acrylic	2.38	2.83
Buffer	5388	5788	Oil	76.46	64.22
Buffer Vessel	5400	5800	SUS	1.05	8.39
Veto	8388	8788	Water	352.61	352.61

Table 2.1: Dimensions of the mechanical structure of the detector.

Figure 2.2: Hanbit nuclear power plant, located in Yonggwang, 250 km south of Seoul. Three other nuclear power plant sites are also located in the south-eastern part of Korea

The data acquisition (DAQ) system of RENO is designed to record the charge and arrival time of PMT hits. The near and far detectors are designed to have the same PMT configuration and readout system. The RENO DAQ employs electronics developed for the Super-Kamiokande experiment.

2.2 Experimental Arrangement

2.2.1 Hanbit Nuclear Power Plant

The RENO detectors are located near the Hanbit (previously known as Yonggwang) nuclear power plant, operated by the Korea Hydro and Nuclear Power Co., Ltd (KHNP), in Yonggwang, the southwest coastal region in South Korea, approximately 250 km from Seoul, as shown in Fig. 2.2. The power plant has six reactors linearly aligned in equal distances of ∼260 m, as shown in Fig. 2.3. These reactors are pressurized water reactors (PWR). The reactor fuelling cycle varies from 12 months to 24 months and the refuellings are performed during plant shutdowns. The total thermal output of the six reactor cores is 16.8 GW_{th}, with each reactor core generating approximately equal power.

2.2.2 Near and Far detectors

One of the main sources of systematic uncertainties is the uncertainty resulting from the neutrino flux of the reactor. To minimize the effects of this problem,

Figure 2.3: Layout of the Hanbit experimental site. The red dots and yellow dots represent reactors and detectors, respectively. Six reactors are spaced approximately equally in a 1280 m span. The near and far detectors are located at a distance of 290 m and 1380 m from the reactor array, respectively. The image taken from Google EarthTM and copyrighted therein. © 2015 Google, DigitalGlobe

Reactor No.	Near Detector (m)	Far Detector (m)
1	667.9	1556.5
2	451.8	1456.2
3	304.8	1395.9
4	336.1	1381.3
5	513.9	1413.8
6	739.1	1490.1

Table 2.2: Distances of the reactor cores from the near and far detectors.

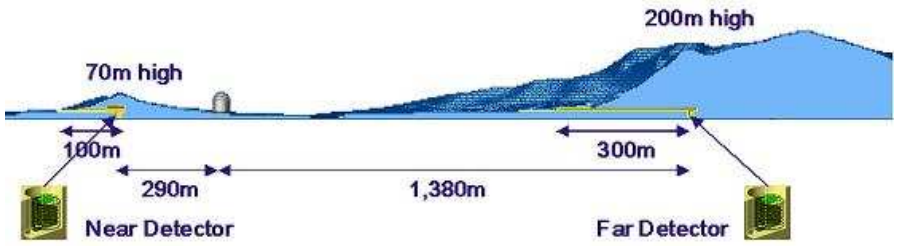

Figure 2.4: Sectional view of the RENO experimental site. The near detector is located under a 70-m hill situated within the perimeter of the power plant, whereas the far detector is located under a 200-m mountain adjacent to the power plant.

two identical detectors, the near and far detectors are employed. Each detector contain 18.7 m^3 of liquid scintillator target doped with 0.1 wt% of gadolinium. The measurement of the ratio of far to near using the two identical detectors significantly reduces the systematic uncertainties in the measurement of θ_{13} owing to the cancellation of their correlated uncertainties. Fig. 2.3 shows the layout of the six reactors and two detectors and Table 2.2 shows the distances between reactors and detectors. The near and far detectors are located at a distance of 294 m and 1384 m from the center of the reactor array, respectively. The near detector is located under an 70-m high (above mean sea level) ridge with an overburden of 110 meter water equivalent (mwe), whereas the far detector is located under a 260-m high mountain with an overburden of 450 mwe as shown in Fig. 2.4.

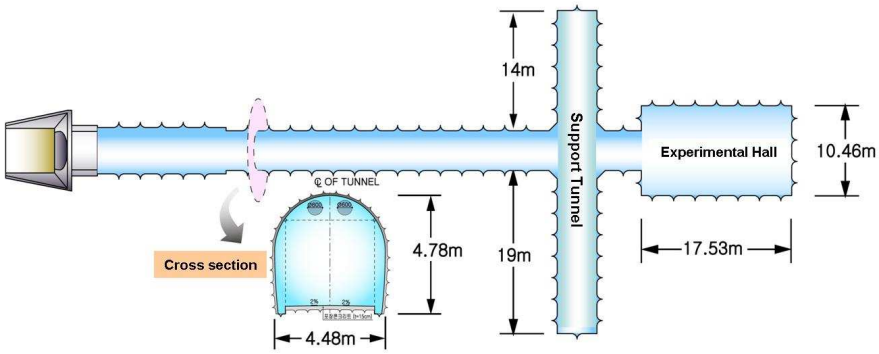

Figure 2.5: Cross-sectional views of the access tunnel and the experimental hall. The tunnels were constructed using the NATM.

2.2.3 Underground Facility and Experiment Halls

The underground laboratories are constructed with two horizontal tunnels, which are 100 m long for the near detector and 300 m long for the far detector, as shown in Fig. 2.5 The tunnels were constructed using the New Austrian tunneling method (NATM). Cross-sectional views of the tunnel and the experimental hall are shown in Fig. 2.5 and a three-dimensional (3D) cross-sectional view of the experimental hall is shown in Fig. 2.6. The access tunnels of the near and far detector sites are 95 m and 272 m long, respectively. A cross-sectional view of the access tunnel is shown in Fig. 2.5. The gradient toward the experimental hall is 0.3% for both tunnels to provide natural drainage. The tunnels were designed to accommodate the passage of a 10-ton truck.

2.3 Detector Setup

The RENO detectors at the near and far sites are identical and consist of a cylindrical target with a radius of 137.5 cm and a height of 315 cm, providing a volume of 18.7 m^3. The detectors consist of a target, γ-catcher, buffer, and veto, arranged concentrically from the centerline to the edge of the detector. A cross-sectional view of the detector is shown in Fig. 2.7.

2.3.1 Target and Gamma Catcher

Structure

The target and the γ-catcher are contained in acrylic vessels, which are transparent to photons with wavelengths above 400 nm. Two important issues for

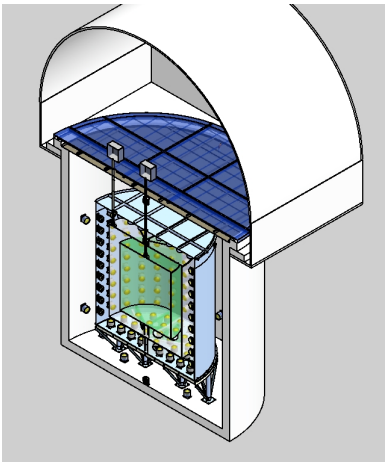

Figure 2.6: 3D cross-sectional view of the experimental hall.

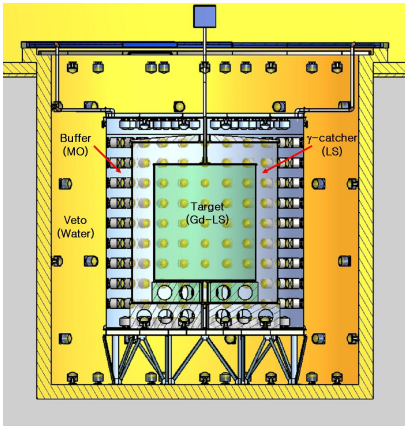

Figure 2.7: Cross-sectional view of RENO detector. The target has a linear alkylbenzene (LAB) based liquid scintillator doped with Gd in a transparent acrylic vessel, surrounded by a 33.2 m^3 unloaded liquid scintillator of γ-catcher and a 76.5 m^3 non-scintillating buffer. 354 and 67 10-inch PMTs are mounted on the buffer and veto vessel walls, respectively.

these layers were considered: the chemical compatibility of the contents and the vessel and mechanical stability.

Considering the chemical compatibility, the liquid scintillating material is required to avoid the chemical interaction with the vessel for both the target and the γ-catcher during of the experiment. At the same time, the γ-catcher vessel is required to be chemically inert to the mineral oil in the buffer layer. Extensive studies have been carried out on the chemical compatibility of these materials for the Chooz experiment and others. The RENO collaboration is also conducting various R&D activities on the chemical interaction of acrylic plastic and other materials used in the experiment.

Mechanically, these vessels are required to withstand mechanical stresses that they are subjected to and maintain their structural integrities during all phases of the experiment. When loaded with liquids, the volume of the vessels can change slightly from their nominal volume. This change is required be maintained within the specified thickness tolerance of 25 mm. The mass of the target vessel is 1.2 tons.

The volume of the target vessel is 19.2 m^3 and the combined mass of the target liquid and vessel with the supporting structure is 17.3 tons. Inside the γ-catcher vessel, the target vessel is mounted on the supporting structure, made of the same acrylic plastic. When both the target and the γ-catcher are filled, the net load on the target supporting structure is 328 kg due to buoyancy. At the center of the top of the vessel, a pipe is installed to connect the target volume to the outside of the detector for the filling of the target liquid and for inserting calibration sources.

The design of the γ-catcher is similar to that of the target, but it has a volume of approximately three times larger. The γ-catcher vessel is a transparent cylinder with a height of 4.4 m, a diameter of 4.0 m, and wall thickness of 3 cm. The γ-catcher vessel is mounted on the supporting structure made of acrylic plastic and located inside the buffer vessel. A pipe connects the top of the γ-catcher vessel and the outside of the detector for liquid filling and for the insertion of the calibration source. The mass of the γ-catcher vessel is 2.8 tons. The combined mass of the γ-catcher vessel and the γ-catcher liquid scintillator is 31.4 tons. When the γ-catcher is immersed in the buffer liquid, the total load on the γ-catcher supporting structure is 2.2 tons.

Acrylic Vessels

The target and γ-catcher vessels are made of polymethylmethacrylate (PMMA), which is a transparent acrylic plastic. The molecular formula of PMMA is (C5O2H8)n and it is also known by trade names, such as Plexiglas, R-Cast, and Lucite. The properties of PMMA are shown in Table 2.3. Using additional ingredients in PMMA, ultraviolet (UV) light below 400 nm can be absorbed. The target and

Properties	Value
Density	1.19 g/cm^3
Melting point	130-140 °C
Refractive index	1.491
Transmittance	92%

Table 2.3: Mechanical and optical properties of cast acrylic, such as Plexiglas GS-233 from Degussa GmbH, Germany and R-Cast from Reynolds Co., USA.

γ-catcher vessels, made of cast acrylic sheets (Plexiglas, GS-233), were supplied by Degussa GmbH, Germany. The cast acrylic sheet has better mechanical and chemical properties than the extruded acrylic sheet. The vessels were manufactured by KOA Tech in Korea. For the convenient production, these vessels are manufactured in several pieces and assembled mostly at the manufacturing site. The vessel parts are bonded by polymerization and the joined sections are treated with an annealing process. The manufacturing precision of the vessels is 0.1% in volume (2 mm in 1 dimension); therefore, a 0.14% difference in the volume of the target vessel between the near and far detector can exist. This difference can be measured and corrected by a mass flow meter and weight measurement.

Chimney

Each target and γ-catcher has a chimney for filling liquids and for transporting calibration sources to and out of the target or the γ-catcher, from the top lid of the veto vessel. The chimney is made of transparent acrylic tubing with a diameter of $\sim$4 inch and a flexible convoluted polytetrafluoroethylene (PTFE) tube connects the buffer vessel and the acrylic tubing for stress relief. The chimney connecting the top lid with the buffer is made of stainless steel pipes extending to the top lid of the veto vessel.

2.3.2 Buffer

The buffer vessel is a stainless steel cylinder, with a height of 5.8 m and diameter of 5.4–m, contains the target, γ-catcher, and buffer liquid. The buffer contains non-scintillating oil to shield the internal scintillating volume from external background sources, including the radioactivity in the PMTs. The buffer vessel also provides mounting surface to the 354 PMTs pointing inward and optically isolates these PMTs from the veto volume. The size of the buffer vessel was determined using Monte Carlo (MC) simulations. The buffer vessel is required to be chemically inert against the mineral oil inside and the water outside. In addition, it is required to withstand the stress arising from the load resulting from the liquids and structures contained by the vessel. The buffer vessel is made of 304L stainless

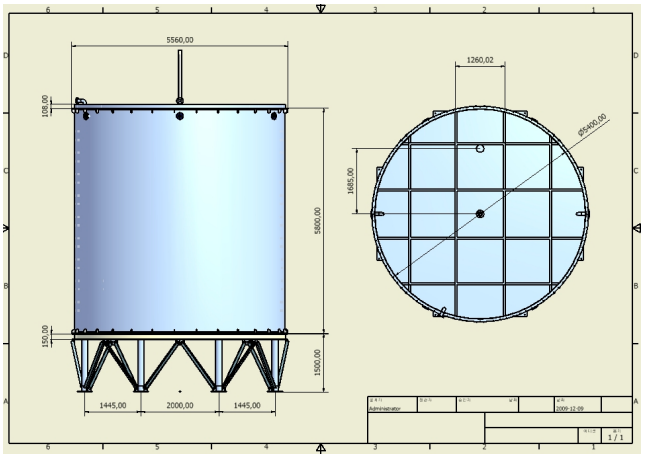

Figure 2.8: External view of the buffer vessel. The vessel consists of stainless steel (304L) and the supporting truss structure consists of nickel-plated steel pipes and rods.

steel with a thickness of 6 mm for the top lid and barrel section and with a thickness of 12 mm for the bottom plate, to provide increased mechanical support. The external view of the buffer vessel is shown in Fig. 2.8. The surface of the vessel is not polished. When the detector is filled with the required liquids, the buffer vessel experiences a buoyant force due to the difference in density between the organic liquids inside the buffer vessel and water in the veto layer. The buoyant force is estimated to be 11.5 tons and the buffer vessel supporting structure is designed to support this force. The buffer vessels are manufactured by Nivak Industrial Co., Ltd., Korea. They are transported as segmented pieces to the experiment site and assembled in the experimental halls. The barrel section consists of eight segments and top and bottom plates, each consisting of three segments. The bottom plate is welded to the barrel section and the top plate is bolted to the barrel section. A total of 354 10-inch PMTs mounted on the inner sidewalls of the buffer vessel, 234 PMTs mounted on the barrel section, and 60 PMTs on the top and bottom plates each, as shown in Fig. 2.9. The PMTs are mounted in upright position on the walls using the a PMT holding structure described in Sect. 2.3.4.

2.3.3 Veto

Design Criteria

The veto system is located outside of the buffer tank exactly adjacent to it.

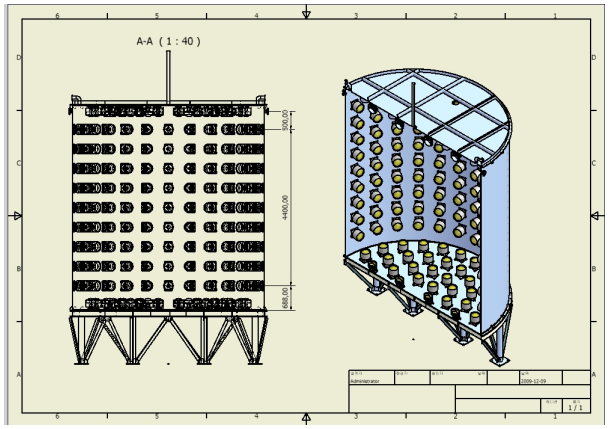

Figure 2.9: Internal detector PMT array in the buffer vessel. A total of 354 10-inch PMTs are mounted on the wall of the vessel using PMT holders.

The main background of the experiment is due to cosmic muons, and it is very important to identify the entering muons because they can produce neutrons via muon–nucleus interaction in the detector. There are also correlated backgrounds from ^{9}Li and ^{8}He in the target and γ-catcher produced by muons. Although the veto system is not included in the trigger, the muon signals in the veto system are used to identify muon-related background events for each candidate event from the neutrino interaction. The veto vessel is required to be chemically compatible with water and sufficiently strong to support all the three inner chambers before filling the liquids.

Structure

The inner diameter and height of the veto vessel are 8.4 m and 8.8 m, respectively. The vessel is constructed with a concrete wall of thickness of 40 cm. The inner surface of the concrete vessel is waterproofed with epoxy resin. The purified water is continuously circulated by a water purification system. There are 67 10-inch waterproof PMTs (R7081 Hamamatsu) attached on the inner surface of the veto vessel. The external surface of the buffer vessel and the internal surface of veto vessel are coated with TiO_2 paint to increase the collection capability of Cherenkov photons in the water. The complete PMT arrangements of both buffer and veto vessels are shown in Fig. 2.10.

2.3.4 PMT

PMT Requirements and Specification

The scintillation lights from the target and γ-catcher are detected by the

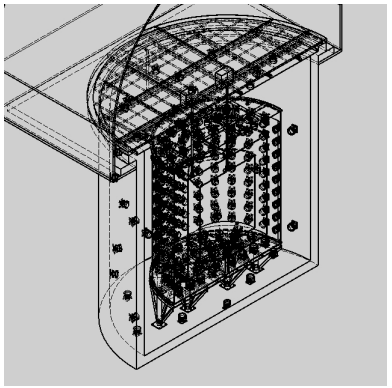

Figure 2.10: Transparent view of PMT arrays showing both the inner and outer PMTs.

PMTs attached on the internal surface of the buffer vessel. The number of detected photoelectrons is measured to be 150 photoelectrons per MeV for an event occurring at the center of the target. As the minimum energy deposited in the detector by a positron emitted in the inverse beta decay is 1.022 MeV, the average number of photoelectrons per PMT in the buffer layer is approximately 0.5. Therefore, the PMTs are required to be able to measure single photoelectrons with high efficiency. The peak-to-valley ratio and the single photoelectron resolution of the PMTs are important parameters. The non-scintillating buffer region is required mainly to shield the γ-catcher and the target from the radioactivity of the PMTs, which needs to be studied to obtain information on the rate of background originating from PMTs. The PMT background events are mostly in the low-energy region of less than 2 MeV and can be incorrectly identified as signals by accidental coincidence with neutron-like background events. As the PMTs are immersed in a layer of mineral oil, it is also important that the complete PMT assembly is required to be chemically inert to mineral oil. The oil proofing is required to be stable for the duration of the experiment. We measured the quantum efficiencies of all PMTs with a relative accuracy of less than 5%. The outlying PMTs were excluded from installation in the detectors.

After considering several performance parameters, such as single photoelectron resolution, afterpulse rate, radioactivity in the PMT, and overall detector performance-to-cost ratio, 10-inch low-background R7081-Low PMTs by Hamamatsu were chosen for RENO. Their specifications are shown at Table 2.4.

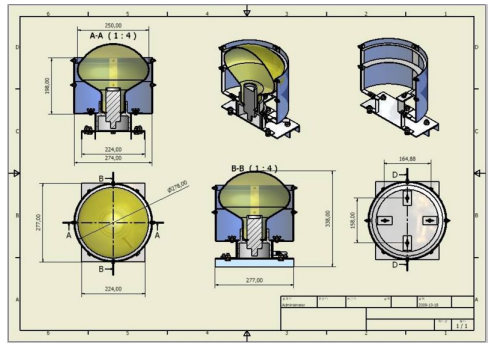

Figure 2.11: Design of the PMT holder. Two stainless steel rims hold the glass of the 10-inch PMT. A cylindrical mu-metal sheet surrounds the individual PMT outside of the rings, to reduce the effect of the magnetic field.

	R7081
Gain($\times 10^7$)	1.0 @ 1500 V
QE @ peak (nm)	25% @390
DC (nA)	50
Size (inch)	10
Weight (g)	1150
Rise Time (ns)	4.3
TTS (ns)	2.9
Afterpulse	2%
Peak-to-valley ratio	3.5

Table 2.4: Specifications of the Hamamatsu R7081 PMTs.

PMT Holder

The PMTs are mounted on the internal wall of the stainless steel buffer vessel. Our aim is to minimize the amount of material while ensuring that the holding structure is as stable as possible. In addition, the distance between the surface of the PMT photocathode and the buffer vessel needs to be minimized. The PMT holder is made of ∼1.5–2.0 mm thick stainless steel. The schematic of the PMT holder is shown in Fig. 2.11. Two rings hold the glass bulb section of the PMT and the front ring defines the photosensitive area. The inner diameter of the rings is 12.3 cm. The side of the structure is surrounded by a mu-metal sheet to reduce the effects of the external magnetic fields. The height of the mu-metal shielding is determined based on a magnetic field survey at the experiment halls.

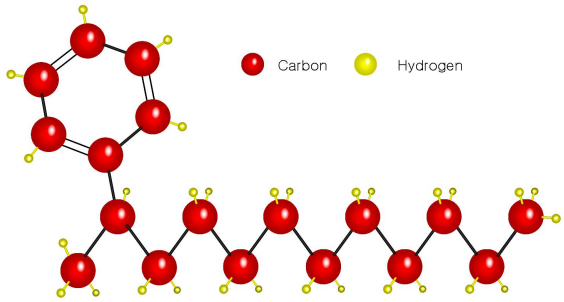

Figure 2.12: Molecular structure of LAB with a linear alkyl chain $C_{12}H_{25}$.

2.4 Liquid Scintillator

In the RENO experiment, linear alkylbenzene (LAB) is used as a base solvent of the liquid scintillator (LS). Previous neutrino experiments typically used pseudocumene (PC or TMB, C9H12, 1,2,4-trimethyl-benzene) as a base solvent of the liquid scintillator, because it provides a higher light yield compared to that of others and has optical clarity. However, it is very toxic and has a low ash point; it is harmful to the human body and to the environment of the experiment. Therefore, LAB is currently used at several neutrino experiments as a replacement. LAB is a safe material and has a high ash point, relatively good light yield, high transmittance, and a large attenuation length. Furthermore, LAB can be purchased at a reasonable price, because it is produced by the Isu Chemical Company in South Korea. Fig. 2.12 shows the molecular structure of LAB. Table 2.4 describes properties of LAB compared with those of PC.

	PC	LAB
Molecular formula	C_9H_{12}	C_nH_{2n+1}-C_6H_5, n ≈ 10–13
Molecular weight (g/mol)	120.19	233∼237
Flash point (°C)	48	130
Density (g/ml)	0.89	0.85
Compatibility (acrylic)	Bad, need diluent	Good
Cost	Moderate	Low
Fluor dissolution	Very good	Moderate
Domestic availability	No	Yes
Toxicity	Toxic fume	Non toxic

Table 2.5: Comparison of PC and LAB.

The organic liquids filling the RENO detector are summarized in Table 2.6.

Region	Radius (mm)	Height (mm)	Volume (m^3)	Type
Target	1388	3176	19.21	0.1% Gd-loaded LS
Target vessel	1400	3200	0.48	Acrylic
γ-catcher	1985	4370	34.37	Unloaded scintillator
γ-catcher vessel	2000	4400	1.20	Acrylic
Buffer	2694	5788	76.64	Non-scintillating oil

Table 2.6: Organic liquids used in various parts of the RENO detector.

2.4.1 Optimization for Liquid Scintillator

Pure LAB absorbs light of wavelength of 260 nm and emits light of longer wavelength with a maximum of 340 nm. The acrylic material used for the target and the γ-catcher vessel rapidly becomes opaque below 390 nm and the quantum efficiency of the installed PMTs (R7081-Low, Hamamatsu) is the most sensitive around the 390 nm region, and still appropriate in the range of ∼400–430 nm. Therefore the scintillation light from LAB needs to be shifted above 400 nm. For this purpose, the RENO experiment uses 2,5-diphenyloxazole (PPO, C15H11NO) as a primary solute and 1,4-bis(2-methylstyryl)-benzene (bis-MSB) as a secondary wavelength shifter. As shown in Fig 2.13, PPO and bis-MSB emit photons at ∼340–440 nm and ∼380–460 nm, respectively.

Even thoughAlthough PPO and bis-MSB is necessary, as additional solute into the LAB decreases the attenuation length; thus,, so we need to optimize the amount of solute needs to be optimized to reach a balance between the benefit of the wavelength shifter and the decrease of in light output from due to the decrease

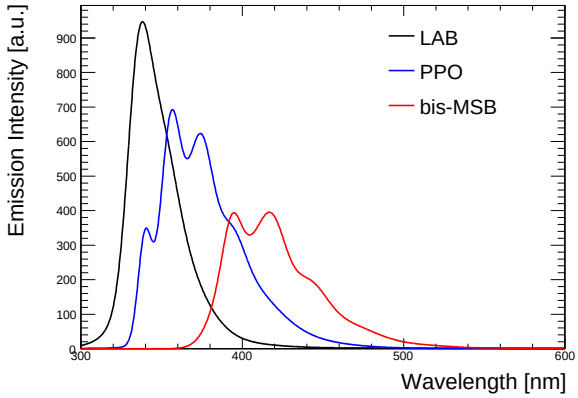

Figure 2.13: Emission spectrum of the solvent LAB (black), the primary fluor PPO (blue), and the wavelength shifter bis-MSB(red).

of in attenuation length. First, We measured the light yield was measured while the amount of PPO wais changed from in the range of ∼1– 20 g/L. Figure 2.14 shows the measured light yield by cahngeas a function of PPO concentration. The light yield is maximalum at an PPO concentration of about ∼3 g/L. Then, We measured the light yield was measured while the amount of bis-MSB wais changed from in the range ∼0– 200 mg/L, and it isas shown in Fig. 2.14. The light yileld becomes saturated at 30 mg/L. Therefore, the amount of solute is determined as PPO 3 g/L for PPO, and 30 mg/L for bis-MSB.

After determining of the amount of the solute, we measured the absorbance of the liquid was measured and converted it to the widely used attenuation length using Beer–Lambert–Bouguer law. The absorbance is given by

$$A = -\log_{10}\left(\frac{I}{I_0}\right), \tag{2.1}$$

where I_0 and I are the flux of the incident and the transmitted lights, respectively. According to the Beer–Lambert–Bouguer law, the attenuation length can be written as

$$\lambda = 0.4343\left(\frac{L}{A_{abs}}\right), \tag{2.2}$$

where L is the length of travel of the light and A_{abs} is the absorbance of a certain wavelength of the light.

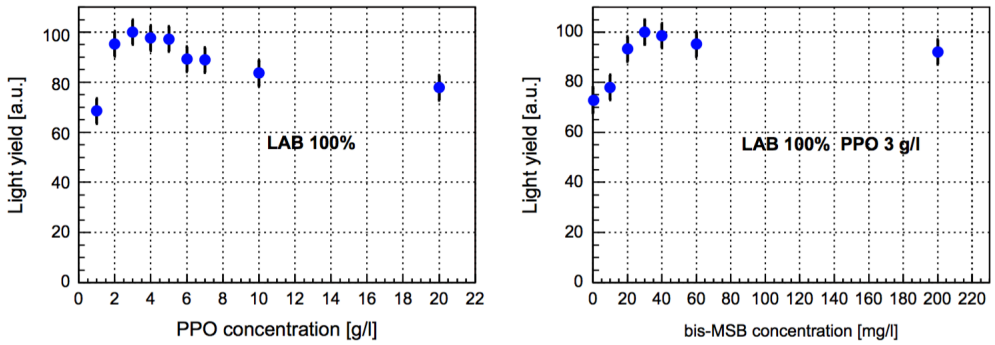

Figure 2.14: Left plot shows relative scintillation light yield of 100% LAB in arbitrary units as a function of PPO concentration. The Right plot shows light yield of 100% LAB and 3 g/L of PPO with as a function of bis-MSB concentration.

Fig. 2.15 shows the measured attenuation length of the LS, LAB, PPO, and bis-MSB. The RENO liquid scintillator has an attenuation length of ∼10 m in the range of ∼400–430 nm.

2.4.2 Gd-loaded Liquid Scintillator

The hydrogen atoms ("free protons") in the liquid scintillator are antineutrino targets in the inverse beta decay reaction. When a neutron is captured by a free proton, gamma rays are emitted with a total energy of ∼2.2 MeV. Nevertheless, a neutron capture on a Gd atom results in an emission of gamma rays with a total energy of ∼8 MeV, which is significantly higher than the energies of the gamma rays from natural radioactivity, which are typically below 3.5 MeV. The mean thermal neutron capture cross section of Gd isotopes is four orders of magnitude larger than that of the proton. Therefore, the liquid scintillator doped with a small amount of Gd is ideal for detecting inverse beta decay events. Gadolinium is a silvery white soft ductile metal belonging to the lanthanide group. It reacts slowly with water, dissolves in acids, and it can form stable organometallic complexes with ligands such as carboxylic acids (R–COOH) and β-diketones. Fig. 2.16 shows the molecular structures of Gd compounds with ligands.

Synthesis of the Gd-Complex

It is difficult to add inorganic Gd salt to an organic liquid scintillator to achieve a stable Gd loaded liquid scintillator. However, two formulations for Gd-loaded liquid scintillator have shown promising results; liquid scintillators where Gd binding with carboxylate (CBX) ligands and with β-diketonate (BDK) lig-

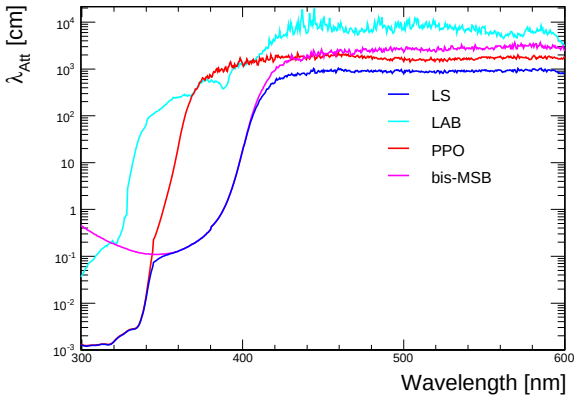

Figure 2.15: Attenuation length of the liquid scintillator. Pure LAB, PPO, bis-MSB are shown as well.

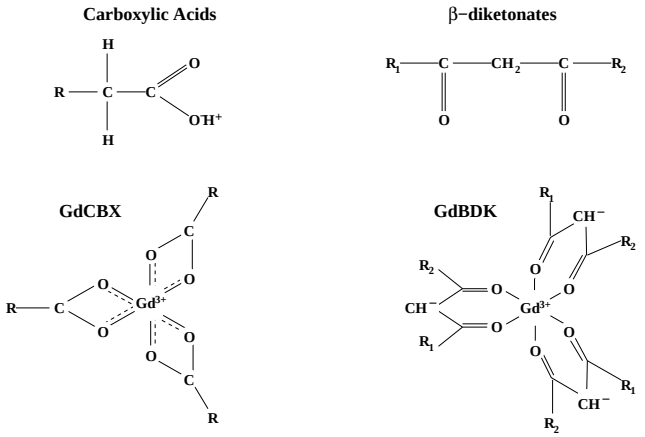

Figure 2.16: Gd compound structures of carboxylic acid and β-diketonate ligands. There are a series of liquid carboxylic acid radicals with different alkyl chains: C2 (acetic acid), C3 (propionic acid), C4 (isobutyl acid), C5 (isovaleric acid), C6 (2-methylvaleric acid, C5H11COOH, HMVA), C8 (ethyl-hexanoic), and C9 (trimethyl-hexanoic).

Figure 2.17: White Gd-TMHA salt following filtration with 0.2 μm pore size Te on membrane filter.

ands. The double Chooz and Daya Bay experiments reported the excellent performance of both BDK and CBX Gd-loaded liquid scintillators. After thorough consideration, we chose to use CBX as our basis for ligands. The Gd-carboxylate compound can be synthetized in three steps:

1. $Gd_2O_3 + 6HCl \rightarrow 2GdCl_3 + 3H_2O$
2. $RCOOH + NH_3 * H_2O \rightarrow RCOONH_4 + H_2O$
3. $3RCOONH_4(\text{aqueous}) + GdCl_3(\text{aqueous}) \rightarrow Gd(RCOO)_3 + 3NH_4Cl$

First, based on step 1, a GdCl3 solution was prepared from Gd2O3. In step 2, 3,5,5-trimethylhexanoic acid (TMHA) was neutralized with ammonium hydroxide. In step 3, two aqueous solutions from steps 1 and 2 were mixed to produce Gd salt. When the two solutions are mixed, white Gd-carboxylate compound (Gd-TMHA) precipitates immediately. These are very pH sensitive reactions . The precipitated Gd-TMHA was thoroughly rinsed with 18 M ultrapure water several times and then dried in a vacuum desiccator. The final Gd-TMHA product is shown in Fig. 2.17. Then, a liquid–liquid extraction technique was used for the second method as shown in Fig. 2.18. Following the reactions, the organic solvent and water can be distinguished owing to the density difference.

2.4.3 Long-term Stability of the Liquid Scintillator

In addition to the light yield, the stability of the Gd-loaded scintillator is another crucial factor. The Gd LS is required to be chemically stable for the duration of the experiment, which is approximately 10 years. To evaluate the long-term stability of the Gd LS, the transmittance values were measured. The results of the transmittance measurements were routinely acquired by a spectrophotometric technique, as shown in Fig. 2.19. To measure these results, the Gd LS samples

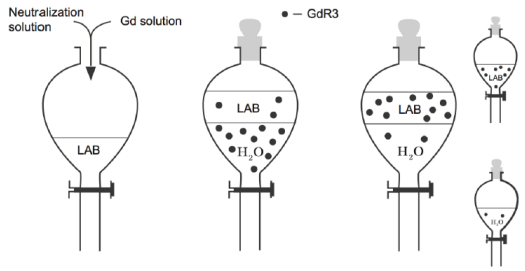

Figure 2.18: Liquid–liquid extraction method. Neutralization solution and Gd solution are mixed into the LAB. The Gd complex is directly dissolved in LAB. Two layers between the LAB and water are separated due to the density difference between the oil and water.

were removed from the target of the detector when the filling of the Gd LS was completed.

However, as time passing, the attenuation length of liquid scintillators starts to decrease, which is indicated by a decrease in the detected number of photoelectrons. Figure B.1 shows that the number of detected photoelectrons at the far and near detectors has decreased since 2013. Organic solvents can be oxidized in the presence of oxygen or water and develop coloration. This oxidization is accelerated by UV light and heat, which can affect the decrease of the attenuation length of the liquid scintillator and decrease the number of detected photoelectrons. Therefore, precautions need to be taken to prevent that moisture or humid air enters the sample. For that reason, since 2015, RENO has been using nitrogen gas to purge oxygen and moisture; therefore, the decrease of the attenuation length of liquid scintillators, such as in Fig. B.1, stopped.

2.5 DAQ and Monitoring System Setup

2.5.1 Front-End Electronics

The antineutrino interaction in the RENO detector produces scintillation lights, and a part of them are converted into photoelectrons by the PMT. To detect the antineutrino event, the RENO detector is equipped with 354 inner PMTs and 67 outer PMTs. The readout system of RENO is designed to record the charge and arrival time of PMT hits. Based on the energy and timing information we can select the neutrino events, reject background events, and reconstruct the vertex of the antineutrino interaction. The near and far detectors are designed to have

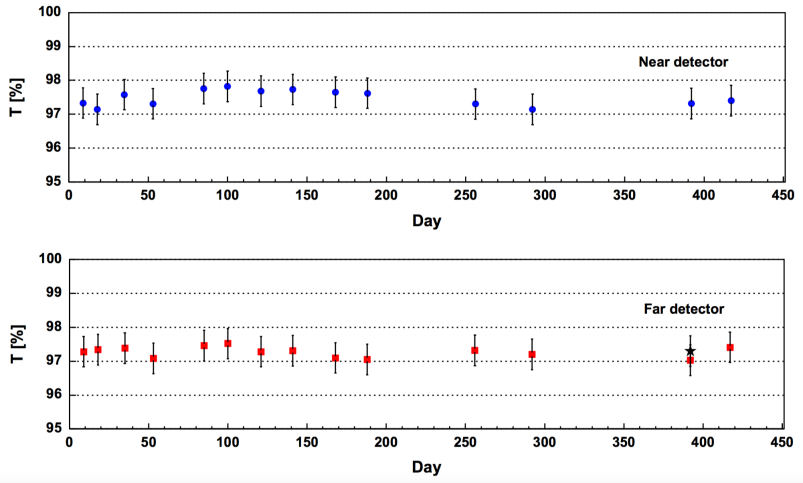

Figure 2.19: Long-term stability results of the Gd-LS as a function of time obtained by measuring the transmittance value at 430 nm.

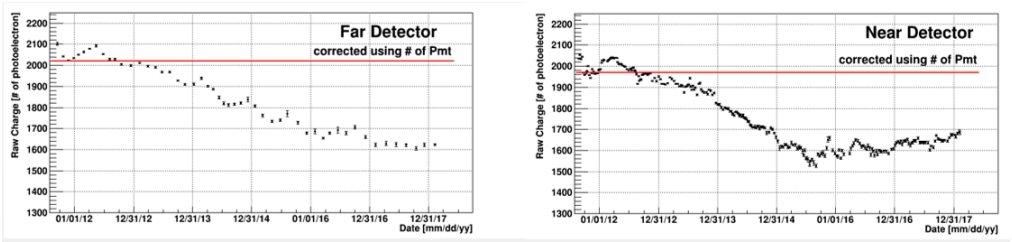

Figure 2.20: Number of detected photoelectrons at the far and near detectors. They are corrected using the number of available PMTs. Charges have decrease since 2013. However, by purging oxygen and moisture using nitrogen gas, charges have stabilized since 2015, or (at the near detector) even started to increase in 2017.

the same PMT configuration and readout system. The RENO DAQ employs electronics developed for the Super-Kamiokande experiment, which uses charge-to-time conversion chips (QTCs) to record hits at 60 kHz with no dead time.

The characteristics of RENO electronics are summarized as follows.

- PMT gain: $\sim 10^7$
- Time window: ∼300 ns
- Dynamic range of PMT signals: ∼1– 1000 photoelectrons
- Time resolution of each PMT signals: ∼1– 1:5 ns
- Data size: ∼ 200 kbyte/s for each detector
- No electronic dead time
- Time resolution between e^+ signal and neutron-like signal : $\sim 10\ ns$

The following section describes the RENO DAQ electronics.

2.5.2 Qbee Board

The QTC-based electronics with Ethernet (QBEE) board is an electronics based on QTC, with an onboard Ethernet card, developed for the Super-Kamiokande experiment and has been used since Sept. 2008. The new electronics system is sufficiently fast to record every PMT hits and its stable data acquisition is guaranteed for over ten years. Each QBEE board is equipped with a 100-Mbps Ethernet card, which is sufficiently fast to transfer all hit information to an online computer without any loss. The hit information is stored in the online storage and then the software triggers are applied.

The PMT pulse generated by a photon hit is fed to a QTC chip. The QTC chip measures the hit time and the charge of the PMT pulse and convert them into a form that can be easily read and stored by the time to digital converters (TDCs). The output of the QTC chip is a logic pulse with its leading edge marking the hit arrival time and its width representing the integrated charge of the PMT pulse. The characteristics of the QTC chip are summarized in Table 2.7.

The operation logic diagram of the QTC chip is shown in Fig. 2.21. The QTC chip integrates the charge of a PMT pulse fed to the chip and outputs a pulse with a width proportional to the integrated charge. The QTC chip produces two gates for its the operation of charge integration operation:, one for charging the capacitor (charge gate) in the QTC chip and the other for discharging the capacitor for to measureing the charge in the capacitor (measure gate). If an incoming PMT pulse exceeds a current threshold, the a 400- ns- wide charge gate

Dynamic range	$0 \sim 2500$ pC
Self trigger	Built-in discriminator
Number of input channels	3
Processing speed	~ 500 ns/cycle
Gain	1/7/49 (3 settings)
Charge resolution	0.05 p.e. (< 25 p.e.)
(Non-) Linearity (Q)	$< 1\%$
Timing resolution	0.3 ns (1 p.e.$= -3$ mV), 0.2 ns(> 5 p.e.)
Power dissipation	< 200 mW/channel

Table 2.7: Characteristics of QTC chips, where. p.e. is denotes photoelectron.

and a 966- ns- wide measurement gate are generated. Therefore, the width of the output pulse from a QTC chip is between in the range of 400 and– 966 ns which is proportional to the size of the integrated charge. A reset signal of 34 ns is generated after the measurement gate; thus,. So the processing time of a QTC chip is 1 μs per cycle. The output pulse from the QTC is fed into a multi-hit TDC where the timing information of all leading and trailing edges are recorded.

A QTC chip receives three analog inputs and processes each input with one of three gains of 1, 7, and 49. The charge resolution is about $\sim$0.1 pC and the its dynamic range is 0.2– to 2500 pC. The timing resolution is 0.3 ns for one photoelectron and 0.2 ns for more than five photoelectrons.

A QBEE board accommodates eight QTC and four TDC chips to process 24 analog inputs. The QBEE board receives an external clock signal of 60 MHz and a periodical trigger signal of 60 kHz from a master clock. The 60- kHz periodical trigger signal initializes the TDC and comes arrives with a timing tag and an event number, which are used to identify the PMT hits in the same trigger. After collecting all the hits, an event is built and selected by software triggers. The adjustable QTC parameters for RENO are 1) the threshold level for a single photoelectron signal and, 2) the length of the charge gate and measurement gate.

2.5.3 DAQ System

The RENO DAQ consists of a data readout using front-end electronics, an event builder, software triggers, a data logger, and run control. Schematic diagrams of the RENO DAQ system are shown in Figs. 2.22 and 2.23.

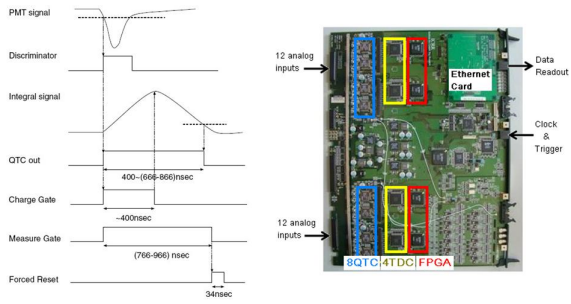

Figure 2.21: Operation logic diagram of the QTC chip and the QBEE board.

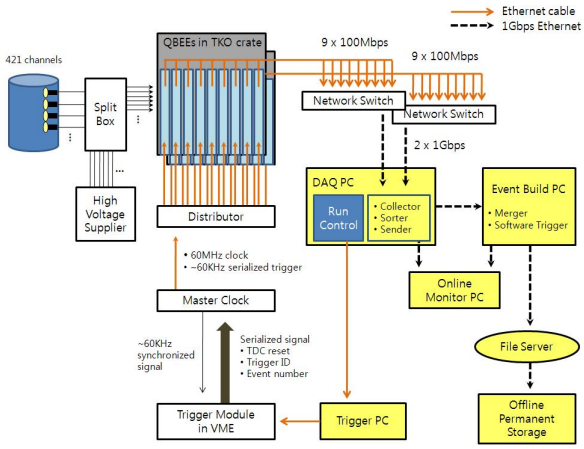

Figure 2.22: Diagram of DAQ system for RENO. There are 18 QBEE boards in two TKO crates collecting the hit signals from 421 PMTs (354 PMTs in the inner detector and 67 PMTs in the veto). The near and far detectors have the same DAQ architecture.

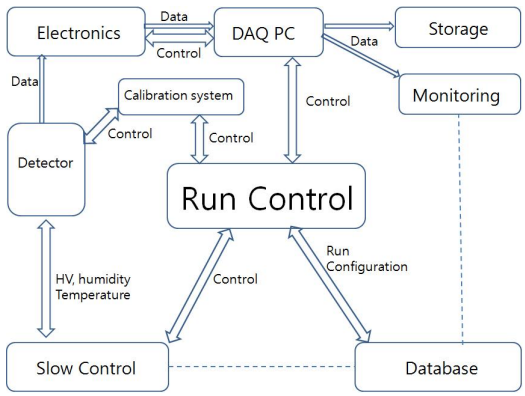

Figure 2.23: Flow diagram of run control for RENO. The run control sends commands to the DAQ component and generates run conditions. Operators use integrated GUI.

Data Readout and Run Control

The front-end electronics for the data readout are based on QBEE boards in the TKO crate and ethernet Ethernet cards on QBEE. A QBEE board receives 24 analog PMT inputs, digitizes them, and sends the signal outputs to the online computer through via an 100- Mbps Eethernet card. The RENO experiment uses 18 QBEE boards for 421 channels per detector, and the data throughput rate is about ∼1.8 Gbps per detector. The near and far detectors have the same DAQ architecture.

The run control sends commands to DAQ components and makes generates run conditions. Shift crewThe operators uses an integrated graphical user interface (GUI), which where can be used to selectthe run mode, trigger type, and detector parameters can be selected. The trigger type can be chosen from one of predefined trigger sets. The detector parameters are high- voltage settings for the PMTs. The "Run Controller" pannel is shown in Fig. 2.24.

Event Builder

All the QBEE boards are driven by a common 60- MHz master clock (MCLK). A 60- kHz periodical trigger and a serialized 32-bit event number are generated by a trigger module, and fanned out via a distributor to all the QBEE boards through via network cables. All the hit data are sorted and merged according to the trigger event number and the timing information.

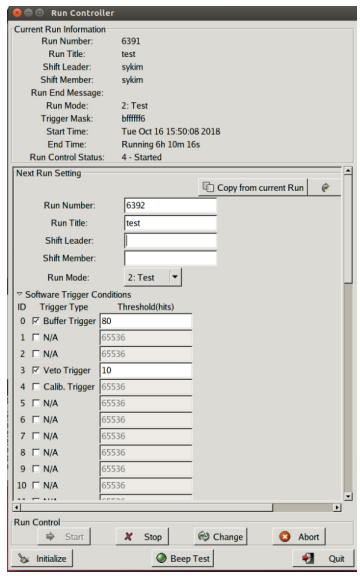

Figure 2.24: Display of the run control panel, where run mode and data acquisition conditions can be selected.

A periodic trigger of 60 kHz makes creates a data block of hits. The order of the data blocks is made determined according to the event number. The hits in a data block are sorted by their hit time and merged. The hit data in the same block are merged, sorted by hit time, and stored with an event number. An event builder constructs events by applying a software trigger to the merged hit data. The merged data Bbefore the application of the software trigger, the merged data are stored for several days and used for monitoring purposes.

Software Trigger

The software triggers are applied to the events constructed by the merger to identify neutrino candidate events, cosmic muon events, or calibration events. The software trigger calculates the total number of hits (multiplicity) within a 50-ns time window and constructs an event if the sum of the hits sum exceeds a certain threshold number. The threshold number of the event is 90 hits (corresponding to $\sim$0.5$\sim$–0.6 MeV) for the inner detector (ID) trigger and 10 hits for the outer detector (OD) trigger from the first data taking acquisition in Aug. 2011 to May. 2017. Since June. 2017, the ID trigger threshold number has been changed to 80 hits. The decrease of the Gd-LS attenuation length and the PMT coverage

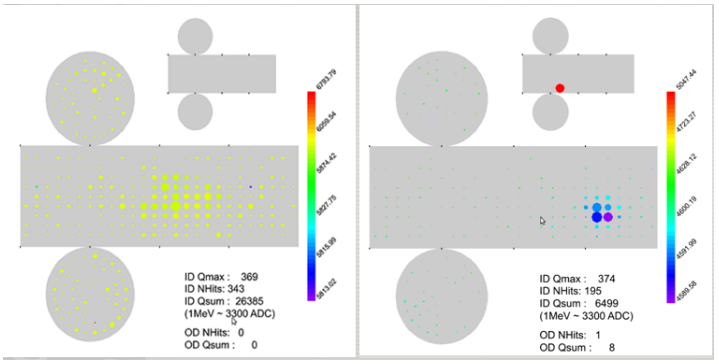

Figure 2.25: RENO event display. The center of the circle indicates the PMT that was hit, the size of the circle is proportional to the charge of the hit, and the color corresponds to the time of the hit.

due to the withdrawal of broken PMTs resulted in the decrease in the number of detected number of photoelectrons and trigger inefficiency at low-energy for the threshold of 90 hits. The time of the first hit time in an event is set to T_0, and the time windows before and after T_0 determine an event gate by software triggers. All PMT hits within this event gate create an event and calculate the sum of charges in time gate (approximately -100–50 ns).

2.5.4 Slow Control and Monitoring system

An online monitoring computer, located in the control room, reads the data from the DAQ host computer via the network. It provides event display and online histograms to monitor the detector performance and variety of additional tasks needed for the efficient monitoring of the detector performance parameters and for the diagnoses of malfunctions of the detector or the DAQ system.

The event display shows the charge and hit time information of the trigger for an individual PMT in real time, as shown in Fig. 2.25. The center of the circle indicates the PMT that was hit, the size of the circle is proportional to the charge of the hit, and the color corresponds to the time of the hit.

The online histograms show the accumulated condition of the DAQ system: the channel of the ID and OD PMT that was hit, the number of hits of the trigger, and trigger histograms. The operators can recognize any problem in the DAQ system from the online histograms. Fig. 2.26 shows the online histogram panel.

The slow control monitors the status of the high-voltage (HV) systems, the temperature of the electronics crates and detectors, fluids levels, and humidity.

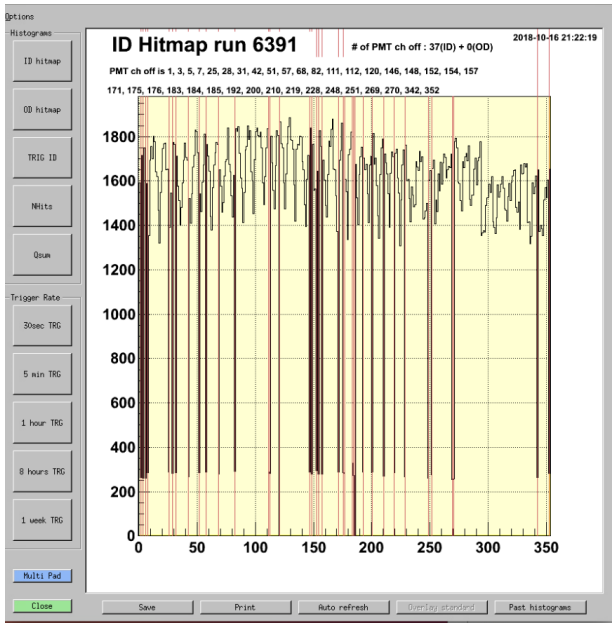

Figure 2.26: Online histogram panel.

In addition, the slow control is able to feed HV for each channel and turn on and off HV remotely. The slow control scheme is shown in Fig. 2.27.

High voltage (∼1700 V) is required to be supplied to the PMTs need to supply high voltage (∼1700 V). Nine 48-channel power supply module (A932AP) in two crates (SY1527), purchased manufactured by CAEN S.p.A., are used at eachboth two detectors. The supplied high voltageHV value should is required to be stable and be checkedmonitored by shift crewoperators. In this needsFor this purpose, the a high voltage monitoring system based on Labview wais developed, using Labview as shown in Fig. 2.28. The status of each high voltageHV channel is displayed by colors. The PMTs which that show provide weird unusual signals or highly flashing are disconnected and shown indicated as bya black circles, as shown in Fig. 2.28.

The experimental environmental conditions, such as temperature and humidity also should are required to be stable during the data acquisition as well. To prevent the damage of the electronics from the humidity and temperature, an air conditioner and a dehumidifier are installed in the experimental hall, in the electronics hut, and in the control room. To monitor the temperature, three thermocouple inside the detector and two thermocouples in the electronics hut and in the control room are installed. The humidity is also monitored by a sensor. For

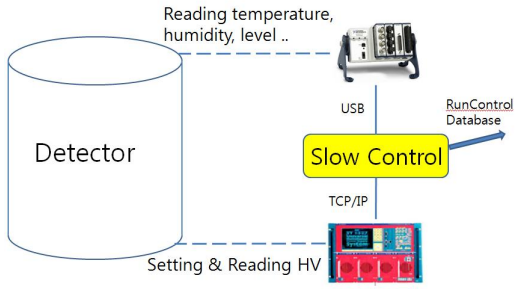

Figure 2.27: Diagram of slow control. The slow control system monitors detector conditions and controls the PMT HV power supplies of the PMT.

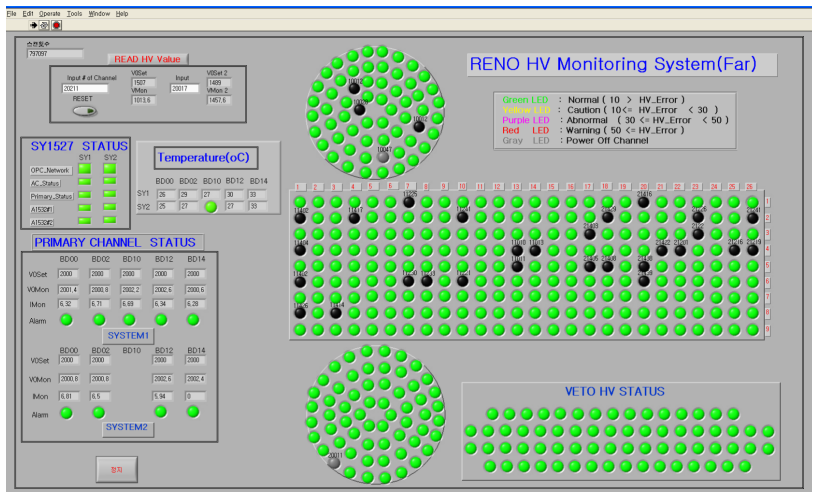

Figure 2.28: RENO HV monitoring system. The broken or highly flashing PMTs are disconnected and indicated by black circles.

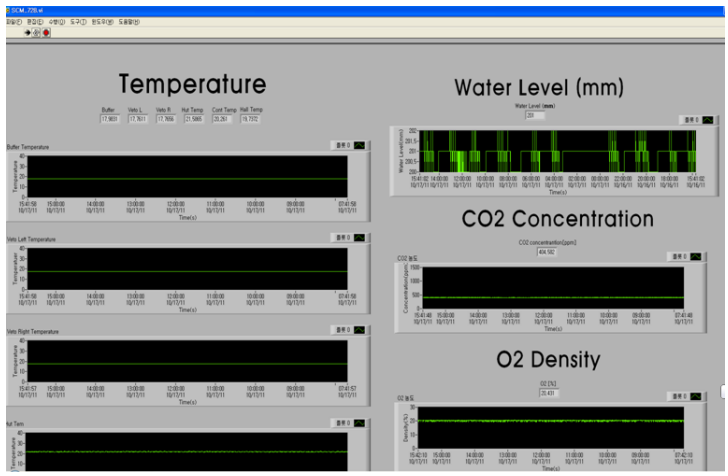

Figure 2.29: RENO slow monitoring system. The temperature, humidity, O2, CO2, and Water level in the OD are monitored.

safety reasons, O_2, CO_2, and Ra sensors are installed. The veto is filled with pure water for the Cherenkov radiation. The water is required to be purified to prevent the deterioration of its quality. Thus, the level of filled water is also monitored by a sensor. If the water level reaches the high setting threshold, the water circulation and purifying system pumps out water in the veto region automatically and refills it with purified water. The operators can check all these environmental conditions by the slow monitoring system, as shown in Fig. 2.29.

Chapter 3

Expected Reactor Antineutrino Flux and Spectrum

3.1 Production of Reactor Neutrino

Reactor neutrinos are emitted as a result of the decay of fission products of fissile isotopes in the reactor core (Fig. 3.1).

The fissile material in a reactor is mainly composed of ^{235}U and ^{239}Pu, which undergo thermal neutron fission. The dominant ^{238}U is fissile only for fast neutrons. However, it also undergoes fission by thermal neutron capture and produces ^{239}Pu as a result

$$n + {}^{238}\text{U} \rightarrow {}^{239}\text{U} \rightarrow {}^{239}\text{Np} \rightarrow {}^{239}\text{Pu}. \tag{3.1}$$

Similarly, ^{241}Pu is generated from ^{239}Pu,

$$n + {}^{239}\text{Pu} \rightarrow {}^{240}\text{Pu} \rightarrow {}^{241}\text{Pu}. \tag{3.2}$$

The contribution of four fissile isotopes, namely ^{235}U, ^{239}Pu, ^{238}U, and ^{241}Pu, is significant, while that of other isotopes is only marginal (0.1%). Fission fragments from these four isotopes sequentially decay and emit electron antineutrinos. The antineutrinos emitted are exceedingly pure and the electron-neutrino contamination is only at a level of 10^{-5} above the inverse decay threshold of 1.8 MeV.

The fission rates of the four fissile isotopes are shown in Fig. 3.2. As shown in Table 3.1, these four isotopes release similar amounts of energy. Therefore, even though the composition of the fissile material in the reactor changes over the

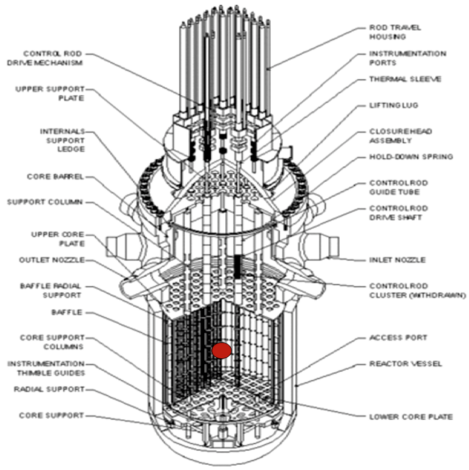

Figure 3.1: A pressurize water reactor core. Red dot is the center of reactor fuel.

Isotope	Mean Energy Per Fission (MeV)
^{235}U	201.7 ± 0.6
^{238}U	205.0 ± 0.9
^{239}Pu	210.0 ± 0.9
^{241}Pu	212.4 ± 1.0

Table 3.1: Mean energy emitted per fission of four main isotopes

refuelling cycle, the average mean energy per fission does not change significantly. Assuming approximately 200 MeV per fission, there are 3.1×10^{19} fissions per GWth. Because one fission results in an average of six neutrino emissions above 2 MeV, the neutrino intensity can be estimated to be 2×10^{20} /(GW_{th} s). Because the neutrinos are radiated isotropically from the reactor core, the inverse square law is applicable to neutrino intensity at a distance. The neutrino energy spectrum from a reactor is shown in

These four isotopes of the reactor fuel β-decay at various energy levels and their neutrino spectra are different from each other as shown in Fig. 3.3.

The neutrino energy spectra from fission processes are parameterized in Refs. [61, 62] using

$$\phi_\nu^{(j)} = exp\left(\sum_{i=0}^{5} a_i^{(j)} E_\nu^i\right) \tag{3.3}$$

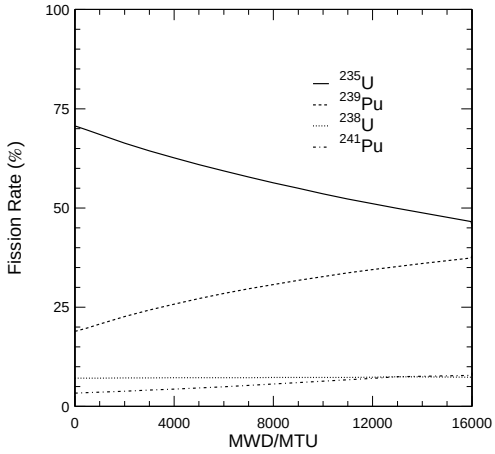

Figure 3.2: The evolution of fission rate of the four dominant fissile isotopes of a typical refuelling cycle.

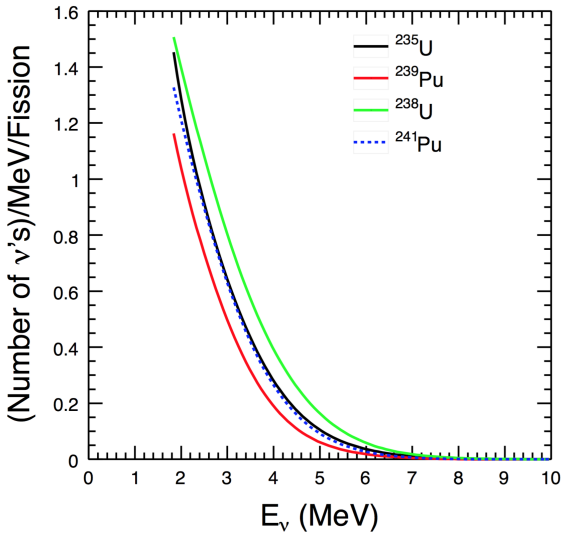

Figure 3.3: The neutrino spectra from fission of four isotopes

where $a_i^{(j)}$ are the fitting parameters for the jth isotope and E_ν is neutrino energy in MeV. The results are shown in Table 3.2 and Fig. 3.3.

Parameter	^{235}U	^{238}U	^{239}Pu	^{241}Pu
a_0	4.367	4.757	4.833×10^{-1}	2.990
a_1	-4.577	-5.392	1.927×10^{-1}	-2.882
a_2	2.100	2.563	-1.283×10^{-1}	1.278
a_3	-5.294×10^{-1}	-6.596×10^{-1}	-6.762×10^{-3}	-3.343×10^{-1}
a_4	6.186×10^{-2}	7.820×10^{-2}	2.233×10^{-3}	3.905×10^{-2}
a_5	-2.777×10^{-3}	-3.536×10^{-3}	-1.536×10^{-4}	-1.754×10^{-3}

Table 3.2: Parameters of the 5th order polynomial for the neutrino flux from the dominant isotopes in the nuclear fuel. Parameters for isotopes ^{235}U, ^{239}Pu, and ^{241}Pu are taken from Ref. [62]and ^{238}U from Ref. [61]. The resulting distributions are shown in Fig. 3.3

The fission rate in a reactor with a power P_{th} is

$$n_{fis} = \frac{P_{th}}{\sum_i f_i \bar{E}_{fi}}, \tag{3.4}$$

where f_i and $\bar{E}_{fi}$ are the fission fraction of the nuclear fuel and the mean energy released per fission of isotope i, respectively, given in Table 3.1, and P_{th} is the reactor power. Then, the number of fissions per second, n_{fis}, is related to the reactor power by $(6.24 \times 10^{18}) \cdot n_{fis}$, where P_{th} is in Watts and E_{fi} in eV, as seen in Eq. 3.4.

The number of neutrinos with energies between $E_{\min}$ and $E_{\max}$ from the fission process of the ith isotope is

$$N_\nu = n_{fis} \cdot \sum_i f_i \int_{E_{\min}}^{E_{\max}} \frac{dN_\nu^{(i)}}{dE_\nu} dE_\nu \tag{3.5}$$

The neutrino flux, which is isotropic about the source, at a distance r is

$$n_\nu(r) = \frac{1}{4\pi r^2} N_\nu. \tag{3.6}$$

3.2 Calculation of Reactor Neutrino Flux

The expected rates and spectra of the reactor antineutrinos are calculated for the duration of the data extraction by taking into account the varying thermal powers, fission fractions of four fuel isotopes, energy release per fission, and fission

and capture cross-sections. The equation to calculate the number of expected antineutrinos in the detector d is as follows

$$N_\nu^d = \frac{N_p}{4\pi R^2} \frac{\sum_i \alpha_i \bar{\sigma}_i}{\sum_i \alpha_i E_i} P_{th} = \frac{N_p}{4\pi R^2} \frac{\bar{\sigma}_5 \left[1 + \sum_i \alpha_i \left(\bar{\sigma}_i/\bar{\sigma}_5 - 1\right)\right]}{E_5 \left[1 + \sum_i \alpha_i \left(E_i/E_5 - 1\right)\right]} P_{th} \tag{3.7}$$

where,

- N_p : the number of target protons.
- R : the distance between the detector and the reactor.
- α_i : the fission fraction of the ith isotope. (^{235}U, ^{238}U, ^{239}Pu, ^{241}Pu))
- $\bar{\sigma}_i = \int \sigma\left(E_\nu\right) \phi_\nu^{(i)} dE$: Total number of IBD events per fission produced in a detector for the ith isotope.
- $\bar{\sigma}_5$: $\bar{\sigma}$ for the ^{235}U.
- E_i : energy released per fission for the ith isotope.
- E_5 : energy released per fission for the ^{235}U.
- P_{th} : reactor thermal power generated.

The above expression can also be expressed as

$$N_\nu^d = \gamma \left(1 + k\right) P_{th} \tag{3.8}$$

where, $\gamma = \frac{N_p \bar{\sigma}_5}{4\pi R^2 E_5}$ is a constant for a given detector and geometry, and $1 + k = \left[1 + \sum \alpha_i \left(\bar{\sigma}_i/\sigma_5 - 1\right)\right] / \left[1 + \sum \alpha_i \left(E_i/E_5 - 1\right)\right]$. $1 + k$ is time-dependent because the fission fraction of the four isotopes evolve with time.

The number of target proton N_p

The target free-proton number is decided by the amount of linear alkyl benzene (LAB) present in the target detector. The free proton number and molecular weight of RENO's LAB molecule are 30 and 240.7, respectively, which are taken from the composition analysis sheet provided by the manufacturer. The density of LAB measured by a densitometer with a resolution of 0.001 is 0.85 g/L . The measured target volume is 18,641 ± 5 L at the near detector and 18637 ± 5 L at the far detector. The number of free proton is calculated by following equation,

$$N_p = \rho N_A V \frac{30}{M_A} \tag{3.9}$$

where ρ is the density of LAB, N_A its Avogadro's number, M_A its molecular weight (240.7), 30 its free proton number, and V the measured volume of the target detector. The calculated number of target protons is 1.189×10^{30} for both near and far detectors. The corresponding uncertainty is 0.5 % and the uncorrelated uncertainty is 0.1 %.

The Distance of The Detector and The Reactor R

The neutrino flux is isotropic about the source, causing the flux to reduce at a rate inversely proportional to the square of the distance. The distances between the detector and the reactor are calculated considering each detector's target center and each reactor's center. The coordinates of the reactor core center and the detector target center were determined from a survey on the national cadastral control points near the power plant and the reactor and detector blue prints. The uncertainties of the baselines are of the order of cm. The distances between each detector and each reactor are shown in Table 3.3.

	Near	Far
R1	660.06	1563.77
R2	444.73	1460.83
R3	301.56	1397.81
R4	339.26	1380.06
R5	519.97	1409.39
R6	746.16	1483.00

Table 3.3: The distance between each detector and each reactor in meters.

Fission Fraction of Isotopes α

The fission fractions of the four isotopes evolve with time, and it causes an increment of 1+k over time. The isotope fraction changes the expected reactor neutrino energy spectrum also. The average fission fraction of each reactor for 2,200 days are summarized in tables 3.4 and 3.5 below.

Reactor	U235	U238	Pu239	Pu241
1	0.565	0.076	0.303	0.056
2	0.571	0.076	0.298	0.055
3	0.569	0.072	0.303	0.056
4	0.582	0.072	0.292	0.053
5	0.571	0.072	0.300	0.056
6	0.589	0.072	0.287	0.052

Table 3.4: The average fission fraction of the 4 isotopes for near detector (2,200 days).

Reactor	U235	U238	Pu239	Pu241
1	0.567	0.076	0.302	0.056
2	0.574	0.076	0.296	0.054
3	0.570	0.072	0.302	0.056
4	0.580	0.072	0.294	0.054
5	0.569	0.073	0.302	0.057
6	0.585	0.072	0.290	0.053

Table 3.5: The average fission fraction of the 4 isotopes for far detector (2,200 days).

Total number of IBD events produced in a detector per fission for the ith isotopes $\bar{\sigma}_i$

For each isotope, the total number of IBD events per fission produced in a detector is calculated by convolving the IBD cross-section with the antineutrino energy spectrum, which is the expected energy spectrum of antineutrinos per fission from the each isotope, as shown Fig 3.4.

Energy Released Per Fission E

The mean energy emitted per fission has been calculated in [39]. and is summarized in Table 3.1.

Reactor Thermal Power Generated P_{th}

The maximum thermal power is 2.90 GWth for the reactor 1 2 and 2.815 GWth for the reactor 3 6. However, the thermal output of the reactors vary by time

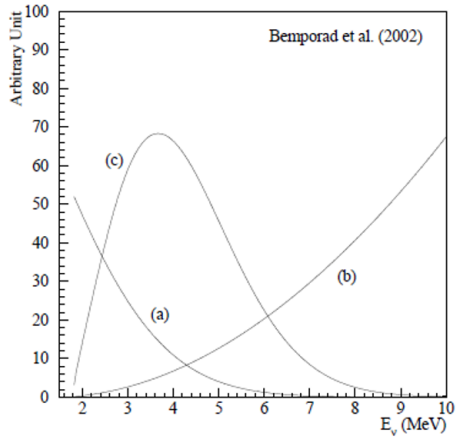

Figure 3.4: Reactor $\bar{\nu}_e$ flux (a), IBD cross-section (b), and interaction spectrum at a detector based on such reaction (c). The cut-off at 1.8 MeV is because of the minimum neutrino energy required for the IBD process.

passing. The thermal power can be calculated by considering the thermal output like maximum P_{th}×thermal output(%), which is provided by KNHP as the daily mean thermal output. The average thermal powers for 2,200 days as shown in Table 3.6.

Reactor	Near	Far
1	81.28	81.32
2	72.47	72.53
3	76.65	76.72
4	74.72	74.79
5	84.53	84.58
6	82.26	82.32

Table 3.6: The average thermal powers for 2,200 days.

Flux Variation Coming from Fuel Burning 1 + k

The increment 1+k is time-dependent as the fission fractions of the four isotopes evolve with fuel burning. Since we were provided with the values of fission fraction and cycle burn-up, which are determined by the reactor-core simulations of ANC for an interval of approximately 1 month from the Korea Hydro & Nuclear Power

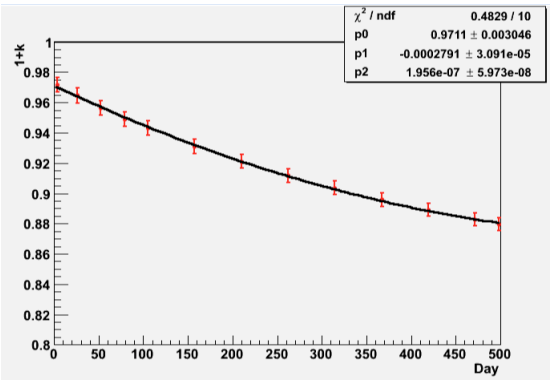

Figure 3.5: Fitting of 1+k factor for reactor 1, cycle 20

Co (KHNP), the everyday 1+k can be predicted by fitting. Fig. 3.5 shows the fitting of 1+k for reactor 1 and cycle 20. The elapsed time (x-axis in Fig. 3.5) is calculated by dividing cycle burn-up by the mean daily burn-up.

Calculated Number of Antineutrino Flux N_ν^d for 2200days of data

BBy substituting the quantities obtained above into Eq. 3.9, the expected number of antineutrino events detected at the detector is determined and summarized in Table 3.7.

Reactor	Far	Near
1	32899.3	153606
2	33259.1	295061
3	37185.5	680556
4	37616.7	500316
5	40838.7	240168
6	35824.6	112359

Table 3.7: Expected flux for 2,200 days of data for far and near detectors. Visible energy range is 1.2∼8 MeV

3.3 Expected Interaction Antineutrino Spectrum

The expected interaction antineutrino spectrum in each detector d can be calculated using the following equation,

$$S_\nu^d = N_\nu^d \left(\sum_i I_i s_\nu^i \right) \tag{3.10}$$

where, $N_\nu^d \left(= \sum_i N_{\nu,i}^d \right)$ is the expected number of antineutrinos obtained above (where $N_{\nu,i}^d$ is the expected number of antineutrino of the ith isotope at the detector d) and $I_i \left(= \frac{N_{\nu,i}^d}{\sum_i N_{\nu,i}^d} \right)$ is the fraction of neutrino interaction at the target by neutrino produced by the isotope species i. The average interaction fractions at each reactor are summarized in the Table 3.8 and 3.9. And $s_\nu^i \left(= \sigma\left(E_\nu\right) \phi_\nu^{(i)} / \int \sigma\left(E_\nu\right) \phi_\nu^{(i)} dE_\nu \right)$ is the normalized interaction spectrum of the ith isotope, as shown on the plot on the left side in Fig. 3.6. From Eq. 3.10, the expected interaction antineutrino spectra are shown in the plots on the middle and right side in Fig. 3.6.

Reactor	U235	U238	Pu239	Pu241
1	0.607	0.124	0.214	0.055
2	0.612	0.124	0.210	0.053
3	0.612	0.119	0.214	0.055
4	0.624	0.118	0.206	0.052
5	0.614	0.119	0.212	0.055
6	0.629	0.118	0.202	0.051

Table 3.8: The average interaction fraction of 4 isotopes for near detector, 2,200 days. This will be changed later.

Reactor	U235	U238	Pu239	Pu241
1	0.608	0.124	0.213	0.055
2	0.615	0.124	0.209	0.053
3	0.613	0.119	0.213	0.055
4	0.622	0.118	0.207	0.053
5	0.612	0.119	0.213	0.056
6	0.626	0.118	0.204	0.051

Table 3.9: The average interaction fraction of 4 isotopes for near detector, 2200day. This will be changed later.

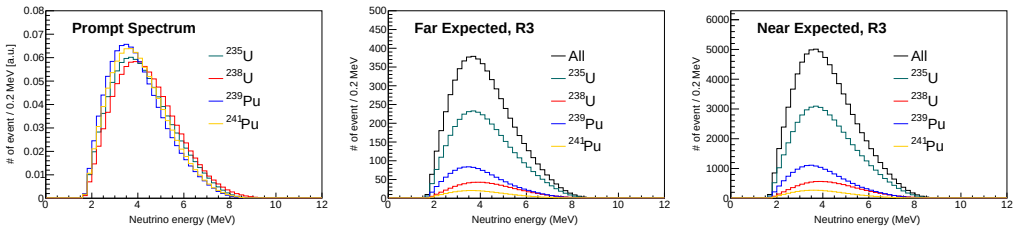

Figure 3.6: Expected interaction spectrum of a neutrino. Left side shows the normalized interaction spectrum for each isotope. Middle shows the expected interaction spectrum of reactor 3 for the far detector and the right side shows the same for the near detector.

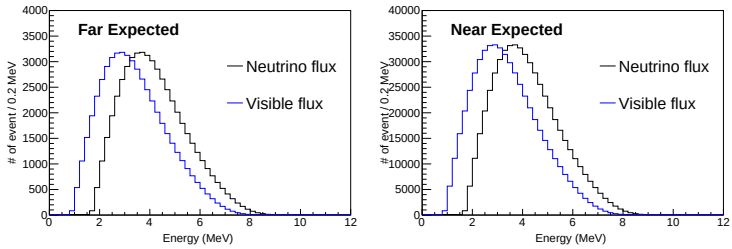

Figure 3.7: Expected neutrino and visible energy spectra. Left plot shows the far detector, and right plot shows the near detector. The black line represents the expected interaction spectrum of a neutrino at the detector. Blue line shows the expected visible spectrum of a neutrino at the detector.

3.4 Systematic Uncertainties of Expected Reactor Neutrino Flux and Spectrum

The systematic uncertainties are of two types: correlated and uncorrelated. The number of correlated systematic uncertainties and the direction in which they occur are the same for both the detectors. Therefore, by using identical detectors, these uncertainties can be canceled out. Uncorrelated systematic uncertainties, however, are independent of each other. This type of uncertainties cannot be canceled out. The systematic uncertainties of expected reactor neutrino flux and spectrum are a result of the thermal power output, fission fractions of the four isotopes, energy released per fission, and capture cross-section. These uncertainties are summarized in Table 3.10.

Parameter	Uncorrelated	Correlated
Baseline	0.03%	-
Thermal Power	0.5%	-
Fission fraction	0.7%	-
Fission reaction cross section	-	1.9%
Reference energy spectra	-	0.5%
Energy per fission	-	0.2%
Combined	0.9%	2.0%

Table 3.10: Systematic uncertainties of Expected Reactor Neutrino Flux

Baseline

The distance from the detector center to reactor fuel center has been precisely measured with an uncertainty below 10 cm. The shortest baseline, which is between reactor 3 and the near detector, is 301.56 m. Therefore, the maximum systematic uncertainty is $0.1/301.56 = 0.03\%$.

Thermal Power

The thermal power of the reactor is measured indirectly, i.e. by calculating the total power supplied at the secondary side of steam generators. The uncertainties of thermal power output are usually less than 0.5% per core and are fully correlated among the reactors.

Fission Fraction

The uncertainties of fission fraction are summarized in Table 3.11 and shown Fig. 3.8.

Isotope	Fractional uncertainty of fission fraction
^{235}U	3.3 %
^{238}U	6.5 %
^{239}Pu	4.0 %
^{241}Pu	11.0 %

Table 3.11: Fractional uncertainties of fission fraction

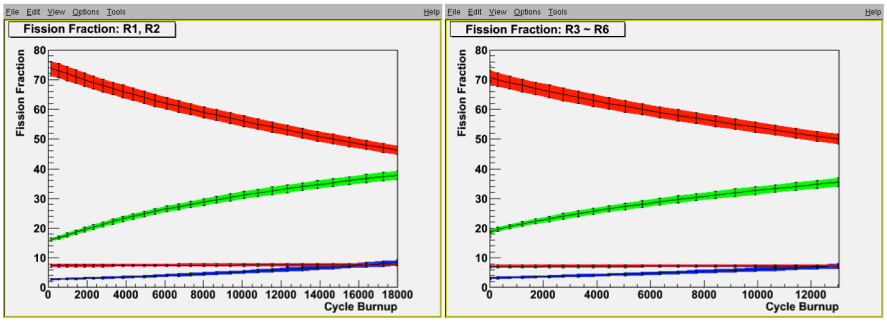

Figure 3.8: Fission fraction variation due to fuel burn-up and its uncertainties. Reactor 1 $\sim$ 2 and Reactor 3 $\sim$ 6 have differences, albeit small. The higher red is ^{235}U. Green is ^{239}Pu. Blue is ^{241}Pu. Lower red is ^{238}U.

Fission Reaction Cross Section and Reference Energy Spectra

Associated antielectron neutrino flux gives 1.9% correlated uncertainty, which is calculated from the neutrino yield per fission and fission spectra.

Energy realsed per fission

As shown in Table 3.1, the thermal energy released per fission gives 0.2% correlated uncertainty.

3.5 Monte Carlo Simulation

As with other particle experiments, extensive studies using Monte Carlo (MC) simulation have been performed for the RENO experiment. The MC studies provide valuable guidance to optimize and determine various design parameters of the detector. It helps to obtain the most cost-effective design without many compromises on sensitivity of the experiment. The MC simulation also helps develop analysis tools for actual data from the experiment. In addition, some of systematic uncertainties can also be estimated from the simulation studies. The RENO detector simulation is modified from glg4sim, a geant4-based program for LS neutrino detectors. The "generic" program has been customized for the RENO detector with a new event generator that provides better physics models. We can obtain the expected flux of the detector with oscillation from the MC. This flux in turn is used for obtaining θ_{13} and $|\delta m^2_{ee}|$. The dead photomultiplier tube (PMT) fraction during the data extraction reported in this manuscript is less than 1% for both near and far detectors. However, the dead PMTs were not accounted for in the RENO MC because the time-dependent charge correction in data compensates the effects of said dead PMTs.

3.5.1 Detector Simulation

The major role of the detector simulation is a data analysis tool. The RENO detector is designed with four concentric cylindrical modules – two active inner modules called target and γ-catcher, and two inert outer modules called buffer and veto as shown in Fig. 3.9. Compared to the past reactor neutrino experiments, an additional active layer, γ-catcher, surrounding the target was added to the detector design to contain gamma rays escaping the target. There are 354, and 67 10-inch PMTs mounted on the buffer vessel wall, and veto wall, respectively, pointing inward, normal to the wall surfaces.

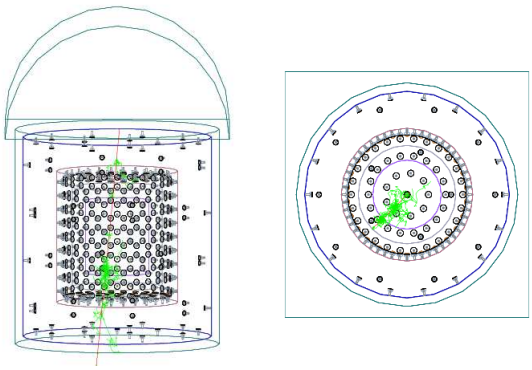

Figure 3.9: Side and top view of the RENO detector simulation with a muon (red line) passing through the target and leaving showers (green lines).

Software Tools

The primary software tool for modeling the RENO detector response, GLG4SIM, is a geant4-based simulation package for LS detectors derived from klg4sim of the KamLAND collaboration. This software was designed for simulation of detailed detector response to particles moving through and interacting with a large volume of LS detector.

The RENO detector has four concentric cylindrical sub-detectors, each filled with Gd-loaded LS, LS without Gd, mineral oil, and water, respectively. The geant4 toolkits are used for simulating the physics processes involving particles with energies above a few keV and propagating through the materials in the sub-detectors. However, the optical photon production and propagation through the liquid scintillator, including processes like absorption, re-emission, and elastic collisions, are handled by custom codes on GLG4SIM. In the detector simulation, the LS consists of LAB for the organic solvent, 1.5 g/l of PPO as a fluor, and 0.3 mg/l of Bis-MSB as a secondary-wavelength shifter. In the target region, 0.1% Gd is loaded. geant4 Neutron Data Library (NDL) version 3.8 gives a reasonable approximation for the continuum gamma spectrum after neutron capture on Gd. However, the discrete lines of high-energy gammas are not included in the NDL version 3.8. However, a GLG4SIM update is available for additional Gd support for accurate modeling of discrete lines of the high-energy gamma rays. The resulting distributions of the neutron capture distance and capture time are shown in Fig. 3.10. GLG4SIM uses a custom simulation code for PMT with detailed PMT geometries. This PMT simulation handles transmission, absorption, and reflection of optical photons at the photocathode. The PMT modeling includes a finite photocathode thickness and wavelength-dependent photocathode efficiency

supplied by the PMT manufacturer.

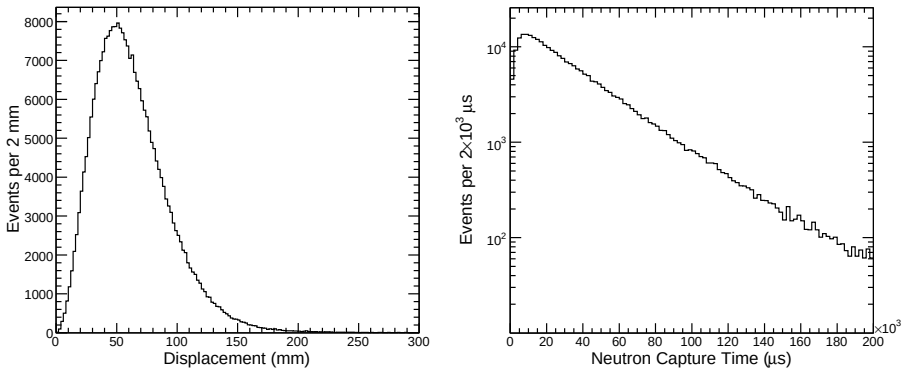

Figure 3.10: Neutron capture distance from IBD events (left) and neutron capture time (right).

Optical Photon Processes

Each photon in the simulation is tracked in the detector until it either reaches a PMT or is lost. The simulation accounts for several light propagation phenomena while tracking the photons. Photons in the scintillator may undergo absorption or elastic scattering (Rayleigh scattering) by solvent and fluor molecules. Attenuation length, λ_{att}, of the liquid scintillator is defined as

$$\frac{1}{\lambda_{att}} = \frac{1}{\lambda_{scat}} + \frac{1}{\lambda_{abs}}, \tag{3.11}$$

where λ_{scatt} and λ_{abs} are the scattering length and the absorption length, respectively. The reciprocal value of the liquid scintillator attenuation length $(1/\lambda_{att}^{LS})$, is equal to the sum of those of scattering lengths and absorption lengths,

$$\frac{1}{\lambda_{att}^{LS}} = \frac{1}{\lambda_{scat}^{LS}} + \frac{1}{\lambda_{abs}^{LS}} = \frac{1}{\lambda_{scat}^{LS}} + \frac{1}{\lambda_{abs}^{solvent}} + \frac{1}{\lambda_{abs}^{fluors}}. \tag{3.12}$$

In the simulation, photons can be either scattered or absorbed by the solvent and fluors according to the corresponding fractions. Because a large fraction of liquid scintillator is solvent, photons are scattered mostly by LAB. It should be noted that the band gap for the lowest-energy electronic transitions in LAB molecules is at 320 nm, and thus absorption by LAB below 320 nm is strong. At

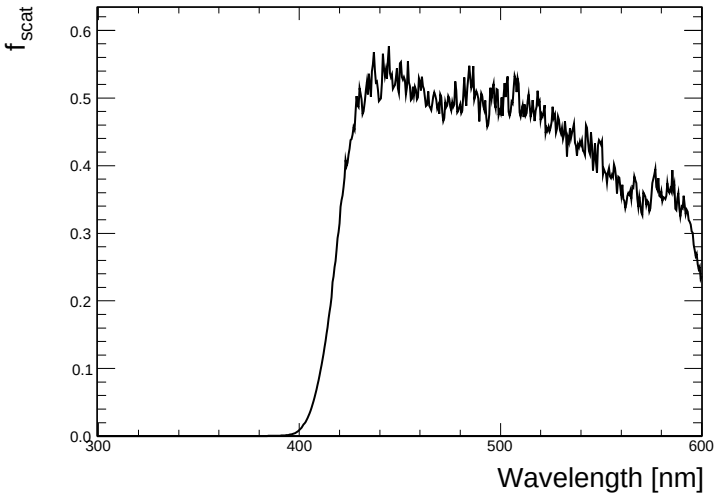

Figure 3.11: Measured scattering fraction of LAB-based liquid scintillator.

wavelengths longer than 320 nm, absorption by LAB drops rapidly and the measured extinction coefficient roughly demonstrates a λ^{-4} dependence, as expected in Rayleigh scattering. The scattering fraction, f_{scatt}, can be obtained from

$$f_{scatt} = \frac{\lambda_{att}^{LS}}{\lambda_{scatt}^{LAB}}. \tag{3.13}$$

Fig. 3.11 shows the measured scattering fraction of an optical photon in the LS. When a photon undergoes elastic scattering, its wavelength remains unchanged but its direction is altered. The direction of a photon after elastic scattering demonstrates a $(1 + \cos^2\theta)$ dependence, where θ is the photon-scattering angle. Absorption of a photon by fluors can be followed by their re-emission, but there is a chance of an absorbing molecule, depending on its quantum yield efficiency, undergoing non-radiative relaxation. The non-radiative relaxation results in the loss of the photon and tracking in the simulation is terminated in such a case. The absorption probability of LAB, PPO, and bis-MSB can be calculated by

$$P_{abs}^{i} = \frac{\lambda_{abs}^{LS}}{\lambda_{abs}^{i}}, \tag{3.14}$$

where i represents LAB, PPO, or bis-MSB. Figure 3.12 shows the measured absorption probability for each component in the liquid scintillator. Re-emission

occurs isotropically, and a re-emitted photon is assigned a longer wavelength than that of the absorbed photon, based on the emission spectrum.

The absorption of photons within the acrylic medium (vessel walls) is simulated according to the absorption probability calculated with the medium's attenuation length. Also, the reflection and refraction of photons at the surface of the acrylic vessel are simulated using Fresnel's law. The refractive indices of all dielectric materials in the detector are measured at different wavelengths and implemented in the simulation. Figure 3.13 shows the measured refractive indices of some of detector materials. After a photon enters a PMT and is absorbed by the photocathode, tracking is terminated. A hit is then made depending on the quantum efficiency of the photocathode.

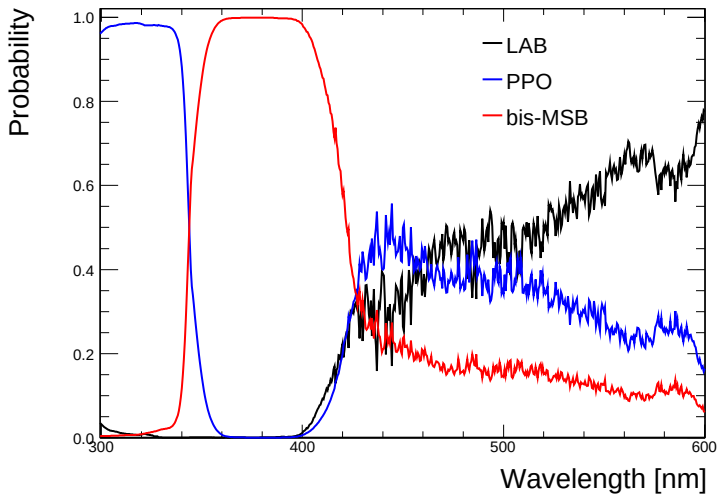

Figure 3.12: Measured absorption probabilities of LAB, PPO, and bis-MSB. These are used in the detector simulation.

3.5.2 Monte-Carlo Event Reconstruction

Vertex Reconstruction

For vertex reconstruction, two independent algorithms, "charge weighting method" and "likelihood method," have been used. The charge weighting method is simple and fast, and is suitable for event display online or as a filter to extract interesting events to apply more sophisticated event-selection criteria. The likelihood method has a better vertex position resolution than the charge weighting method,

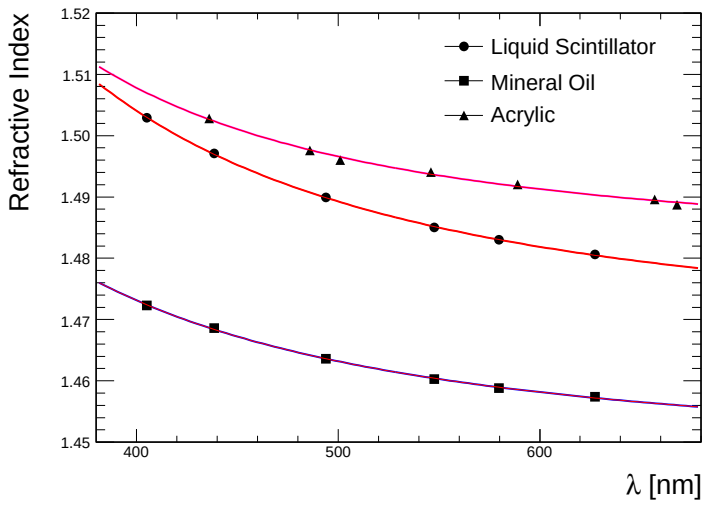

Figure 3.13: Measured refractive indices of liquid scintillator, mineral oil, and acrylic.

but it requires more CPU time and therefore is used as an offline reconstruction method. The event vertex in the charge weighting method is calculated as

$$\vec{r}_{vtx} = \frac{\sum_{i=PMT} n_i \vec{r}_i}{\sum_{i=PMT} n_i}, \tag{3.15}$$

where n_i is the number of photoelectrons on the ith PMT and $\vec{r}_i$ is the vector pointing from the center of the detector to the ith PMT. The number of photoelectrons is calculated by $n_i = c_i q_i$, where q_i and c_i are the amount of charge measured on the ith PMT and the charge to number of photoelectron conversion factor on that PMT. Because the reconstructed vertex position calculated with the charge weighting method is inherently closer to the center of the detector than it is to the actual vertex position, linear corrections are applied based on the detector simulation results. The position resolution is found to be ~ 38 cm for a 1 MeV gamma ray as shown in Fig. 3.14, and it improves further for a higher energy gamma.

The likelihood method uses not only the number of scintillation photons detected by the PMTs, but also the arrival time of those photons. The expected

number of photoelectrons on the ith PMT can be written as

$$\nu_i = N_{tot} \frac{A_i \cdot f(\cos\theta_i)}{4\pi R_i^2} \epsilon_i \cdot \prod_j e^{-R_{ij}/\lambda_j}, \tag{3.16}$$

where N_{tot} is the total number of optical photons generated, A_i and ϵ_i are the frontal area of the cathode and quantum efficiency of the PMT, respectively, R_{ij} is the distance from the vertex to the PMT in medium j, and λ_j is the attenuation length of the j^{th} medium in between the vertex and the PMT. The effective area of the PMT's photocathode, seen from the incident angle, θ_i is accounted for in function $f(\cos\theta_i)$.

The likelihood is then written as

$$\mathcal{L} = \prod_{i=PMT} \mathcal{G}(n_i, \vec{r}; \nu_i, \sigma_i) \cdot \mathcal{T}(t_i; n_i, R_i), \tag{3.17}$$

where $\mathcal{G}(n_i; \nu_i, \sigma_i)$ is the Gaussian probability with mean, ν_i and width, σ_i. $\mathcal{T}(t_i; n_i, R_i)$ is the probability of having the first hit of n_i hitting the ith PMT to have a hit time of t_i. The number of observed photoelectrons, n_i, is calculated from the charge output of PMT using the charge-to-photoelectron conversion factor from calibrations. The negative log likelihood is then minimized using MINUIT to find the vertex position and the total number of optical photons created.

Energy Reconstruction

To convert p.e. to prompt energy (MeV) for IBD events, we derive the conversion function using the same procedure as data, which is described in the section 5.3. That is, we obtain raw p.e. from ^{137}Cs, ^{68}Ge, H-capture, ^{60}Co, C-capture and Gd-capture, which are located at the target's center. The following table 3.12. shows the source raw p.e., which are used for MC energy conversion. 1 million events are used for n-Gd and 400,000 events are used for the other sources.

Source	Range	Fitting Function	Far raw p.e.	Near raw p.e.
^{137}Cs	$[-2\sigma,+2\sigma]$	Single G.	147.63 ± 0.14	143.45 ± 0.14
^{68}Ge	$[-4\sigma,+3\sigma]$	7^{th} poly. + G.	223.37 ± 0.94	216.45 ± 0.94
nH	$[-2\sigma,+2\sigma]$	Single G.	538.26 ± 0.28	522.86 ± 0.28
^{60}Co	$[-4\sigma,+3\sigma]$	7^{th} poly. + G.	583.10 ± 1.00	565.94 ± 1.00
nC	$[-2\sigma,+2\sigma]$	Single G.	1226.31 ± 0.61	1191.89 ± 0.61
nGd	$[-4\sigma,+3\sigma]$	7^{th} poly. + two G.	1931.63 ± 0.95	1880.64 ± 0.95

Table 3.12: MC raw photo electron of calibration sources, which is used for conversion function.

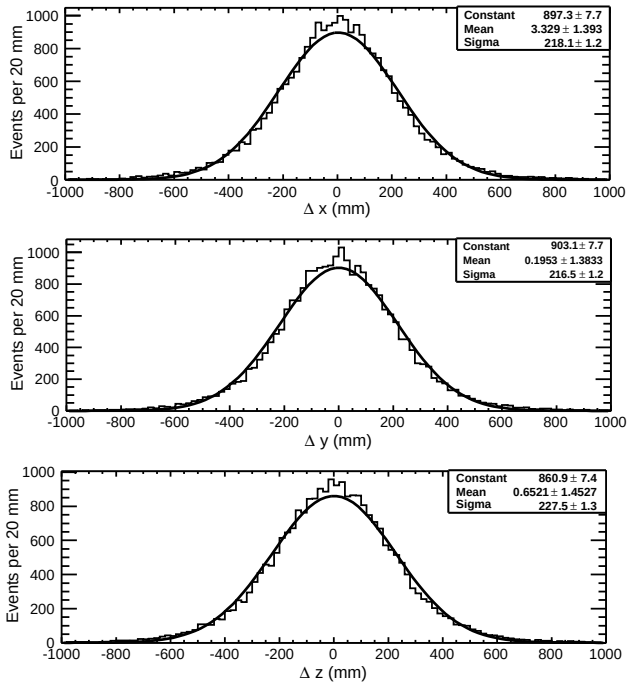

Figure 3.14: Difference between reconstructed and generated vertex positions for 1 MeV γ rays in random direction in the target using a simple weighting method.

Based on the corrected raw p.e., we obtain the p.e.-to-MeV conversion function by fitting it with the following function.

$$\text{Function of P.E. / MeV (MeV)} = P_0 - \frac{P_1}{1 - \exp(-P_2 \cdot \text{MeV} - P_3)} \tag{3.18}$$

where, p.e. is the photoelectron, MeV is the prompt energy (MeV), and P_0, P_1, P_2, P_3 are the fitting parameters. The fitting results are shown in Fig. 3.15 and Table 3.13.

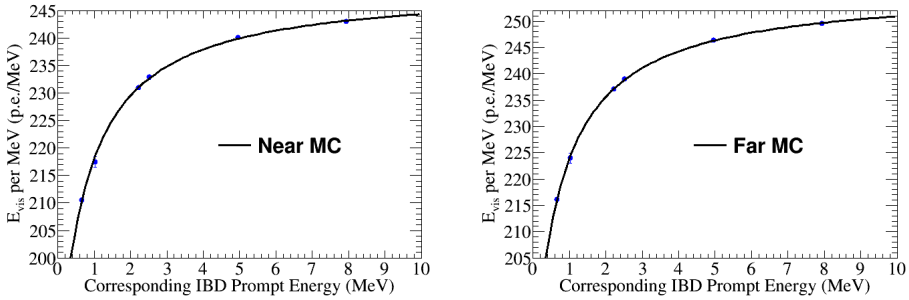

Figure 3.15: Energy conversion function for MC. Left is the near detector. Right is the far detector.

Parameter	far	near
P_0	256.19 ± 0.26	249.46 ± 0.26
P_1	0.0118 ± 0.0014	0.0100 ± 0.0090
P_2	0.000208 ± 0.000023	0.000184 ± 0.000166
P_3	0.000156 ± 0.000019	0.000136 ± 0.000121

Table 3.13: The fitting results of energy conversion function

MC Prompt Energy Spectrum

We have tuned the MC parameters and obtained MC conversion for near and far detectors, respectively. Energy resolution correction factor was also obtained. We can now produce an MC energy spectrum to compare with data. Fig. 3.16 shows the final reconstructed MC spectrum without the oscillation effect.

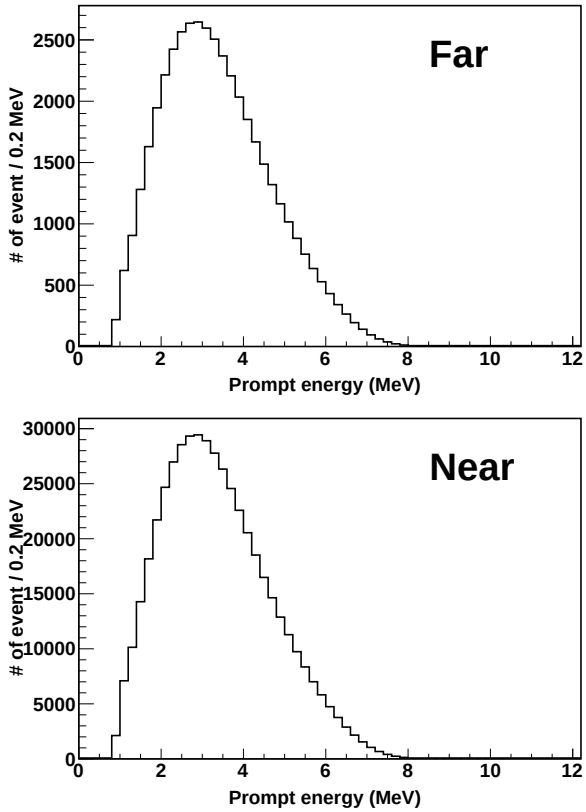

Figure 3.16: MC prompt energy spectrum without oscillation effect, reconstructed after applying energy-resolution correction. Far MC spectrum is shown on top. Near MC spectrum is shown in bottom.

Chapter 4

Event Reconstruction

Obtaining reconstructed energy and vertex is essential for selecting the IBD candidate events against various backgrounds. In the following subsections, we describe the energy and vertex reconstructions of the triggered events.

4.1 Energy Reconstruction

Before extracting data, it was necessary to set the threshold value to separate noise and event. So, we compared single photon electron response with different threshold values. Fig. 4.1 shows the overlay of charge distribution. No major variation with the threshold values was observed, and thus we chose the highest value, -1.0 mV, to lower background. We set the PMT gain value to 1.0×10^7. When a photoelectron enters the PMT, the QBEE board receives 1.6 pC from it. For this, we placed the ^{137}Cs radioactive source on the detector center. With 354 PMTs in buffer and ^{137}Cs source producing around 120∼130 hits, the ^{137}Cs gave an almost single photoelectron response at each PMT. To determine the exact high voltage value, we registered data with four different high voltages – 1,400, 1,500, 1,600, and 1,700 V – and fitted the results together with the gain function

$$\text{PMT Gain} = A \cdot V^N \tag{4.1}$$

where, V is the voltage. A and N are the fitting parameters.

From the fitted value, we can calculate the exact voltage that gives 1.0×10^7 gain. Fig. 4.2 shows the example of a fitted channel. After fitting all the PMT channels, we set a suitable high voltage at each channel and re-gather data to check the gain setting. Fig. 4.3 shows the result. X-axis represents PMT gain. It can be seen that the gain variation among PMTs is below 3%.

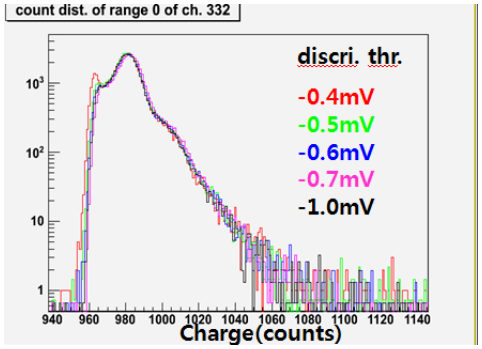

Figure 4.1: Charge distribution of single photoelectron. Different threshold shows almost similar shape.

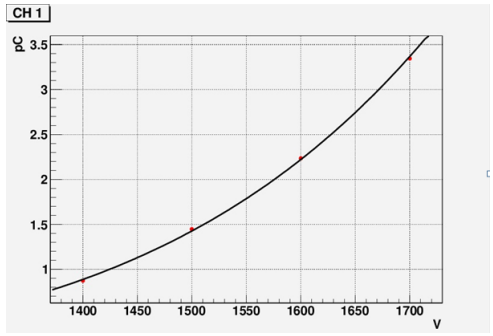

Figure 4.2: Curve fitting with four data points. X-axis represents the high voltage value of PMT and Y-axis represents the output value converted to pC. 1.6 pC is a desirable gain value.

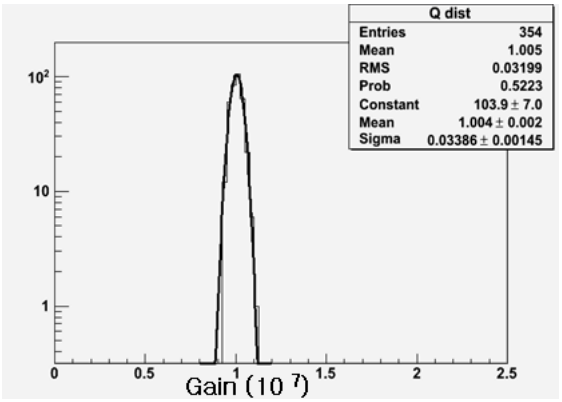

Figure 4.3: Final result of PMT gain matching is shown. The variation among PMTs is below 3% at near and far detector.

4.2 Muon Energy Reconstruction

Cosmogenic muons introduce the main background in the IBD candidates. The intrinsic muon energy cannot be reconstructed, but its deposited energy inside the detector can be reasonably measured as visible energy proportional to its path length. The muon deposit energy (E_μ) is reconstructed by the measured $Q_{\rm tot}$ with a conversion factor of 250 photoelectrons per MeV. A muon is identified in an event with deposit energy greater than 70 MeV. Due to the saturation of the DAQ electronics, however, the muon deposit energy cannot exceed the maximum value of ∼1,700MeV as shown in Fig. 4.4.

Due to a decrease in the attenuation length of Gd-LS and the removed malfunctioning PMTs, the muon deposit energy spectra vary, and the muon rates are reduced. That is shown in Fig. 4.5. The muon charge correction is designed to fit both muon energy spectrum and muon rate with a reference for high muon energy region ($E_\mu > \sim$1.0GeV). Fig. 4.6 and 4.7 show the corrected muon deposit energy spectrum and the stability of muon rate. A more detail process for muon energy correction is described in Appendix A.

4.3 Vertex Reconstruction

Event vertex information is useful for removing accidental backgrounds because of the uncorrelated distances between prompt and delayed candidates. A photon with energy of a few MeV traveling through the liquid scintillator will lose most of its energy within a very short distance. Therefore, optical photons originating

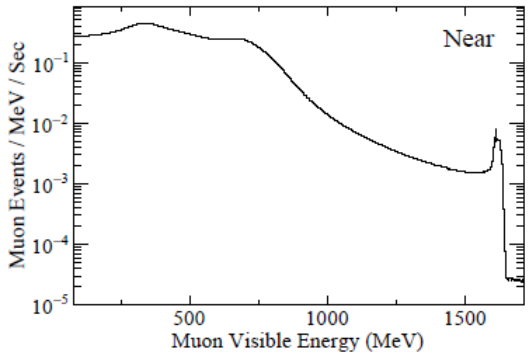

Figure 4.4: Muon deposit energy distribution for the near detector. Maximum energy of ∼1700 MeV is due to the saturation of the DAQ electronics.

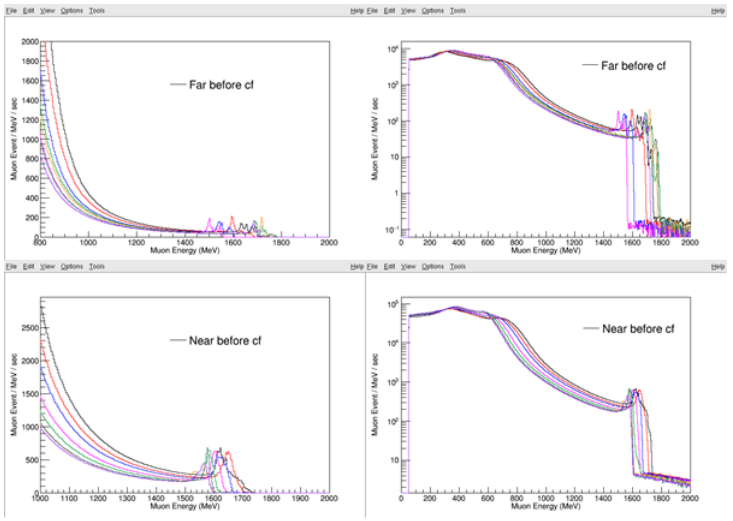

Figure 4.5: Muon deposit energy distribution without correction. These spectra are normalized by lifetime. Black spectrum is for data before ^{252}Cf contamination and is taken as the reference. Other colored spectra show different shapes with the reference and their event rates reduce over time.

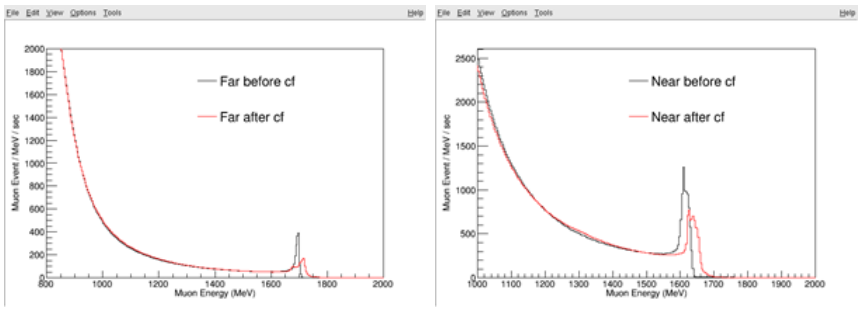

Figure 4.6: Muon deposit energy distribution with correction. Left side is the far detector data and right side is the near detector. Muon energy spectra and muon event rates for data after ^{252}Cf contamination (red) are well matched with the reference (black) for the high muon-energy region($E_\mu > \sim$1.0GeV).

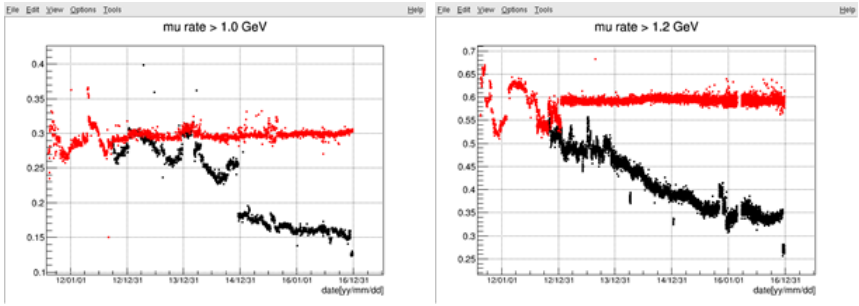

Figure 4.7: Stability of muon event rates over time. Left side is for the far detector data and right side for the near detector. Without proper muon energy correction, muon event rates grow lower (black dots). After applying muon energy correction, muon show constant event rate (red dots).

from scintillation processes would be highly localized. Assuming that the propagation of optical photons is not affected by the detector materials and that the PMTs are arranged uniformly on the surface encapsulating the scintillation volume, a simple and fast method is adopted to reconstruct an event vertex using an individual PMT charge as a weighting factor to the position of a hit PMT. A reconstructed vertex, $\vec{r}_{\rm vtx}$, is obtained as a charge weighted average of locations of all the hit PMTs,

$$\vec{r}_{\rm vtx} = \frac{\sum_i (Q_i \cdot \vec{r}_i)}{\sum_i Q_i} \tag{4.2}$$

where Q_i is the charge collected by the i^{th} PMT, and $\vec{r}_i$ is a position vector of the PMT from the center of the RENO detector. This method results in $\vec{r}_{\rm vtx}$ with a position-dependent offset from the true vertex position, mainly due to geometrical effects. If the detector is spherical, then $\vec{r}_{\rm vtx}$ becomes the true vertex with a correction factor of 1.5 at all points in the detector. However, the RENO detector has a cylindrical shape, and correction factor depends on the event vertex position. A correction factor depending on $\vec{r}_{vtx}$ is obtained using a simple numerical calculations that take into account a simple geometrical shape of the detector and the effective attenuation length of ID materials. For the RENO detector, the correction factor is calculated using a simple Monte Carlo calculation. Assuming the surface of the cylinder is a photosensitive area with uniform efficiency, then Q_i in Eq. 4.2 over a unit area can be written as

$$Q_i = \frac{(\vec{r}_i - \vec{r}_{\rm o}) \cdot \hat{\nu}}{|\vec{r}_i - \vec{r}_{\rm o}|^3} exp(-|\vec{r}_i - \vec{r}_{\rm o}|/\lambda) \tag{4.3}$$

where $\vec{r}_{\rm o}$ is the vector pointing the true event vertex position from the center of the detector and $\hat{\nu}$ is the unit vector pointing outward from the surface of the photosensitive area that $\vec{r}_i$ is pointing at. The attenuation length of the liquids, λ, which is assumed to be 1.2×10^4 mm, is accounted for in this calculation. For a given true input vertex position, $\vec{r}_{\rm o}$, a Monte Carlo calculation is used to get the mean output vertex position, $\vec{r}_{\rm vtx}$. Then, the positions are compared to get the correction factors for the radial component ρ and z component of $\vec{r}_{\rm vtx}$ as a function of $\vec{r}_{\rm vtx}$. The calculated correction factors are shown on the left side of Fig. 4.8. The results of the reconstructed vertex are shown on the right side of Fig. 4.8. Naıve method refers to the weighting method using Eq. 4.2 with a fixed correction factor of 1.5, which is a correction factor for the spherical detector, and the improved method refers to the weighting method corrected with Eq. 4.3.

The performance of the vertex reconstruction was verified with three calibration source datasets: ^{137}Cs, ^{68}Ge, and ^{60}Co. Each radioactive source is deployed in the target along the axis of cylinder from z = 1,200 to 1,200 mm at 300 mm

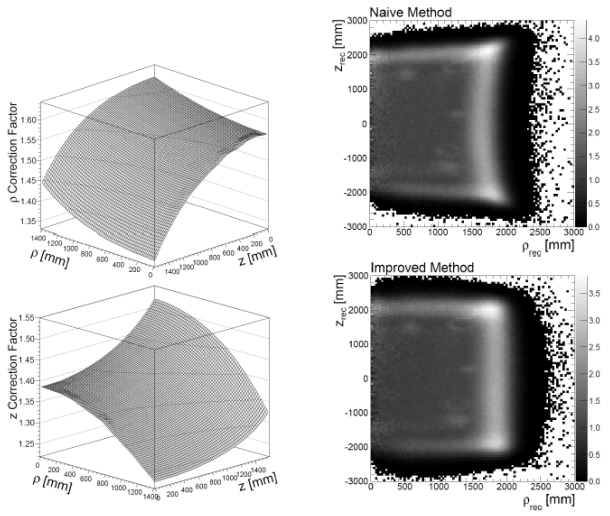

Figure 4.8: The left side is the correction factors to ρ and z calculated with a Monte Carlo method. The right side shows the reconstructed event vertex density distributions of background events in ρ-z using the naıve and improved methods. The external γ background events highlight the reconstructed outer boundary of the γ-catcher. The naıve method has position-dependent biases.

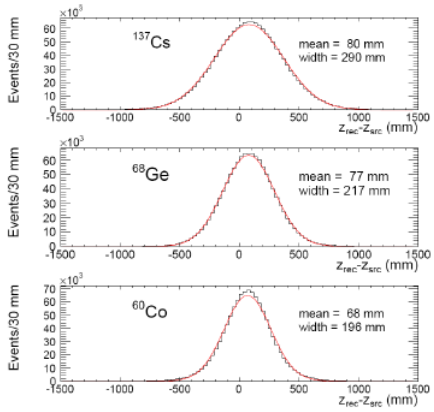

Figure 4.9: The residual of the reconstructed and source z-positions, $z_{rec}z_{src}$, for ^{137}Cs, ^{60}Co, and ^{68}Gesource samples for near detector for all source z-positions. The mean and width of Gaussian fit (red line) to the distribution are also shown.

intervals. Fig. 4.9 shows that the vertex resolution is about 20 cm at 1 MeV and improves at higher energies. X-axis in Fig. 4.9 is z_{rec} z_{src}, where z_{src} is the true source z-position and z_{rec} is the reconstructed z-position.

Fig. 4.10 shows a reasonable agreement between the reconstructed and actual source positions. The difference is as large as $\sim$7% for ^{137}Cs and less than $\sim$5% for the other two sources with gamma-ray energies larger than 1 MeV. However, such a bias is not really problematic because the requirement of a delayed signal naturally selects the target events without any information about the event vertex.

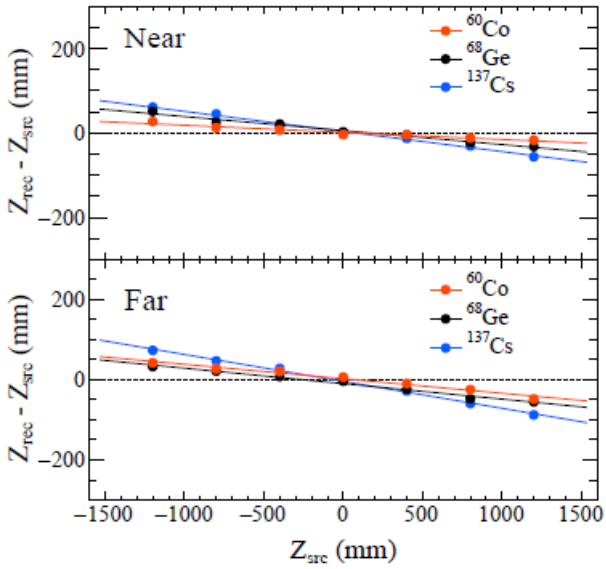

Figure 4.10: Difference between reconstructed vertices (Z_{rec}) and actual positions (Z_{src}) of ^{137}Cs, ^{68}Ge, and ^{60}Co sources. The reconstructed vertices show systematic deviations from the true positions at the source locations away from the center. The systematic shifts reduce as the source energy increases.

Chapter 5

Energy Calibration

Since the measurement of θ_{13} mainly depends on the systematic uncertainties in the relative parameters between near and far detectors, it is important to examine detector performance in greater detail. There are two major motivations for having an system of energy calibration. First, the characteristics of the events in the energy range of 1∼10 MeV depend on the positions of the event vertex since the scintillation lights travel through the liquid scintillator, acrylic vessel, and buffer oil. The vertex position-dependence of energy measurement can be understood by placing a radioactive source at various locations inside the liquid scintillator and measuring the energy deposit. The detailed optical parameters of the liquid scintillator, acrylic vessel, and stainless steel tank of the two detectors can be obtained and compared. Second, the scintillation and optical properties of liquid scintillators become changed during the long data-taking period. Hence, it is important to monitor the detector response throughout the duration of the experiment. In addition, the day and night oscillation occurring in the energy measurement due to temperature and other environmental factors inside and outside the detector also warrants constant monitoring to ensure the regular calibration source run. Moreover, delayed signal is used daily monitoring data and obtaining the daily charge correction factor.

5.1 Radioactive Sources

To calibrate the detector response for the IBD of reactor antineutrinos, several radioactive sources are used, and these have a μCi level or lower activities: ^{137}Cs, ^{68}Ge, ^{60}Co, and ^{252}Cf . The characteristics of the radioactive sources are summarized in Table 5.1. ^{252}Cf is important because it is the neutron source for this study. The ^{252}Cf source can help verify the neutron capture on gadolinium in the target region. The size of the radioactive source is limited by the attenuation

length (0.511 MeV gamma ray) in case of a positron source. The attenuation length of the 0.511 MeV gammas in the LS is approximately 10 cm. Therefore, the overall size of the source should be several times smaller than the attenuation length to minimize the amount of scintillation light getting scattered by the source itself. The overall size of the source is 2 cm $\times$ 3 cm. The source is enclosed in an acrylic container when registering source data. The material encapsulating the source should be compatible with the scintillator materials, and polytetrafluoroethylene (PTFE) could be one of the best candidate materials. Fig. 5.1 shows the spectra of source data.

type	sources	energy (keV)	calibration
e^+	^{68}Ge	511(2)	position E threshold
γ	^{137}Cs	662	gamma
	^{60}Co	1173+1333	multiple gamma
neutron	^{252}Cf	neutron + $\sim$10 MeV	neutron efficiency

Table 5.1: A list of radioactive sources for RENO detector calibration.

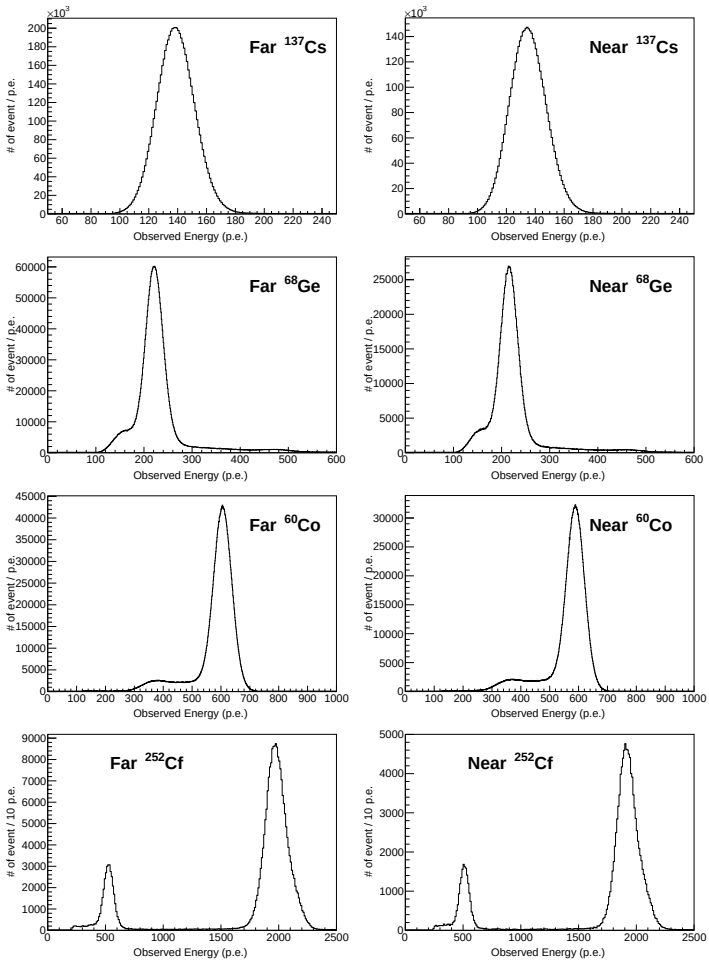

Figure 5.1: Spectra of source data. Left side is far and right side is near.

5.2 Source Driving System

The main goal of using radioactive sources for the calibration is to measure the energy scale, resolution, and vertex position dependence of energy measurement. Therefore, we need to locate with high precision the source at the desired point. To achieve this, we developed a 1D/3D source driving system that it is operated with custom computer software MCU. The 1D system consists of a stepping motor-driven pulley with a polyethylene wire attached to it. The encapsulated source container is connected at the end of the wire with a weight made by te on to counter the buoyant force of the liquid scintillator. The system has a z-position

accuracy of the order of a few mm, which is much smaller than the vertex position resolution (a few cm) of the detector. We made two 1D source driving systems at each detector. One is for target and the other is for the γ-catcher region. At the target region, the z-axis is exactly at the center of the target vessel and at the side of the detector for the γ-catcher case Fig. 5.2 shows the design of the 1D driving system. Using the 3D driving system, the calibration source can be placed in the target region only. This system consists of four lods that can connect with each other, and there is a robot arm at the end of these lods. The robot arm can be folded, and it can have three points for locating the source container. Moreover, the robot arm can be rotated, allowing to locate the source at the center, the three-side position, and all the phi angles. Fig. 5.3 shows the design of the 3D calibration system, and Fig. 5.4 shows the 1D/3D calibration system installed at the detector.

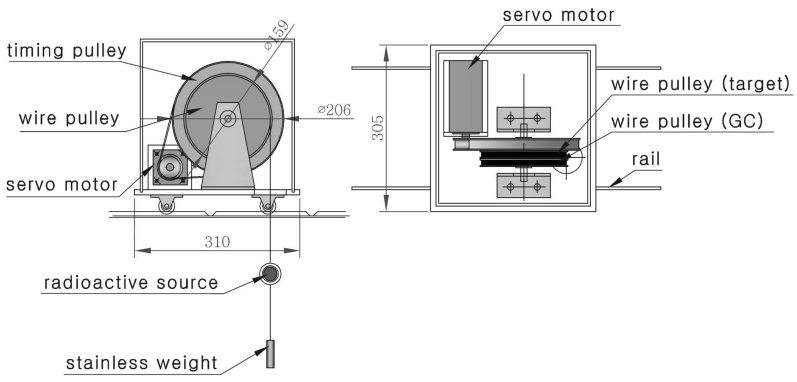

Figure 5.2: Design of 1D source driving system.

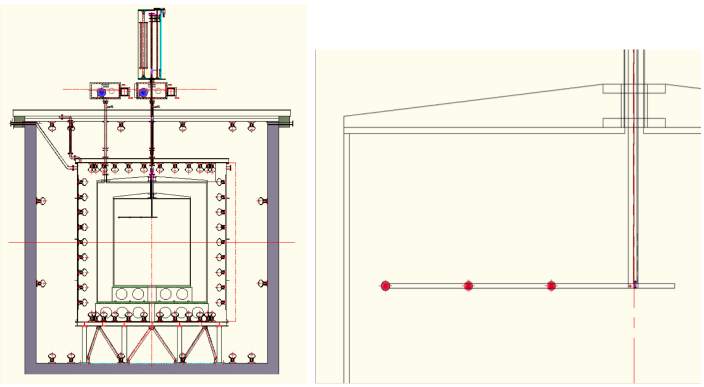

Figure 5.3: Design of 3D calibration system. The plot on left shows cutaway view of 3D calibration system installing in the detector. The red dot on the right plots corresponds to the position of the calibration source in the robot arm.

Figure 5.4: Installed 3D system. Two installed 1D systems are also shown.

5.3 Energy Conversion Function

In the previous section, source data and IBD candidates were well controlled for the time variation. From these corrected data, the p.e. values and corresponding MeV values can be known. This makes the conversion of p.e. to MeV possible. Fig. 5.5 shows the relation between p.e. and MeV of the each point. The points for ^{137}Cs, ^{68}Ge, ^{60}Cosource data are represented. The n-H point is obtained from

^{252}Cf source data. The n-C point is added to obtain an well-fitted energy conversion function, which is obtained from ^{210}Po^{9}Be source data as shown Fig. 5.6. This n-C point was taken once in April 2012, and the n-Gd point was obtained from a delayed signal of the IBD candidates. Each point is converted to a uniformly distributed positron event, which corresponds to the prompt signal of the IBD candidates, from the center-distributed source data except n-Gd point as following equation.

$$\text{P.E./MeV} = \frac{\text{mean p.e. of source data} \cdot C_{center-to-Uniform} \cdot C_{\gamma-to-e^+}}{\text{MeV value of source data}} \quad (5.1)$$

where, the mean p.e. of source data is taken from the charge corrected and other corrected source data or charge-corrected delay of IBD candidates. $C_{center-to-Uniform}$ represents the values taken in November 2012, which is the reference date summarized in Table 5.2. Taken from source data, $C_{\gamma-to-e^+}$ is the correction factor for the conversion of a positron to γ-ray photons. These correction factors are derived by comparing positron MC to source MC. The $C_{\gamma-to-e^+}$ are summarized in Table 5.3. Lastly, the results of Equation 5.1 are summarized in Table 5.4

These points show the nonlinear response of scintillating energy for the IBD prompt signal, which is well described by a fitted parametrization. The quenching effect in the scintillator and Cherenkov radiation is main reason of the nonlinear response at lower energies Therefore, the model of energy-conversion function has to take into account this quenching effect. The following empirical formula is used for the fit function,

$$Q^c_{\text{tot}}/E_{\text{true}} = P_0 - P_1/[1 - \exp(-P_2 \cdot E_{\text{true}} - P_3)], \quad (5.2)$$

where E_{true} is in MeV. The fit parameter P_0 determines a saturation level P_1 that corresponds to the magnitude of nonlinearity, and P_2 and P_3 are related to the shape of the nonlinearity.

The fitting results are shown in Fig. 5.5 and Table 5.5.

	far	near
Center-to-Uniform correction factor	1.0050 ± 0.0014	1.0060 ± 0.0006

Table 5.2: Center-to-Uniform correction factor at the November 2011.

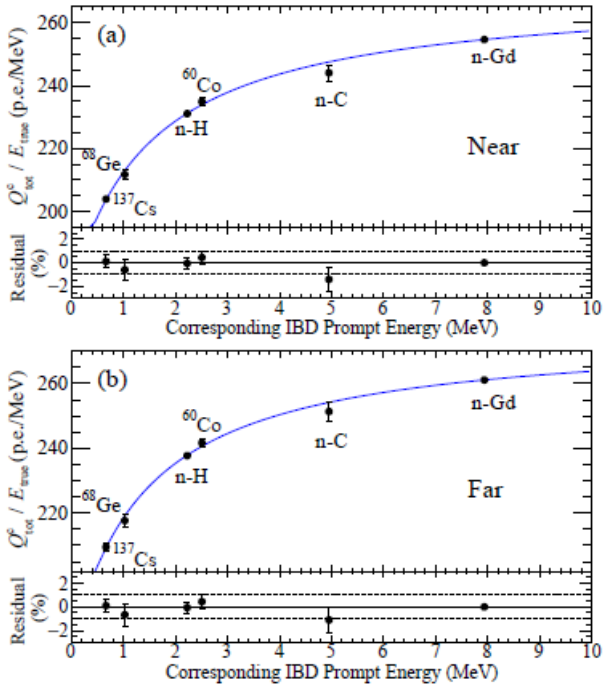

Figure 5.5: Nonlinear response of scintillating energy obtained from the visible energies of γ-rays coming from several radioactive sources and IBD delayed signals in the near and far detectors. The curves are the best fit results to the data points and the charge-to-energy conversion functions. The n-C sample is obtained from the ^{210}Po^{9}Be source and the n-H sample from the ^{252}Cf source. The lower panels show fractional residuals of all calibration data points from the best fit.

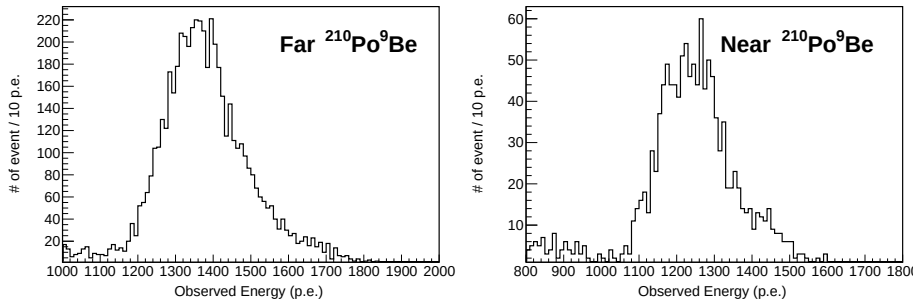

Figure 5.6: Photoelectron distribution of carbon capture event of ^{210}Po^{9}Be source data. Left side is the far detector. Right side is the near detector.

γ-to-e^+ correction factor	far	near
^{137}Cs	0.9647 ± 0.0004	0.9643 ± 0.0004
^{58}Ge	1.0199 ± 0.0003	1.0190 ± 0.0003
n-H	0.9745 ± 0.0002	0.9743 ± 0.0002
^{60}Co	1.0223 ± 0.0002	1.0234 ± 0.0002
n-C	0.9896 ± 0.0001	0.9895 ± 0.0001
n-Gd	1.0257 ± 0.0002	1.0256 ± 0.0002

Table 5.3: γ-to-e^+ correction factor from MC.

p.e./MeV	far	near
^{137}Cs	209.49 ± 1.16	203.95 ± 1.07
^{58}Ge	217.66 ± 2.10	211.77 ± 1.75
n-H	237.73 ± 1.07	231.10 ± 1.04
^{60}Co	241.67 ± 1.45	234.95 ± 1.29
n-C	251.35 ± 2.85	244.06 ± 2.58
n-Gd	261.10 ± 0.11	254.63 ± 0.05

Table 5.4: p.e./MeV values of each calibration source data

Parameter	far	near
P_0	275.9 ± 1.0	270.1 ± 1.3
P_1	0.0170 ± 0.0015	0.0170 ± 0.0025
P_2	0.000123 ± 0.000012	0.000116 ± 0.000012
P_3	0.000174 ± 0.000018	0.000179 ± 0.000030

Table 5.5: The fitting results of energy conversion function

Deviation of all calibration data pointing towards the best fit is within 1% as shown in Fig. 5.5 in the lower panel for the top and bottom plots. According to the energy calibration, the observed charge $Q_{\rm tot}$ at the far detector is ∼220 p.e. per MeV at 1 MeV, and ∼250 p.e. per MeV at 5 MeV.

The effective attenuation lengths of the near and far detectors differ by 1.4% at 430 nm wavelength, which is estimated by the PMT charge response to the radioactive source at detector center. The LS-light yields of the two detectors differ by 2.7% at ∼1 MeV. The dead PMT fraction during data extraction reported here is less than 1% for both near and far detectors, and the difference between

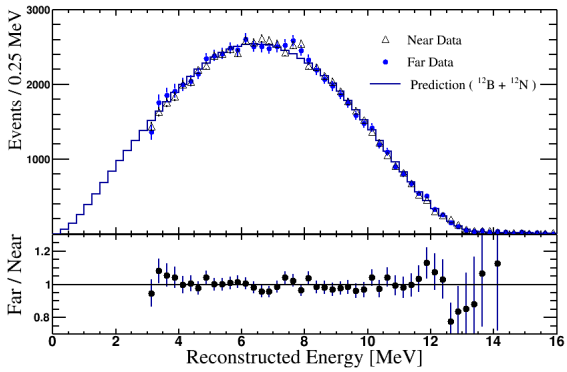

Figure 5.7: Comparison of observed and predicted energy spectra of the electrons from β-decay of unstable isotope ^{12}B, with minute contribution from ^{12}N, produced by cosmic muons. The spectra are overlaid after scaling the total number of events in the near detector to that in the far detector. The far-to-near ratio of the spectra is also shown in the lower panel. A small excess near 8 MeV is seen in both near and far detectors and could be the residual background events from the neutron capture on Gd.

them is less than 0.5%. This difference is compensated when the charge-to-energy conversion is performed using the conversion function obtained for each detector.

Cosmogenic ^{12}B and ^{12}N samples were used to check the validity of the charge-to-energy conversion functions. These isotopes are generated by cosmic muons interacting with carbons in the scintillator. The positron charge-to-energy conversion functions were modified to convert the charge in the β-decay events by subtracting a charge value corresponding to the positron annihilation. Fig. 5.7 shows good agreement in the energy distributions between the near and far data as well as between data and MC. This demonstrates the working of the obtained parametrization for the nonlinear response of electron scintillating energy for energies ranging from 3 to 14 MeV within the statistical fluctuation of the data sample. This also demonstrates the validity of the positron energy conversion function not only for the IBD energy region (up to 8 MeV) but also for the extended energy region (up to 14 MeV).

5.4 Energy Scale

The energy scale difference between the near and far detectors contributes to the uncorrelated systematic uncertainties associated with a relative measurement of

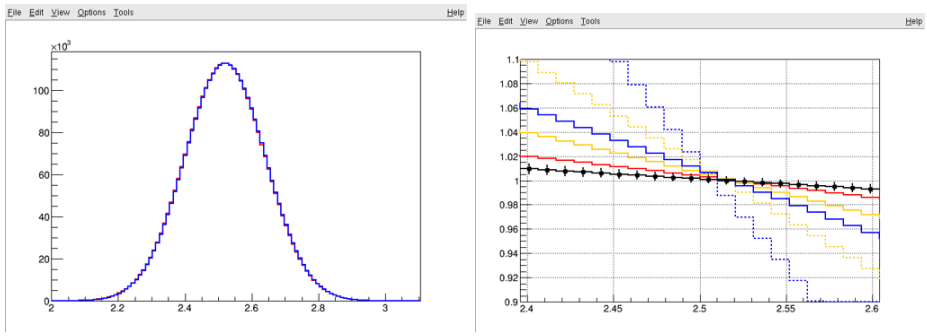

Figure 5.8: Comparison of ^{60}Co source data energy spectrum. The ratio of far to near indicates the energy scale difference, and it is estimated by using the ratio of shifted near to near.

spectra at the two detectors, whereas the absolute energy scale does not contribute to the correlated uncertainties. The energy scale difference is measured by comparing the near and far spectra of calibration data as shown in Fig. 5.8. Left side of Fig. 5.8 shows the ^{60}Co source data energy spectrum from the far and near detector. These spectra are almost the same, but not identical. The ratio of far to near is shown in the right side of Fig. 5.8 as a black graph. Other red, yellow, and blue histograms are represent the ratio of the shifted near to near. By using the shifted nearby serverl percentage, the energy scale difference between the far and near spectra can be estimated. The results of the estimated energy scale difference are shown in Fig. 5.9, and the uncorrelated uncertainty of energy scale difference was found to be less than 0.15 %.

5.5 Energy Resolution

The energy resolution is measured by the delayed signal of n-Gd and n-H data. Moreover, there are two energy resolution curves for two time periods: before ^{252}Cf contamination and after ^{252}Cf contamination, which were divided on October 2012.

The fitting model is defined as following equation.

$$\text{Resolution(E)} = \sqrt{\frac{P_0}{E} + P_1} \tag{5.3}$$

where, E is the visible energy, P_0 and P_1 are the fitting parameter. The fitting results are summarized in Table 5.6, 5.7, and Fig. 5.10, 5.11.

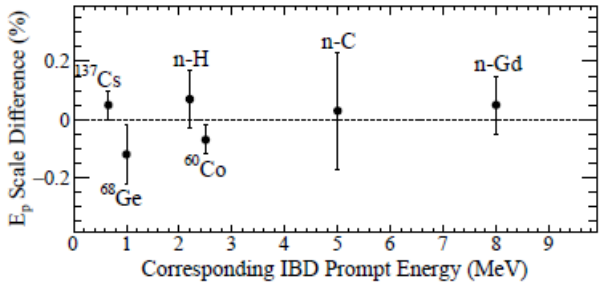

Figure 5.9: Energy-scale difference between the near and far detectors. The prompt energy difference between the two detectors is measured by comparing the energy spectra of the γ-ray sources obtained using the charge-to-energy conversion functions. All calibration data show the values of the difference less than 0.15%

Parameter	far	near
P_0	$8.521\times10^{-3} \pm 4.234\times10^{-1}$	$7.665\times10^{-3} \pm 4.011\times10^{-1}$
P_1	$-3.274\times10^{-8} \pm 1.012\times10^{-1}$	$2.734\times10^{-6} \pm 9.623\times10^{-2}$

Table 5.6: The fitting results of the energy resolution function for a period before ^{252}Cf contamination

Parameter	far	near
P_0	$8.921\times10^{-3} \pm 4.374\times10^{-1}$	$8.438\times10^{-3} \pm 4.363\times10^{-1}$
P_1	$1.015\times10^{-5} \pm 1.045\times10^{-1}$	$1.624\times10^{-4} \pm 1.075\times10^{-1}$

Table 5.7: The fitting results of the energy resolution function for period after ^{252}Cf contamination

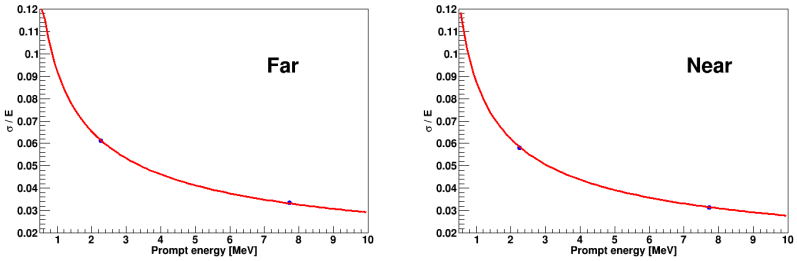

Figure 5.10: Energy resolution of far and near detectors for a period before ^{252}Cf contamination. The top plot shows the near detectors and the bottom plot shows the far detector. Blue dots are data points for the delayed signals of n-H and n-Gd, and the red line is the fitting result curve.

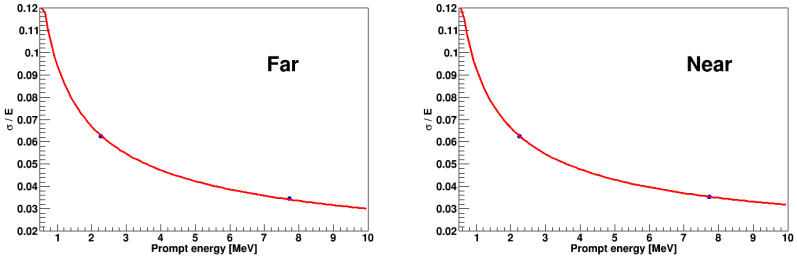

Figure 5.11: Energy resolution of far and near detectors for a period after ^{252}Cf contamination. The top plot shows the near detector and the bottom plot shows the far detector. Blue dots are data points for the delayed signals of n-H and n-Gd, and the red line is the fitting result curve.

Chapter 6

Event Selection for IBD Candidates

6.1 Data Sample

RENO had started gathering data in August 2011, and has since been operating continuously with an accumulated average DAQ efficiency of 95.90%(93.76%) for far (near) detectors, respectively. However, this data does not contain a calibration radiactive source data and has bad data, which is identified by abnormal behavior in the hit map, charge distribution and event rate. Fig. 6.1 shows three datasets and daily detection efficiency of both detectors.

There are mainly two datasets—set A and set B. These sets are divided by ^{252}Cf contamination on October 2012. Set A contains the normal data before ^{252}Cf contamination And set B contains ^{252}Cf contaminated data because a tiny fraction of ^{252}Cf source was dissolved in Gd-LS while taking calibration data on September 28^{th}, 2012 at the far detector and October 27^{th}, 2012 at the near detector. To remove the backgrounds induced from the ^{252}Cf contamination, several Cf removal cuts were developed, but were applied only to set B. Another set, C, was not used at the near detector because of its DAQ inefficiency from UPS noise. The UPS was installed at both the detectors on January 2013, and the one at the near detector had caused electric noise. This noise is considered as the data instead of real signals, so some energy of event is lost in the near detector

In this analysis, we use all data of sets A and B at the far detector, and data of sets A and B except C at the near detector, which are a total of 2,193.04 (1,807.88) live days of data with negligible uncertainties in the far (near) detector, recorded from August 2011 to February 2018 for extracting the neutrino mixing parameters θ_{13} and $|\Delta m^2_{ee}|$.

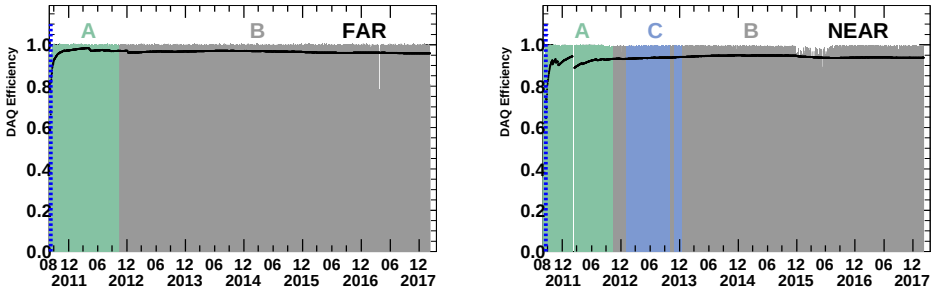

Figure 6.1: Dataset and Data-taking efficiency of RENO. The left plot shows the far detector and the right plot shows the near detector. Sets A and B are divided because of ^{252}Cf contamination. Set C at the near detector is excluded because of DAQ inefficiency due to UPS noise.

Detector	Data set	Date	DAQ Live time (days)
Far	Set A	11^{th} 8, 2011 $\sim$ 27^{th} 9, 2012	384.53
	Set B	28^{th} 9, 2012 $\sim$ 7^{th} 2, 2018	1808.51
	Total	11^{th} 8, 2011 $\sim$ 7^{th} 2, 2018	2193.04
Near	Set A	19^{th} 8, 2011 $\sim$ 27^{th} 10, 2012	379.66
	Set B	28^{th} 10, 2012 $\sim$ 7^{th} 2, 2018	1428.22
	Total	19^{th} 8, 2011 $\sim$ 7^{th} 2, 2018	1807.88
Near	Ups on	21^{th} 1, 2013 $\sim$ 18^{th} 10, 2013	267.80
	(excluded)	14^{th} 11, 2013 $\sim$ 31^{th} 12, 2013	

Table 6.1: Data sets of data sample.

6.2 Backgrounds

There are several background contributions to prompt and delayed-like events, which include ambient γ-rays from surrounding rocks or detector materials, neutrons entering into the detector, spallation products produced by cosmic muons, flashing lights from PMTs, and electronic noise. Two main components of background for the IBD candidates are correlated and uncorrelated pairs of prompt and delayed-like events. Because of a much shallower overburden for the near detector than the far detector, the former suffers a higher rate of cosmogenic backgrounds. The correlated IBD backgrounds are due to fast neutrons, β-n emitters from cosmogenic ^{9}Li/^{8}He isotopes, and ^{252}Cf contamination in the target.

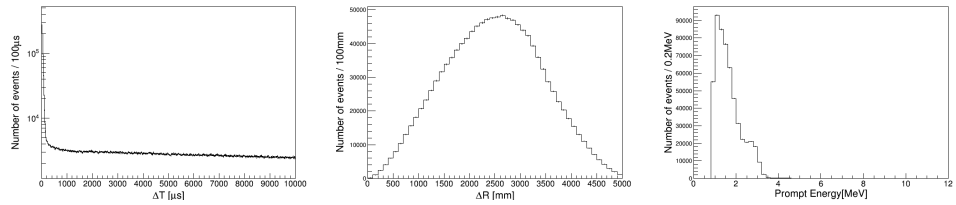

Figure 6.2: Properties of accidental background. The left plot shows the time difference(=ΔT) between the prompt and delayed signals. The accidentals are observed only in the ΔT > 1-ms region. The plot at the middle shows the distance,(=ΔR), between prompt and delayed signals from accidental events. The accidental events have no ΔR correlation. The plot on the right shows the prompt energy spectrum of the accidental background.

6.2.1 Accidental Background

The uncorrelated IBD background is due to accidental coincidences from the random association of a prompt-like event due to radioactivity and a delayed-like neutron capture. Prompt-like events are mostly ambient γ-rays from the radioactivity in the PMT glasses, LS, or surrounding rock. Most of the ambient radioactivity generates γ-rays of energies below 3 MeV. The delayed-like events come from captured neutrons produced by cosmic muons in the surrounding rocks or in the detector. These backgrounds are completely statistical accidents, such that the prompt and delayed signals of the accidental backgrounds have no temporal and spatial correlations, as shown in Fig. 6.2. The accidental backgrounds are removable using the properties of these statistical and accidental backgounds. .

6.2.2 Fast Neutron Background

The fast neutrons are produced by cosmic muons passing the surrounding rock and the detector. There are 3 types of fast neutron backgrounds.

First, the fast neutrons with energy over 10 MeV can be elastically scattered several times from the protons in the target or in the γ-catcher and captured in the target volume. The signals of quenched proton recoil scintillation can be the prompt signal in the region 1 MeV < E < 50 MeV and the thermalized neutrons can be captured with the same time-distribution as the neutrino signal.

Second, some neutrons are produced by cosmic muons without recoil protons and are captured in the detector within 100 μs. A single neutron capture signal has some probability of accidentally falling within the time window of a preceding signal caused by natural radioactivity in the detector, producing an accidental

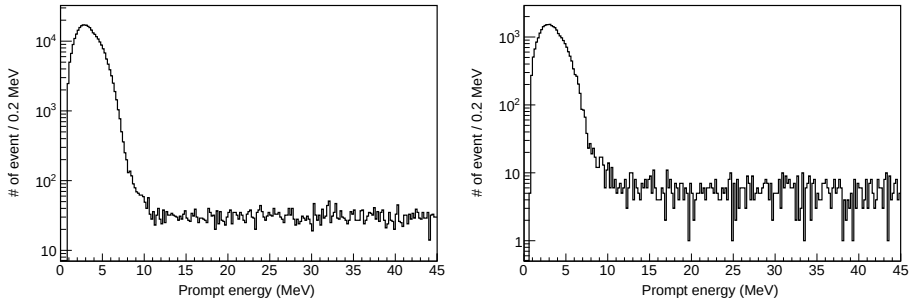

Figure 6.3: Spectra of fast neutrons. Left side is the near detector, and right side is the far detector. The energy spectrum of a fast neutron appears flat in the region 10 MeV $<$ E $<$ 50 MeV.

background. In that case, the prompt and delayed signals are maed from different sources, and form an uncorrelated background.

Third, multiple neutrons are produced within a short period of time and are captured by hydrogen or gadolinium within a short span of time (order of $\sim$ 10 μs). The first neutron capture event could be prompt signal and the next gadolinium-captured neutron event could be delayed signal. Hence, this type of fast neutron background has two peaks; around 2.2 MeV and 8 MeV.

For these reasons, the prompt- and delayed-signal pair of fast neutrons occur before or after the prompt event. The fast neutron background can be reduced using this property.

6.2.3 Cosmogenic $^9Li/^8He$ Background

The ^{9}Li/^{8}He β-n emitters are produced mostly by energetic cosmic muons because their production cross-sections in carbon increase with muon energy.

^{8}He decays by $\beta^- + n$ (16%, $Q_{\beta^-} = 10.653$ MeV) with a half-life time of 119 ms. ^{9}Li decays by $\beta^- + n$ (49.5%, $Q_{\beta^-} = 13.606$ MeV) with a half-life time of 178.3 ms. The $\beta^- + n$ decay gives a prompt and delayed signal similar to IBD events. The production rates of these long-life cosmogenic isotopes were initially studied by rock dating groups. There is a lot of data available on the production rates of ^{10}Be and ^{26}Al from silicon and oxygen by cosmic muons. The production cross-sections of ^{8}He and ^{9}Li in carbon have been measured with accelerator muon beams at an energy of 190 GeV at the European organization for nuclear research, CERN [63]. Their combined cross-section is $\sigma(^9\mathrm{Li} + ^8\mathrm{He}) = (2.12 \pm 0.35)$ μb. The energy-dependent production cross-section is estimated by $\sigma_{tot} = E_\mu^{0.73}$, where E_μ is the muon energy in GeV.

Applying a 2-s veto for the muons, the KamLAND experiment reported that their ^{8}He and ^{9}Li backgrounds are correlated by showering muons, which has more than 10^{6} photoelectrons. For the RENO experiment, we plan to apply a 1-ms veto for non-showering muons of the order of 100 ms for showering muons. This veto on the showering muons will further reduce the ^{8}He and ^{9}Li background rates by about 70%.

6.2.4 ^{252}Cf Contamination Background

The ^{252}Cf contamination background comes from the contamination of Gd-LS by a small amount of ^{252}Cf that was accidentally introduced into both detectors during the calibrations of October 2012. It was found that the source container did not have a tight seal owing to a loose O-ring. As a result, when the source was submerged in Gd-LS during source calibrations, the Gd-LS seeped into the source container and a small amount of dissolved ^{252}Cf leaked into Gd-LS. Bottom-left plot of Fig. 6.4 shows the ^{252}Cf source and its package. -Bottom-right plot of Fig. 6.4 shows the source container and the O-ring, which is in the middle of the container. Among the ∼2,200 days data sample, data after first 400 days in the far (near) detector were contaminated by ^{252}Cf. Thus, a set of ^{252}Cf background removal criteria, which will be described later, are applied to data taken during these periods. It is known that a ^{252}Cf decay emits 3.7 neutrons per fission on an average with a mean energy of 2.1 MeV per neutron via α-emission (96.9%) and spontaneous fission (3.1%).

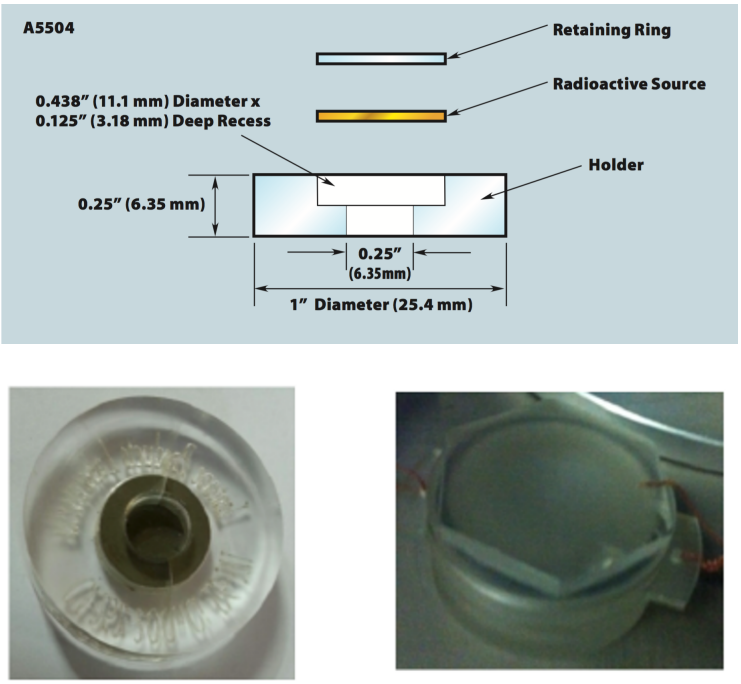

Figure 6.4: The ^{252}Cf source is mounted in a plastic holder to separate it from and exposed to GdLS. Left bottom plot is the picture of the ^{252}Cf source and its pakage. Right bottom plot is the source container.

6.3 IBD Selection Requirements

Event selection criteria help obtain IBD candidate events without distorting the spectral shape of IBD signal events. Because an IBD candidate requires a delayed signal from a neutron capture on Gd in Gd-LS, a fiducial volume naturally becomes the entire target region without requiring a vertex position. As a result, the detection efficiency is enhanced by some spill-in of the IBD events. Applying the IBD selection criteria yields 103,212 (850,666) candidate events with E_{p} between 1.2 and 8.0 MeV for a live time of 2,193.04 (1807.88) days in the far (near) detector, in the time period between August 2011 and February 2018. IBD events with $E_{\mathrm{p}} < 1.2$ MeV include IBD events that occur in or near the target vessel wall and deposit positron kinetic energy in the wall without producing scintillation lights. These events are reconstructed to have visible energy near the positron annihilation energy of 1.02 MeV, but are not well reproduced by the MC prediction. The IBD signal loss by $E_{\mathrm{p}} > 1.2$ MeV requirement is roughly 2% in both detec-

tors. The prompt events occurring near the target vessel wall could lose some of their energy to a non-scintillating target wall causing slight modifications to their prompt energies. However, the wrong energy measurement affects both the near and far detectors in the same way, and thus has a negligible effect on the overall results. The magnitudes and spectral shapes of the remaining backgrounds are estimated using background-enriched samples and subtracted from the final IBD candidate samples.

6.3.1 Removal of γ-Rays from Radioactivity, Noise and Flashers

As described in the previous section, energetic particles and gamma rays emanating from the radioactive decay of isotopes in the inner detector can form accidental backgrounds as well as correlated backgrounds. Some of these backgrounds emanate from the detector vessels, surrounding rocks, the PMT glasses, and the mineral oil in the buffer. And these backgrounds can be reduced by using properties of the border event.

Removal of γ-Rays from Radioactivity

These border events have a large maximum PMT charge (Q_{max}) to total charge (Q_{tot}) ((*i.e.* Q_{max}/Q_{tot})) ratio as the events deposit energy at the buffer and near the PMT, and the PMT nearest to the events receives a much larger number of photoelectrons than the other PMTs. Therefore, the Q_{max}/Q_{tot} ratio, which has an energy-dependent efficiency, is useful for reducing such radioactive backgrounds. This means that the lower the energy of the event, the lower the number of photoelectrons that hits the PMT. Add to this, the Q_{max}/Q_{tot} of high-energy events is relatively larger than that of low-energy events. In other words, the lower the energy of the event, the lower the efficiency. Fig. 6.5 shows the energy-dependent efficiency of the Q_{max}/Q_{tot} cut. This efficiency affects the spectral analyses because it could be a large systematic uncertainty when measuring $|\Delta m^2_{ee}|$. To avoid this systematic uncertainty, the efficiency of Q_{max}/Q_{tot} cut has to be almost 100 %. Fig. 6.6 shows that efficiency becomes almost 100% when the cut threshold is 0.07. Therefore, $Q_{max}/Q_{tot} > 0.07$ cut is applied to IBD candidate events.

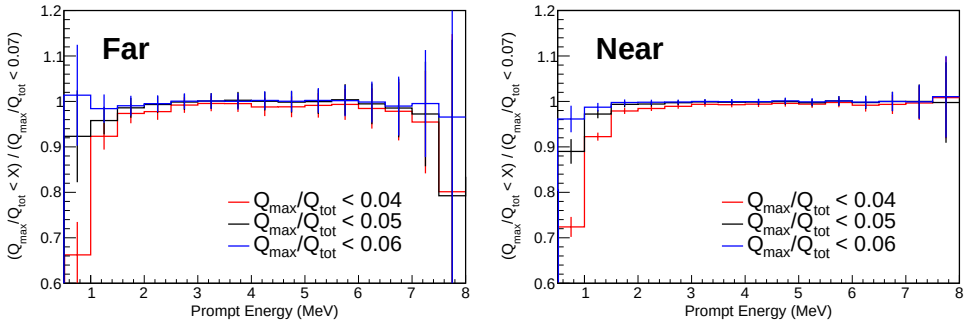

Figure 6.5: IBD spectrum with respect to the case in which $Q_{max}/Q_{tot} < 0.07$. The left plot shows the far detector and the right plot shows the near detector. With the assumption that the efficiency of $Q_{max}/Q_{tot} < 0.07$ is 100 %, this plot indicates that the Q_{max}/Q_{tot} cut efficiency is energy dependent.

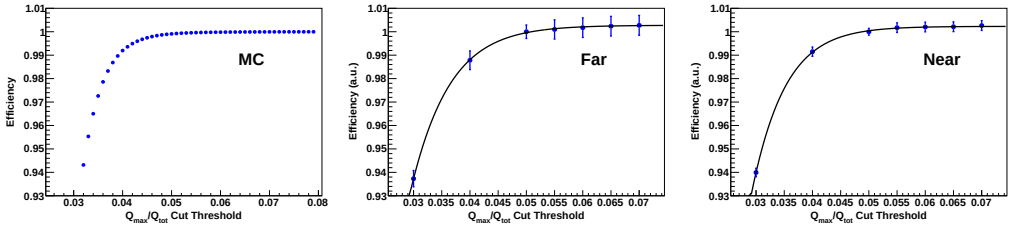

Figure 6.6: Q_{max}/Q_{tot} cut efficiency. The left plot shows MC. The middle plot shows the far detector, and the right plot shows the near detector. The black line is the fitting result of a logistic function. The cut efficiency at 0.07 is 99.99 $\pm$ 0.02% at both detectors, according to the fitting results.

Removal of Flasher Events

Sometimes PMTs spontaneously emit greater intensities of light, which can be triggers. This event, called a flasher, is not yet fully understood. For maintaining purity of signal, PMTs with high flash rates are removed from the DAQ system. Where the discharge of flasher events is suspected in PMTs, and the flasher event has a particular hit time and charge pattern, so the flasher event can be removed without signal loss. Typically, flasher events occur before hit-time 0 (t0) and hold a greater amount of charge, as shown in Fig. 6.7. It is more efficient to remove the flashers using the time and charge information between -400 $\sim$ 800 ns than -100 $\sim$ 50 ns, so that the removal cut uses the same Qmax/Qtot as the γ-rays

from radioactivity removal cut. However, a difference between the two cuts is that the flasher removal cut uses a wider time-window. For the 100% efficiency, the threshold of flasher removal cut is also 0.07. Therefore, the flasher removal cut includes the γ-ray from the radioactivity removal cut as well.

- γ-ray and flasher removal Q_{max}/Q_{tot} (-400 $\sim$ 800 ns) < 0.07

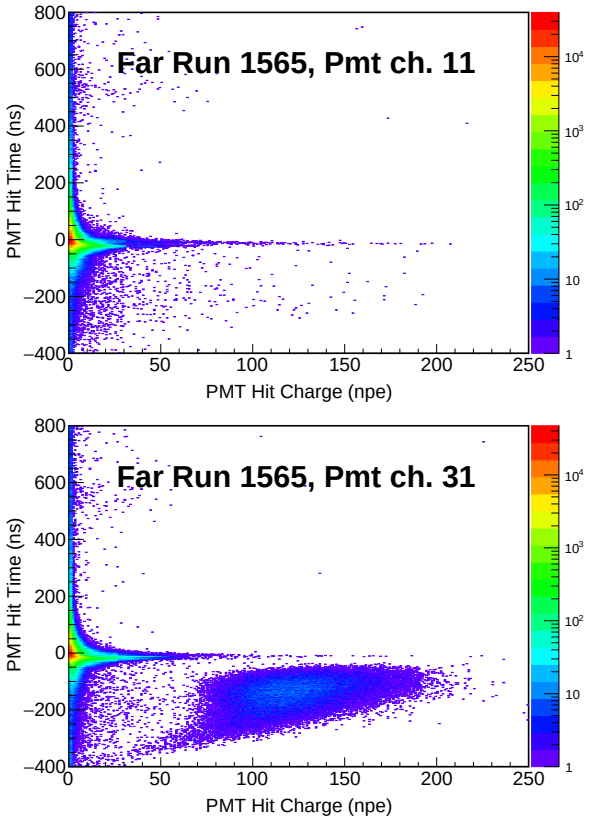

Figure 6.7: PMT hit time and charge distribution. The top plot shows the normal PMT and the bottom plot shows the flasher PMT. The flasher PMT has an abnormal structure (high hit charge and early hit time) compared with that of the normal PMT.

However, sometimes flashers cannot be removed by the flasher cuts, Q_{max}/Q_{tot} (-400 $\sim$ 800 ns) < 0.07, mentioned above. These flasher events have a rate of approximately 0.05 times the Q_{max}/Q_{tot} and usually affect the delayed signals and increase the rate of accidental background. Removal of these flasher events

is not easy;, however, they can still be removed because of properties that allow them to occur at a specific time period around a specific PMT. By monitoring the rate of accidental background or delayed signals, we could identify the specific time period of flasher events. To identify where the flasher events might occur, we introduced three variables for flasher removal: Q_{max}PMT, Q_{max}/Q_{tot} (-400 $\sim$ 800 ns) and Q_{ave}/Q_{max} (-400 $\sim$ 800 ns). As mentioned previously, it is more efficient to use the time and charge information between -400 $\sim$ 800 ns than -100 $\sim$ 50 ns. Q_{max}PMT is defined as a PMT that has the greatest amount of charge among all PMT hits in an event. Q_{ave} is average charge of the PMTs neighboring the Q_{max}PMT. When a flasher event occurs, the charges of PMT hits are distributed mainly around a Q_{max}PMT. The lower Q_{ave} means that the charge is more concentrated on a Q_{max}PMT. Therefore, flasher events usually have large Q_{max}/Q_{tot} (-400 $\sim$ 800 ns) and low Q_{ave}/Q_{max} (-400 $\sim$ 800 ns). By using these three properties, additional flasher removal cuts can be developed. Fig. 6.8 shows the basic procedure of additional flasher cuts. More details are in Appendix C.

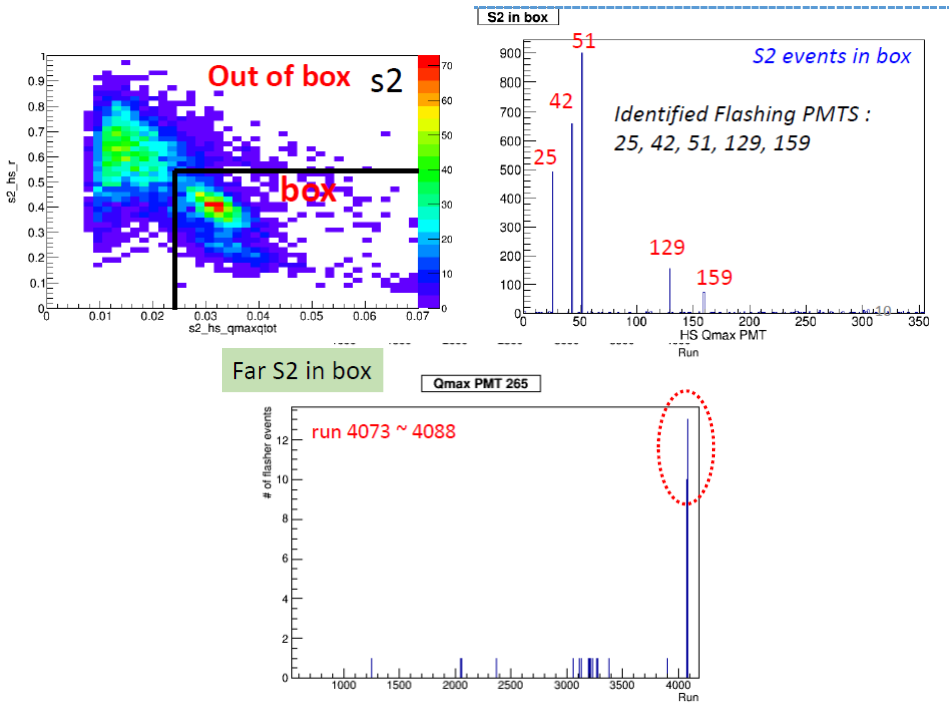

Figure 6.8: Procedure of additional flasher cuts. Top-left plot shows 2D-scattered distribution of Q_{ave}/Q_{max} (-400 $\sim$ 800 ns) (Y-axis) and Q_{max}/Q_{tot} (-400 $\sim$ 800 ns) (X-axis). The flasher events create a hotspot at the large Q_{max}/Q_{tot} (-400 $\sim$ 800 ns) and low Q_{ave}/Q_{max} (-400 $\sim$ 800 ns). Top-right plot shows the Q_{max}PMTs in the box in the top-left plot. The flasher events occur around these Q_{max}PMTs. The plot at the bottom identifies the time period at which the flasher events occurred.

6.3.2 Removal of Accidental Background

A radioactive isotope (*i.e.* radionuclide) is an atom with an unstable nucleus. These isotopes undergo radioactive decay and emit gamma(s) and/or subatomic particles such as alpha particles, electrons, and positrons, *etc.* Some radioactive isotopes such as ^{40}K, ^{60}Co, ^{232}Th, and ^{238}U, are naturally abundant in detector materials and the rocks around the detector hall. Energetic gammas and particles emanating from the radioactive decay of isotopes in the inner detector can form accidental as well as correlated backgrounds. Especially, signals produced by radioactive gamma rays or electrons can mimic the prompt signal of the inverse beta decay. Then, this background can form an accidental background with the single neutron events induced by cosmic muons.

The rate of signals resulting from radioactive gamma or electron emission, which can mimic the prompt signal of the IBD process, is ∼50 Hz. However, the expected IBD rate is approximately 70 events per day in the far detector and 700 events per day in the near detector. Therefore, reducing the non-relevant events is important to obtain a IBD process from the reactor neutrino. Three properties come to the fore when removing accidental events from IBD events: energy threshold, temporal correlation, and spatial correlation between the prompt and delayed signal.

Energy threshold

The prompt signal from the IBD process is transmitted by the positron. This signal must has an energy of at least 1.022 MeV, which is also the pair annihilation energy. As seen in the expected prompt energy spectrum in Fig. 1.5, the prompt positron often will not be 10 MeV or higher. The delayed signal is a neutron which is captured to Gd, and has a narrow gaussian distribution around 8 MeV. So far these conditions have been suitable for an ideal case only. The RENO detector has some inefficiencies, e.g. γ-rays can escape the LS region while they still have energy. Hence, the detector cannot observe their total energy. For these reasons, the energy threshold of a positron signal has been maintained above 0.75 MeV and below 12 MeV, and the energy threshold of the delayed signal has been maintained above 6 MeV and below 12 MeV. From the required energy threshold, the IBD candidate is reduced by the order of 10^{-2}. The energy threshold cuts are as follows

- 0.75 MeV < Prompt signal energy (E_p) < 12 MeV
- 6 MeV < Delayed signal energy (E_d) < 12 MeV.

Time Coincidence

The IBD reaction is commonly used for neutrino detection, as it produces a positron and a neutron. During the IBD process, a positron deposits kinetic energy and gets annihilated after colliding with an electron. The neutron becomes thermalized before being captured; hence, there should be a time difference (ΔT) between the positron event and neutron-capture event. The neutron capture cross-section becomes larger as the neutron kinetic energy becomes smaller by thermalization. Therefore, ΔT can be modeled as an exponentially decreasing function. Fig. 6.9 shows the ΔT of both the detectors. The mean Δt is almost the same at $\sim$ 26 μsec. Here, the cut of time coincidence has been fixed as 3 times the mean time difference (2 μs − 100 μs). The prompt and delayed candidate

signals are reduced by 0.5% because of the time coincidence cut and assuming that the event rate, which can be prompt of IBD process, is 50 Hz.

- 2 μs < Time difference between prompt and delayed signal (ΔT) < 100 μs

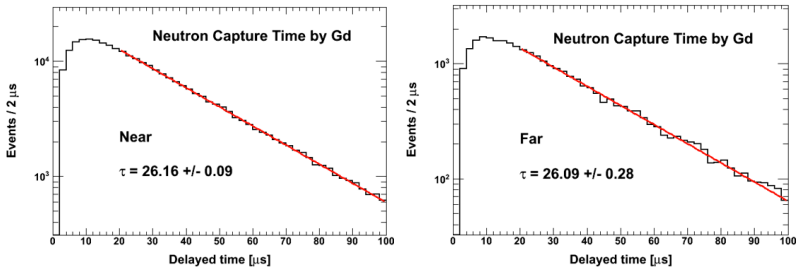

Figure 6.9: Time difference between prompt and delayed signals. The left side shows the near detector and the right side shows the far detector. The red Line is a fit of the simple exponential function. These two detectors have a similar mean-time difference $\sim$ 26 μs.

Spatial Correlation

The energy of neutron from the IBD is in the order of keV. For this reason, the neutron cannot go far from the IBD point of occurrence. Therefore, there is a strong spatial correlation between the IBD's prompt and delayed signals. However, accidental backgrounds have no spatial correlation and thus can permit a greater distance between the prompt and the delayed signals than the IBD pairs can. This spatial information can be a useful tool to remove the accidental background.

Fig. 6.10 shows the ΔR distributions of the near detector data. The tight accidental cut sample has almost no events that have ΔR > 2.0 m (0.001%). Therefore, the ΔR cut is maintained lower than 2.0 m with almost zero signal loss.

- Distance between the prompt and delayed signals (ΔR) < 2.0 m

From Fig. 6.11, ΔR cut could reduce the accidental backgrounds by 30$\sim$50%.

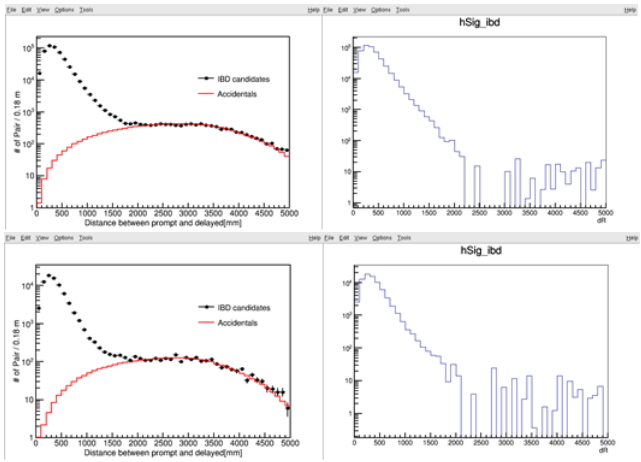

Figure 6.10: Distance between the prompt and delayed signals. The top plots are of the far detector, and bottom plots are of the near detector. Left side shows ΔR of IBD candidates and accidental events. Right side shows ΔR of IBD signals. From these plots, the signal with ΔR $>$ 2.0 m is 0.001% of the total sample.

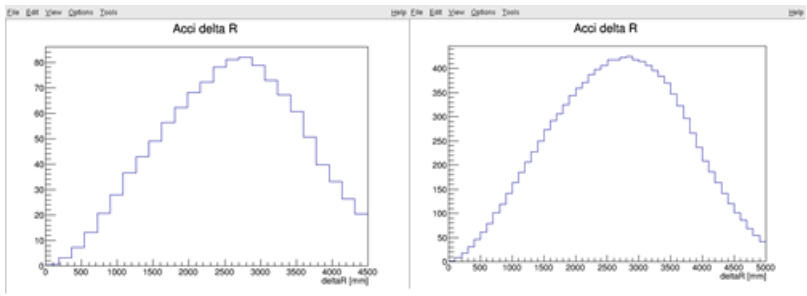

Figure 6.11: Random ΔR distributions of the far(left), near(right) detector. ΔR $>$ 2.0 m reduces the accidental background by 30$\sim$50%

Buffer and Veto Trigger Veto

There are some components that have a buffer and veto trigger following the prompt signal. There are a few events from the prompt signal after 100 μs. According to Fig. 6.12, we decided to reject the pairs that have a buffer and veto trigger within 100 μs of the prompt. The signals rejected by this veto cut are shown in Fig. 6.13. They are mainly low-energy backgrounds of $\sim$2 MeV.

- Zero Buffer and Veto trigger within (0 μs, 100 μs) of prompt signal

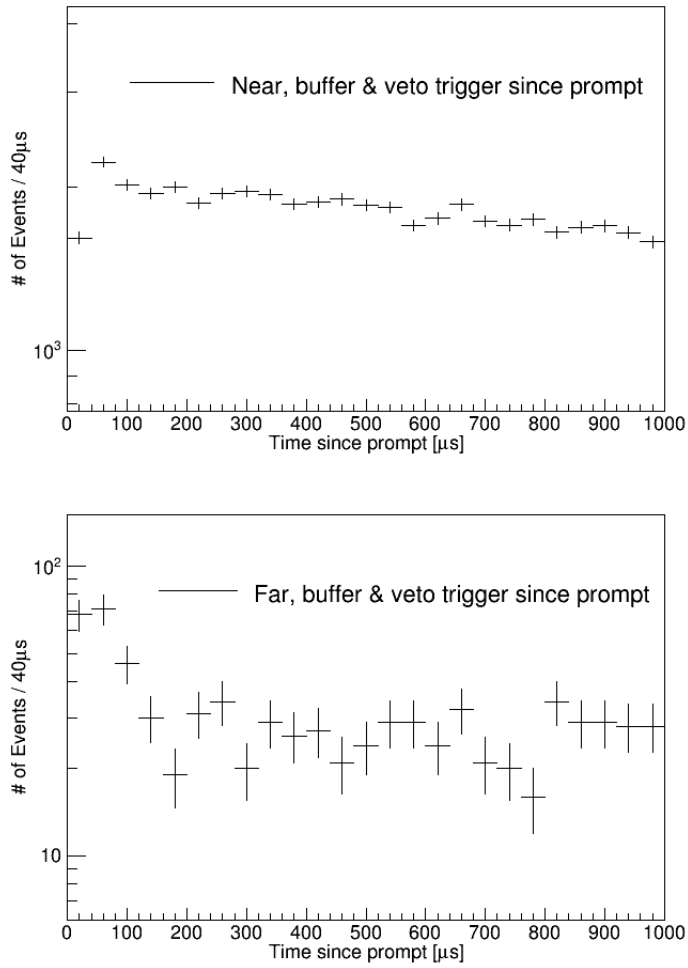

Figure 6.12: Buffer and veto trigger time-distribution since prompt. The top plot shows the near detector and the bottom plot shows the far detector.

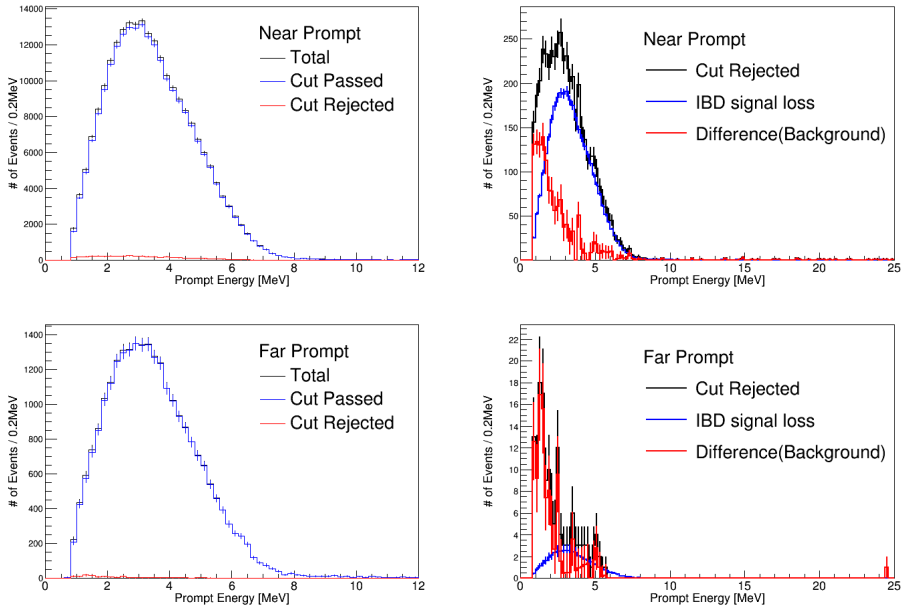

Figure 6.13: Prompt spectra before and after buffer and veto trigger beyond 100 μs veto cut. The upper plots are of the near detector and the lower plots are of the far detector. The plots on the right are before applying the cut (black), after applying the cut (blue), and rejected by the cut (red). The plots on the left are rejected by the cut (black), predicted signal loss due to the cut (blue), and the difference between the two histograms (red). The black histogram in the plots on the left show the background rejected by the cut.

6.3.3 Removal of Cosmogenic $^9Li/^8He$ Background

Neutrons can be produced as a result of interactions between muons and the protons inside or outside the detector. Such neutrons could enter the detector, get captured, and mimic the prompt or delayed signals of the IBD candidates. For that reason, these events from the muon need to be cut. We chose to reject the events that occur within 1 ms after the muon event passing. This veto time-window (1 ms) was decided considering the efficiency. There are two types of muons: one which passes through the buffer (muon1) and the other which shortly passes through the veto region before depositing a large amount of energy in said veto (muon2). The observed energy of the reactor neutrino events is below 12 MeV. However, muon1 deposited a large amount of energy at the buffer region. We defined a muon1 event as that which deposited at the buffer an amount of

energy greater than 70 MeV. Muon2 deposited a large amount of energy at the veto region but a small amount of energy at the buffer. The criteria for muon2 is energy deposit of more than 20 MeV at the buffer and number of hits greater than 50 in the veto region. Muon1 can deposit very high energies. If muons have enough energy, they can help produce ^{9}Li or ^{8}He. As mentioned in the previous section, ^{9}Li/^{8}He decay with a long lifetime also emits neutrons, and can mimic the IBD process and give a severe background. To reduce the ^{9}Li and ^{8}He backgrounds, the range of cut time has to be much longer than that of any other veto cuts. Because the half-life of ^{9}Li is 119.1 ms and 178.3 ms for ^{8}He, the ^{9}Li and ^{8}He events are timely correlated with the muons. They can be selected from the time distribution since the last muon (t) for all the IBD candidate events, and the time distribution can be modeled by a combination of two exponential functions.

$$f(t) = A \cdot \exp\left(-\frac{t}{\lambda}\right) + B \cdot \exp\left(-\frac{t}{T}\right), \ \frac{1}{\lambda} = \frac{1}{\tau} + \frac{1}{T} \tag{6.1}$$

where A and B are the magnitudes of ^{9}Li and ^{8}He and other IBD candidates, T is the mean time interval between two adjacent muons and the inverse of muon rate, τ is the lifetime of ^{9}Li and ^{8}He, and λ is the effective lifetime of ^{9}Li and ^{8}He due to interruption by the muons.

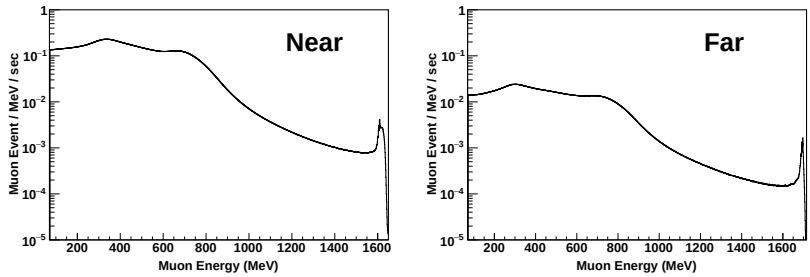

Figure 6.14: Muon visible energy spectra. The left plot shows the muon spectrum of the near detector and the right plot shows the muon spectrum of the far detector. The spectrum shows a peak around 1,600 MeV. The muon deposit energy is directly proportional to the length of the trajectory in the detector. Therefore, the maximum muon energy is dependent on detector size.

Depending on the muon visible energy, different ranges of time windows for rejecting muon-associated events are used. The ranges are optimized so that ^{9}Li/^{8}He backgrounds are rejected maximally with low IBD signal loss. For the optimization, we divided muon energy into finer intervals of 0.1 GeV from 0.9 to 1.5 GeV and 0.05 GeV from 0.8 to 0.9 GeV at the far detector, and 0.1 GeV interval

from 1.1 to 1.6 GeV at the near detector. Figs. 6.15, 6.16 show the time difference from muons for various muon energy bins and the rejected prompt energy distribution of various muon time-cut criteria for the far and near detector.

The optimized cuts are as follows:

- Muon 1 (Far : 0.07 $\sim$ 0.85 GeV , Near : 0.07 $\sim$ 1.1GeV) : Veto all events within a 1 ms window following muon 1.

- Muon 2 (Far, Near : 20 $\sim$ 70 MeV , the number of hits in the outer detector $>$ 50) : Veto all events within a 1 ms window following muon 2.

- Far Muon A ($>$ 1.5 GeV) : Veto all events within a 1000 ms window following muon A

- Far Muon B (1.3 $\sim$ 1.5 GeV) : Veto all events within a 800 ms window following muon B

- Far Muon C (1.1 $\sim$ 1.3 GeV) : Veto all events within a 500 ms window following muon C

- Far Muon D (0.85 $\sim$ 1.1 GeV) : Veto all events within a 100 ms window following muon D

- Near Muon A ($>$ 1.6 GeV) : Veto all events within a 800 ms window following muon A

- Near Muon B (1.4 $\sim$ 1.6 GeV) : Veto all events within a 300 ms window following muon B

- Near Muon C (1.3 $\sim$ 1.4 GeV) : Veto all events within a 200 ms window following muon C

- Near Muon D (1.1 $\sim$ 1.3 GeV) : Veto all events within a 50 ms window following muon D

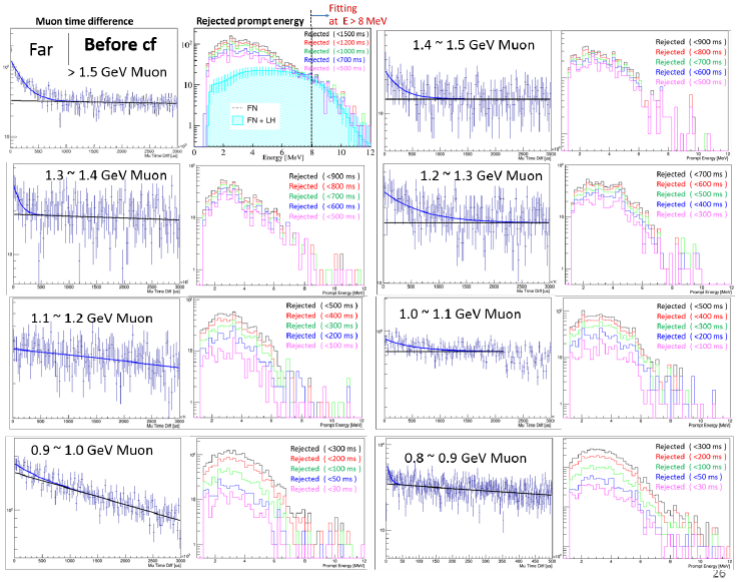

Figure 6.15: The time difference from muons for various muon energy bins, and the rejected prompt energy spectrum by the muon time-difference cut for far data before ^{252}Cf contamination.

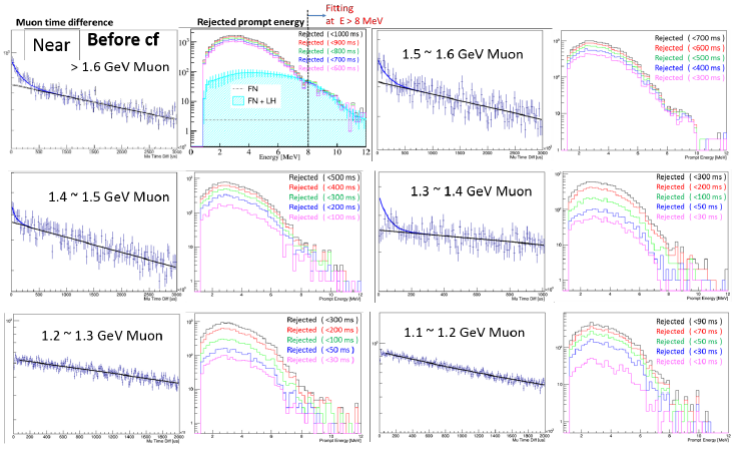

Figure 6.16: The time difference from muons for various muon energy bins, and the rejected prompt energy spectrum by the muon time-difference cut for near data before ^{252}Cf contamination.

The optimized muon veto cut criteria and their signal loss, rejected ^{9}Li/^{8}He , and remaining ^{9}Li/^{8}He for muons A, B, C, and D are summarized in table **??**. These are data before ^{252}Cf contamination. For data after ^{252}Cf contamination, muon energy spectra and event rates are corrected to the reference (before ^{252}Cf contamination), so same criteria are applied (Details are in Section 4.2 and Appendix A)

Muon Energy	Veto cut	Signal loss (%)	Rejected ^{9}Li/^{8}He (/day)	Remaining ^{9}Li/^{8}He (/day)
Before cuts	-	-	-	3.99 ± 0.36
$>$ 1.5GeV	$<$ 1000ms	4.03 ± 0.28	1.64 ± 0.21	2.35
1.4 $\sim$ 1.5GeV	$<$ 800ms	5.42 ± 0.28	2.08 ± 0.22	1.91
1.3 $\sim$ 1.4GeV	$<$ 800ms	7.06 ± 0.32	2.28 ± 0.23	1.71
1.2 $\sim$ 1.3GeV	$<$ 500ms	8.76 ± 0.34	2.31 ± 0.24	1.68
1.1 $\sim$ 1.2GeV	$<$ 500ms	11.14 ± 0.37	2.42 ± 0.24	1.57
1.0 $\sim$ 1.1GeV	$<$ 100ms	11.95 ± 0.37	2.48 ± 0.25	1.51
0.9 $\sim$ 1.0GeV	$<$ 100ms	13.77 ± 0.39	2.52 ± 0.24	1.47
0.85 $\sim$ 0.9GeV	$<$ 100ms	15.53 ± 0.40	2.76 ± 0.26	1.23

Table 6.2: The optimized muon time-cut criteria for far. The rejected, remaining ^{9}Li/^{8}He and signal loss for each muon energy bin are the values accumulated from the veto cuts in the higher muon energy bins.

Muon Energy	Veto cut	Signal loss (%)	Rejected ^{9}Li/^{8}He (/day)	Remaining ^{9}Li/^{8}He (/day)
Before cuts	-	-	-	19.33 ± 1.37
$>$ 1.6GeV	$<$ 800ms	7.34 ± 0.08	6.57 ± 0.57	12.76
1.5 $\sim$ 1.6GeV	$<$ 300ms	9.59 ± 0.09	7.72 ± 0.49	11.61
1.4 $\sim$ 1.5GeV	$<$ 300ms	11.94 ± 0.09	8.54 ± 0.68	10.79
1.3 $\sim$ 1.4GeV	$<$ 200ms	13.97 ± 0.10	9.07 ± 0.72	10.26
1.2 $\sim$ 1.3GeV	$<$ 50ms	14.70 ± 0.10	9.34 ± 0.73	9.99
1.1 $\sim$ 1.2GeV	$<$ 50ms	15.83 ± 0.10	9.65 ± 0.75	9.68

Table 6.3: The optimized muon time cut criteria for near. The rejected, remaining ^{9}Li/^{8}He and the signal loss for each muon energy bin are the accumulated values from the veto cuts in the higher muon energy bins.

6.3.4 Removal of Fast Neutron Background

The true IBD event consists of just a pair of one prompt and one delayed signal. So, if the pair has multiple prompt or delayed signals, it is not an IBD event. However, IBD candidates from fast neutrons transmit signals with high probability before and after the prompt signal. From this, fast neutron background is rejected using triggers in the vicinity of an IBD candidate pair. For the cut efficiency, three types of trigger cuts are used. In addition, other backgrounds from multiple neutrons are rejected by the time cut between adjacent IBD pairs.

- No any trigger within (-300 μs, 0 μs) of prompt signal
- Zero Buffer trigger within (0 μs, 200 or 800 μs) of prompt signal (800 for only far after ^{252}Cf contamination data)
- No prompt-like trigger (0 μs, 1000 μs) of prompt signal (only after ^{252}Cf contamination data)
- No adjacent IBD pairs within 500 μs or 1 sec (1sec for only far after ^{252}Cf contamination data)

Any Trigger Veto

Fig. 6.17 shows the component, which has time correlation with prompt signal. If the pair is a true IBD, then it will have no signal before the prompt. Therefore, this component is not an IBD signalm but a background. According to Fig. 6.17, we decided to reject pairs with any trigger within 300 μs before the prompt. Fig. 6.18 shows the rejection by this veto cut. The rejected signals consist of mainly 2.2 MeV hydrogen-capture and 8 MeV gadolinium-capture events. This means that the signals rejected by this cut are from multiple neutron events.

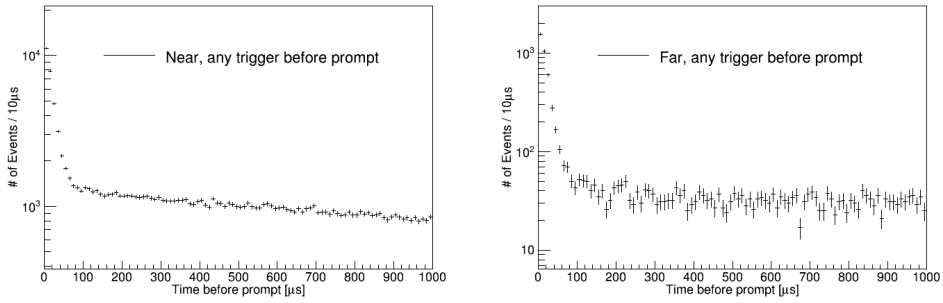

Figure 6.17: Any trigger time-distribution before prompt. The left plot shows the near detector and the right plot shows the far detector.

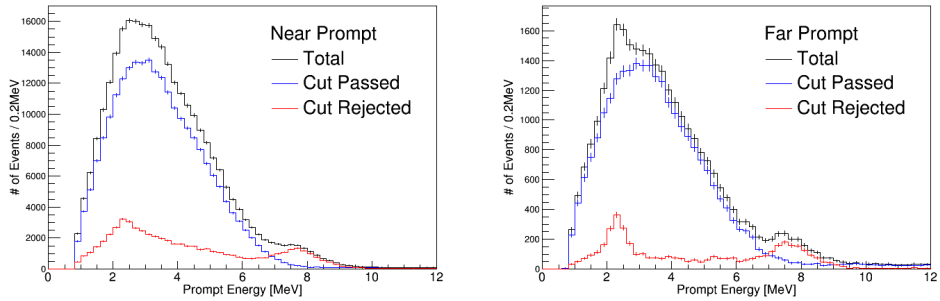

Figure 6.18: The prompt spectra before and after any trigger before the 300 μs veto cut. The left plot shows the near detector and the right plot shows the far detector. The black histogram shows IBD candidates before applying the cut. Blue shows after applying the cut. Red shows rejected by the cut. The red line consists mainly of hydrogen and gadolinium neutron capture events

Buffer Trigger Veto

There are some components that have a buffer trigger following the prompt signal besides the delayed neutron signal, as shown in Fig. 6.19. In 6.13, we had rejected pairs that have buffer triggers within 200 μs after the prompt. Only after the ^{252}Cf contamination of the far detector did we extend buffer trigger cuts from 200 μs to 800 μs to reject ^{252}Cf induced backgrounds. The signals rejected by this veto cut are shown in Fig. 6.20. The rejected signals mainly consist of the flat component (= fast neutron, as will be discussed in chapter 7) and some gaussian-distributed background around 10 MeV, and came from mainly ^{252}Cf contaminated backgrounds.

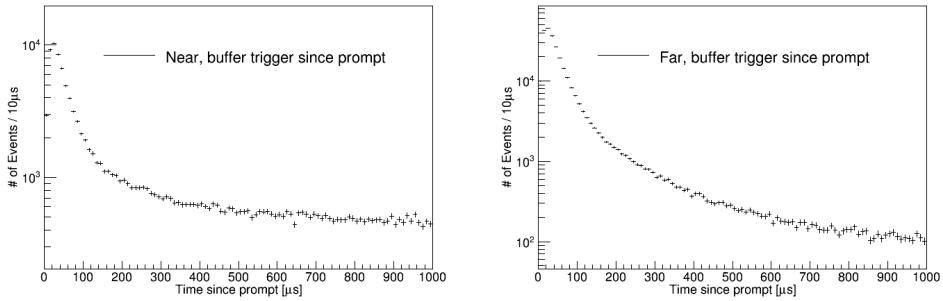

Figure 6.19: Buffer trigger time distribution since prompt. The left plot shows the near detector and the right plot shows the far detector.

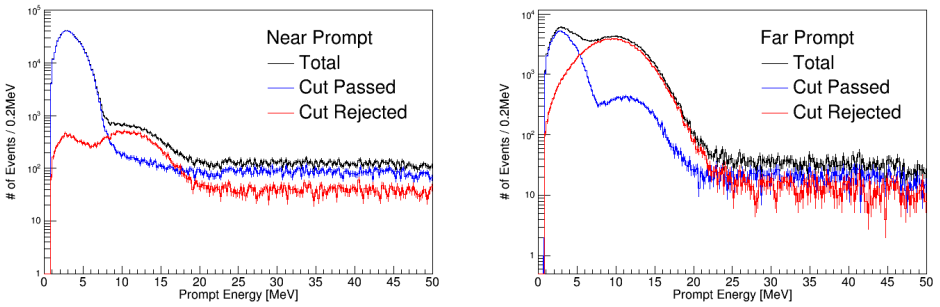

Figure 6.20: The prompt spectra before and after buffer trigger after the 200 (left side, near detector) or 800 (right side, far detector after ^{252}Cf contamination)μs veto cut. The black histogram is the IBD candidates before applying the cut. Blue one is those after applying the cut. Red one is those rejected by the cut. The red line mainly consists of fast neutron events and ^{252}Cf component around 10 MeV.

Prompt-like Trigger Veto

The prompt-like trigger is the buffer trigger that comes after the muon veto cuts, Qmax/Qtot cut, and flasher cut, but with no energy cut applied. As shown Fig. 6.21, the component that is time correlated with the prompt-like trigger is smaller than that correlated with the buffer trigger and any other trigger. We decided to rejected pairs of post- ^{252}Cf contamination data for both the far and near detectors, which had a prompt-like trigger within 1,000 μs after the prompt.

Fig. 6.22 shows the rejected signals by this veto cut. The rejected events seem also fast neutron background and ^{252}Cf contaminated background.

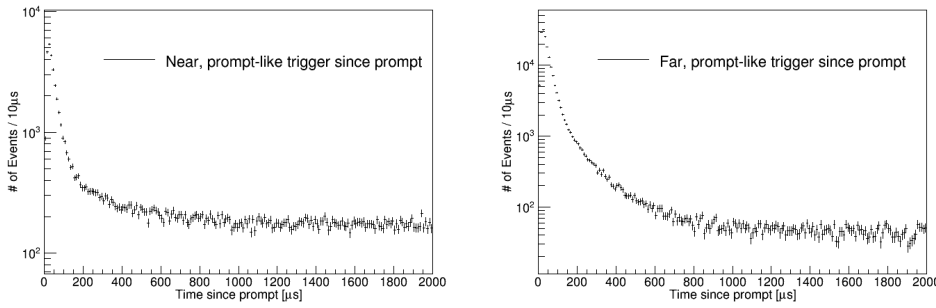

Figure 6.21: Prompt spectra before and after prompt-like trigger, after 1,000 μs veto cut. The right plots are before applying the cut (black), after applying the cut (blue), and rejected by the cut (red). The left plots are rejected by the cut (black), predicted signal loss due to the cut (blue), and the difference between these two histograms (red). The black histogram in the left plots shows the background rejected by the cut.

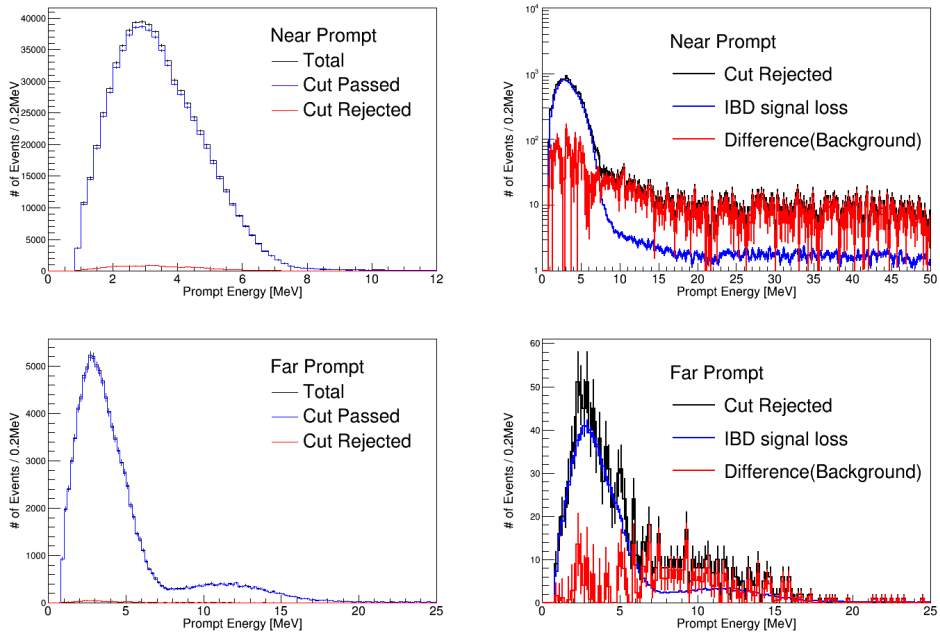

Figure 6.22: Prompt spectra before and after prompt-like trigger after 1000 μs veto cut. The right plots are before applying the cut (black), after applying the cut (blue), and rejected by the cut (red). The left plots are rejected by the cut (black), predicted signal loss due to the cut (blue) and the difference between these two histograms (red). The black histogram in the left plots shows the rejected background by the cut.

Removal of Adjacent IBD pairs (Multiplicity cut)

Even after applying the above cuts to remove fast neutrons and ^{252}Cf contaminated backgrounds, the backgrounds still remain. To eliminate these backgrounds, we developed multiplicity cuts that remove subsequent IBD pairs within 500 μs or 1 sec(for only the far detector after obtaining ^{252}Cf contamination data), from Fig. D.3, which shows the time difference between the IBD candidate pairs. This cut eliminates events due to multiple neutrons, multiple interactions of a neutron with protons in the ID, and ^{252}Cf contamination background. Events rejected by the multiplicity cut are described in Fig. 6.24. Multiplicity 500 μs cut rejects backgrounds in 2.2 MeV and 8 MeV, which come from multiple neutrons. Multiplicity 1 sec cut rejects additional backgrounds at 1 MeV and 10 MeV, which come from ^{252}Cf contamination backgrounds.

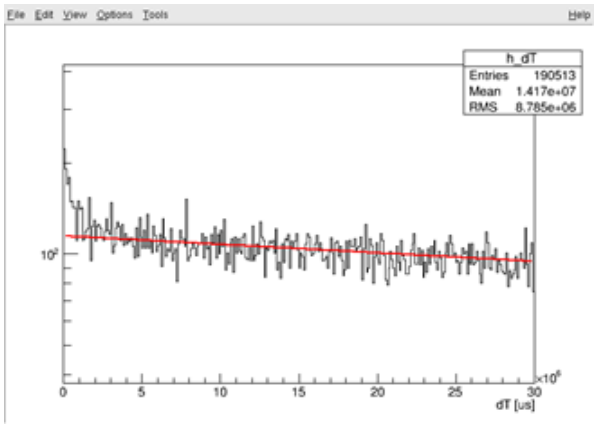

Figure 6.23: Time difference between IBD candidate pairs.

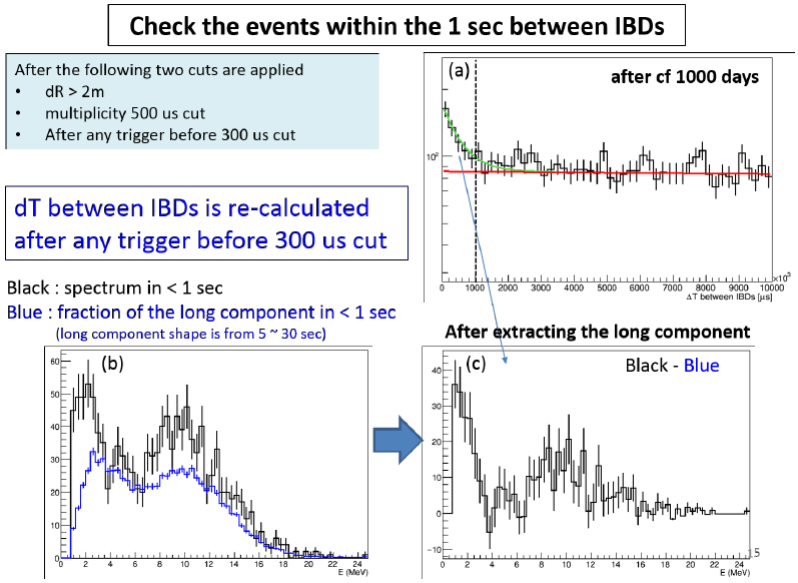

Figure 6.24: Prompt spectra before and after multiplicity 500 μs cut and 1 sec cut.

6.3.5 Further Removal of ^{252}Cf Contamination Background

A small amount of ^{252}Cf source was accidentally introduced into the near and far detectors during the detector calibration of October 2012. Most of multiple

neutron events coming from the ^{252}Cf contamination are removed by stringent multiplicity requirements. However, additional cuts are developed to remove additional ^{252}Cf contaminated background using temporal and spatial correlation of IBD candidates and prompt candidate accompanied. The dissolved ^{252}Cf source still stays at narrow region of the detectors. Therefore, the removal of ^{252}Cf hotspot region by using the reconstructed vertex is very effective.

Removal by Temporal and Spatial Correlation with Prompt Candidates

When ^{252}Cf decays, multiple neutrons (An average of $\sim$3.7 per fission with mean energy of 2.1 MeV) and gammas are emitted via α-emission (96.9%) and spontaneous fission (3.1%). So, ^{252}Cf causes many IBD-like pairs in a short time interval and many prompt candidates (called single events) having temporal and spatial correlations with prompt signals of the IBD-like pairs.

Cf removal cuts using temporal and spatial correlations with prompt signals of the IBD-like pairs are categorized as Cf cut A and Cf cut B according to the time sequence of prompt-like candidate events with prompt signals from the IBD-like pairs. Fig. 6.25 schematically describe ^{252}Cf removal cut A and B. The criteria Ep $>$ 3 MeV is applied because the ^{252}Cf removal cuts associated with single events below 3 MeV would increase signal loss significantly. Fig. 6.26 shows the prompt energy shapes of IBD candidates rejected by the ^{252}Cf removal cuts A and B.

Below cuts are only applied to the period after ^{252}Cf contamination with $Q_{max}/Q_{tot} < 0.04$.

- Cf cut A : No prompt-like trigger greater than 3 MeV within (0 sec, 10 sec) and (0, 400 mm) of prompt signal (near detector)

- Cf cut A : No prompt-like trigger greater than 3 MeV within (0 sec, 30 sec) and (0, 500 mm) of prompt signal (far detector)

- Cf cut B : No prompt-like trigger greater than 3 MeV within (-10 sec, 0 sec) and (0, 400 mm) of prompt signal (near detector)

- Cf cut B : No prompt-like trigger greater than 3 MeV within (-30 sec, 0 sec) and (0, 500 mm) of prompt signal (far detector)

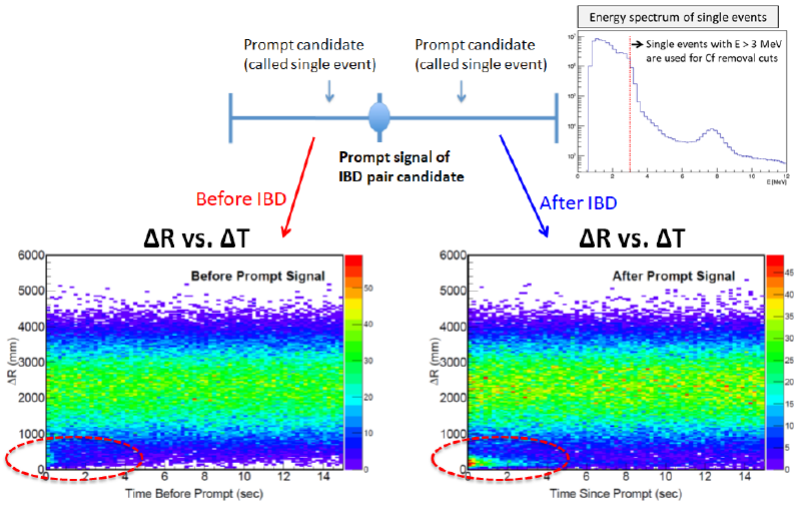

Figure 6.25: 2D scatter plots (ΔR vs. ΔT) that show spatial and time correlation of prompt signals with single events for after ^{252}Cf contamiated period. Upper-right histogram is the energy spectrum of the prompt candidate (called single events). The single events with E > 3 MeV are used for Cf removal cuts because single events below 3 MeV cause large deadtime when used for Cf removal cut.

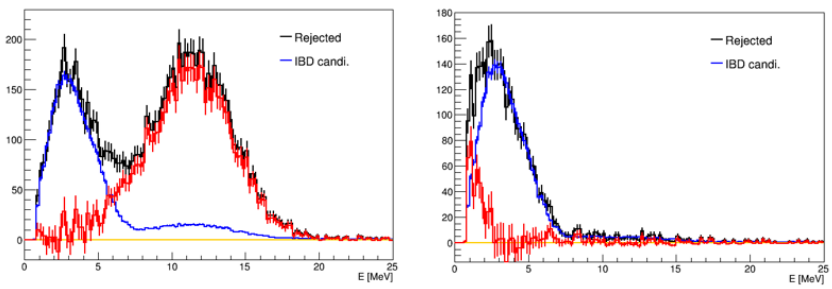

Figure 6.26: Prompt spectra before and after applying cf cut A(left) and B(right).

Removal around ^{252}Cf Contaminated Hotspot Region

Hotspot removal cut is a spatial veto requirement for rejecting some Cf background events whose vertices seem to be concentrated on a small spatial region. Fig. 6.27 shows the vertex distributions of the far detector(Z distribution, R^2 distribution, and X–Y distribution) and the hotspot region. There is no signifi-

cant hotspot region at the near detector due to small amounts of ^{252}Cf contaminated backgrounds at the near detector. From this, we determined the criteria for hotspot removal as follows.

- Removal of Hotspot (Far): No prompt signals in the region $\sqrt{(X-125mm)^2+(Y-125mm)^2} < 500$mm and Z < -1100 mm

Fig. D.5 shows the prompt energy shapes of IBD candidates rejected by the removal of ^{252}Cf hotspot region. The red histograms are the background shapes rejected after subtracting IBD candidates from the deadtime. We can see the hotspot-removal cut-rejected Cf background of the 8-MeV component in the post ^{252}Cf contamination data.

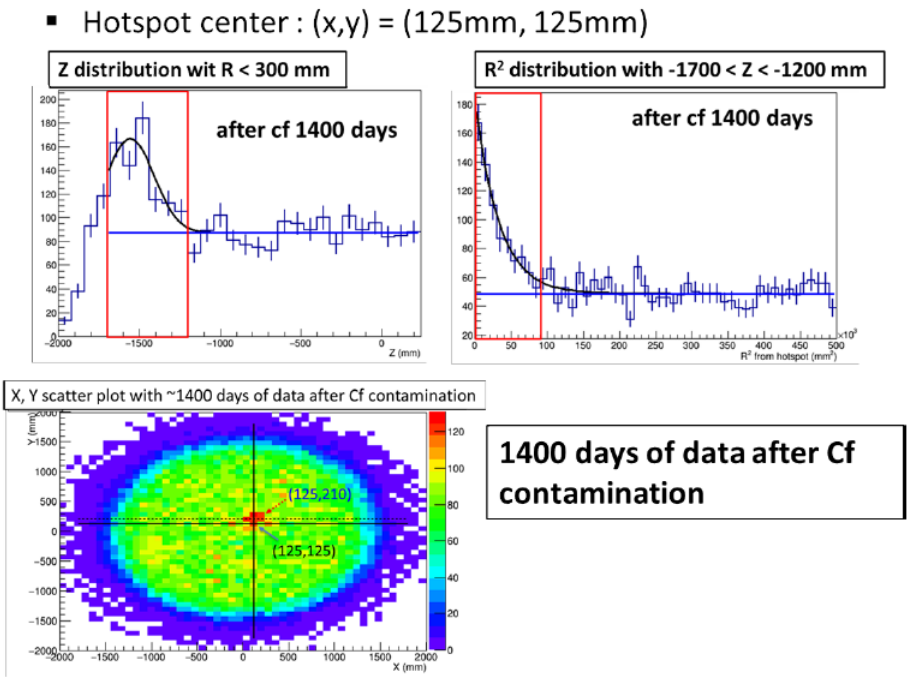

Figure 6.27: Z, R^2 and X–Y distributions of the hotpot region with data gather after the ^{252}Cf contamination period.

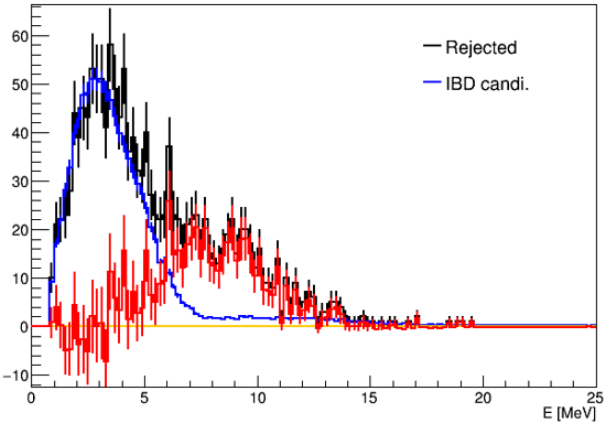

Figure 6.28: Prompt spectra before and after removal of hotspot region.

6.4 Signal Loss due to Selection Requirements

6.4.1 Timing Veto with Muon or Trigger Information

If the trigger is within the cut time range [0,Δt] relative to the prompt of the IBD event, the IBD event is lost by the cut. Because there is no correlation between the prompt of the IBD event and adjacent trigger, signal loss is just the probability that at least one of the triggers is within the cut time window [0,Δt] relative to the prompt of the IBD event. It can be calculated by the Poisson probability distribution as follows

$$P(0, \Delta t) = 1 - e^{-R_{trg}\Delta t} \tag{6.2}$$

where R_{trg} is the averaged trigger rate for the data period. The signal losses from the timing veto cut with muon or trigger information are calculated by eq. 6.2. However, there is some case-by-case modification in 6.2. More details on this are given in Appendix D.

6.4.2 Remval of Flasher Events

Flasher events usually effect the delayed signals and create accidental backgrounds. As shown in Fig. 6.2, the prompt spectrum of an accidental background is completely different from that of the IBD signals, as shown in Fig. 6.29. Also, by using their specific properties, the flasher events can be removed with high

accuracy. Therefore, the signal loss from the removal of flasher events is insignificant. In fact, this loss is not easy to calculate. For example, even Eq. 6.2 cannot be used to calculate the loss. Instead, the signal loss from the removal of the flasher events is estimated by performing a spectral fit to the rejected IBD candidate. The signal losses are lower than $\sim$0.5% in both far and near detectors.

6.4.3 Removal of ^{252}Cf Contamination Background

There are three types of ^{252}Cf removal cuts: timing veto cut, cuts around the hotspot region, and spatial and temporal correlated cuts. The timing Cf removal cuts can also be calculated by Eq. 6.2. The spatial correlated Cf removal cut (hotspot removal cut) is calculated from the signal loss at set A, which does not contain ^{252}Cf contamination. The signals, rejected by removal of hotspot for set A, are not background from ^{252}Cf contamination, but the IBD or other backgrounds. Therefore, the loss from hotspot removal cut can be easily estimated. Lastly, the loss from spatial and temporal correlated cuts (Cf cuts A and B) is also calculated by modifying Eq. 6.2. For the calculation of signal loss of Cf cuts A and B, we calculate the random rate of single events that satisfy Cf cuts A and B, except the ΔT correlation. Further details on this are available in Appendix D.

6.5 Summary

Applying the IBD event selection criteria, the observed IBD candidate events are 850,666 (103,212) at the near (far) detector from sets A and B, which have a total of 1,807.88 (2,193.04) days of live data. Tables **??** below summarize the observed IBD candidates for set A and set B.

	Set A	Set B	Set A+B
Observed IBD candidates	23536	79676	103212
DAQ live time (days)	384.47	1808.51	2193.04

Table 6.4: Event rate of the observed IBD candidates at $1.2 < E_p < 8.0$MeV. for the far detector.

	Set A	Set B	Set A+B
Observed IBD candidates	221140	629526	850666
DAQ live time (days)	379.66	1428.22	1807.88

Table 6.5: Event rate of the observed IBD candidates at $1.2 < E_p < 8.0$ MeV for the near detector.

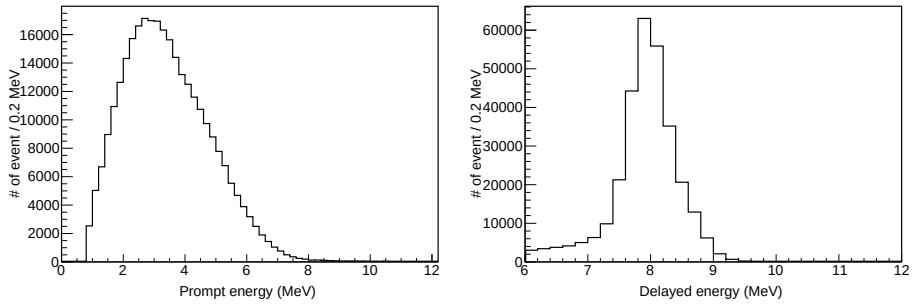

Figure 6.29: Prompt and delayed signal spectrum of observed IBD candidates

Tables 6.6, 6.7 below are summary of the signal loss for set A and set B. More details on this are given in Appendix D.

Selection cut	Set A	Set B	Set A+B
Any Trigger before 300μs	3.679 ± 0.001	3.364 ± 0.001	3.419 ± 0.001
Buffer Trigger after 200(800)μs	1.440 ± 0.001	5.265 ± 0.001	4.594 ± 0.001
Buffer & Veto Trigger after 100μs	0.188 ± 0.001	0.187 ± 0.001	0.187 ± 0.001
Prompt-like Trigger after 1000μs	-	0.781 ± 0.004	0.644 ± 0.003
Adjacent IBD pairs within 500μs(1sec)	0.000 ± 0.000	0.984 ± 0.016	0.811 ± 0.013
Muon Veto cut	18.127 ± 0.005	18.370 ± 0.003	18.328 ± 0.003
Cf cut A	-	3.310 ± 0.027	2.730 ± 0.022
Cf cut B	-	3.421 ± 0.026	2.821 ± 0.021
Hotspot removal	-	1.640 ± 0.049	1.352 ± 0.040
Additional flasger cut	0.064 ± 0.029	0.634 ± 0.047	0.536 ± 0.039
Combined	22.471 ± 0.005	33.120 ± 0.054	31.252 ± 0.045

Table 6.6: Signal loss for the far detector. Buffer Trigger veto cut is 200μs for set A and 800μs for set B. Adjacent IBD pair cut is within 500μs for set A and within 1 sec for set B.

Selection cut	Set A	Set B	Set A+B
Any Trigger before 300μs	13.172 ± 0.001	12.982 ± 0.001	13.022 ± 0.001
Buffer Trigger after 200μs	1.149 ± 0.001	1.053 ± 0.001	1.073 ± 0.001
Buffer & Veto Trigger after 100μs	1.430 ±0.001	1.550 ± 0.001	1.525 ± 0.001
Prompt-like Trigger after 1000μs	-	2.005 ± 0.005	1.584 ± 0.004
Adjacent IBD pairs within 500μs	0.000 ± 0.000	0.000 ± 0.000	0.000 ± 0.000
Cf cut A	-	1.318 ± 0.004	1.041 ± 0.003
Cf cut B	-	1.362 ± 0.004	1.076 ± 0.003
Additional flasger cut	0.014 ± 0.004	0.072 ± 0.006	0.060 ± 0.005
Combined	37.420 ± 0.005	40.270 ± 0.006	39.671 ± 0.005

Table 6.7: Signal loss for the near detector.

Chapter 7

Estimation of Remaining Backgrounds

The remaining backgrounds after meeting the event selection requirements are subtracted from the final IBD candidate sample. The following subsections describe how to obtain the spectral shapes and rates of the remaining backgrounds. Since the rates and shapes of all the remaining backgrounds are measured from background-enriched samples, their uncertainties are expected to be further reduced as more data is gathered.

7.1 Accidental Background

A random coincidence of prompt-like and delayed-like signals may accidentally survive the application of several selection cuts. An accidental background is characterized by temporally and spatially uncorrelated coincidences between prompt and delayed signals. An accidental background sample is obtained by temporal dissociation between prompt- and delayed-like events, i.e., $\Delta T > 1$ ms for the IBD sample with no ΔR requirement. ΔT and ΔR of an accidental background are shown in Fig. 7.1. The prompt energy spectra of the accidental backgrounds of the near and far detectors are shown in Fig. 7.2. The energy-bin-uncorrelated uncertainty in the accidental background spectrum is obtained from the statistical error in the background-enriched sample

The remaining background rate in the final sample is estimated by measuring the rate of random spatial associations in the IBD signal region of $\Delta R < 2.0$ m, extrapolated from the background-dominated region of $\Delta R > 1.75$ m using ΔR distribution of the accidental background spectrum as shown in Fig. 7.3. The χ^2

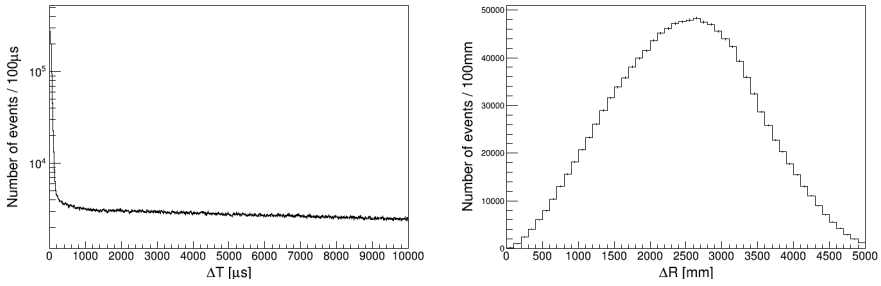

Figure 7.1: Properties of accidental background. The left plot shows the time difference(=ΔT) between the prompt and delayed signals. Accidentals occur in the $\Delta T > 1$ ms region only. The right plot shows the distance (=ΔR) between the prompt and delayed signals from the accidental events($\Delta T > 1$ ms). The accidental events show random ΔR correlation.

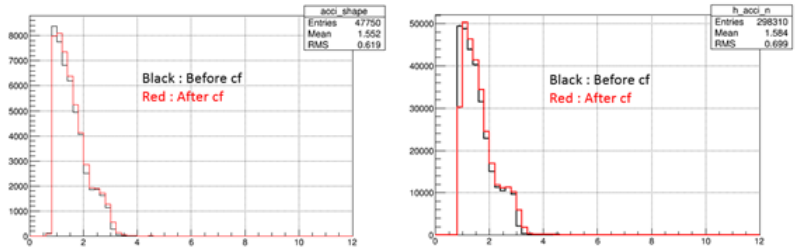

Figure 7.2: Prompt energy spectra of accidental backgrounds obtained from accidental background-enriched samples selected by temporal association larger than 1 ms. Left side is the far detector and right side is the near detector.

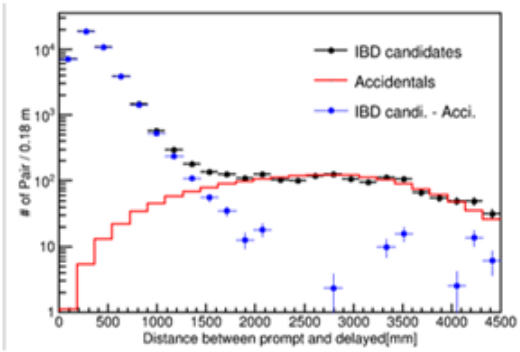

Figure 7.3: Fitting results of accidental estimation by ΔR method.

fitting function for the estimation of accidental background is

$$\chi^2 = \sum_i \left(\frac{\Delta R^i_{IBD} - \gamma \cdot \Delta R^i_{Acci.}}{\sqrt{\Delta R^i_{Acci.}}} \right)^2 \tag{7.1}$$

where, ΔR^i_{IBD} and $\Delta R^i_{Acci.}$ are the ith bin of IBD (Accidental) ΔR distribution. The fitting parameter γ represents a normalization factor between the ΔR distribution of the accidental sample and the ΔR distribution of the accidental background in the IBD sample. The measured accidental background in the final IBD sample is

$$Accidental(1.2 \sim 8.0MeV, \Delta R < 2.0m) = \gamma \cdot \Delta R^{1.2\sim8.0MeV,\Delta R<2.0m}_{Acci.} \tag{7.2}$$

The energy-bin-uncorrelated uncertainty is obtained from the fitting error.

$$\delta^{Bin-uncor.}_{Acci.} = \gamma \cdot \Delta R^{1.2\sim8.0MeV,\Delta R<2.0m}_{Acci.} \cdot \delta n^{1.2\sim8.0MeV}_{Acci.} \tag{7.3}$$

where $\delta n^{1.2\sim8.0MeV}_{Acci.}$ is the uncertainty of the normalized accidental spectrum. The energy-bin-correlated uncertainty is

$$\delta^{Bin-cor.}_{Acci.} = \delta\gamma \cdot \Delta R^{1.2\sim8.0MeV,\Delta R<2.0m}_{Acci.} \tag{7.4}$$

The obtained accidental background rates and uncertainties are summarized in Table 7.1.

Detector	Data Set	Rate	Total Uncert.
Far	Set A	0.390	0.020
	Set B	0.470	0.011
	Set A+B	0.456	0.010
Near	Set A	2.300	0.049
	Set B	2.602	0.029
	Set A+B	2.539	0.025

Table 7.1: Estimated rate of accidental background in per day, energy range: 1.2 $\sim$ 8 MeV.

7.2 Fast Neutron Background

An energetic neutron produced from a muon can travel many meters, transmitting energy to a proton by elastic scattering and finally being captured on Gd or H. The recoil proton due to neutron scattering can be a prompt, and the Gd-captured neutron can be a delayed of the IBD candidate. To estimate the fast neutron rate, when extending the prompt energy criteria to $\sim$50 MeV, the IBD candidates under the extended prompt energy criteria have a flat high-energy tail above 12 MeV. In dataset B (after ^{252}Cf contamination), ^{252}Cf contaminated background around 10 MeV is observed; therefore, the flat energy spectrum above 22 MeV is observed. The fast neutron background rate in the final IBD candidate sample is estimated by extrapolating it from the background dominant energy region of 12 $< E_{\rm p} <$ 45 MeV to the IBD signal region of 1.2 $< E_{\rm p} <$ 8.0 MeV, assuming a flat background spectrum as shown in Fig. 7.4. In dataset B, the fast neutron is fitted to the energy region of 22 $< E_{\rm p} <$ 45 MeV because of the ^{252}Cf contamination backgrounds. A fast neutron-enriched sample can be obtained by selecting IBD candidates that are accompanied by any prompt candidates of $E_{\rm p} > 0.7$ MeV within a subsequent 1 ms window. The prompt events of this sample show a distribution consistent with a flat spectrum in the IBD signal region as shown in Fig. 7.5.

Fig. 7.5 shows the prompt energy spectrum of the fast neutron background control samples. These control samples are taken from select IBD candidate prompt events, which are followed by a prompt-like candidate event within 1 ms. This is described in Fig. 7.6. The high-energy cosmic muons usually make multiple neutrons. Therefore, the prompt of fast neutron background could be followed by the capture of multiple neutrons. In Fig. 7.6, a spectrum of prompt-like candidate event shows neutron capture on H or Gd. Moreover, the delayed signal of IBD candidate is also a neutron-capture event. Therefore, these multiple

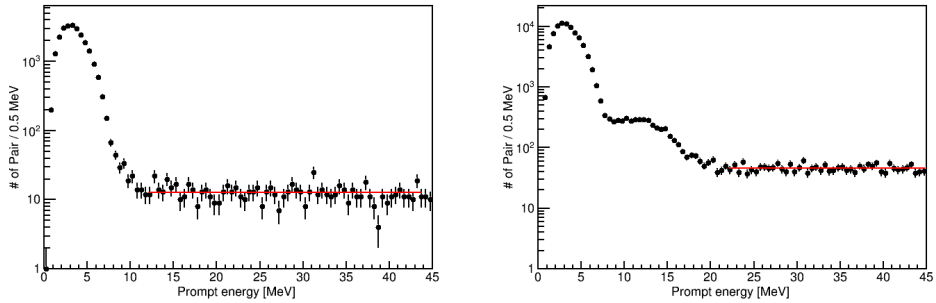

Figure 7.4: Prompt energy spectrum of IBD candidates including flat fast neutron spectrum at $E_{\mathrm{p}} > 12$ MeV(far). Left plot is for set A (before ^{252}Cf contamination) and right plot is for set B (after ^{252}Cf contamination). Remaining amount of fast neutrons is estimated from the 0^{th} polynomial function fit. ^{252}Cf backgrounds exist around 10 MeV; thus, fast neutron background fitting for dataset B is done in the energy region of > 22 MeV.

neutrons indicate that the prompt of IBD candidate event could be a fast neutron background with a flat energy spectrum.

The background rate uncertainty is obtained from the fitting error of the flat spectrum. The assumption of the flat background spectrum in the signal region is checked and validated by a fast neutron background-enriched sample.

The spectral shape uncertainty of the fast neutron background includes a possible deviation from the flat spectrum. In order to estimate this deviation, the background-dominated region in Fig. 7.5 is fitted with a first order polynomial as an alternative model.

The obtained fast neutron background rates and uncertainties are summarized in Table 7.2

Detector	Data Set	Rate	Total Uncert.
Far	Set A	0.451	0.017
	Set B	0.347	0.009
	Set A+B	0.365	0.008
Near	Set A	2.009	0.045
	Set B	1.755	0.028
	Set A+B	1.808	0.024

Table 7.2: Estimated rate of fast neutron background in per day, energy range: $1.2 \sim 8$ MeV.

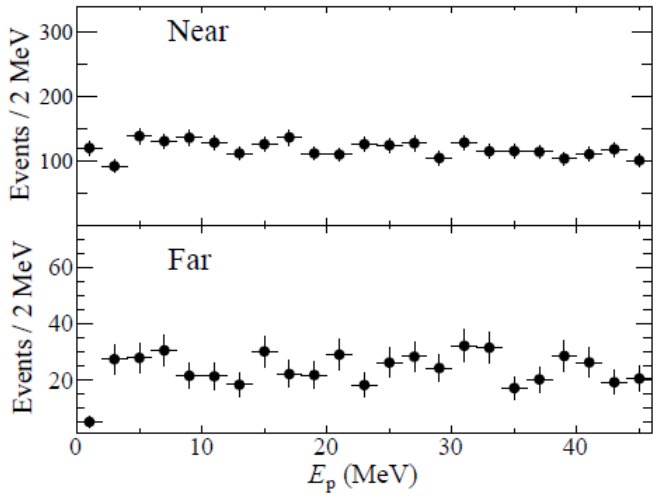

Figure 7.5: Prompt energy spectra of fast neutron-enriched samples in the near and far detectors.

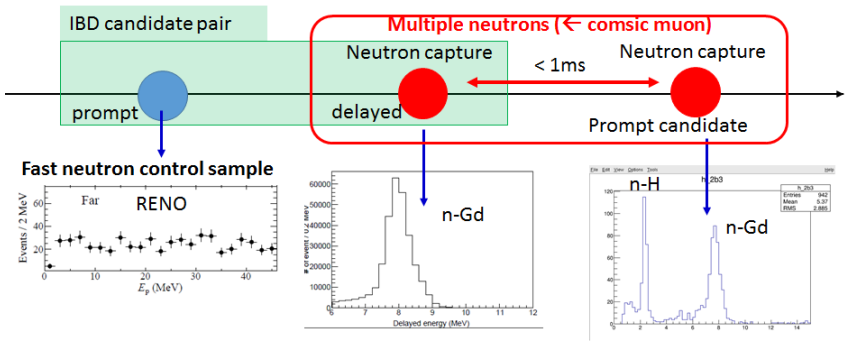

Figure 7.6: Diagram for selecting the fast neutron background enriched control sample. Cosmic muon may induce multiple neutrons.

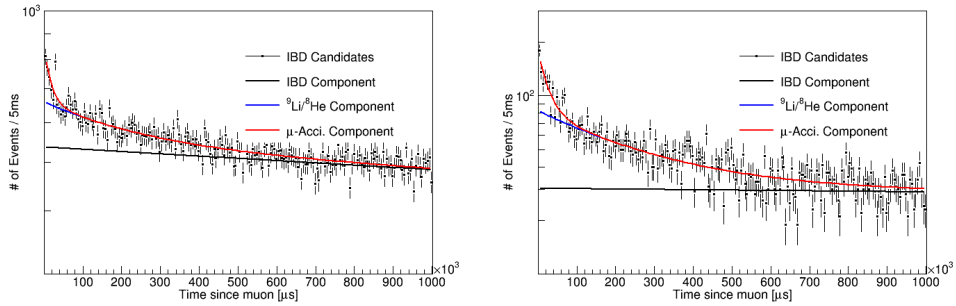

Figure 7.7: Decay time distribution of the IBD-like pairs from their preceding energetic muons in the near (left plot) and far (right plot) detectors. The ^{9}Li/^{8}He background is clearly seen with a measured mean decay time of ∼250 ms (combination of almost ^{9}Li ∼257ms and a few ^{8}He ∼172ms) while muon-induced accidental background events are observed right after the preceding muons.

7.3 Cosmogenic $^9Li/^8He$ Background

^{9}Li/^{8}He are produced by the interaction between cosmic muons and carbon in the detector. These isotopes have β and neutron cascade decay modes. Since ^{9}Li has a half-life of 0.178 sec and a Q value of 13.6 MeV, and ^{8}He has a half-life of 0.119 sec and a Q value of 10.7 MeV, these isotopes are hard to distinguish from those in the IBD process. The spectral shape of the ^{9}Li/^{8}He background is obtained using a sample of IBD-like pairs which are produced within 500 ms (400 ms) by energetic muons of $E_\mu > 1.6$ GeV (> 1.5 GeV) for the near (far) detector. The distribution of time difference between an energetic muon and a subsequent IBD candidate is shown in Fig. 7.7. Based on their observed spectra, the shortest decay time component is found to be the muon-induced accidental background followed by the ^{9}Li/^{8}He background. The IBD signals are temporally uncorrelated with muon events and their time differences are distributed according to the IBD rate. The measured mean decay time of ∼250 ms indicates predominant production of ^{9}Li over ^{8}He.

The measured ^{9}Li/^{8}He background shapes as shown in Fig. 7.8 are obtained by subtracting the energy spectra of the IBD signal and the muon-induced accidental background from those of the ^{9}Li/^{8}He background-enriched samples. The size of the IBD signal and the muon-induced accidental background are determined by performing a fit to the decay time distribution using three exponential functions. The spectral shape uncertainty comes from the statistical uncertainty of the ^{9}Li/^{8}He background-enriched sample because of the subtraction and, there-

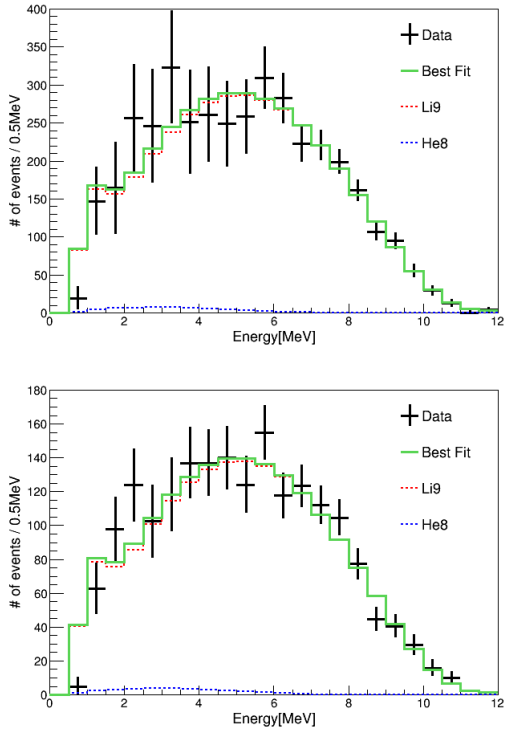

Figure 7.8: Measured ^{9}Li/^{8}He background spectra obtained from the enriched samples of 2,200 live days of data after subtracting the IBD signal and the muon-induced accidental background from those of the enriched sample. The MC ^{9}Li/^{8}He background spectra (green histograms) are overlaid with data where the relative fractions between ^{9}Li and ^{8}He are obtained from the fits to the data.

fore, is expected to reduce as further data is added. The ^{9}Li and ^{8}He background shapes are also obtained from MC for comparison. The relative fraction between ^{9}Li and ^{8}He is determined by a performing fit to the measured ^{9}Li/^{8}He spectrum. The estimated ^{8}He component is 1.53±3.87% (1.66±4.18%) for the near (far) detector.

The background rate in the IBD signal region of $E_{\mathrm{p}} < 8$ MeV is estimated by extrapolating from the background dominant region of $E_{\mathrm{p}} > 8$ MeV, using the measured background spectrum as shown in Fig. 7.9. The background rate in the region of 8 MeV $< E_{\mathrm{p}} <$ 12 MeV is estimated by a performing fit to the IBD candidate data, using the measured ^{9}Li/^{8}He background spectrum, measured fast neutron background, measured ^{252}Cf background, and MC IBD expectation. The

spectral fitting function is

$$\chi^2 = \sum_{i=8\sim12MeV} \left(\frac{O_i - E_i}{\sqrt{O_i}}\right)^2 + \left(\frac{f}{\sigma_f}\right)^2 + \sum_i \left(\frac{f_{s_i}}{\sigma_{f_{s_i}}}\right)^2 \tag{7.5}$$

where, O_i is IBD candidate data, and E_i is

$$E_i = \alpha \cdot n^i_{LH} + n^i_{IBD-MC} + (1 + f + f_{s_i}) \cdot n^i_{FN} \tag{7.6}$$

n_{LH} ,n_{IBD-MC} and n_{FN} represent their shapes. The fitting parameter α represents the amount of ^{9}Li/^{8}He . The IBD shape is derived from the expected flux using MC. The fast neutron component is constrained by the magnitude (bin-correlated) uncertainty (=f) and shape (bin-uncorrelated) uncertainty(=f_{s_i}).

The ^{9}Li/^{8}He obtained in the final sample is

$$^9Li/^8He(1.2 \sim 8.0MeV) = \alpha \cdot n_{LH}^{1.2\sim8.0MeV} \tag{7.7}$$

The energy-bin-uncorrelated spectral uncertainty is obtained from the measured ^{9}Li/^{8}He spectral uncertainty,

$$\delta^{Bin-uncor.}_{LiHe} = \alpha \cdot \delta n_{LH}^{1.2\sim8.0MeV} \tag{7.8}$$

The energy-bin-correlated uncertainty is obtained from the fit error of the background rate in the region of $E_{\rm p} > 8$ MeV,

$$\delta^{Bin-cor.}_{LiHe} = \delta\alpha \cdot n_{LH}^{1.2\sim8.0MeV} \tag{7.9}$$

The results of the ^{9}Li/^{8}He estimation are summarized in Table 7.3.

Detector	Data Set	Rate	Total Uncert.
Far	Set A	1.289	0.225
	Set B	0.912	0.090
	Set A+B	0.978	0.084
Near	Set A	6.475	0.653
	Set B	4.740	0.300
	Set A+B	5.104	0.274

Table 7.3: Estimated rate of ^{9}Li/^{8}He background in per day, energy range: 1.2 $\sim$ 8 MeV.

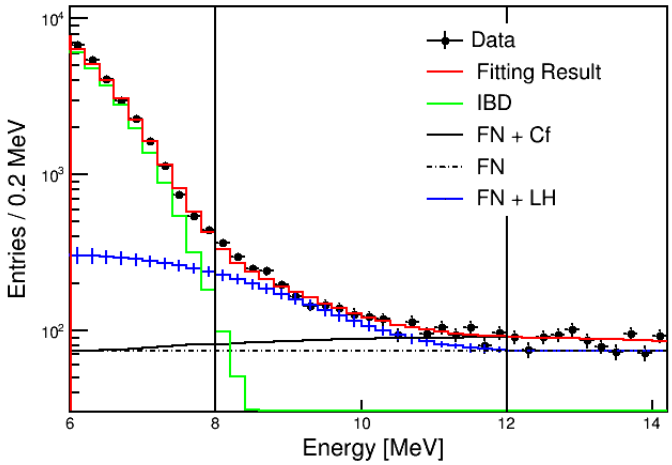

Figure 7.9: Estimation of the remaining ^{9}Li/^{8}He background rate in the signal region by using the measured rate in the background dominant region; 8 MeV $< E_{\mathrm{p}} <$ 12 MeV in the near detector. ^{9}Li/^{8}He is estimated after fitting the ^{252}Cf background in the energy region of 12 MeV $< E_{\mathrm{p}} <$ 22 MeV (described in section 7.4). The background rate in the signal region of $E_{\mathrm{p}} <$ 8 MeV is estimated by extrapolating from the background dominant region using the measured background spectrum.

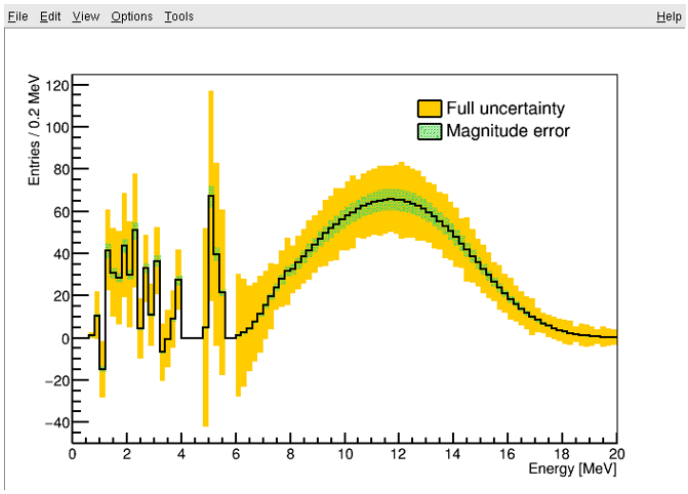

Figure 7.10: ^{252}Cf background shape in the far detector.

7.4 ^{252}Cf Contamination Background

The ^{252}Cf contamination yields multiple neutron events. These neutrons could easily mimic the IBD candidate pairs. Most of these backgrounds are eliminated by Cf removal cuts. ^{252}Cf contamination background is estimated based on the rejected and remaining samples after event selection requirements.

The residual ^{252}Cf background spectrum in the far detector is shown in Fig. 7.10.

The estimation method is the similar to ^{9}Li/^{8}He . The χ^2 fitting function for ^{252}Cf background adds an extra term, $\beta \cdot n^i_{Cf}$, to the function of ^{9}Li/^{8}He . ^{252}Cf background is estimated before estimating the ^{9}Li/^{8}He background at the energy region $>$ 12 MeV to remove the effect of said ^{9}Li/^{8}He background. The equations to calculate the amount, shape uncertainty, and magnitude uncertainty are similar to that of the ^{9}Li/^{8}He equations. However, there is a correlation between the obtained ^{9}Li/^{8}He and the backgrounds from ^{252}Cf . This correlation is taken into account at the magnitude uncertainty of ^{9}Li/^{8}He . The obtained backgrounds from ^{252}Cf in the final sample are

$$Backgrounds from ^{252}Cf(1.2 \sim 8.0MeV) = \beta \cdot n_{Cf}^{1.2\sim 8.0MeV} \tag{7.10}$$

The energy-bin-uncorrelated uncertainty is obtained from the measured ^{252}Cf

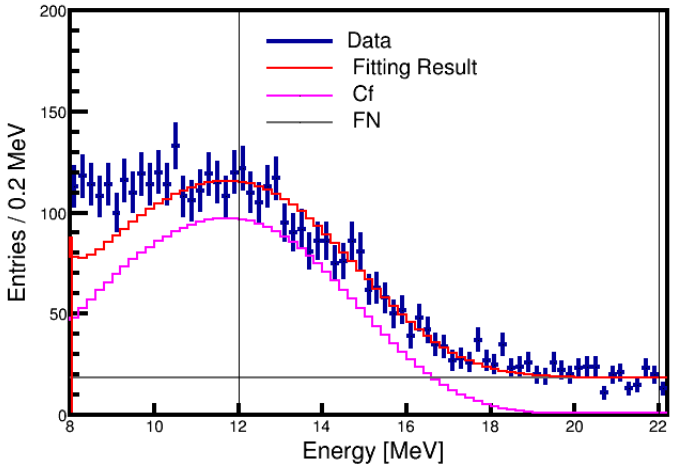

Figure 7.11: Estimation of the remaining ^{252}Cf background rate in the far detector. Fitting result in the region 8 MeV $< E_{\mathrm{p}} <$ 12 MeV was not fitted with data because the ^{9}Li/^{8}He background required to fit these difference will be estimated later.

spectral uncertainty,

$$\delta_{Cf}^{Bin-uncor.} = \beta \cdot \delta n_{Cf}^{1.2\sim 8.0MeV} \tag{7.11}$$

The energy-bin-correlated uncertainty is obtained from the fitting error of the background rate in the region of $E_{\mathrm{p}} > 12$ MeV,

$$\delta_{Cf}^{Bin-cor.} = \delta\beta \cdot n_{Cf}^{1.2\sim 8.0MeV} \tag{7.12}$$

The results of the ^{252}Cf estimation are summarized in Table 7.4.

Detector	Data Set	Rate	Total Uncert.
Far	Set A	-	-
	Set B	0.516	0.054
	Set A+B	0.426	0.045
Near	Set A	-	-
	Set B	0.103	0.021
	Set A+B	0.081	0.017

Table 7.4: Estimated rate of ^{252}Cf background in per day, energy range: 1.2 $\sim$ 8 MeV.

7.5 Summary of Backgrounds and Background Reduction since 500 live-day Result

The results of the background estimation are summarized in Tables 7.5, 7.6.

Backgrounds	Set A	Set B	Set A+B
Accidental	0.390 ± 0.020	0.470 ± 0.011	0.456 ± 0.010
Fast Neutron	0.451 ± 0.017	0.347 ± 0.009	0.365 ± 0.008
^{9}Li/^{8}He	1.289 ± 0.225	0.912 ± 0.090	0.978 ± 0.084
^{252}Cf	-	0.516 ± 0.054	0.426 ± 0.045
Total	2.130 ± 0.227	2.245 ± 0.106	2.225 ± 0.096

Table 7.5: Summary of estimated background rate per day for the far detector.

Backgrounds	Set A	Set B	Set A+B
Accidental	2.300 ± 0.049	2.602 ± 0.029	2.539 ± 0.025
Fast Neutron	2.009 ± 0.045	1.755 ± 0.028	1.808 ± 0.024
^{9}Li/^{8}He	6.475 ± 0.653	4.740 ± 0.300	5.104 ± 0.274
^{252}Cf	-	0.103 ± 0.021	0.081 ± 0.017
Total	10.78 ± 0.656	9.200 ± 0.303	9.532 ± 0.277

Table 7.6: Summary of estimated background rate per day for the near detector.

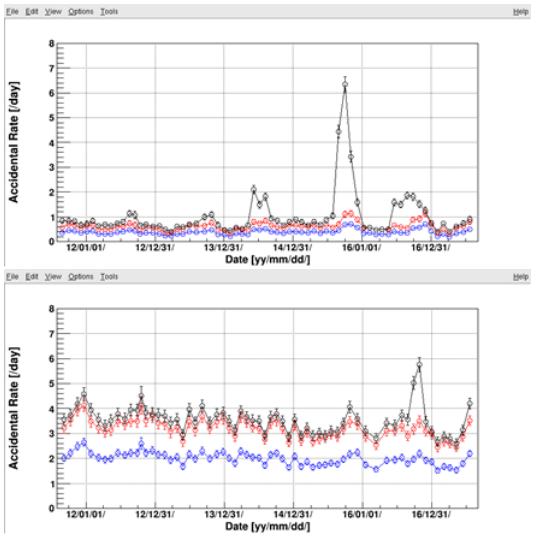

Figure 7.12: Time-dependent accidental background rates. Black is before applying the flasher cuts and ΔR <2m. Applying flasher cuts (Red) reduces accidental rate for a particular period. Applying ΔR <2m (Blue) reduces accidental rate to ∼50%, for the whole time period.

7.5.1 Background Reduction since 500 live-day Result

The results of the background rates and their uncertainties reduced drastically since 500th live day [9].

Prompt signal energy spectrum of accidental background is distributed mainly around 1∼2MeV, and the measurement of $|\Delta m^2_{ee}|$ is very sensitive around 1∼2MeV. Therefore, the reduction of accidental background rates and uncertainties enables more precise measurement of $|\Delta m^2_{ee}|$. Accidental background is reduced mainly by two methods: by applying flasher cut for the non-rejected flasher events by general flasher cut - Q_{max}/Q_{tot} (-400 $\sim$ 800 ns) $<$ 0.07. High flashing events could be accidental background as high probability. More details are described in section 6.3.1 and Appendix; and applying tither requirement of spatial coincidence between IBD candidate pairs - ΔR <2m. This is also described in section 6.3.2. Fig. 7.12 shows the time-dependent accidental background rates. Applying flasher cuts and ΔR <2m reduces accidental background rates.

^{9}Li/^{8}He backgrounds are reduced by optimizing cut criteria that reject cosmic-muon-associated background. This is described in section 6.3.3.

The stringent requirements for ^{252}Cf contamination background removal cut further reduced the ^{252}Cf contamination background, which changed from no

prompt-like trigger greater than 3 MeV within (-10sec, 10 sec) and (0, 400 mm) of the prompt signal (far detector) to within (-30 sec, 30 sec) and (0, 500 mm). Further details are given in section 6.3.5.

Reduced background rates and uncertainties are summarized in Tables **??**. Values in parentheses are fractions of the amount of background rates reduced to 500 live days the background rates. By way of exception, ^{252}Cf contamination background rates and uncertainties for the 500 live days are actually for data of the last 100 live days.

Data	Accidental	Fast Neutron	^{9}Li/^{8}He	^{252}Cf
500 live-day	0.97 ± 0.03	0.48 ± 0.02	1.54 ± 0.23	0.737 ± 0.096
2200 live-day	0.456 ± 0.010	0.365 ± 0.008	0.978 ± 0.084	0.426 ± 0.045
	(-53.0%)	(-24.0%)	(-36.5%)	(-42.2%)

Table 7.7: Background rate and uncertainties reduction since 500 days results for the far detector.

Data	Accidental	Fast Neutron	^{9}Li/^{8}He	^{252}Cf
500 live-day	6.89 ± 0.09	2.28 ± 0.04	8.36 ± 0.82	0.063 ± 0.040
2200 live-day	2.539 ± 0.025	1.808 ± 0.024	5.104 ± 0.274	0.821 ± 0.017
	(-53.0%)	(-24.0%)	(-36.5%)	

Table 7.8: Background rate and uncertainties reduction since 500 days results for the near detector.

Fig. 7.13 shows the background reduction. Open histogram is for the 500 live-day result(except ^{252}Cf contamination background, which is for the last 100 day result from the 500 live days result), and filled histogram is for the 2200 live days result.

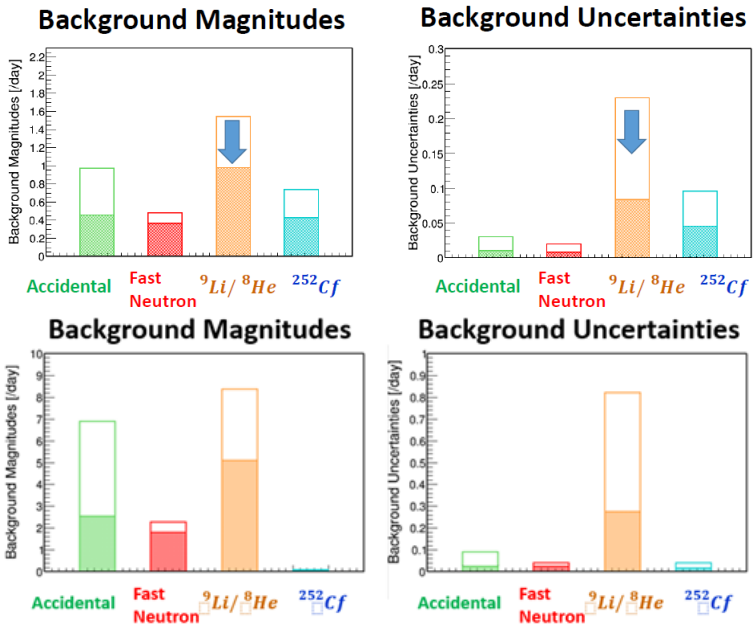

Figure 7.13: Background rate reduction (left) and Background uncertainties reduction (right). Top plots are for the far detector, and bottom plots are for the near detector. 500 days results are represented as empty histogram, and 2,200 days results are represented with filled histogram.

Chapter 8

Systematic Uncertainty

8.1 Detector Related Uncertainties

The detector-related uncertainties are categorized into correlated and uncorrelated uncertainties, between the near and far detectors. The correlated uncertainty is common to both near and far detectors, and thus cancel out for the far-to-near relative measurement while the uncorrelated uncertainty remains. An individual detector efficiency is measured from an IBD signal-enriched sample, and its uncertainty is given by a statistical uncertainty, and uncorrelated and correlated systematic uncertainties.

8.1.1 Detection Efficiecny

Efficiency of Gd Capture

Neutrons from IBD interactions are captured dominantly on Gd or H. The Gd capture fraction depends mainly on the relative Gd concentration in the LS. The Gd capture fraction is measured by the ratio of neutron capture on Gd to the total neutron capture on Gd or H, using ^{252}Cf source data taken at the detector center. A ^{252}Cf source sample, including H capture delayed events, is obtained by requiring prompt- and delayed-event pairs satisfying $4 < E_{\mathrm{p}} < 12$ MeV and $1.5 < E_{\mathrm{d}} < 12$ MeV, respectively. An additional neutron candidate of $1.5 < E_{\mathrm{d}} < 3$ MeV or $6 < E_{\mathrm{d}} < 10$ MeV within 200 μs from the prompt event of a coincidence pair is required to ensure the delayed events are neutron capture events originating from ^{252}Cf decay. Fig. 8.1 shows the energy distribution of the delayed signal for the ^{252}Cf source data. The obtained delayed energy distributions show a good agreement between near and far detectors.

The solid line in figure 8.1 is MC shape for the correction of lost signal in the Gd capture fraction measurement. We obtained the Gd capture fraction from the

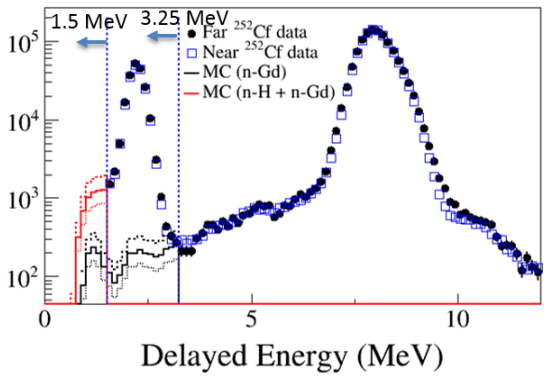

Figure 8.1: Comparison of delayed energy distribution of neutron captures on H or Gd using ^{252}Cf source data. The solid line in the figure is MC shape for the correction of the lost signal in the Gd capture fraction measurement.

ratio of the n-Gd events with $E_{\mathrm{d}} > 3.25$ MeV to the total neutron capture events with $E_{\mathrm{d}} > 1.5$ MeV. The Gd capture fraction measured using ^{252}Cf source data is summarized in Table 8.1 with the uncertainties. Uncorrelated uncertainty is given by Gd concentration difference and the correlated uncertainty is dominated by Gd capture cross-section uncertainties [64]. The measured values of the Gd capture fractions are constant in time within their uncertainties. Table 8.2 summarizes the Gd capture fraction obtained from IBD MC and the correction factor to be applied.

	Near	Far	Weighted mean
Gd capture fraction (%)	84.96 ± 0.03	84.88 ± 0.07	84.95 ± 0.03
Correlated	0.79		
Uncorrelated	0.01		

Table 8.1: Summary of Gd capture fraction. The result is given by the measurement using ^{252}Cf source data. Error of Gd capture fraction for each near and far comes from statistics.

	IBD far MC	IBD near MC
Gd capture fraction (%)	88.42 ± 0.04	88.40 ± 0.04
Correction factor	0.967	

Table 8.2: Gd capture fraction obtained from IBD MC and the correction factor to be applied.

Efficiency from Spill-in Events

In the IBD analysis using n-Gd capture events, we needed a delayed signal from neutron capture on Gd. Thus, the vertex positions of most of the Gd capture events are in the target vessel region because Gd is loaded in the target only. The spill-in events enhance the detection efficiency of the IBD signals in the target because of additional IBD signals occurring outside the target but with its neutron capture by Gd occurring inside the target. On the other hand, the reactor $\overline{\nu}_e$ interaction occurring at the target edge may be lost because of an n-H capture in the γ-catcher region. Such an event loss is accounted for in the delayed energy requirement efficiency. Because the number of acrylic spill-in events are quite sensitive to trigger Nhit(number of hits) threshold, we produce MC with the best tuned trigger Nhit threshold. Additionally, the γ-catcher spill-in is affected by the H capture cross-section. Although we tuned MC as much as we could, there was still some difference in the ΔT distribution between data and MC in the spill-in dominant region. Hence, we derived the correction factor for the MC spill-in fraction by fitting the latter with the ΔT distribution of data. Table 8.3 summarizes the corrected spill-in fraction (%) and uncertainties for each category. The final spill-in fraction is given by the weighted mean of near and far. Table 8.4 is the final summary. The uncorrelated systematic uncertainty is estimated as 0.04% due to differences of Gd concentration and the acrylic wall thickness of the target vessel between the near and far detectors. The correlated uncertainty is estimated as 0.66% based on the delayed time distribution of spill-in events at $\Delta T > 200$ μs deviating from that of IBD events in the target.

	Near	Far
Spill-in/target (%)	2.272 * (0.610 ± 0.021) = 1.386 ± 0.048	2.223 * (0.782 ± 0.111) = 1.738 ± 0.247
Correlated uncertainties	$\delta\epsilon/\epsilon$	
Oscillation parameter	0.001	
Weighting factor of spill-in MC	0.007	
Acrylic thickness (± 0.3 mm)	0.004	
Trigger Nhit threshold (± 1)	0.000	
MC-data difference	0.886	
Total	$\delta\epsilon/\epsilon = 0.886$ $\delta\epsilon$ = 0.886*0.7450 = 0.660	
Uncorrealeted uncertainties		
Acrylic thickness (± 0.1 mm)	0.001	
Difference between near and far	0.042	

Table 8.3: Summary of corrected spill-in fraction (%) and each uncertainty. 0.8989 is the correction factor for the H capture cross-section difference between data and MC

	Near	Far	Weighted mean
Spill-in efficiency (%)	101.386 ± 0.048	101.738 ± 0.247	101.40 ± 0.05
Correlated	0.66		
Uncorrelated	0.04		

Table 8.4: Summary of spill-in efficiency (%) and uncertainties.

Uncertainties from IBD Cross Section and The Number of Target Protons

An expected number of IBD interactions was determined from the reactor flux, IBD cross-section, and total number of free protons in the target. The uncertainty of the IBD cross-section is calculated from a theoretical calculation [65], and does not depend on the detectors. Therefore, there is only the correlated uncertainty for IBD cross-section, which is 0.13%.

The number of free protons in the target is estimated as $(1.189 \pm 0.003) \times 10^{30}$ based on the measurements of LAB density (0.856±0.001 g/cm^3) and target volume. The uncorrelated systematic uncertainty of the number of free protons is

0.03%, which was estimated from the measured volume difference of four liters between the near and far target vessels. The correlated uncertainty is 0.7%, which was estimated from the resolution of a densitometer.

8.1.2 IBD Selection Efficiency

Efficiency from $Q_{\max}/Q_{\text{tot}}$ Cut

The purpose of $Q_{\max}/Q_{\text{tot}} < 0.07$ cut, where Qmax is the maximum charge of a PMT, is to eliminate PMT flasher events and external γ-ray events. The efficiency of the $Q_{\max}/Q_{\text{tot}} < 0.07$ criterion is obtained using an IBD candidate sample with almost no accidental background events selected by a stringent spatial correlation requirement of $\Delta R < 0.3$ m. The $Q_{\max}/Q_{\text{tot}}$ distribution of this sample predicts an expected IBD signal loss in the region of $Q_{\max}/Q_{\text{tot}} > 0.07$, by extrapolating from the region of $Q_{\max}/Q_{\text{tot}} < 0.07$, using an expected shape of the MC. Fig. 8.2 shows $Q_{\max}/Q_{\text{tot}}$ distribution of IBD data and various fitted shapes at $Q_{\max}/Q_{\text{tot}} > 0.07$ for the estimation of systematic uncertainty for shape and magnitude of the fitting line. The red dotted line is considered the worst case, in which the signals do not decrease at $Q_{\max}/Q_{\text{tot}} > 0.07$. The blue dotted line is the case in which the signals decrease in a straight line to Qmax/Qtot = 0.1. Efficiency obtained from MC and the correction factors are summarized in Table 8.6. The correlated uncertainty is estimated from shape and magnitude uncertainties at $Q_{\max}/Q_{\text{tot}} > 0.07$. The uncorrelated uncertainty for $Q_{\max}/Q_{\text{tot}}$ cut efficiency is taken from the difference between near and far. As a side note, the efficiency measured using data include spill-in events. To present the efficiency for only the target, the data-driven measurement result should be corrected using MC. According to MC, the ratio of target to target + spill-in is 1.00004. This is quite a negligible difference. So, applying the correction would make no difference. The final efficiency for the target only for near data, far data, weighted mean, and uncorrelated and correlated uncertainties are summarized in Table 8.5.

Cut	Near	Far	Weighted mean
$Q_{\max}/Q_{\text{tot}} < 0.07$	100.00 ± 0.002	99.98 ± 0.01	100.00 ± 0.002
Correlated	0.01		
Uncorrelated	0.02		

Table 8.5: Efficiency (%) of $Q_{\max}/Q_{\text{tot}} < 0.07$ cut estimated from IBD data.

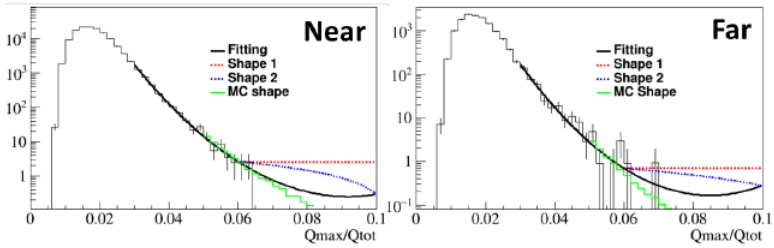

Figure 8.2: $Q_{\max}/Q_{\text{tot}}$ distribution of IBD data and fitting lines for $Q_{\max}/Q_{\text{tot}} > 0.07$. Dotted lines are various shape at $Q_{\max}/Q_{\text{tot}} > 0.07$ for the estimation of systematic uncertainty for shape and magnitude of the fitting line. $\Delta R < 0.3$ m is applied to reduce the background.

	Target MC	Target+Spill-in MC	Correction factor
$Q_{\max}/Q_{\text{tot}} < 0.07$	99.99 ± 0.0003	99.99 ± 0.0003	1.000

Table 8.6: Efficiency (%) of $Q_{\max}/Q_{\text{tot}} < 0.07$ cut obtained from MC and correction factors

DAQ Efficiency

In RENO detectors, an event is triggered and recorded when the number of hit ID PMTs is larger than 90 (changed to 80 since July 2017 as described in section 2.5.3), and this criteria is well below the 1.02 MeV minimum energy of an IBD positron signal. The DAQ efficiency is measured by the IBD signal loss due to the requirement of ID Nhit threshold, and it can be measured using MC. In MC, however, we found that the MC Nhit is different from data as a result of not implementing the charge simulation or noise hit. Therefore, the same Nhit threshold as in data cannot be applied to MC. We tuned proper Nhit threshold for MC by comparing energy spectrum of acrylic spill-in-dominant events between data and MC. The tuned Nhit criteria for MC is 84 for both near and far MCs. A final result is given by the weighted mean of near and far efficiencies, which are measured using IBD MC, and it is summarized in Table 8.7 along with the uncertainties. Uncorrelated uncertainty is given by the difference between near and far, and the correlated uncertainty is given by the uncertainty of trigger Nhit criteria tuning. The trigger efficiency is also measured for the events at the detector center using radioactive sources and consistent with the MC result within the uncertainty. The position-dependent DAQ inefficiency contributes to the inefficiency near the

trigger threshold below ∼0.8 MeV. Our trigger efficiency measured using a ^{137}Cs source (E = 0.63 MeV) is roughly 50% at the threshold energy of 0.5∼0.6 MeV and almost 100% at 0.8 MeV. The uncorrelated systematic uncertainty of the trigger efficiency is estimated as 0.01% from the difference between near and far efficiencies. The correlated uncertainty of the trigger efficiency is estimated as 0.01% from the ambiguity in finding a MC equivalent N_{hit} threshold.

	Near	Far	Weighted mean
DAQ (target only)	99.77 ± 0.05	99.78 ± 0.13	99.77 ± 0.05
Correlated	0.01		
Uncorrelated	< 0.01		

Table 8.7: DAQ efficiency of target only, which is measured from IBD MC. The final result is given by the weighted mean of near and far.

Efficiency from Prompt Energy Requirement

In RENO IBD selection, we selected events with prompt energy in the 1.2 $< E_{\text{p}} <$ 8.0 MeV region. IBD candidates with $E_{\text{p}} <$ 1.2 MeV include prompt signals of positrons occurring in or near the target acrylic vessel, which deposit most of the kinetic energy in the acrylic. $E_{\text{p}} >$ 8.0 MeV is the background-dominant region.

Prompt energy cut efficiency is defined as the fraction of prompt signals with $1.2 < E_{\text{p}} < 8.0$ MeV to all prompt signals. We measure the efficiency using background-subtracted IBD data for 1.2 MeV threshold. The efficiency measured using data include spill-in events. To present the efficiency for target only, we correct the data-driven measurement result using MC. A final result for target only is summarized in Table 8.8 with the uncertainties. Uncorrelated uncertainty is given by the uncorrelated energy scale uncertainty (± 0.15%), and the correlated uncertainty is given by the correlated energy scale uncertainty (± 1.0%).

Cut	Near	Far	Weighted mean
Prompt energy cut ($1.2 < E_{\text{p}} < 8.0$ MeV)	98.78 ± 0.03	98.66 ± 0.09	98.77 ± 0.03
Correlated	0.09		
Uncorrelated	0.01		

Table 8.8: Summary of prompt energy cut efficiency for target.

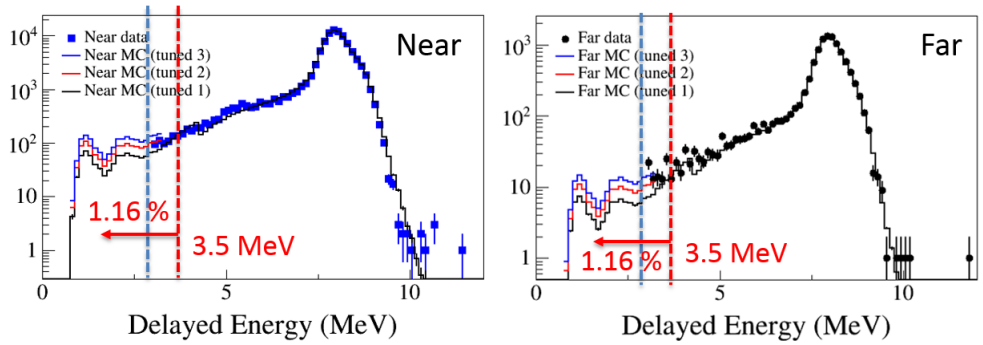

Figure 8.3: Delayed energy distribution of IBD data. The solid lines are MC shape to correct lost signals in the low-energy region.

Efficiency from Delayed Energy Requirement

In RENO IBD selection, we select events with delayed energy in the $E_{\rm d} >$ 6.0 MeV region to select only Gd capture. The efficiency of the delayed energy requirement is determined by the fraction of delayed events in the $E_{\rm d} > 6.0$ MeV region out of the total number of delayed events of neutron capture on Gd. An IBD event-enriched sample is used for estimating the efficiency, and is obtained by requiring IBD candidates to have $4 < E_{\rm p} < 8$ MeV to eliminate accidental and fast neutron backgrounds and $3.5 < E_{\rm d} < 12$ MeV to accept lower-energy delayed events. However, since the selection by the energy window is not perfect, the difference between the selection from the energy window and the true selection is corrected using MC. Fig. 8.3 shows the delayed energy distribution of IBD data and MC shape to correct lost signals at the low energy region. The efficiency is measured using data include spill-in events. To present the efficiency for target only, we correct the data-driven measurement result using MC. According to MC, the ratio of target to target + spill-in is 1.00049 (= 94.69 / 94.64, shown in Table 8.10). The efficiency for target only is obtained by multiplying this correction factor by the efficiency measured using data. The result is summarized in Table 8.9 with the uncertainties. The uncorrelated uncertainty is given by the uncorrelated energy scale difference (± 0.15%,) and the correlated uncertainty is given by correlated energy scale difference (± 1.0%) and MC correction. Table 8.10 summarizes the absolute delayed energy cut efficiency obtained from IBD MC. The efficiency measured by MC is different from data and needs to be corrected by a factor of 0.9733.

Cut	Near	Far	Weighted mean
Delayed energy cut	92.15 ± 0.08	92.05 ± 0.26	92.14 ± 0.08
Correlated	0.69		
Uncorrelated	0.05		

Table 8.9: Summary of dealyed energy cut efficiency for target.

MC	Absolute delayed energy cut efficiency (%)	Correction factor
Target	94.69 ± 0.03	-
Target+Spill-in	94.64 ± 0.03	0.9733
Acrylic	81.00 ± 1.19	-
γ-catcher	80.12 ± 0.36	-

Table 8.10: Absolute delayed energy cut efficiency (%) obtained from IBD MC and correction factor for MC. $E_{\rm p} > 4$ MeV is applied like the measurement in data.

Efficiency of Time Coincidence

The efficiency of the time coincidence requirement is determined by the fraction of IBD events with $2 < \Delta T < 100$ μs out of total IBD events, where ΔT is time difference between prompt and delayed signals of IBD interaction. An IBD signal-enriched sample is obtained by requiring IBD candidate events with $4 < E_{\rm p} < 8$ MeV in order to eliminate accidental backgrounds. Fig. 8.4 shows ΔT distributions of the neutron capture on Gd for the near IBD signal-enriched samples and IBD MC. The data and MC distributions are normalized by $30 \sim 100$ μs. There is some discrepancy between data and MC distributions in low and high ΔT regions. The fraction of spill-in events of MC is fitted to match with ΔT distribution data in high ΔT regions. The fitted spill-in MC is reduced by a factor of 0.57 compared to its original spill-in fraction. ΔT cut efficiency is defined as the ratio of the number of IBD signals with $2 < \Delta T < 100$ μs and the number of IBD signals with $0 < \Delta T < 1000$ μs.

We measured the capture time cut efficiencies using IBD data and MC, respectively. To exclude spill-in and background components, we fitted the ΔT distribution using several exponential functions and estimated the efficiency for the target component only. The result, which is measured using near IBD data, is summarized in Table 8.11 along with the uncertainties. Uncorrelated uncertainty is given by 0.1% change in the Gd concentration. The correlated uncertainty is

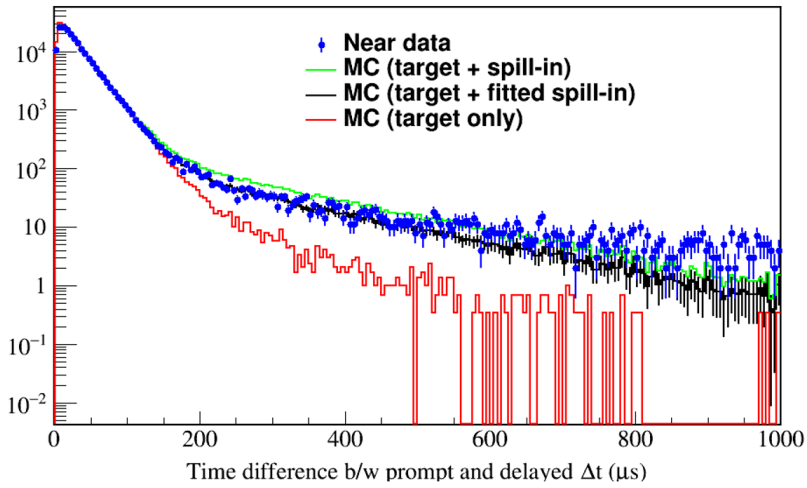

Figure 8.4: ΔT distribution of near IBD data and IBD MC. The data and MC distributions are normalized by $30 \sim 100$ μs. The black line is the spill-in fraction of MC adjusted to match the data distribution.

given by the error of capture time measurement from near data and the difference between data and MC at < 2 μs. Table 8.12 summarize the absolute ΔT cut efficiency obtained from IBD MC and the correction factors.

Cut	Near	Far	Weighted mean
ΔT cut	96.60 ± 0.04	96.57 ± 0.10	96.59 ± 0.04
Correlated	0.45		
Uncorrelated	0.01		

Table 8.11: Summary of ΔT cut efficiency for target, which is measured using IBD data.

MC	Absolute ΔT cut efficiency (%)	Correction factor
Target	96.33 ± 0.02	1.0011
Target+Spill-in	95.16 ± 0.03	1.0011
Acrylic	78.31 ± 0.56	-
γ-catcher	41.29 ± 0.15	-

Table 8.12: Absolute ΔT cut efficiency (%) obtained from IBD MC and correction factor for MC. $E_{\rm p} > 4$ MeV and $E_{\rm d} > 6$ MeV are applied like the measurement in data.

Efficiency of Spatial Coincidence

ΔR is the distance between the prompt and delayed signals of IBD interaction. $\Delta R < 2.0$ m is applied for the reduction of accidental backgrounds. ΔR cut efficiency is estimated using an IBD candidate sample, for which all the IBD selection cuts except the ΔR cut are applied. Fig. 8.5 shows the ΔR distribution of IBD candidates with and without accidental background subtraction at $Q_{\rm max}/Q_{\rm tot} < 0.015$. $Q_{\rm max}/Q_{\rm tot} < 0.015$ is applied to reduce accidental backgrounds. The efficiency measured using data include spill-in events. To present the efficiency for the target only, we correct the data-driven measurement result using MC. According to MC, the ratio of target to target + spill-in is 1.000001(shown is Table 8.14). This is quite a negligible difference, and thus applying it would make no difference. The correlated uncertainty is estimated as 0.02% based on varying ΔR requirement by the resolution of the reconstructed vertex, 0.3 m. The uncorrelated systematic uncertainty is estimated as 0.02% from the efficiency difference between the near and far detectors. These efficiencies and uncertainties are summarized in Table 8.13. Efficiency for $\Delta R < 2.0$ m cut obtained from MC is summarized in Table 8.14 along with the correction factor. The efficiency is almost 100% for both data and MC, and the correction factor for MC is 1.000.

Cut	Near	Far	Weighted mean
$\Delta R < 2.5$m	99.99 ± 0.005	100.00 ± 0.01	100.00 ± 0.004
Correlated	0.02		
Uncorrelated	0.02		

Table 8.13: Summary of ΔR cut efficiency for target, which is estimated from IBD data.

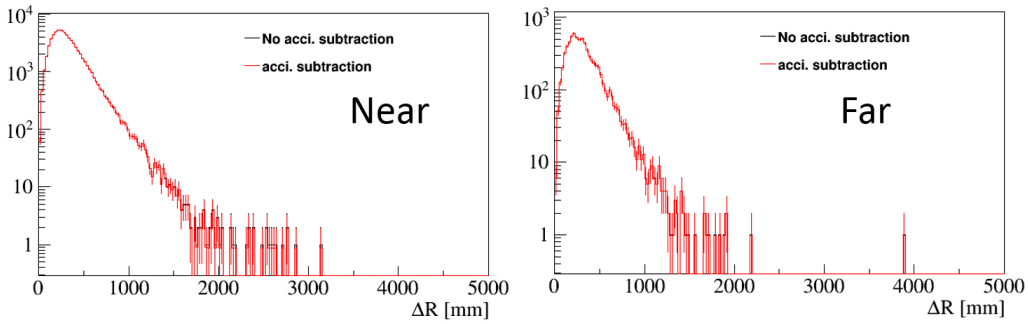

Figure 8.5: ΔR distribution of IBD candidates with and without accidental background subtraction for $Q_{\max}/Q_{\text{tot}} < 0.015$

MC	$\Delta R < 2.5$m cut	Correction factor
Target	99.9973 ± 0.0002	1.000
Target+Spill-in	99.9972 ± 0.002	1.000
Acrylic	99.9927 ± 0.0026	-
γ-catcher	99.9897 ± 0.0026	-

Table 8.14: ΔR cut efficiency (%) obtained from IBD MC and correction factor for MC.

8.1.3 Summary of Detection and IBD Selection Efficiencies

The detection and IBD selection efficiencies are summarized in Table 8.15. Their identical performances minimize the uncorrelated systematic uncertainties and allow the cancellation of correlated systematic uncertainties for the ratio measurement. The fully combined measured efficiency is 75.55 ± 0.11 (stat.) ± 0.13 (uncorrelated) ± 1.46 (correlated) % for weighted mean of near and far.

In the rate and spectral fits, the uncertainty of the far-to-near detection efficiency ratio is taken into account for one of the pull parameter uncertainties. We obtained the uncorrelated uncertainty of the efficiency ratio as 0.23% by combining the uncorrelated uncertainty and the weighted statistical errors of the measured values, as shown in Eq. 8.1.

$$\frac{0.7555 \pm 0.0011(stat.) \pm 0.0013(sys.)}{0.7555} = 1 \pm 0.0023 \tag{8.1}$$

	Efficiency (%)	Uncorrelated (%)	Correlated (%)
Detection			
Gd capture fraction	84.95 ± 0.03	0.1	0.79
Spill-in correction	101.40 ± 0.05	0.04	0.66
IBD cross section	-	-	0.13
Target protons	-	0.03	0.70
IBD selection cuts			
$Q_{\max}/Q_{\text{tot}} < 0.07$	100.00 ± 0.002	0.02	0.01
DAQ efficiency	99.77 ± 0.05	0.01	0.01
Prompt energy cut	98.77 ± 0.03	0.01	0.09
Delayed energy cut	92.14 ± 0.08	0.05	0.69
Capture time cut	96.59 ± 0.04	0.01	0.45
$\Delta R < 2.0$ m	100.00 ± 0.004	0.02	0.01
Combined	75.55 ± 0.11	0.13	1.46

Table 8.15: Summary of detection and IBD selection efficiencies and their uncertainties for the target. The final values are given by the weighted mean of near and far.

8.2 Reactor Related Uncertainty

The systematic uncertainties related to the reactor arises due to various causes. The expected reactor neutrino flux depends on the baseline distance, fission fraction of four major isotopes, mean energy released per fission, thermal power of the reactor, and the cross-section of the fission reaction. The main causes of the reactor-related uncertainties are thermal power of the reactor and fission fraction of the four isotopes.

The positions of the two detectors and six reactors were surveyed using global positioning system (GPS), and the baseline distances between the detectors and reactors were calculated with accuracy less than 10 cm.

The thermal power of the reactor is measured in an indirect way at the secondary steam generator of the reactor with 0.5% uncertainty.

The uncertainty from the fission fraction of the four isotopes is calculated from a pseudo experiment. Also. the flux change due to the uncertainty of fission fraction, calculated from the pseudo experiment, is 0.5%. The maximum difference with the varying fission fraction is 0.6%. Therefore, we determined the systematic uncertainty arising from the fission fraction as 0.7%.

The systematic uncertainties related with the reactor are not from the difference between the far and near detectors. Even though their origin is from the

reactor only, the systematic uncertainties related to the reactor are not canceled out by comparing the far and near detectors, because the flux contributions of each reactor are different at the far and near detectors due to the difference in baseline, as summarized in Table 8.16. Further details on this uncertainties are provided in section 3.4.

Parameter	Uncorrelated	Correlated
Baseline	0.03%	-
Thermal Power	0.5%	-
Fission fraction	0.7%	-
Fission reaction cross section	-	1.9%
Reference energy spectra	-	0.5%
Energy per fission	-	0.2%
Combined	0.9%	2.0%

Table 8.16: Systematic uncertainties of Expected Reactor Neutrino Flux

8.3 Energy Scale Uncertainty

The energy scale difference between the near and far detectors contributes to the uncorrelated systematic uncertainties associated with the relative measurement of the spectra at two the detectors, while the correlated uncertainties to the absolute energy scale does not. The energy scale difference is found to be less than 0.15%, as shown in Fig. 8.6 and described in section 5.4. We determined an energy scale uncertainty of 0.15%.

The energy scale is assumed to be linear in the energy value,

$$E(\epsilon) = E_0(1+\epsilon) \tag{8.2}$$

Then, the expected energy distribution with the energy scale offset ϵ^d is

$$T_i^d(1+\epsilon^d) \simeq T_i^d + \epsilon^d \left(\frac{\partial T_i^d}{\partial \epsilon^d}\right)_{\epsilon^d=0} \tag{8.3}$$

It is not easy to obtain the differential term from the histograms of the expected energy distribution due to limited statistics. Instead, a function $f(E)$ is used to fit T_i^d, so that the differential term can be obtained from the fitting function. The fitting function is as follows,

$$f(E) = exp\left(\sum_{i=0}^{6} p_i E^{i-3}\right) \tag{8.4}$$

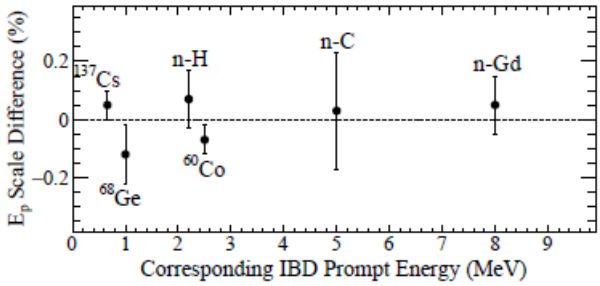

Figure 8.6: Energy-scale difference between the near and far detectors. The prompt energy difference between the two detectors is estimated by comparing the energy spectra of γ-ray sources obtained using the charge-to-energy conversion functions. All calibration data show the values of differences less than 0.15%

The differential term is approximated by the finite difference;

$$\frac{\partial T_i^d}{\partial \epsilon^d} = \frac{f_+(E(1+\epsilon^d)) - f_-(E(1-\epsilon^d))}{2\epsilon^d} \tag{8.5}$$

where

$$f_\pm(E(1\pm\epsilon^d)) = f(E(1\pm\epsilon^d))\frac{\int f(E)dE}{\int f(E(1\pm\epsilon^d))dE} \tag{8.6}$$

and $\epsilon = 0.0015$. The fit to an MC positron energy spectrum and its differential term are shown in Fig. 8.7.

8.4 Background Uncertainty

The uncertainties in the background were described in Chapter 7. The uncertainties in the background are of two types: shape uncertainty (bin-uncorrelated) and magnitude (bin-correlated) uncertainty. These are summarized in Table 8.17. The energy-dependent background uncertainty inputs for measuring θ_{13} and $|\Delta m^2_{ee}|$ are summarized in Fig. 8.8. The uncertainty from $^9Li/^8He$ background is dominant for almost all energy regions, except $E_{\rm p} < 2.0$ MeV due to the uncertainty from accidental background. Maximum oscillation occurs at 1.0 MeV $< E_{\rm p} <$ 2.0 MeV region; thus, the reduction of the accidental background uncertainties contributes to measuring the $|\Delta m^2_{ee}|$ with much smaller error. Additionally, the shape uncertainty from ^{252}Cf contaminated background at the far detector is also large.

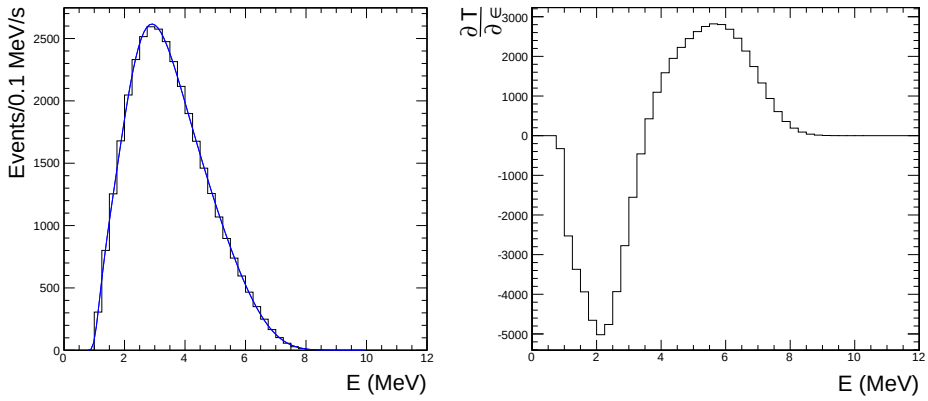

Figure 8.7: The positron energy spectrum is fitted with the function in Eq. 8.4 (left). The differential $\frac{\partial T}{\partial \epsilon}$ of the positron energy spectrum constructed using the fit function (right).

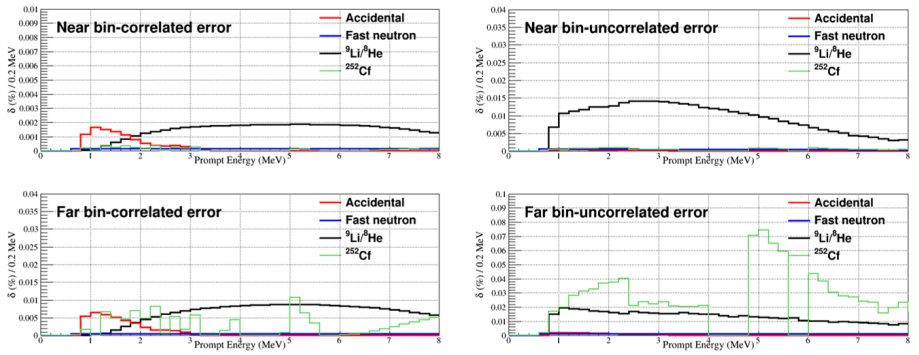

Figure 8.8: Magnitude (bin-correlated) uncertainties and shape (bin-uncorrelated) uncertainties of the backgrounds.

8.5 Summary of Systematic Uncertainty

All uncorrelated systematic uncertainties used to measure θ_{13} and $|\Delta m^2_{ee}|$ are summarized in Table 8.17. Correlated uncertainties are canceled out using the far-to-near ratio method. Background uncertainties are fractional uncertainties of the background magnitude.

Uncertainty source			Uncorrelated
Reactor			0.9%
Detection efficiency			0.23%
Energy scale			0.15%
	Rate (/day)	Bin-correlated	Bin-uncorrelated
Total background	9.53 (near)	0.57% (near)	3.21% (near)
	2.23 (far)	1.35% (far)	5.44% (far)
Accidental	2.54 (near)	0.40% (near)	0.17% (near)
	0.46 (far)	0.85% (far)	0.38% (far)
Fast Neutron	1.81 (near)	0.22% (near)	0.75% (near)
	0.37 (far)	0.41% (far)	0.82% (far)
$^9Li/^8He$	5.10 (near)	0.87% (near)	5.43% (near)
	0.98 (far)	1.97% (far)	3.61% (far)
^{252}Cf contaminated	0.08 (near)	4.92% (near)	19.4% (near)
	0.43(far)	2.46% (far)	20.6% (far)

Table 8.17: Summary of the systematic uncertainties. Correlated uncertainties of reactor-related uncertainty, detection efficiency, and energy scale are canceled out by using far-to-near ratio method, and thus not used when measuring θ_{13} and $|\Delta m^2_{ee}|$.

Chapter 9

Results of θ_{13} and $|\Delta m^2_{ee}|$ Measurement

9.1 Observed and Expected IBD Rates

The observed daily rates of IBD candidates after subtracting backgrounds in the near and far detectors are shown in Fig. 9.1. The reactors were turned off for fuel replacement and maintenance. The expected rates assuming no oscillations are shown for comparison. The observed IBD rate in the far detector is clearly lower than the expected one, indicating reactor $\overline{\nu}_e$ disappearance. The expected rates with the best-fit parameters are also shown and agree well with the observed IBD rates.

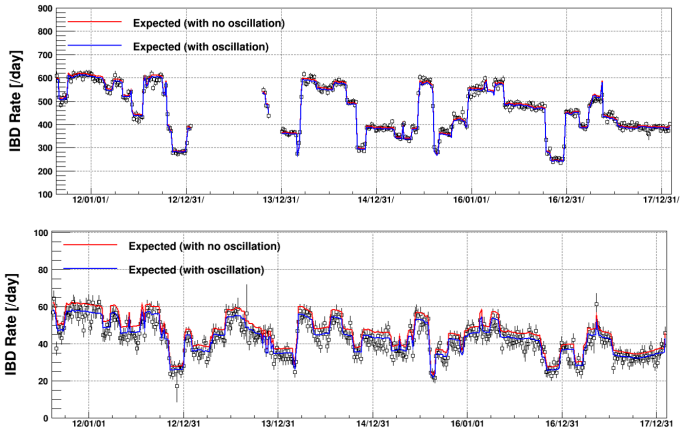

Figure 9.1: Measured daily-average rates of reactor $\overline{\nu}_e$ after subtracting backgrounds in the near and far detectors as a function of date (top plot for near and bottom plot for far). The red curves are the expected rates for no oscillation. The blue curves are the expected rates with the best-fit parameters and agree well with the measured ones.

Data Set A : before ^{252}Cf contamination		
Detector	Near	Far
Number of selected events	221140	23536
Total Background Rate (per day)	10.78 ± 0.66	2.13 ± 0.23
IBD rate after background subtraction	571.7 ± 1.40	59.09 ± 0.46
DAQ live time (days)	379.66	384.47
Accidental rate	2.30 ± 0.05	0.39 ± 0.02
^{9}Li/^{8}He rate	6.48 ± 0.65	1.29 ± 0.23
Fast neutron rate	2.01 ± 0.05	0.45 ± 0.02
Data Set B : after ^{252}Cf contamination		
Detector	Near	Far
Number of selected events	629526	79676
Total Background Rate (per day)	9.20 ± 0.30	2.25 ± 0.11
IBD rate after background subtraction	431.60 ± 0.63	41.81 ± 0.19
DAQ live time (days)	1428.22	1808.51
Accidental rate	2.60 ± 0.03	0.47 ± 0.01
^{9}Li/^{8}He rate	4.74 ± 0.30	0.91 ± 0.09
Fast neutron rate	1.76 ± 0.03	0.35 ± 0.01
^{252}Cf rate	0.10 ± 0.02	0.52 ± 0.05

Data Set A + B : total period		
Detector	Near	Far
Number of selected events	850666	103212
Total Background Rate (per day)	9.53 ± 0.28	2.24 ± 0.10
IBD rate after background subtraction	461.00 ± 0.58	44.82 ± 0.18
DAQ live time (days)	1807.77	2193.04
Accidental rate	2.54 ± 0.03	0.46 ± 0.01
^{9}Li/^{8}He rate	5.10 ± 0.27	0.98 ± 0.08
Fast neutron rate	1.81 ± 0.02	0.37 ± 0.01
^{252}Cf rate	0.08 ± 0.02	0.43 ± 0.04

Table 9.1: Event rate of the observed IBD candidates and the measured background at $1.2 < E_p < 8.0$ MeV. These rates are given in per day.

9.2 Comparison of Observed and Expected IBD Spectra

Fig. 9.2 shows a spectral shape comparison between the observed IBD prompt spectrum after subtracting backgrounds, and the prediction from a reactor $\overline{\nu}_e$ model [54, 66] using the far-to-near ratio measurement result. The fractional difference between data and prediction is also shown in the lower panel. A clear discrepancy is observed in the region of 5 MeV in both detectors. To compare the spectral shape, the MC predicted spectrum is normalized to the observed spectrum in regions excluding $3.6 < E_{\rm p} < 6.6$ MeV. The excess of events is estimated at approximately 3% of the total observed IBD events in both detectors.

Furthermore, the 5-MeV excess is observed to be proportional to the reactor thermal power where the rate is calculated from the events in excess in the $3.6 < E_{\rm p} < 6.6$ MeV region relative to the nominal model prediction [54, 66].

9.3 Rate Only Analysis

In the rate-only analysis, the oscillation amplitude of neutrino survival probability is extracted from information on the observed reactor $\overline{\nu}_e$ rates only, without using the prompt energy spectra. We observe a clear deficit of reactor $\overline{\nu}_e$ in the far detector. Using the deficit information, a rate-only analysis obtains the value of $\sin^2 2\theta_{13}$ as 0.087±0.0050(stat.)±0.0054(syst.), where the world average value of $|\Delta m^2_{ee}| = (2.56 \pm 0.06) \times 10^{-3}$ eV^2 is used [**?**]. The χ^2 fit for the result is described below. The systematic error of $\sin^2 2\theta_{13}$ is reduced from 0.007 to 0.0054, mainly due to the reduced background magnitudes and uncertainties, relative to the

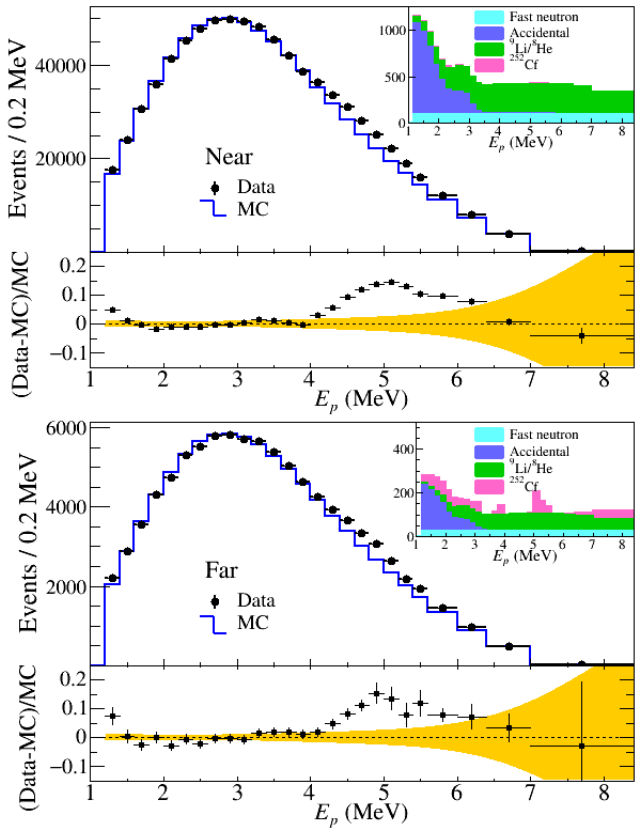

Figure 9.2: Spectral shape comparison of observed and expected IBD prompt events in the (a) near and (b) far detectors. The observed spectra are obtained by subtracting the remaining background spectra as shown in the insets. The expected spectrum are obtained from the best-fit oscillation results, discussed later on, that are applied to the no-oscillation MC spectra. The expected spectra are normalized to data spectra in the regions excluding $3.6 < E_{\rm p} < 6.6$ MeV. The discrepancy between data and MC prediction is clearly seen at 4–6 MeV. The observed excess is correlated with the reactor power, and corresponds to 3% of the total number of IBD events. The deviation from the expectation is larger than the uncertainty of the expected spectrum (shaded band).

500-live-day result [9]. In addition, the statistical error is reduced from 0.009 to 0.0050. Note that the largest reduction in the background rate and uncertainty comes from the ^{9}Li/^{8}He background.

9.3.1 χ^2 Fitting of Rate Only Analysis

The χ^2 for the rate-only analysis is based on the pull parameter method described in Ref. [67], which takes care of correlations between various systematics. It is represented as

$$\chi^2 = \sum_{P=SetA,SetB} \left\{ \frac{\frac{N_{obs}^{F,P}}{N_{obs}^{N,P}} - \frac{N_{exp}^{F,P}}{N_{exp}^{N,P}}}{U^P} \right\}^2 + \chi^2_{penalty} \tag{9.1}$$

where

$$N_{exp}^{F,P} = \sum_{r=1}^{6} \left[\left(1 + \xi + \xi_F^{SetB} + f_r\right) \cdot N_{exp}^{F,P,r} \right] - b_F^P - \beta_F^P \cdot S_{LH}^F \tag{9.2}$$

$$N_{exp}^{N,P} = \sum_{r=1}^{6} \left[\left(1 + \xi_N^{SetB} + f_r\right) \cdot N_{exp}^{N,P,r} \right] - b_N^P - \beta_N^P \cdot S_{LH}^N \tag{9.3}$$

$$U^P = \frac{N_{obs}^{F,P}}{N_{obs}^{N,P}} \sqrt{\frac{N_{obs}^{F,P} + N_{bkg}^{F,P}}{\left(N_{obs}^{F,P}\right)^2} + \frac{N_{obs}^{N,P} + N_{bkg}^{N,P}}{\left(N_{obs}^{N,P}\right)^2}} \tag{9.4}$$

and

$$\begin{aligned} \chi^2_{penalty} &= \left(\frac{\xi}{\sigma_\xi}\right)^2 + \sum_{d=F,N} \left(\frac{\xi_d^{SetB}}{\sigma_{\xi_d}}\right)^2 \\ &\quad + \sum_{r=1}^{6} \left(\frac{f_r}{\sigma_{f_r}}\right)^2 + \sum_{P,d} \left(\frac{b_d^P}{\sigma_{b_d}^P}\right)^2 + \sum_{d} \left(\frac{S_{LH}^d}{\sigma_{LH}^d}\right)^2 \end{aligned} \tag{9.5}$$

Here, the parameters are defined as follow.

- $N_{obs}^{d,P}$: Number of background subtracted IBD, d = detector (far, near), P = data set (Set A, Set B)
- $N_{exp}^{d,P}$: Number of expected IBD, d = detector (far, near), P = data set (Set A, Set B)

- $N_{bkg}^{d,P}$: Number of total background, d = detector (far, near), P = data set (Set A, Set B)
- ξ : Pull parameter of detection efficiency
- σ_{ξ} : Uncertainty of detection efficiency
- ξ_d^{setB} : Pull parameter of uncommon detection efficiency for data set B only, d = detector (far, near).
- σ_{ξ_d} : Uncertainty of uncommon detection efficiency for data set B only, d = detector (far, near).
- f_r : Pull parameter for the reactor Thermal power and isotope fraction for reactor (r = $1 \sim 6$)
- σ_{f_r} : Uncertainty of the neutrino flux from thermal power for reactor (r = $1 \sim 6$)
- b_d^p : Pull parameter for the accidental, fast neutron, magnitude part of ^{9}Li/^{8}He and ^{252}Cf background, d = detector (far, near), P = data set (Set A, Set B)
- $\sigma_{b_d^p}$: Combined uncertainty for the accidental, fast neutron, magnitude uncertainty of ^{9}Li/^{8}He and ^{252}Cf background, d = detector (far, near), P = data set (Set A, Set B)
- β_d^p : shape uncertainty of ^{9}Li/^{8}He shape, d = detector (far, near)), P = data set (Set A, Set B)
- S_{LH}^d : Pull parameter for the ^{9}Li/^{8}He background shape uncertainty, d = detector (far, near)
- $\sigma_{S_{LH}}^d$: normalized uncertainty for the ^{9}Li/^{8}He Background, d = detector (far, near)

The χ^2 values are calculated separately two datasets A and B because the IBD selection cut and its detection efficiency are different in each dataset an the ^{252}Cf backgrounds are only obtained for dataset B. Therefore, the systematic uncertainties are different. The detection efficiency uncertainty is the relative ambiguity between the far and near detectors. Hence, it is located only in terms of the far expected IBD. The uncommon detection efficiencies are the independent ambiguities in the far and near detectors because they pertain to the statistics of their own data. The uncommon detection efficiencies are too small at the dataset A; hence, they are applied only to set B. The values of pull parameter ξ_d^{setB} have

the fixed value "0" in the dataset A term. The reactor pull parameter has only a reactor index, and is commonly located in both the numerator and denominator. This means that the correlation between far and near detectors from the reactor uncertainties is taken into account in the χ^2 function. Background uncertainty pull term takes into account a combination of all background uncertainties except the shape uncertainty of ^{9}Li/^{8}He. Since, ^{9}Li/^{8}He is estimated with same the ^{9}Li/^{8}He template for both datasets A and B, the shape uncertainty of ^{9}Li/^{8}He is correlated between datasets A and B. For this reason, the shape uncertainty of ^{9}Li/^{8}He is applied separately for datasets A and B.

9.4 Rate and Spectrum Analysis

In the rate and spectrum analysis, the oscillation amplitude and frequency of neutrino survival probability are measured based on information on the observed reactor $\overline{\nu}_e$ rates and spectra. We observed a clear energy-dependent deficit of reactor $\overline{\nu}_e$ in the far detector. Even though there is the unexpected structure around 5 MeV, the oscillation amplitude and frequency can be determined from a fit to the measured far-to-near ratio of IBD prompt spectra. The determination is not affected by the presence of the 5-MeV excess due to its cancellation for the ratio measurement. For determination of $|\Delta m^2_{ee}|$ and $\sin^2 2\theta_{13}$, a χ^2 with the pull parameter terms of systematic uncertainties is constructed using the spectral ratio measurement and is minimized by varying the oscillation and pull parameters.

9.4.1 χ^2 Fitting of Rate and Spectrum Analysis

The following χ^2 function is used for the rate and shape analysis,

$$\begin{aligned}\chi^2 &= \sum_{i=1}^{\mathrm{N_{bins}}} \frac{(O_i^{\mathrm{F/N}} - T_i^{\mathrm{F/N}})^2}{U_i^{\mathrm{F/N}}} + \sum_{d=\mathrm{N,F}} \left(\frac{b^d}{\sigma^d_{\mathrm{bkg}}}\right)^2 \\ &\quad + \sum_{r=1}^{6} \left(\frac{f}{\sigma^r_{\mathrm{flux}}}\right)^2 + \left(\frac{\epsilon}{\sigma_{\mathrm{eff}}}\right)^2 + \left(\frac{\eta}{\sigma_{\mathrm{scale}}}\right)^2, \end{aligned} \tag{9.6}$$

where $O_i^{\mathrm{F/N}}$ is the observed far-to-near ratio of the IBD candidates in the i-th E_{p} bin after background subtraction, $T_i^{\mathrm{F/N}} = T_i^{\mathrm{F/N}}(b^d, f, \epsilon, \eta; \theta_{13}, |\Delta m^2_{ee}|)$ is the expected far-to-near ratio of IBD events, and $U_i^{\mathrm{F/N}}$ is the statistical uncertainty of $O_i^{\mathrm{F/N}}$.

The expected ratio $T_i^{\mathrm{F/N}}$ is calculated using the reactor $\overline{\nu}_e$ model, IBD cross section, and the detection efficiency together with the signal loss due to the timing veto criteria, and folding of the $\overline{\nu}_e$ survival probability and detector effects. The

systematic uncertainty sources are embedded by pull parameters (b^d, f, ϵ, and η) with associated uncertainties ($\sigma^d_{\rm bkg}$, $\sigma^r_{\rm flux}$, $\sigma_{\rm eff}$, and $\sigma_{\rm scale}$). The pull parameters allow variations from the expected far-to-near ratio of IBD events within their corresponding systematic uncertainties. The pull parameters b^d and η introduce deviations from the expected spectra accounting for the effects of the associated energy-dependent systematic uncertainties. For the spectral deviations, the energy-bin correlated and uncorrelated uncertainties are separately taken into account. The uncorrelated reactor-flux systematic uncertainty $\sigma^r_{\rm flux}$ is 0.9%, the uncorrelated detection and timing veto systematic uncertainty $\sigma_{\rm eff}$ is 0.2%, the uncorrelated energy-scale systematic uncertainty $\sigma_{\rm scale}$ is 0.15%, and the background uncertainty $\sigma^d_{\rm bkg}$ is 3.3% and 5.6% for near and far detectors, respectively. The χ^2 is constructed as the sum of two periods, before (∼400 days) and after (∼1800 days) ^{252}Cf contamination. A profile likelihood method is used to incorporate the systematic uncertainties in the fit. The best-fit values obtained from the rate and spectrum analysis are $\sin^2 2\theta_{13} = 0.0896 \pm 0.0048(\text{stat.}) \pm 0.0047(\text{syst.})$ and $|\Delta m^2_{ee}| = [2.68 \pm 0.12(\text{stat.}) \pm 0.07(\text{syst.})] \times 10^{-3}$ eV^2 with $\chi^2/\text{NDF} = 47.4/66$, where NDF is the number of degrees of freedom. This result is consistent with that of the rate-only analysis within their errors. Another fit result is also obtained assuming an independent pull parameter for each energy bin to allow maximum variation of the background shapes within their uncertainties. The total systematic errors for both $\sin^2 2\theta_{13}$ and $|\Delta m^2_{ee}|$ remain almost unchanged by the fit.

Table 11.1 presents systematic uncertainties of $\sin^2 2\theta_{13}$ and $|\Delta m^2_{ee}|$ from several uncertainty sources. The uncertainties of energy-scale and backgrounds are the dominant sources of the total systematic uncertainty for $|\Delta m^2_{ee}|$. The measured value of $|\Delta m^2_{ee}|$ corresponds to $|\Delta m^2_{32}| = (2.63 \pm 0.14) \times 10^{-3}$ eV^2 ($|\Delta m^2_{32}| = [2.73 \pm 0.14] \times 10^{-3}$ eV^2) for the normal (inverted) neutrino mass ordering, using measured oscillation parameters of $\sin^2 \theta_{12} = 0.307 \pm 0.013$ and $\Delta m^2_{21} = (7.53 \pm 0.18) \times 10^{-5}$ eV^2 [13].

	$\delta\lvert\Delta m^2_{ee}\rvert$ ($\times 10^{-3}$ eV^2)	$\delta(\sin^2 2\theta_{13})$
Reactor	$+0.010, -0.004$	$+0.0031, -0.0032$
Detection efficiency	$+0.010, -0.005$	$+0.0033, -0.0033$
Energy scale	$+0.064, -0.065$	$+0.0015, -0.0013$
Backgrounds	$+0.018, -0.021$	$+0.0021, -0.0021$
Total	$+0.068, -0.067$	$+0.0048, -0.0047$

Table 9.2: Systematic uncertainties from various uncertainty sources. The dominant sources of the total systematic uncertainties for $|\Delta m^2_{ee}|$ are the uncertainties of energy-scale.

The values of $\delta(\sin^2 2\theta_{13})$ and $\delta|\Delta m^2_{ee}|$ measured by rate-only analysis and rate+shape analysis are summarized in Table 9.3.

	$\sin^2 2\theta_{13}$	$\lvert\Delta m^2_{ee}\rvert(\times 10^{-3}\ eV^2)$
Rate Only	0.087±0.0050±0.0054	2.56±0.06 (fixed)
Rate + Shape	0.0896±0.0048±0.0047	2.68±0.12±0.07

Table 9.3: Measured $\sin^2 2\theta_{13}$ and $|\Delta m^2_{ee}|$. Values are represented as mean ± stat. error ± sys. error. $|\Delta m^2_{ee}|$ of rate-only is fixed value [**?**].

Figure 9.3 compares the observed, background-subtracted spectrum at the far detector with the one expected with no oscillation and the one expected with the best-fit oscillation parameters at the far detector. The expected spectrum with no oscillation is obtained by weighting the spectrum at the near detector with no-oscillation assumption in order to include the 5-MeV excess. The expected spectrum with the best-fit oscillation parameters is obtained by applying the measured values of $\sin^2 2\theta_{13}$ and $|\Delta m^2_{ee}|$ to the one expected with no oscillation at the far detector. The observed spectrum at the far detector shows a clear energy-dependent disappearance of reactor $\overline{\nu}_e$ events consistent with neutrino oscillations.

Figure 9.4 shows 68.3, 95.5, and 99.7% C.L. allowed regions for the neutrino oscillation parameters $|\Delta m^2_{ee}|$ and $\sin^2 2\theta_{13}$.

9.5 Energy and Baseline-dependent Reactor $\overline{\nu}_e$ Disappearance

The survival probability of reactor $\overline{\nu}_e$ is a function of a baseline L over neutrino energy E_ν as written in Eq. 1.11. Due to having multiple reactors as neutrino sources, an effective baseline L_{eff} is defined by the reactor-detector distance weighted by the IBD event rate from each reactor. Note that L_{eff} is time dependent due to the IBD event rate weighting. The neutrino energy E_ν is converted from the IBD prompt energy. A daily L_{eff}/E_ν distribution of the IBD events is obtained from the background subtracted IBD event spectrum and the daily L_{eff}. The observed L_{eff}/E_ν distribution is obtained by summing up the daily distributions weighted by a daily IBD rate. The measured survival probability is obtained by the ratio of the observed IBD events to the expected ones with no oscillation in each bin of L_{eff}/E_ν. Fig. 9.5 shows the measured survival probability of reactor $\overline{\nu}_e$ in the far detector as a function of L_{eff}/E_ν. A predicted survival probability is obtained from the observed probability distribution in the near detector and the

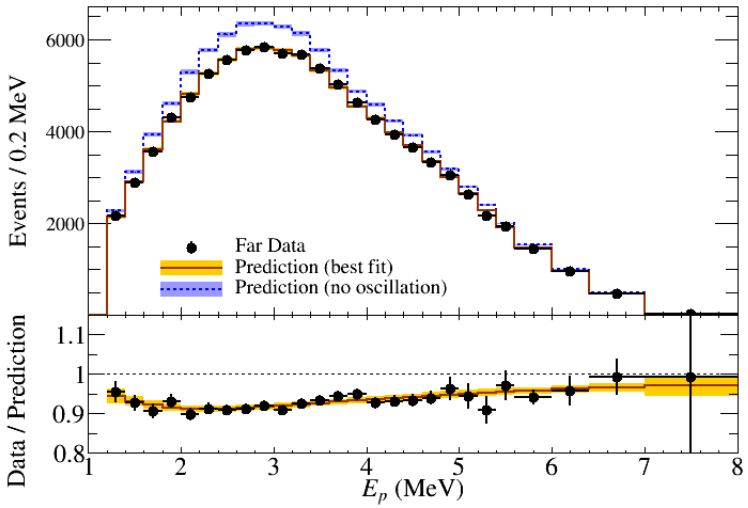

Figure 9.3: Plot on top shows the comparison of the observed IBD prompt spectrum in the far detector (dots) with the no-oscillation prediction (blue shaded histogram) obtained from the measurement in the near detector. The prediction from the best-fit oscillation parameters is also shown as yellow shaded histogram. Both blue and yellow bands represent uncertainties. Plot on bottom shows the ratio of IBD events measured in the far detector to the no-oscillation prediction (dots) and the ratio from the MC simulation with best-fit results folded in (shaded band). Errors are statistical uncertainties only although both statistical and systematic uncertainties are included in the χ^2 fitting.

best–fit oscillation values. Because of the observed 5-MeV excess, the expected L_{eff}/E_ν distribution is derived from the measured spectrum in the near detector instead of the IBD MC spectrum. A clear L_{eff}/E_ν-dependent disappearance of reactor $\overline{\nu}_e$ is observed and demonstrates the periodic feature of neutrino oscillation.

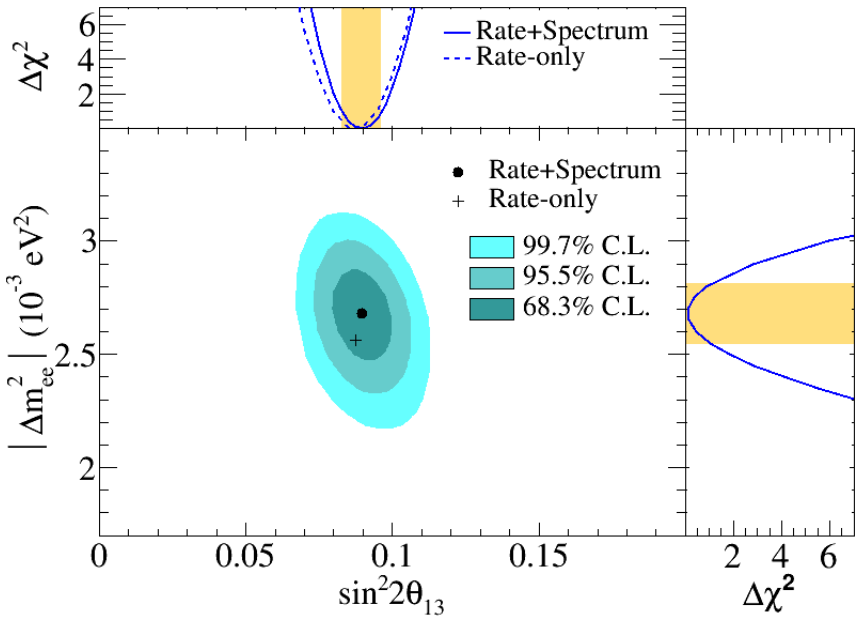

Figure 9.4: Allowed regions of 68.3, 95.5, and 99.7% C.L. in the $|\Delta m^2_{ee}|$ vs. $\sin^2 2\theta_{13}$ plane. The best-fit values are shown as the black dot. The $\Delta\chi^2$ distribution for $\sin^2 2\theta_{13}$ (top) and $|\Delta m^2_{ee}|$ (right) are also shown with an 1 σ band. The rate-only result for $\sin^2 2\theta_{13}$ is shown as the cross.

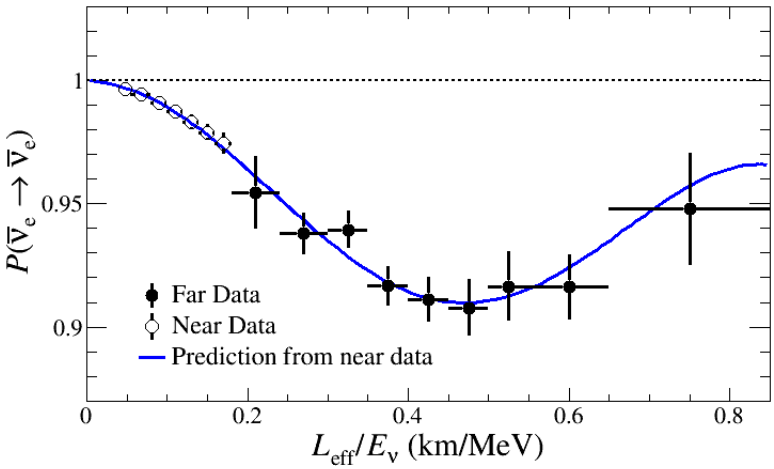

Figure 9.5: Measured reactor $\overline{\nu}_e$ survival probability in the far detector as a function of L_{eff}/E_ν. The curve is a predicted survival probability, obtained from the observed probability in the near detector, for the best-fit values of $|\Delta m^2_{ee}|$ and $\sin^2 2\theta_{13}$. The L_{eff}/E_ν value of each data point is given by the average of the counts in each bin.

Chapter 10

Fuel-dependent Variation of Antineutrino Yield and Spectrum

We measured the reactor antineutrino flux as a function of an effective fission fraction, $F_i(t)$, given by

$$F_i = \sum_{r=1}^{6} \frac{W_{th,r}(t)\overline{p}_r(t) f_{i,r}(t)}{L_r^2 \overline{E}_r(t)} / \sum_{r=1}^{6} \frac{W_{th,r}(t)\overline{p}_r(t)}{L_r^2 \overline{E}_r(t)} \tag{10.1}$$

where $f_{i,r}(t)$ is the fission fraction of the i-th isotope in the r-th reactor, $W_{th,r}(t)$ is the r-th reactor thermal power, $p_r(t)$ is the mean survival probability of antineutrinos from the r-th reactor, and L_r is the distance between the near detector and the r-th reactor. An average antineutrino energy produced by a reactor is

$$\overline{E}_r(t) = \sum_{i=1}^{4} f_{i,r}(t) e_i \tag{10.2}$$

where e_i is the average energy released per fission.

The upper panel of Fig. 10.1 shows the time variation of the effective fission fraction of ^{235}U as observed by the near detector. The effective fission fraction is obtained from the daily thermal power and fission fraction data of each reactor core, provided by the Hanbit nuclear power plant.

For examining the fuel-dependent variation of reactor antineutrino yield and spectrum, eight groups of equal data size are sampled according to eight different values of the ^{235}U fission fraction. A time-averaged effective fission fraction ($\overline{F}_{i,j}$)

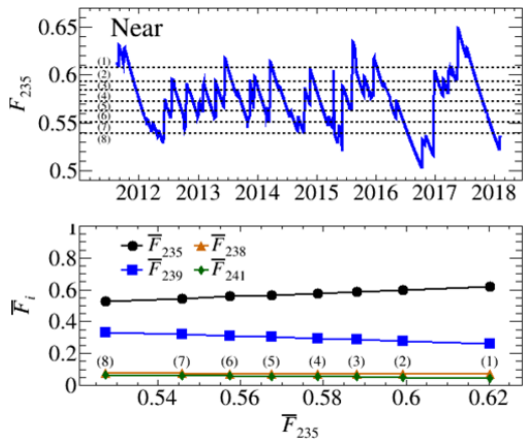

Figure 10.1: Plot on top shows effective ^{235}U daily fission fraction ($\overline{F}_{235}$) in the near detector according to Eq. 10.1. The daily $\overline{F}_{235}$ is obtained from reactor information provided by the Hanbit nuclear power plant. Plot on bottom shows relative fission fractions for the primary fuel isotopes of ^{235}U, ^{239}Pu, ^{241}Pu, and ^{238}U. The numbers in the parentheses represent eight data groups with different $\overline{F}_{235}$ fission fractions.

of the i-th isotope in the j-th data group is calculated as,

$$\overline{F}_{i,j} = \int \sum_{r=1}^{6} \frac{W_{th,r}(t)\overline{p}_r(t)f_{i,r}(t)}{L_r^2\overline{E}_r(t)} \Big/ \int \sum_{r=1}^{6} \frac{W_{th,r}(t)\overline{p}_r(t)}{L_r^2\overline{E}_r(t)} \tag{10.3}$$

The time-averaged effective fission fractions of the four isotopes in each group are shown as a function of the time-averaged fission fraction of ^{235}U ($\overline{F}_{235}$) and ^{239}Pu ($\overline{F}_{239}$) in the lower panel of Fig. 10.1.

An average IBD yield per fission of the j-th data group ($\overline{y}_{f,j}$) is given by,

$$\overline{y}_{f,j} = \sum_{i=1}^{4} \overline{F}_{i,j} \cdot y_i \tag{10.4}$$

where an instantaneous IBD yield per fission (y_i) is calculated

$$y_i = \int \sigma(E_\nu)\phi_i(E_\nu)dE_\nu \tag{10.5}$$

$\sigma(E_\nu)$ is the IBD reaction cross section, and $\phi_i(E_\nu)$ is the reactor antineutrino spectrum.

The IBD yield y_i of a fissile isotope is sensitive to its reactor antineutrino spectrum because the IBD cross-section increases with antineutrino energy. A model-independent IBD yield of $\overline{y}_{f,j}$ is determined by counting the number of events in each data group using the following relationship,

$$N_j = \overline{y}_{f,j} \sum_{r=1}^{6} \frac{N_p}{4\pi L_r^2} \int dt \left[\frac{W_{th,r}(t)\overline{P}_r(t)}{\sum_i f_{i,r}(t)E_i} \right] \epsilon_d(t) \tag{10.6}$$

where N_j is the number of IBD events in the j-th group, N_p is the number of target protons, $P_r(t)$ is the mean survival probability, and $\epsilon_d(t)$ is the detection efficiency including the signal loss due to timing veto requirements. The IBD yield of an isotope per fission is determined by matching the observed N_j with its corresponding value of $\overline{y_{f,j}}$ for each data group. No fission-fraction dependent IBD yield expects a flat distribution of $\overline{y}_f$ as a function of $\overline{F}_{235}$.

Fig. 10.2 measured distribution of $\overline{y}_f$ as a function of $\overline{F}_{235}$ or $\overline{F}_{239}$ for the eight data groups. We observe a clear correlation between $\overline{y}_f$ and $\overline{F}_{235}$, indicating dependence of IBD yield per fission on the isotope fraction of ^{235}U. A linear function is used for a fit with the eight data points. The red solid line shows the best fit with χ^2/NDF= 5.94/6. The horizontal line represents an average IBD yield per fission of (5.84 $\pm$ 0.13) $\times 10^{43} cm^2$/fission and an expected distribution for no-fuel-dependent IBD yield per fission if the reactor antineutrino spectra from the four isotope fission processes are identical. This result rules out the no-fuel-dependent variation of the IBD yield per fission at 6.6σ confidence level. Therefore, we conclude that the variation of the $\overline{y}_f$ as a function of $\overline{F}_{235}$ comes from unequal IBD yields between different isotope fission processes because of the difference in their antineutrino energy spectra. The blue dotted line represents the predicted IBD yield per fission after scaling the Huber–Mueller model by -6.0% with χ^2/NDF= 9.12/6. The slightly smaller slope of the best-fit result compared to the scaled model prediction may indicate that the model overestimated the contribution of the ^{235}U isotope to the IBD yield.

For simultaneous determination of y_{235} and y_{239}, a χ^2 function with the pull parameter terms of systematic uncertainties is constructed using the observed IBD yield per fission and is minimized by varying the free parameters of y_{235} and y_{239}, and the pull parameters. The subdominant isotopes of ^{238}U and ^{241}Pu have not been included in the fitting parameters. We took 10% as the ^{238}U yield uncertainty and 5% as the ^{241}Pu yield uncertainty. The correlated uncertainties of thermal power, fission reaction cross-section, energy per fission, and detection

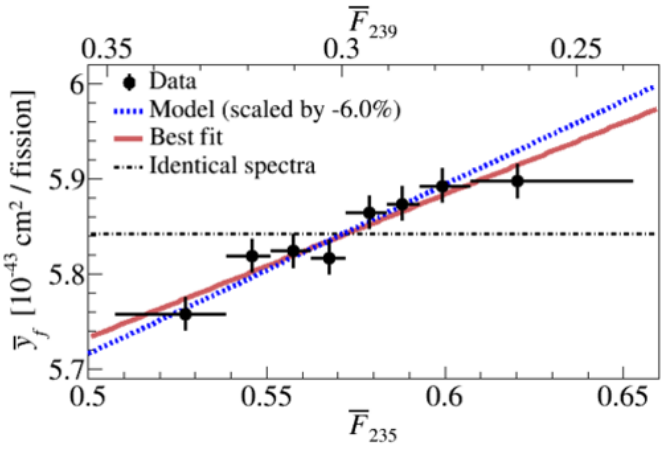

Figure 10.2: IBD yield per fission of $\overline{y_i}$ as a function of the effective fission fraction of ^{235}U. The measured yield variation $\mathrm{d}\overline{y}_f/\mathrm{d}\overline{F}_{235}$ (black dots) is compared to the scaled Huber– Mueller model prediction (blue dotted line) and the best fit of the data (red solid line). Errors are the statistical uncertainties only.

efficiency are taken into account in the χ^2 calculation. The χ^2 is given by

$$\chi^2 = \sum_{j=1}^{8} \left(\frac{\overline{y}_{obs,j} - \overline{y}_{exp,j}}{\sigma_{obs,j}} \right)^2 + \left(\frac{\xi_{238}}{\sigma_{238}} \right)^2 + \left(\frac{\xi_{241}}{\sigma_{241}} \right)^2 + \left(\frac{\xi_{th}}{\sigma_{th}} \right)^2 + \left(\frac{\xi_{xs}}{\sigma_{xs}} \right)^2 + \left(\frac{\xi_{en}}{\sigma_{en}} \right)^2 + \left(\frac{\xi_{det}}{\sigma_{det}} \right)^2 \; where,$$

$$\overline{y}_{exp,j} = \left[\overline{F}^j_{235} \cdot y_{235} + \overline{F}^j_{239} \cdot y_{239} + \overline{F}^j_{238} \cdot y_{238}(1+\xi_{238}) + \overline{F}^j_{241} \cdot y_{241}(1+\xi_{241}) \right] \cdot (1 + \xi_{th} + \xi_{xs} + \xi_{en} + \xi_{det}) \tag{10.7}$$

where $\overline{y}_{obs,j}$ is the observed IBD yield per fission averaged over the four isotopes in the j-th data group, $\sigma_{obs,j}$ is the statistical uncertainty of $\overline{y}_{obs,j}$, $\overline{y}_{exp,j}$ is the expected IBD yield per fission averaged over the four isotopes, $\overline{F}^j_i$ is the time-averaged effective fission fraction of the i-th isotope for the j-th data group, σ_{238} and σ_{241} are the uncertainties of y_{238} (10%) and y_{241} (5%), respectively, σ_{th}, σ_{xs}, σ_{en} and σ_{det} are the uncertainties of thermal power (0.22%), fission reaction cross-section (1.9%), energy per fission (0.2%), and detection efficiency (1.04%), respectively, ξ_{238} and ξ_{241} are the pull parameters of y_{238} and y_{241}, respectively, and ξ_{th}, ξ_{xs}, ξ_{en} and ξ_{det} are the pull parameters for thermal power, fission reac-

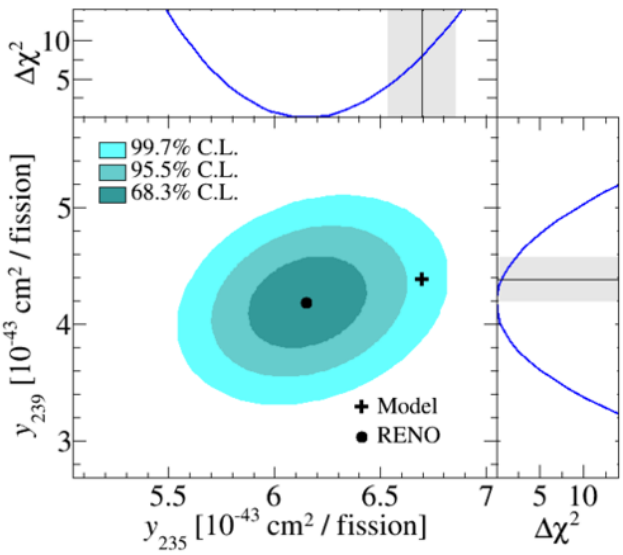

Figure 10.3: Combined measurement of y_{235} and y_{239}. The shaded contours are allowed regions and the dot is the best fit. The cross shows the prediction of the Huber–Mueller model. The top and right side panels show one dimensional $\Delta\chi^2$ profile distributions for y_{235} and y_{239} while the grey shaded bands represent the model predictions.

tion cross section, energy per fission, and detection efficiency, respectively.

The best-fit results are $y_{235} = (6.15 \pm 0.19) \times 10^{43} cm^2$/fission and $y_{239} = (4.18 \pm 0.26) \times 10^{43} cm^2$/fission. Fig. 10.3 shows the combined measurement of y_{235} and y_{239}. The best-fit value of y_{235} is smaller than the prediction from the Huber—Mueller model at 2.8 σ while the best-fit y_{239} is consistent with the prediction within 0.8 σ. This indicates that the re-evaluation of the ^{235}U IBD yield per fission may most probably solve the reactor antineutrino anomaly.

A fractional 5 MeV excess with respect to the total observed IBD events is examined for a possible correlation between the 5-MeV excess and $\overline{F}_{235}$. The five groups of equal data size are sampled according to five different values of $\overline{F}_{235}$. The 5-MeV excess is calculated by subtracting the MC-predicted event rate from the observed event rate in the $3.8 < \mathrm{Ep} < 7$ MeV region. Fig. 10.4 shows the fractional 5-MeV excess as a function of $\overline{F}_{235}$. The horizontal dotted line is the best fit with a zeroth-order polynomial function indicating a constant 5-MeV excess fraction with the average excess fraction of (2.55 ± 0.07) %. The red solid line is the best fit with the first-order polynomial function. We observed a suggestive correlation between the fractional 5-MeV excess and $\overline{F}_{235}$. The hypothesis of a

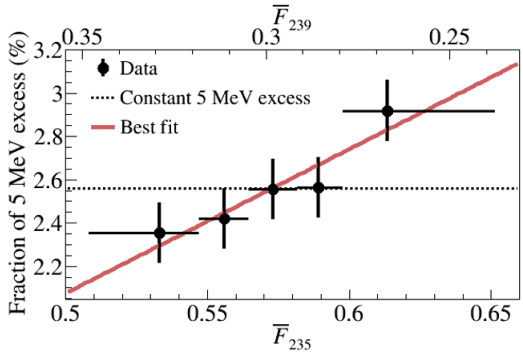

Figure 10.4: Fractional 5-MeV excess as a function of $\overline{F}_{235}$. The red line is the best fit to data and the dotted line represents a constant 5-MeV excess fraction.

constant 5-MeV excess fraction was hence negated at 2.9 σ. Although the current result shows a marginal dependence of the fractional 5-MeV excess on $\overline{F}_{235}$, further accumulated data may reveal the source of the 5-MeV excess.

Chapter 11

Summary and Discussion

Using approximately 2,200 live days of data, RENO has observed a clear energy-dependent disappearance of reactor $\overline{\nu}_e$ using two identical detectors, and has obtained $\sin^2 2\theta_{13} = 0.0896 \pm 0.0048(\text{stat.}) \pm 0.0047(\text{syst.})$ and $|\Delta m^2_{ee}| = [2.68 \pm 0.12(\text{stat.}) \pm 0.07(\text{syst.})] \times 10^{-3}$ eV^2 with $\chi^2/\text{NDF} = 47.4/66$ based on the measured disappearance expected from neutrino oscillations. The systematic uncertainty of $|\Delta m^2_{ee}|$ has been significantly reduced from 0.12×10^{-3} [9] to 0.07×10^{-3} due to the improvement in background uncertainty reduction, especially the most dominant accidental background and ^{252}Cf contamination background rate and its uncertainty around 1 MeV.

Table 11.1 shows the systematic uncertainties of $\sin^2 2\theta_{13}$ and $|\Delta m^2_{ee}|$ from various sources. The systematic error of $\sin^2 2\theta_{13}$ is similar to statistical error of $\sin^2 2\theta_{13}$; thus, systematic error must be reduced for further improving the measurement of $\sin^2 2\theta_{13}$. Reactor-related systematic uncertainties make the largest contribution to the systematic error of $\sin^2 2\theta_{13}$; however, it is difficult to control reactor-related systematic uncertainties. Instead, the detection efficiency and background uncertainties could be reduced by performing greater statistics of control samples. On the other hand, the statistical error of $|\Delta m^2_{ee}|$ is larger than the systematic error of $|\Delta m^2_{ee}|$. Hence, further statistical analysis will give an increasingly improved measurement of $|\Delta m^2_{ee}|$. In addition to this, energy-scale systematic uncertainties, which make the largest contribution to the systematic error of $|\Delta m^2_{ee}|$, could be reduced by improving energy calibration.

Fig. 11.1 shows the comparison of this result with other experimental results. In Fig. 11.1, $|\Delta m^2_{32}|$ is compared instead of $|\Delta m^2_{ee}|$, and the measured value of $|\Delta m^2_{ee}|$ corresponds to $|\Delta m^2_{32}| = (2.63 \pm 0.14) \times 10^{-3}$ eV^2 ($|\Delta m^2_{32}| = [2.73 \pm 0.14] \times 10^{-3}$ eV^2) for the normal (inverted) neutrino mass ordering.

Especially, it would provide important information on the determination of the leptonic CP phase and neutrino mass ordering when combined with the results

	$\delta\lvert\Delta m^2_{ee}\rvert$ ($\times 10^{-3}$ eV^2)	$\delta(\sin^2 2\theta_{13})$
Reactor	$+0.010, -0.004$	$+0.0031, -0.0032$
Detection efficiency	$+0.010, -0.005$	$+0.0033, -0.0033$
Energy scale	$+0.064, -0.065$	$+0.0015, -0.0013$
Backgrounds	$+0.018, -0.021$	$+0.0021, -0.0021$
Total	$+0.068, -0.067$	$+0.0048, -0.0047$

Table 11.1: Systematic uncertainties from various uncertainty sources. The dominant sources of the total systematic uncertainties for $|\Delta m^2_{ee}|$ are the uncertainties of the energy scale.

of an accelerator neutrino beam experiment. Fig. 11.2 is the measurement of θ_{13} and δ_{CP} phase at T2K experiment [10] and the measurement of $\sin^2 2\theta_{13}$ from reactor neutrino experiments [72, 13]. T2k experiment used a muon beam and measured θ_{13} and δ_{CP} phase from eq. 11.1 of survival probability of muon neutrino and electron neutrino. The black graph represents the normal mass ordering and red graph represents the inverted mass ordering.

$$\begin{aligned} P(\nu_\mu \to \nu_e) \simeq\ & \sin^2\theta_{23}\sin^2 2\theta_{13}\sin^2\frac{\Delta m^2_{31}L}{4E} \\ & - \frac{\sin 2\theta_{12}\sin 2\theta_{23}}{2\sin\theta_{13}}\sin\frac{\Delta m^2_{21}L}{4E}\sin^2 2\theta_{13}\sin^2\frac{\Delta m^2_{31}L}{4E}\sin\delta_{\mathrm{CP}} \\ & + (\text{CP even term, solar term, matter effect term}) \end{aligned} \tag{11.1}$$

In addition to this, the measurements of $\sin^2 2\theta_{13}$ from reactor neutrino experiments [72, 13] are represented with yellow and red bar. Eq. 11.2 is the survival probability of an electron neutrino, which is used for reactor neutrino experiments. It gives exceedingly precise measurements of $\sin^2 2\theta_{13}$.

$$P(\bar{\nu}_e \to \bar{\nu}_e) \simeq 1 - \sin^2 2\theta_{13}\sin^2\left(\frac{\Delta m^2_{ee}L}{4E}\right) \tag{11.2}$$

The intersection of the results from the accelerator and reactor experiments helps determine the δ_{CP} phase and neutrino mass ordering with more precision. In addition to this, a vastly improved measurement of $\sin^2 2\theta_{13}$ from the reactor neutrino experiments will give help to determine the δ_{CP} phase with more precision.

Additionally, we could observe the fuel-composition-dependent variation of antineutrino yield due to large statistics ($\sim$1800 live-day in near detector). We observed a clear correlation between the $\overline{y}_f$ and $\overline{F}_{235}$, indicating the dependence

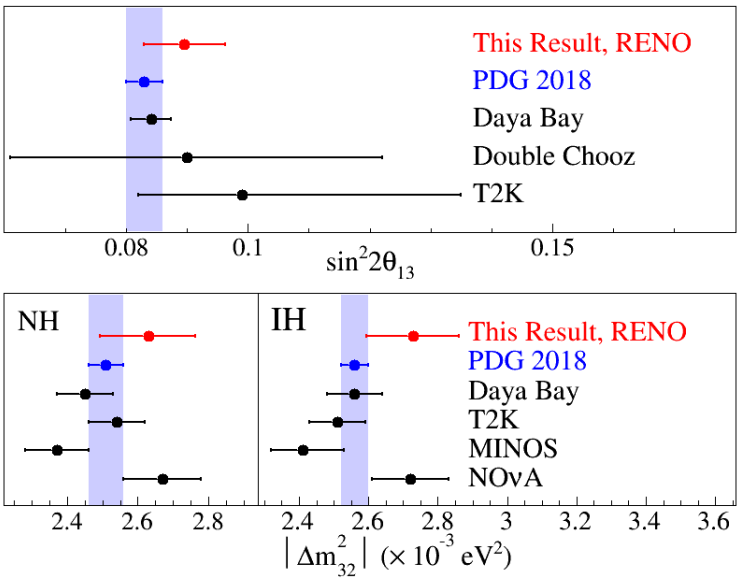

Figure 11.1: Comparison of experimental results on $\sin^2 2\theta_{13}$ and $|\Delta m^2_{32}|$. The world average values [13] and the experimental results of Daya Bay [68], Double Chooz [69], T2K [70], MINOS [71], and NOνA [11] are used.

of IBD yield per fission on the isotope fraction of ^{235}U. This result rules out the hypothesis of no-fuel-dependent variation of IBD yield per fission at 6.6σ confidence level. Therefore, we conclude that the variation of the $\overline{y}_f$ as a function of $\overline{F}_{235}$ comes from unequal IBD yields between different isotope fission processes because of the difference in their antineutrino energy spectra. For the simultaneous determination of y_{235} and y_{239}, a χ^2 with pull parameter terms of systematic uncertainties is constructed using the observed IBD yield per fission and is minimized by varying the free parameters of y_{235} and y_{239}, and the pull parameters. The best-fit results are $y_{235} = (6.03 \pm 0.21) \times 10^{43} cm^2$/fission and $y_{239} = (4.17 \pm 0.29) \times 10^{43} cm^2$/fission. The best-fit value of y_{235} is smaller than the prediction from the Huber–Mueller model at 3.4 σ, while the best-fit y_{239} is consistent with the prediction within 0.8 σ. This indicates that a re-evaluation of the ^{235}U IBD yield per fission may mostly solve the reactor antineutrino anomaly. In addition, a fractional 5-MeV excess with respect to the total observed IBD events was examined for a possible correlation between the 5-MeV excess and the $\overline{F}_{235}$. We observed a suggestive correlation between the fractional 5MeV excess and $\overline{F}_{235}$. The hypothesis of a constant 5-MeV excess fraction was negated at 2.9 σ.

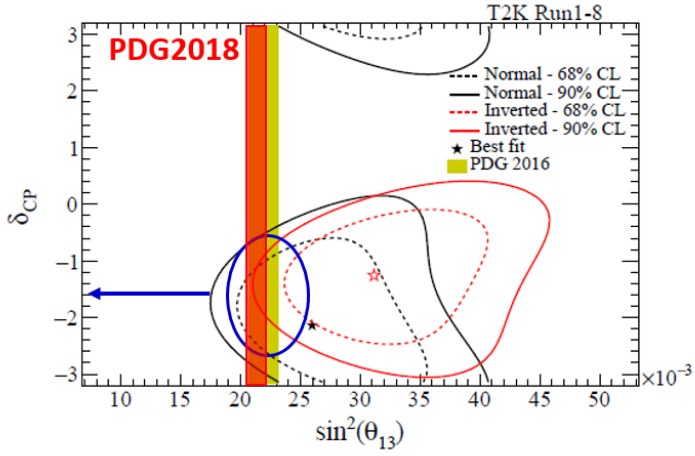

Figure 11.2: Combination of the measurements from accelerator experiment [10] and reactor neutrino experiments [72, 13]. More improved measurement of $\sin^2 2\theta_{13}$ from the reactor neutrino experiments(from [72] to [13]) helps determine the δ_{CP} phase and neutrino mass ordering.

Appendix A

Muon Energy Correction

A.1 Motivation

The muon deposit energy (E_μ) is reconstructed by the observed $Q_{\rm tot}$ with a conversion factor of 250 photoelectrons per MeV. A muon is identified by an event with the deposit energy greater than 70 MeV. Due to the saturation of the DAQ electronics, the muon deposit energy cannot exceed the maximum value, $\sim$1700MeV. The muon energy is mainly used to reject ^{9}Li/^{8}He background, which is correlated with cosmic muons. Due to a decrease in the attenuation length of the Gd-LS, the deposit muon energy also decreases. To correct this decrease, a conventional muon energy correction method was applied by matching maximum peak, as shown in Fig. A.1. The black distribution is for data before ^{252}Cf contamination, and other distributions are for data after ^{252}Cf contamination. These distributions are normalized by lifetime. Even the muon energy is corrected, the rate and spectrum of muon are different over time. Decreased muon rate affects the selection cuts for removal of ^{9}Li/^{8}He background. For this reason, a new muon energy correction was developed so that the muon rate and energy spectrum could be consistent with the reference (before ^{252}Cf contamination) over time.

A.2 New Muon Energy Correction

The conventional muon energy correction method used a maximum peak of muon energy spectrum. For this method, only one parameter was used for the correction; all muon energy was shifted by one correction factor to match the maximum peaks. However, to correct muon rate and spectrum, several parameters are required. Therefore, muon energy correction is energy dependent. For the $E_\mu >$ 1.5GeV region, correction is required to be similar to the conventional correction.

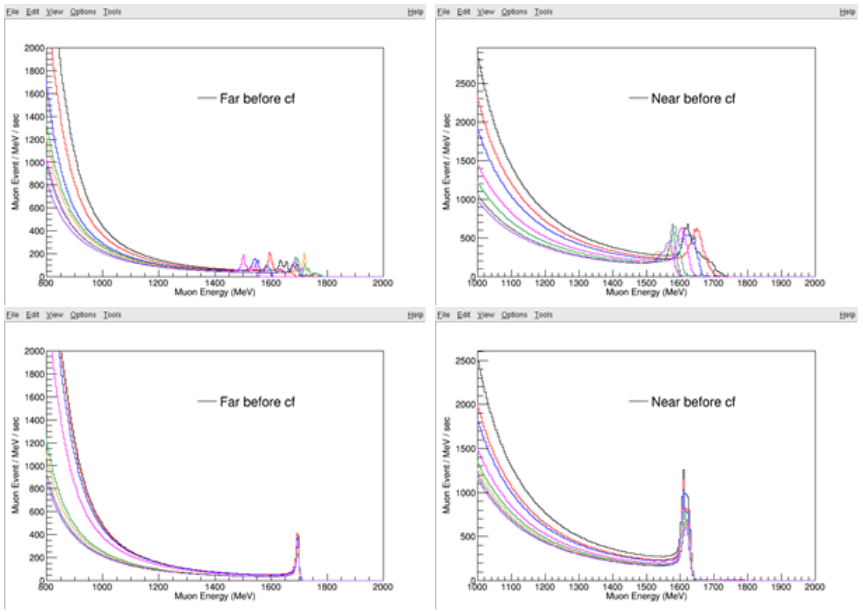

Figure A.1: Muon deposit energy distribution. The maximum energy of ∼1700 MeV occurs because of the saturation of DAQ electronics. The plots on top are without muon energy correction, and the ones at the bottom are with a conventional muon energy correction method. Black distribution is for data before ^{252}Cf contamination, and other distributions are shown against time. The conventional muon energy correction does not fully correct the muon rate and energy spectrum.

For the $E_\mu < 1.5$GeV region, more corrections are needed than the conventional method. To satisfy these conditions, χ^2 fitting is introduced. High muon energy (used for ^{9}Li/^{8}He removal selection cut) is divided into four ranges: 0.85∼1.1, 1.1∼1.3, 1.3∼1.5 and >1.5GeV for the far, and 1.1∼1.3, 1.3∼1.4, 1.4∼1.6, and > 1.6GeV for the near. For each energy range, the muon rates are required to be same as the reference values (before ^{252}Cf contamination). When muon rates and spectrum for all ranges become consistent with the reference, the χ^2 fitting function is,

$$\chi^2 = \sum_{i=1}^{4} \frac{(R_{data,i} - R_{ref,i})^2}{\sigma_i^2} \tag{A.1}$$

where i is one energy range (i = 1∼4), R is muon rate for each energy range, which is calculated from muon energy spectrum with lifetime normalized. σ_i is a weighting factor; given five for i = 4, and given 1 for i = 1∼3. R_{data} is parameterized by four parameters that consist of a new correction factor. The new correction factor is,

$$\begin{aligned} correction factor &= 1.0 && (E_\mu > P1) \\ &= 1.0 + P2 * (P1 - E_\mu)^{P3} && (P4 < E_\mu < P1) \\ &= 1.0 + P2 * (P1 - P4)^{P3} && (E_\mu < P4) \end{aligned} \tag{A.2}$$

The correction factor becomes unity for $E_\mu >$ P1. P1 is 1,700 MeV for far and 1,620MeV for near. P2 and P3 determine the slope and shape of the correction. In addition to this, for $E_\mu <$ P4, the correction factor remains the same when $E_\mu =$ P4. This energy-dependent correction factor is shown as Fig. A.2.

A.3 Result of New Muon Energy Correction

After applying the new muon energy correction factor, muon rate and spectrum are found to be consistent with the reference. Fig. A.3 shows the corrected muon rate for the far and near. Black graph is for the conventional correction method. Muon rate decreases with the conventional correction method over time. The new muon-energy corrected muon rate, on the other hand, shows uniform behavior.

Fig. A.4 shows the corrected muon energy spectrum. Plots on the left are for the conventional correction and those on the right are for the new correction. By using the new correction, it can be seen that muon energy spectrum (normalized by lifetime) is well matched with the reference.

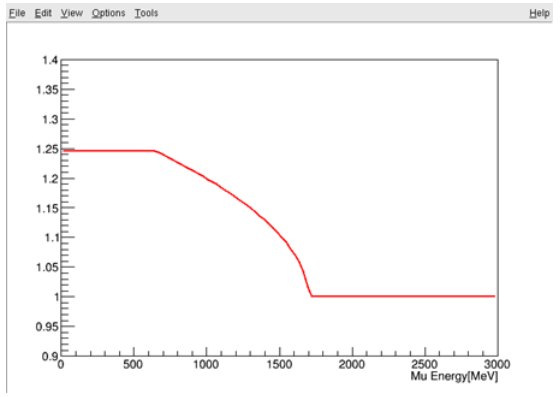

Figure A.2: Muon energy correction factor shows energy-dependent behavior.

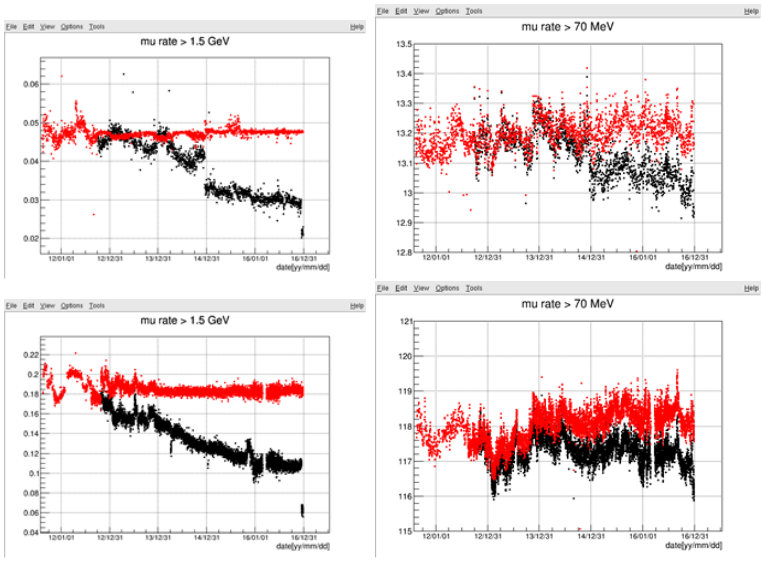

Figure A.3: Muon event rate after applying muon energy correction. Black represents the conventional correction and red represents the new correction. The plots on top are for the far and the plots at the bottom are for the near (left is $E_\mu > 1.5$GeV and right is $E_\mu > 70$MeV).

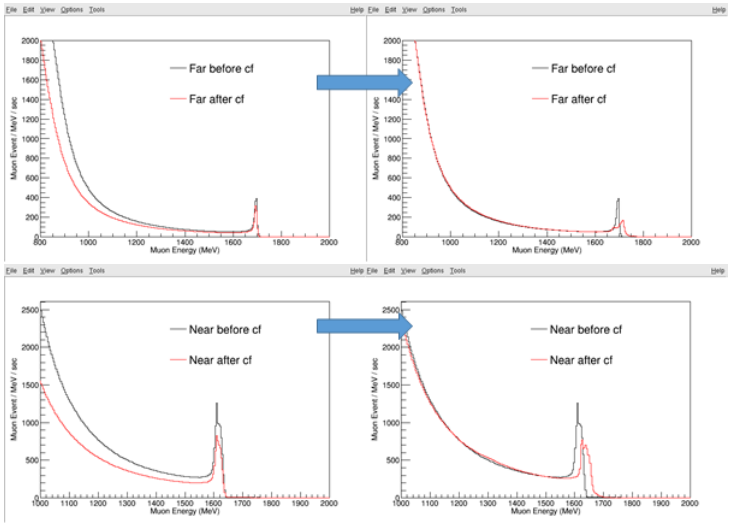

Figure A.4: Muon energy spectrum with conventional and new corrections. Plots on the top are for far and plots at the bottom are for near. Plots on the left are for conventional correction and plots on the right are for the new correction.

Appendix B

Charge Correction

B.1 Temporal and Spatial Variation of Raw Charge

By reducing the Gd-LS attenuation length and the PMT coverage due to the withdrawal of broken PMTs, the number of detected photoelectrons was decreased. In addition to this, the spatial response also changes with time, because the effect of the decrease in Gd-LS attenuation length varies with its position in the detector. This is shown in Fig. B.1 and Fig. B.2. Bottom plots of Fig. B.2 are the scattered plots of R^2 vs Z, where R is the distance between the reconstructed vertex and the center of the detector, and Z is the z-axis position of the reconstructed vertex.

To compensate these decrease of raw charge and different spatial response, temporal and spatial charge correction is required.

B.2 Making Charge Correction

As shown in Fig. B.2, spatial response of raw charge varies with time. Thus, the entire time period is divided by several terms (7 in near, 5 in far as shown in Fig. B.4). For each time period, the scattered plots of R^2 vs Z are also divided into several districts, which have similar raw charges (near in Fig. B.3 and far in Fig. B.4). The outermost district is defined as the 'edge', which has many spill-in events from γ-catcher region, because the prompt spectrum of 'edge' is different from that of the inner region. For each divided district of each time period, a temporal charge correction factor is developed. For a district of any time period, the delayed signal of several events ($\sim$ 1,000) is fitted (Fig. B.5). The ratio of each peak and the reference become the charge correction factor of that district(eq. B.1). For example, Fig. B.6 shows the charge correction factor of near for time period 3. Each line is the charge correction factor of each district.

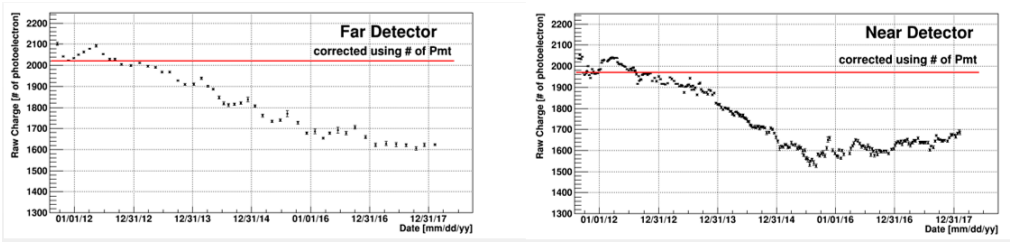

Figure B.1: Number of detected photoelectrons at the far and near detectors, corrected using the number of available PMTs. The amount of charge has decreased since 2013. However, by purging oxygen and moisture using nitrogen gas, the amount of charge has stabilized since 2015, and, at the near detector, it even started to increase in 2017.

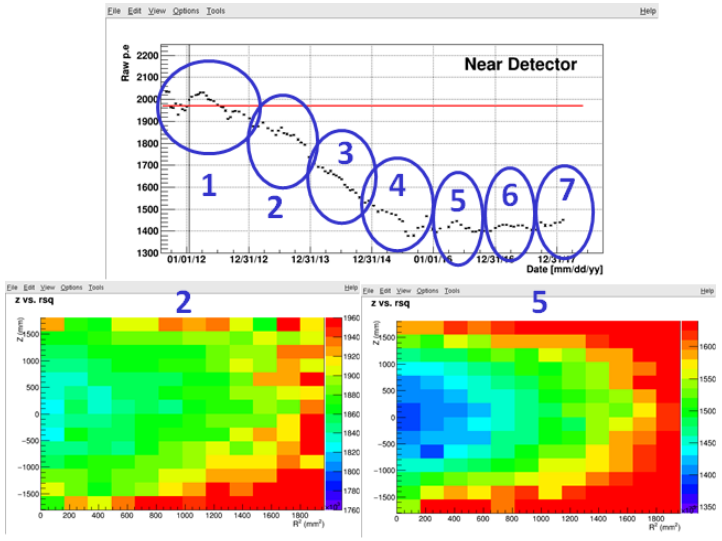

Figure B.2: Near temporal and spatial raw charge stability. It decreases with decrease in Gd-LS attenuation length. Charge has stopped decreasing since late 2015 due to N2 purging. All data for 2,200 days is divided into 7 intervals of time. Each interval has a different spatial response of raw charge. Here shows for period 2 and 5.

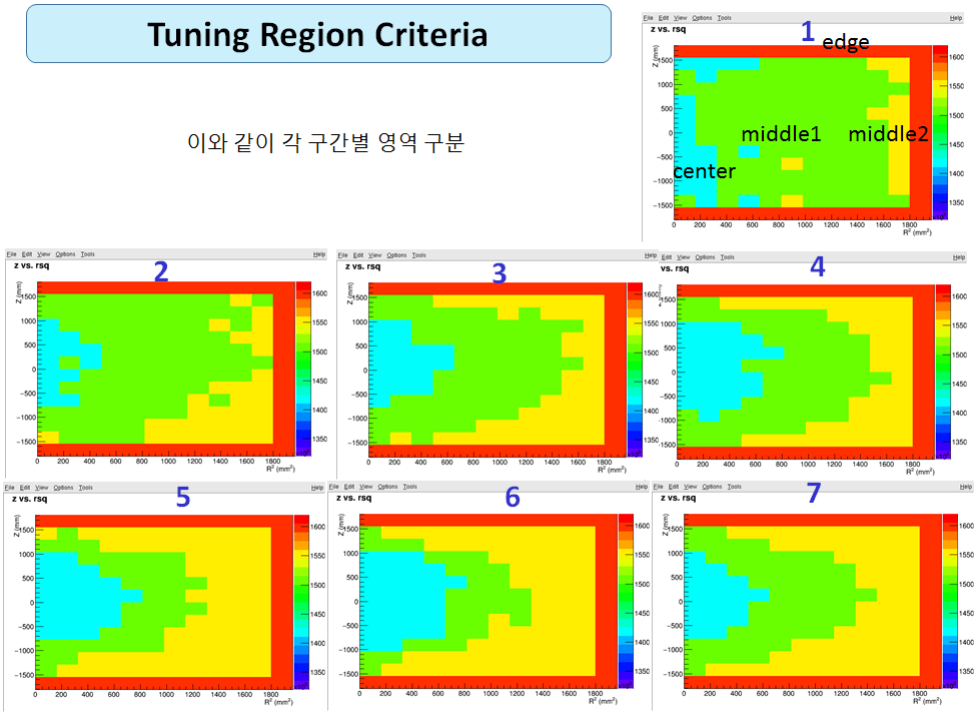

Figure B.3: Diagram of district divided over 7 near time periods. Each time period has different division of detector.

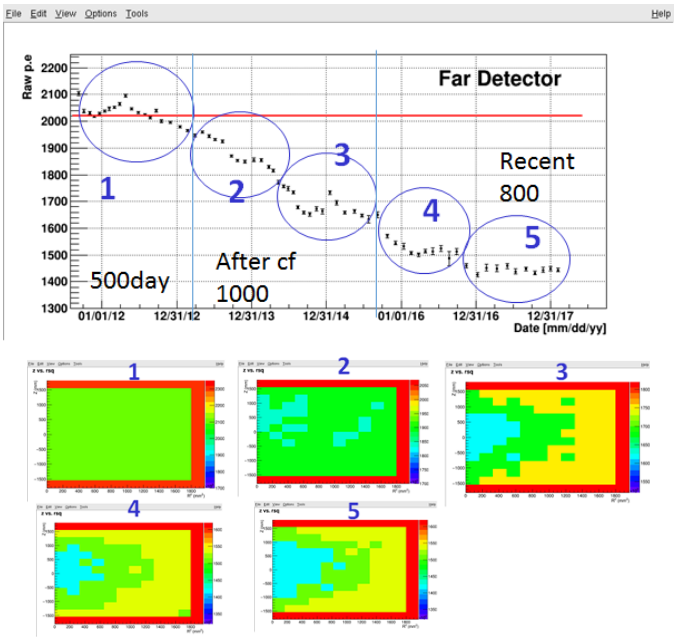

Figure B.4: Far time-dependent and spatial raw charge stability. All data for 2,200 days is divided into 5 time periods.

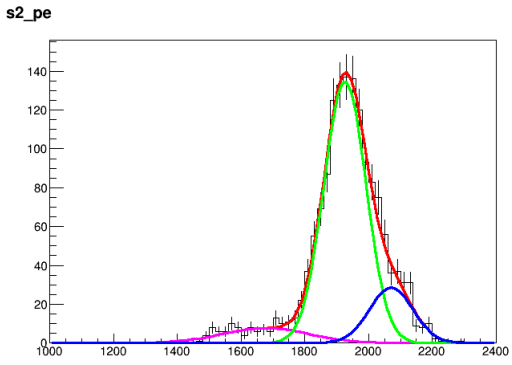

Figure B.5: 3 Gaussian fit of delayed signal. n-Gd capture has two peaks of 7.937 and 8.536 MeV, respectively. Tail spectrum due to the energy loss in acrylic wall.

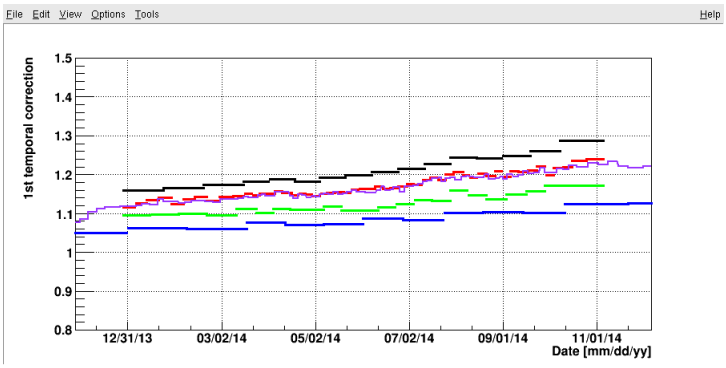

Figure B.6: Temporal charge correction factors for near time period 3. Black represents the center, red represents the middle1, green represents middle2, and blue represents the edge. Purple line is represents the old charge correction.

$$\text{Charge correction factor} = \text{Reference p.e./each peak (for 7.937MeV)} \quad \text{(B.1)}$$

B.3 Stability Check after Applying Charge Correction

The charge correction factor for each district for each time period is applied, and the stability of the corrected charge needs to be verified. Fig. B.7 and B.8 below show the stability of the prompt and delayed signals. The corrected charge is in good agreement with the charge from the first 500 live days, when the Gd-LS attenuation length had not decreased yet.

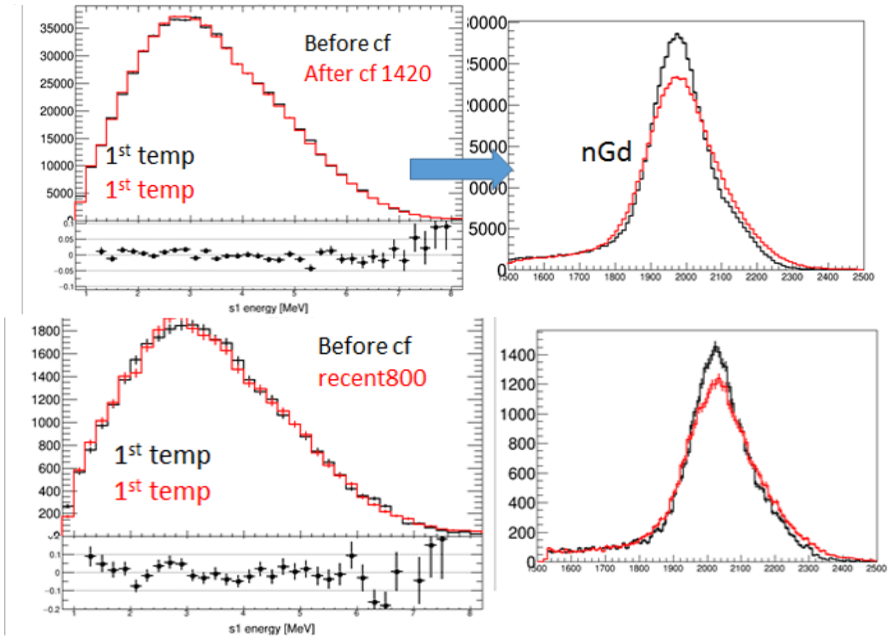

Figure B.7: Comparison of prompt and delayed spectra (before ^{252}Cf contamination is black, and after ^{252}Cf contamination is red). Plots on top are for the near and plots at the bottom are for the far.

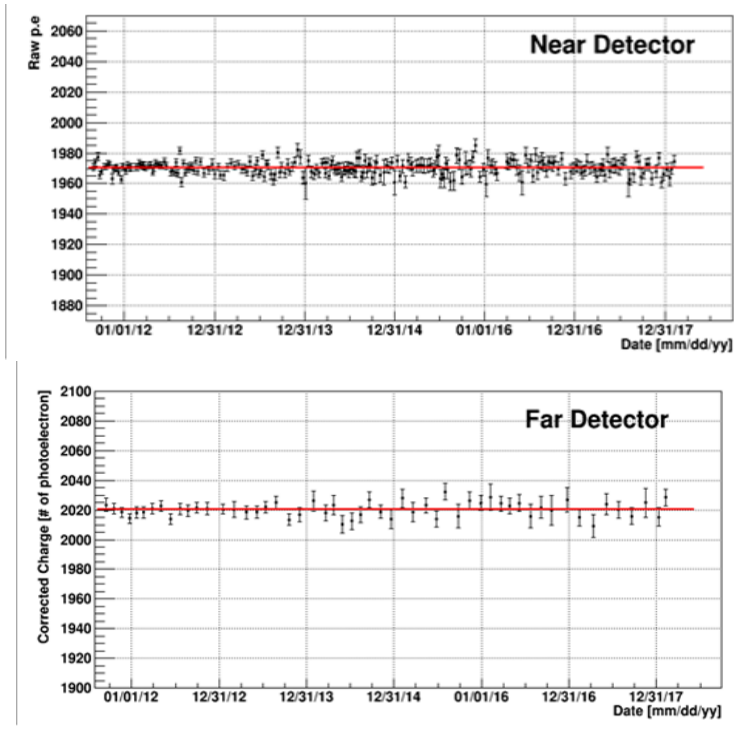

Figure B.8: S2 stability for corrected charge. These show good stability. Plots on top are for the near and plots at the bottom are for the far.

Appendix C

Development of Flasher Cut

As described in section 6.3.1, flashers cannot always be rejected by the flasher cut Q_{max}/Q_{tot} (-400 $\sim$ 800 ns) < 0.07. These flasher events can be removed because of particular properties that allow them to occur at a specific time period and around a specific PMT. To identify where the flasher events occur, we introduced three variables for flasher removal: Q_{max}PMT, Q_{max}/Q_{tot} (-400 $\sim$ 800 ns), and Q_{ave}/Q_{max} (-400 $\sim$ 800 ns). Q_{max}PMT is defined as a PMT that has the largest amount of charge among all PMT hits of an event. Q_{ave} is the averaged charge of the neighborhood PMTs of Q_{max}PMT. When a flasher event occurs, the charges of PMT hits are distributed mainly around a Q_{max}PMT. The lower Q_{ave} means the charge is more concentrated on a Q_{max}PMT. Therefore, flasher events usually have large Q_{max}/Q_{tot} (-400 $\sim$ 800 ns) and low Q_{ave}/Q_{max} (-400 $\sim$ 800 ns). By using these three properties, additional flasher removal cuts can be developed.

C.1 Finding highly flashing Q_{max}PMT

To develop flasher removal cut, firstly, it is required to find highly flashing Q_{max}PMT. There are 354 ID PMTs. The event rate for each PMT should be compared. If a PMT is highly flashing, it has a high event rate than the other PMTs. There are three methods to find highly flashing Q_{max}PMT.

C.1.1 Condition on Q_{max}/Q_{tot} and Q_{ave}/Q_{max}

As mentioned above, flasher events may occur around a specific PMT. Thus, flasher events usually show high Q_{max}/Q_{tot} and low Q_{ave}/Q_{max}. For this reason, in Fig. C.1, the highly flashing Q_{max}PMT can be found by using a condition on Q_{max}/Q_{tot} and Q_{ave}/Q_{max}. For all the events on the top-left plot of Fig. C.1, no PMT shows an exceptionally high rate. However, for events in the red box (in

top-right plot of Fig. C.1), a specific PMT shows an exceptionally high rate.

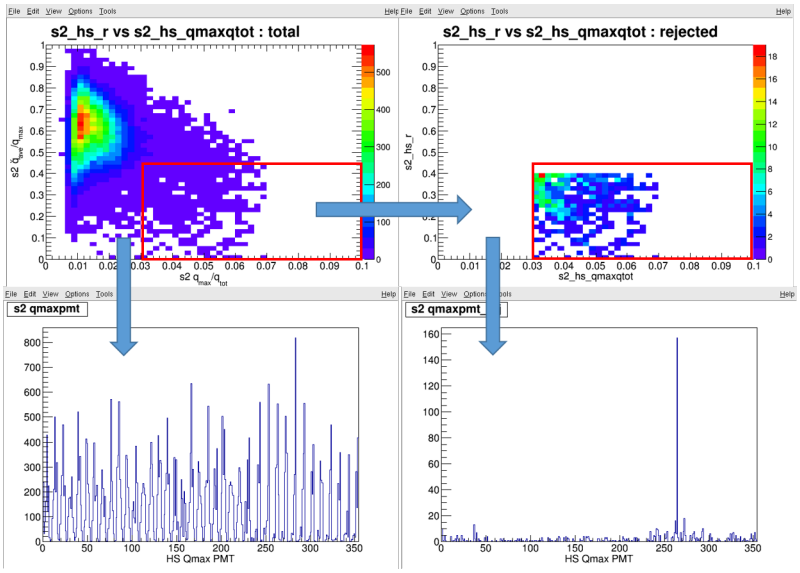

Figure C.1: Finding highly flashing Q_{max}PMT using a condition on Q_{max}/Q_{tot} and Q_{ave}/Q_{max}. In the red box, a specific, highly flashing Q_{max}PMT can be found easily.

C.1.2 Condition on Large ΔR

Highly flashing Q_{max}PMT also can be selected using ΔR between IBD prompt and delayed signals. While pairs of IBD signal have time and spatial correlations, pairs of accidental background do not have the same. Moreover, flasher events that can be accidental backgrounds also do not have time and spatial correlations. Therefore, for large ΔR, accidental backgrounds are dominant while few IBD signals exist. Using this property, highly flashing Q_{max}PMT can be easily found for large ΔR. In Fig. C.2, several specific Q_{max}PMT show high event rates for $\Delta R > 2$m.

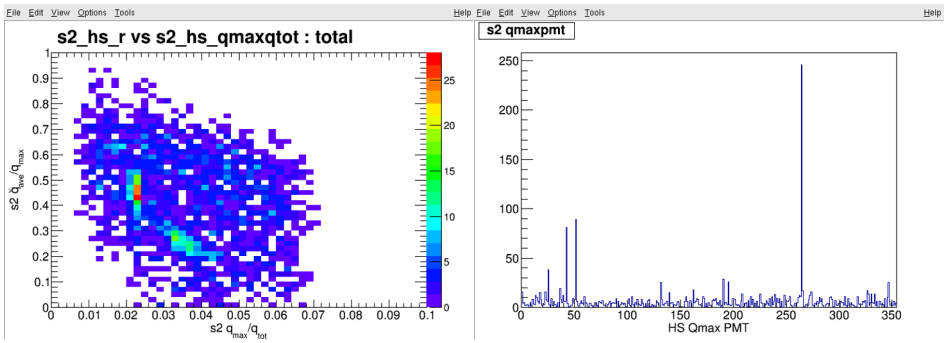

Figure C.2: Finding highly flashing Q_{max}PMT using condition of $\Delta R > 2$m.

C.1.3 Condition on Accidental Background Rate

Highly flashing Q_{max}PMTs, which may appear around a specific time period, affect the accidental background rate. There are several time periods at which accidental backgrounds are high due to flasher events. Therefore, highly flashing Q_{max}PMT can be picked up when limiting the time period with high accidental background rates. In Fig. C.3, several time periods are selected and the event rates of Q_{max}PMTs are checked for each time period. By repeating this procedure, almost all flasher events can be removed and accidental background rates become flat for all time periods.

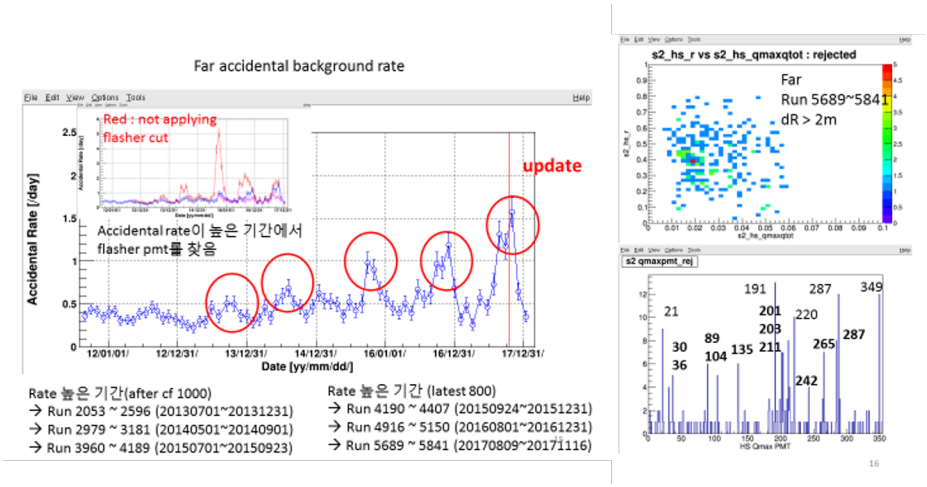

Figure C.3: Finding highly flashing Q_{max}PMT using accidental background rate. Plot on the left shows the accidental background rate of far data against time. There are several time periods that have high accidental background rate. On right-hand side plot, many Q_{max}PMTs are found for a specific time period.

C.1.4 Development of Flasher Cut

A flasher cut is developed for each highly flashing Q_{max}PMT found. In Fig. C.4, a 2D scattered plot of Q_{ave}/Q_{max} vs Q_{max}/Q_{tot} and event rate are illustrated for the events that have a specific Q_{max}PMT. In this plot, flasher events occur at a specific hotspot region. The criteria for Q_{ave}/Q_{max} and Q_{max}/Q_{tot} is aimed at eliminating flasher events without removing IBD signals. A specific time period is determined when event rate is high. Therefore, the developed flasher cut has three criteria: Q_{max}PMT, condition on Q_{ave}/Q_{max} and Q_{max}/Q_{tot}, and a specific time period. The same procedure was repeated for all selected highly flashing Q_{max}PMTs.

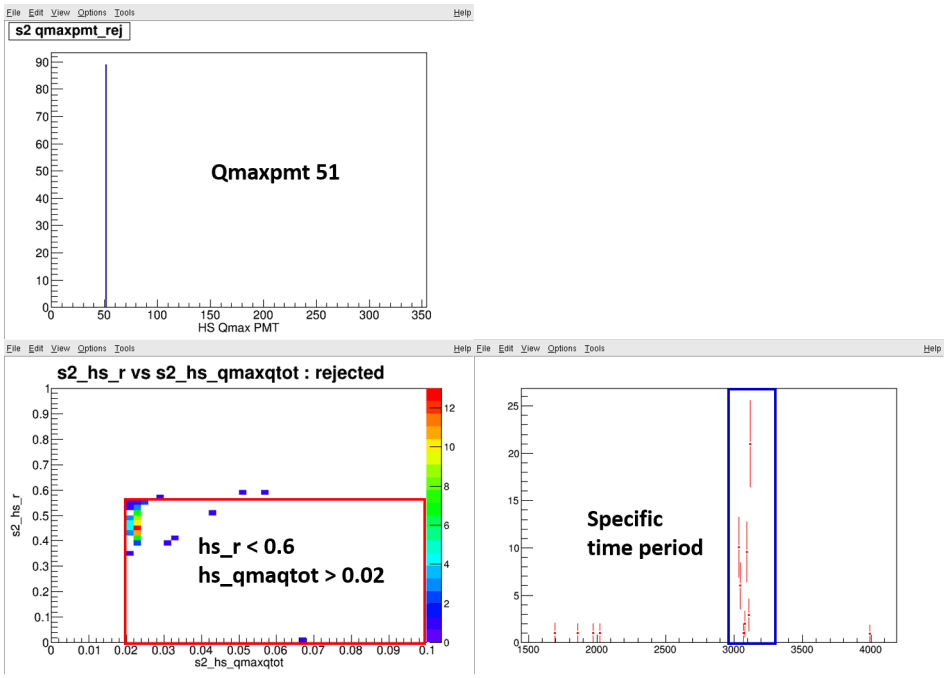

Figure C.4: Development of flasher cut. For Q_{max}PMT 51, 2D scattered plot and event rate are checked, and the criteria are determined for flasher cut.

Fig. C.5 shows the events rejected by the flasher cut developed for the far data after ^{252}Cf contamination. Top-left is a 2D scattered plot of Q_{ave}/Q_{max} vs Q_{max}/Q_{tot}. Several hotspot regions are shown. Top-right shows the event rate of Q_{max}PMTs. Flasher events occurred around specific PMTs. The middle plots show the prompt and delayed energy spectra, while rejected events are shown in the red histogram. The prompt spectrum rejected by the flasher cut has the shape of the accidental background. The rejected delayed energy spectrum does not n-Gd capture peak around 8MeV. In the bottom plot, there are several time periods at which the rejected event rate is high.

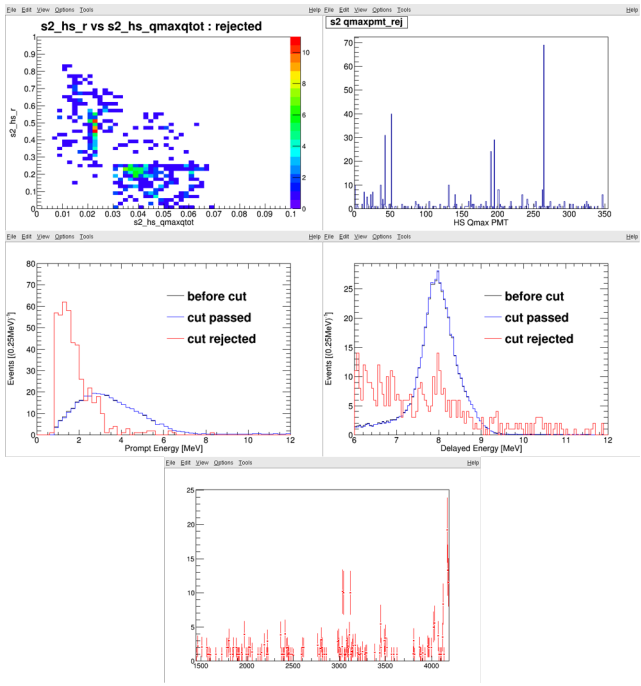

Figure C.5: Plots for rejected events by flasher cut developed for far data after ^{252}Cf contamination. Rejected flasher events have specific time periods and Q_{max}PMTs.

Appendix D

More Details of Signal Loss due to IBD Selection Requirements

D.1 Timing Veto with Muon or Trigger Information

As mentioned in section 6.4, if the trigger is within the cut time range [0,Δt] relative to the prompt of the IBD event, the IBD event is lost by the cut. Because there is no correlation between the prompt of the IBD event and the adjacent trigger, signal loss is just the probability that at least one of the triggers is within the cut time window [0,Δt] relative to the prompt of the IBD event, and it can be calculated by Poisson probability distribution.

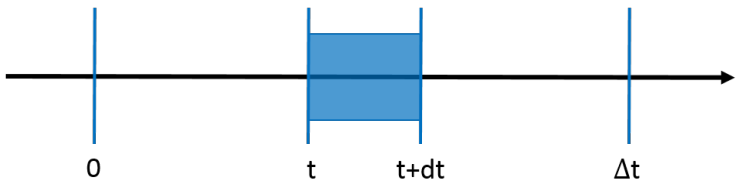

Figure D.1: Diagram of timing veto cut. One trigger is within [t,t+dt] and no trigger is within [0,t].

Fig. D.1 shows the diagram of timing veto cut. The probability of signal loss

for the timing veto cut [t,t+dt] is

$$dP = P[(N(t) - N(0)) = 0] \cdot P[(N(t+dt) - N(t)) = 1] = e^{-R_{trg}t} \cdot R_{trg}dt \quad \text{(D.1)}$$

The total probability is

$$P(0, \Delta t) = \int_0^{\Delta t} dP = 1 - e^{-R_{trg}\Delta t} \quad \text{(D.2)}$$

where R_{trg} is averaged trigger rate for the data period.

The signal losses from timing veto cut with muon or trigger information are calculated by eq. D.2. In table 6.6, 6.7, any trigger before 300μs, muon veto cut, and prompt-like candidate trigger after 1 ms are calculated by this method. Buffer trigger after 200(800)μs cut and buffer & veto trigger after 100μs cut are also calculated using trigger rate; however, a modified equation was used in this study.

When calculating signal loss of the buffer trigger after 200(800)μs cut and buffer & veto trigger after 100μs cut, delayed signal(buffer trigger) can appear between 'prompt' and 'trigger event', or after 'trigger event'. The used coincidence between the prompt and delayed signals is 100μs. Therefore, the modified equation for signal losses of buffer trigger after 200(800)μs cut and buffer & veto trigger after 100μs cut is,

$$Signal\ loss = \frac{\int_0^{100\mu s} f(t')e^{-\frac{t'}{26\mu s}}dt'}{\int_0^{100\mu s} e^{-\frac{t'}{26\mu s}}dt'} \quad \text{(D.3)}$$

$100\mu s$ is the coincidence between the prompt and delayed signals. $26\mu s$ is the mean capture time. Any prompt event cannot appear between prompt and delayed; thus, the trigger event rate is altered. f($t^{'}$) is different for buffer trigger after 200(800)μs cut D.4 and buffer & veto trigger after 100μs cut D.5.

$$f(t^{'}) = \int_0^{t'} e^{-(R_{buf}-R_{prompt})t} \cdot (R_{buf} - R_{prompt})dt + \int_{t'}^{200\ or\ 800\mu s} e^{-R_{buf}t} \cdot R_{buf}dt \quad \text{(D.4)}$$

$$\begin{aligned} f(t') = &\int_0^{t'} e^{-(R_{buf\&veto}-R_{mu})t} \cdot (R_{buf\&veto} - R_{mu})dt \\ &+ \sum_i P_i \int_{t'}^{100\mu s} e^{-(R_{buf\&veto}-R_i)t} \cdot (R_{buf\&veto} - R_i)dt \\ &+ P_0 \int_{t'}^{100\mu s} e^{-R_{buf\&veto}t} \cdot R_{buf\&veto}dt \end{aligned} \quad \text{(D.5)}$$

R_{buf}, $R_{buf\&veto}$ are buffer, and buffer & veto trigger rates. R_{prompt} is the prompt-like trigger rate. R_{mu} is the muon rate. P_i are probabilities that a prompt-like candidate can appear within 0∼1ms, 1ms∼50ms, 50∼200ms, 200∼300ms, and 300∼800ms since t', which are the criteria of muon veto timing cuts. For these cases, muon rates(R_i) are removed from the $R_{buf\&veto}$. If a prompt candidate appears after 800 ms from t' (probability is $P_0 = 1 - \sum_i P_i$), no event rate is removed from $R_{buf\&veto}$.

Below table D.1 and D.2 show the muon rate, table D.3 shows the rate of trigger event, and table D.4 shows the signal loss calculated with these rates. Prompt candidate rate is measured by exponential function fitting of ΔT distribution between IBD prompt and prompt-like candidate event, as shown in Fig. D.2.

Muon type	Rate(Hz)		Signal loss(%)	
	set A	set B	set A	set B
A (> 1.5 GeV, 1000ms)	0.047	0.047	4.639	4.621
B (1.3∼1.5 GeV, 800ms)	0.045	0.046	3.545	3.641
C (1.1∼1.3 GeV, 500ms)	0.096	0.100	4.664	4.875
D (0.85∼1.1 GeV, 100ms)	0.560	0.560	5.445	5.438
1 (0.07∼0.85 GeV, 1ms)	12.39	12.43	1.232	1.235
2 (20∼70 MeV, 1ms)	0.258	0.259	0.026	0.026
Combined	13.40	13.44	18.127	18.370

Table D.1: Rate and signal loss of muon veto timing cuts for the far detector.

Muon type	Rate(Hz)		Signal loss(%)	
	set A	set B	set A	set B
A (> 1.6 GeV, 800ms)	0.103	0.105	7.944	8.068
B (1.4∼1.6 GeV, 300ms)	0.177	0.174	5.173	5.084
C (1.3∼1.4 GeV, 200ms)	0.123	0.131	2.426	2.595
D (1.1∼1.3 GeV, 50ms)	0.471	0.465	2.326	2.299
1 (0.07∼1.1 GeV, 1ms)	116.6	117.1	11.01	11.05
2 (20∼70 MeV, 1ms)	0.785	0.902	0.078	0.090
Combined	118.28	118.87	26.021	26.202

Table D.2: Rate and signal loss of muon veto timing cuts for the near detector.

Event Type	Far (Rate[Hz])		Near (Rate[Hz])	
	set A	set B	set A	set B
Any Trigger	138.359	127.491	589.078	582.394
Buffer Trigger	77.013	68.645	60.521	55.492
Buffer & Veto Trigger	23.136	22.954	208.381	206.353
Prompt Candidate	49.185	40.949	30.468	25.993

Table D.3: Rate of trigger event.

Veto	Far (%)		Near (%)	
	set A	set B	set A	set B
Any Trigger before 300μs	3.679	3.364	13.172	12.982
Buffer Trigger after 200(800)μs	1.440	5.265	1.149	1.053
Buffer & Veto Trigger after 100μs	0.188	0.187	1.430	1.550
Prompt-like Trigger after 1000μs	-	0.781	-	2.005

Table D.4: Signal loss of trigger timing veto. Buffer trigger veto cut for the far detector is 200μs for set A and 800μs for set B.

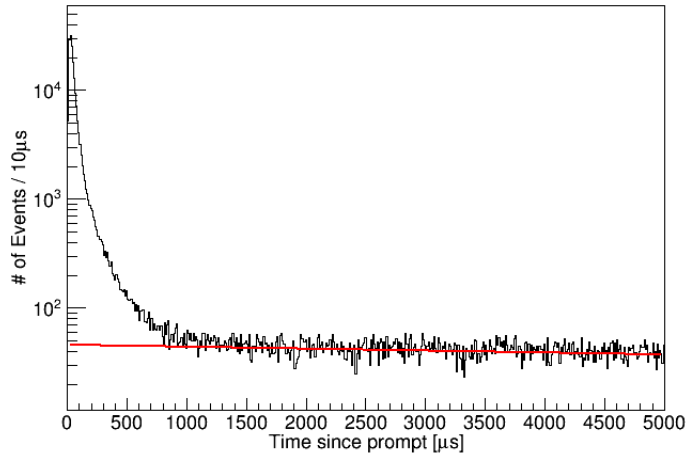

Figure D.2: Prompt-like trigger time distribution after prompt for the far detector. Prompt-like trigger rate is measured by fitting using an exponential function.

D.2 Removal of Adjacent IBD Pairs

With multiplicity cut, adjacent IBD pairs are removed within the 500 μs or 1 sec (for only far after ^{252}Cf contaminated data). Basically, eq. D.2 is used for calculating the signal loss of multiplicity cut. The average event rate of IBD is measured using exponential function fitting, shown in Fig. D.3.

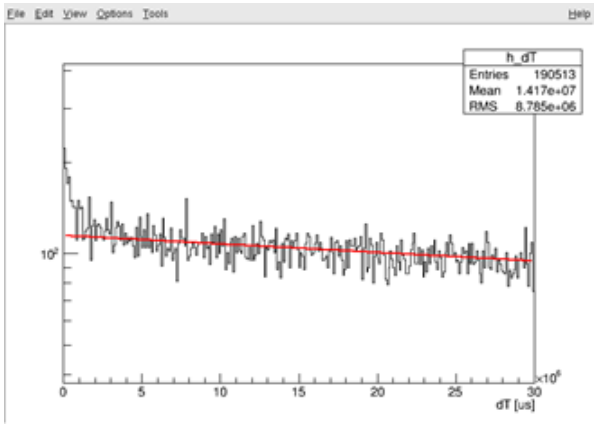

Figure D.3: Time difference between IBD candidate pairs.

For near, or far, before ^{252}Cf , multiplicity cut is applied within 500 μs. Since the average rate of IBD is $\sim$ 0.005Hz, the signal loss with 500 μs cut is almost zero. Therefore, only signal loss from far after ^{252}Cf contamination (within 1 ms)is calculated here.

However, when the cut condition is satisfied, two IBD events are usually removed. So, the signal loss becomes twice the basic one, which is calculated by eq. D.2. Additionally, if three or more IBD pairs are removed due to multiplicity, the signal loss becomes 3/2, 4/3, ... (n+1)/n times the basic one. Eq. D.6 shows the signal loss of multiplicity cut.

$$Signal\ loss = basic\ signal\ loss \cdot \sum_{n=1} \frac{n+1}{n} P(n+1) \tag{D.6}$$

where, $P(n)$ is the probability when n IBD pairs are multiplied within 1 ms, $\frac{n+1}{n}$ is the correction factor for rejecting n+1 IBD pairs with n cut conditions.

Table D.2 below shows the average event rate of IBD pairs and signal loss of multiplicity cut for the data of far after ^{252}Cf contamination.

Data	Rate[Hz]	Signal loss(%)
Fat set B	0.0055	0.9838 ± 0.0159

Table D.5: Average rate of IBD and signal loss of multiplicity cut. The basic signal loss calculated from D.2 is 0.5512%, and with correction factor D.6, the total signal loss is 0.9838%.

D.3 Removal of Flasher Events

Signal loss from additional flasher cut is measured by a spectral fit. Fig. D.4 shows the prompt energy spectra rejected by flasher cuts with IBD prompt spectrum scaled by signal loss, which is measured by a spectral fit at $4 < E < 8$ MeV. The measured signal losses are described in table D.3.

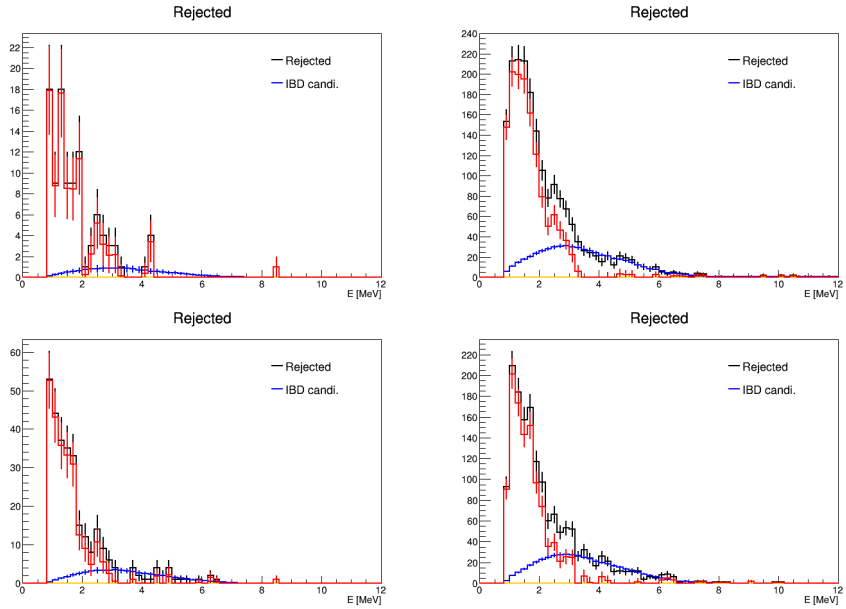

Figure D.4: Prompt spectra rejected by flasher cuts. Each signal loss is measured by a spectral fit at $4 < E < 8$ MeV. Plots on top are for the far detector, and plots a the bottom are for the near detector. Left and right plots are for before and after ^{252}Cf contamination.

	Signal loss(%)	
	set A	set B
Far	0.064 ± 0.029	0.634 ± 0.047
Near	0.014 ± 0.004	0.072 ± 0.006

Table D.6: Signal loss for flasher cuts, which are measure by spectral fit at 4 $< E <$ 8 MeV.

D.4 Removal of ^{252}Cf Contamination Background

D.4.1 Removal of Hotspot

Signal loss from the removal of a hotspot is measured by a spectral fit. In Fig. D.5, the rejected energy spectrum by the removal of a hotspot is fitted with an IBD candidate spectrum at the $1 < E < 4$ MeV energy region. The signal loss is 1.640 ± 0.049%.

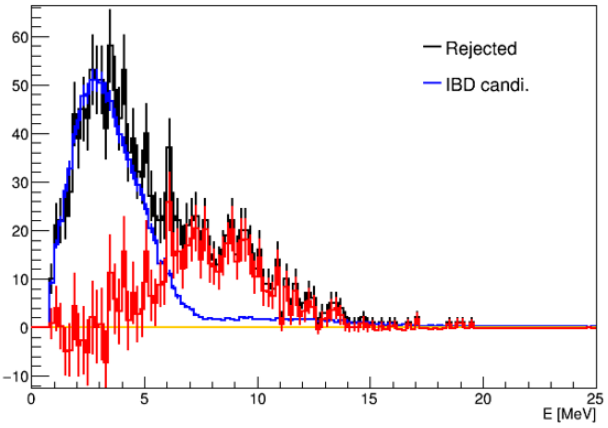

Figure D.5: Prompt spectra before and after removal of hotspot region.

D.4.2 ^{252}Cf background Removal by Temporal and Spatial Correlation with Prompt Candidates

Cf removal cuts using temporal and spatial correlations between prompt-like candidate events and prompt events of IBD candidate are categorized as Cf cut A and Cf cut B, according to the time sequence of prompt-like candidate events with prompt signals of the IBD-like pairs.

- Cf cut A : No prompt-like trigger greater than 3 MeV within (0 sec, 10 sec) and (0, 400 mm) of prompt signal (near detector)
- Cf cut A : No prompt-like trigger greater than 3 MeV within (0 sec, 30 sec) and (0, 500 mm) of prompt signal (far detector)
- Cf cut B : No prompt-like trigger greater than 3 MeV within (-10 sec, 0 sec) and (0, 400 mm) of prompt signal (near detector)
- Cf cut B : No prompt-like trigger greater than 3 MeV within (-30 sec, 0 sec) and (0, 500 mm) of prompt signal (far detector)

The signal loss of each cf cut A(B) is estimated using eq. D.2. However, it is not easy to calculate the event rate for cf cut A(B). To estimate the random rate of prompt-like candidate events, prompt-like candidates that satisfy cf cut A(B) criteria (ΔR, prompt energy, Q_{max}/Q_{tot}) excepted timing correlation criteria (30sec for the far data and 10 sec for the near) are counted. Instead, 50 sec $\sim$ 300 sec (for cf cut A) and 30 sec $\sim$ 300 sec (for cf cut B) since the IBD prompt are applied to count random rate. In addition, if another IBD pair appears within 300 sec, prompt-like candidate and livetime are not counted after that IBD pair, because this IBD could have temporal and spatial correlations between prompt-like candidate events and prompt events of the IBD candidate. For example, in Fig. D.6, only one prompt-like candidate event is counted with a livetime of 120 sec, but not the two prompt-like candidate events with a livetime of 250 sec.

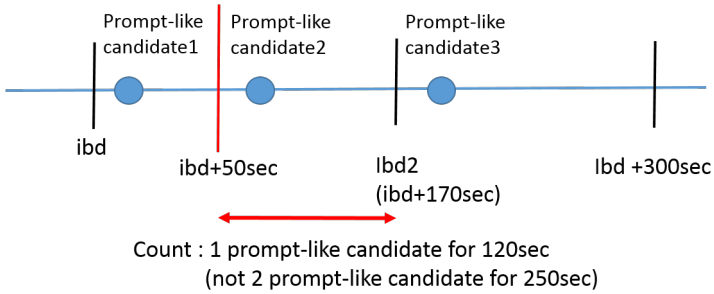

Figure D.6: Diagram for counting prompt-like candidate events and livetime for cf cut A(B). Here, only one prompt-like candidate event is counted with a livetime of 120sec.

The count of prompt-like candidate, livetime, and signal loss are shown in table D.4.2.

Fig. D.7 shows the prompt energy spectra of events rejected by cf cut A(B).

	# of prompt-like	Livetime(sec)	Event rate[Hz]	Signal loss(%)
Far Cf cut A	14693	13096770.86	$1.122\times10^{-}3$	3.310 ± 0.027
Far Cf cut B	17047	14693509.16	$1.160\times10^{-}3$	3.421 ± 0.026
Near Cf cut A	108857	82017499.15	$1.327\times10^{-}3$	1.318 ± 0.004
Near Cf cut B	126898	92565638.93	$1.371\times10^{-}3$	1.362 ± 0.004

Table D.7: The count of prompt-like candidate, livetime, and signal loss for cf cut A(B).

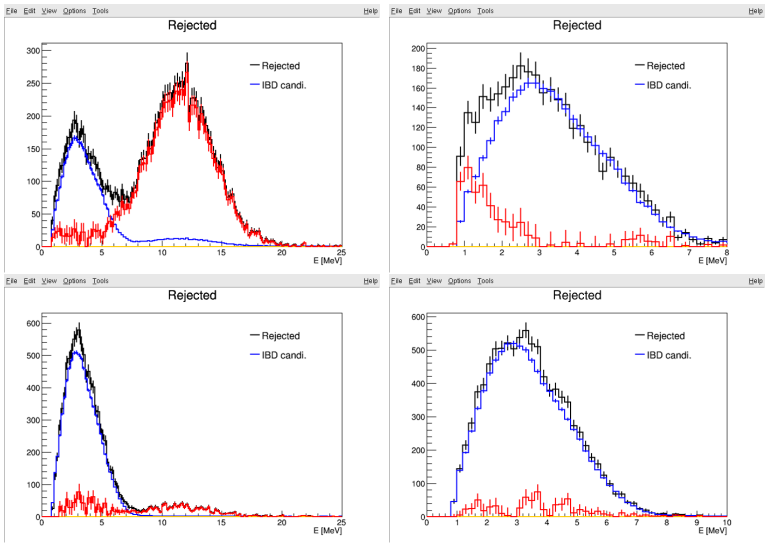

Figure D.7: Prompt energy spectra of events rejected by cf cut A(B). Plots on top are for the far detector and plots at the bottom are for the near detector. Left and right plots are for before and after ^{252}Cf contamination.

Bibliography

[1] B. Pontecorvo, Sov. Phys. JETP **7** (1958) 172.

[2] Z. Maki,M. Nakagawa, and S. Sakata, Prog. Theor. Phys. **28** (1962) 870.

[3] Y. Fukuda *et al.*, (Super-Kamiokande Collaboration), Phys. Rev. Lett. **81** (1998) 1562-1567.

[4] Q.R. Ahmad *et al.*, (SNO Collaboration), Phys. Rev. Lett. **87** (2001) 071301.

[5] Q.R. Ahmad *et al.* (SNO Collaboration), Phys. Rev. Lett. **89** (2002) 011301.

[6] J.K. Ahn *et al.* (RENO Collaboration), Phys. Rev. Lett. **108** (2012) 191802.

[7] F.P. An *et al.* (Daya Bay Collaboration), Phys. Rev. Lett. **108** (2012) 171803.

[8] Y. Abe *et al.* (Double Chooz Collaboration), Phys. Rev. Lett. **108** (2012) 131801.

[9] S.H. Seo *et al.* (RENO Collaboration), Phys. Rev. D 98. 012002 (2018).

[10] K. Abe et al. (T2K Collaboration), Phys.Rev.Lett. 121 (2018) no.17, 171802.

[11] P. Adamson et al. (NOVA Collaboration), Phys. Rev. Lett. 118, 151802 (2017).

[12] B. Pontecorvo, Zh. Eksp. Theo. Fiz. **34**, 247 (1957).

[13] M. Tanabashi et al. (Particle Data Group), Phys. Rev. D 98, 030001 (2018).

[14] C.L. Cowan Jr., F. Reines, F.B. Harrison, H.W. Kruse, and A.D. McGuire, Science, vol. **124**, no. 3212, (1956) 103104.

[15] K. Eguchi *et al.* (KamLAND Collaboration), Phys. Rev. Lett. **90** (2003) 021802.

[16] T. Araki *et al.* (KamLAND Collaboration), Phys. Rev. Lett. **94** (2005) 081801.

[17] H. Kwon *et al.* Phys. Rev. D**24** 1097, (1981).

[18] J. Vuilleumier *et al.* Phys. Lett. B**114** 298, (1982).

[19] G. K. *et al.* Phys. Lett B**138** 449, (1984).

[20] G. Zacek *et al.* Phys. Rev. D**34** 2621, (1986).

[21] A. Afonin *et al.* JETP Lett. **41** 435, (1985).

[22] A. Afonin *et al.* JETP Lett. **45** 247, (1987).

[23] A. Afonin *et al.* JETP Lett. **54** 253, (1991).

[24] G. Vidyakin *et al.* JETP Lett. **59** 390, (1994).

[25] B. Ackhar *et al.* Phys. Lett. B**338** 383, (1994).

[26] Chooz Collaboration, M. Apollonio *et al.* Phys. Lett. B**420** 397, hep-ex/9907037, (1998).

[27] Palo Verde Collaboration, F. Boehm *et al.* Prog. Part. Nucl. Phys. **40** 253, (1998).

[28] Palo Verde Collaboration, F. Boehm *et al.* Phys. Rev. D**64** 112001, (2001).

[29] Palo Verde Collaboration, Boehm, *et al.*, Physical Review Letters **84** (2000) 3764.

[30] Palo Verde Collaboration, Boehm, *et al.*, Physical Review D **62** (2000) 072002.

[31] Chooz Collaboration, M. Apollonio, *et al.*, European Physical Journal C **27** (2003) 331.

[32] Yeh M, Garnov A, Hahn RL. Nucl. Instrum. Methods A **578**:329 (2007).

[33] Park JS, *et al.* (RENO Collab.) Nucl. Instrum. Methods A **707**:45 (2013).

[34] Beriguete W, *et al.* Nucl. Instrum. Methods A **763**:82 (2014).

[35] K. Schreckenbach, G. Colvin, W. Gelletly, and F. Von Feilitzsch, Phys. Lett. B **160**, 325 (1985).

[36] A. A. Hahn *et al.*, Phys. Lett. B **218**, 365 (1989).

[37] H. V. Klapdor and J. Metzinger, Phys. Rev. Lett. **48**, 127 (1982).

[38] P. Vogel, G. K. Schenter, F. M. Mann, and R. E. Schenter, Phys. Rev. C **24**, 1543 (1981).

[39] V. I. Kopeikin, Preprint Kurchatov Institute of Atomic Energy, Moscow IAE-4305/2 (1998).

[40] See a talk given by Larstem Heeger at UW undergraduate colloquium in Feb. 27, 2013.

[41] P. Huber and T. Schwetz, Phys. Rev. D **70**, 053011 (2004).

[42] P. Vogel and J. Engel, Phys. Rev. D **39**, 3378 (1989).

[43] D. H. Wilkinson, Nucl. Phys. A**377**, 474 (1982).

[44] C. Bemporad, G. Gratta, and P. Vogel, Rev. Mod. Phys. **74**, 297 (2002).

[45] H. Minakata and S. Watanabe, Phys. Lett. B 468, 256 (1999).

[46] H. Minakata et al., Phys. Rev. D 70, 059901 (E) (2004).

[47] H. Nunokawa, S. Parke, and R. Zukanovich Funchal, Phys. Rev. D **72**, (2005) 013009.

[48] Abe K, *et al.* (T2K Collaboration) Phys. Rev. Lett. **112**:061802 (2014).

[49] P. Adamson *et al.* (MINOS Collaboration), Phys. Rev. Lett. **110**, (2013) 251801.

[50] F.P. An *et al.* (Daya Bay Collaboration), Phys. Rev. Lett. **115**, (2015) 111802.

[51] A. C. Hayes, J. L. Friar, G. T. Garvey, G. Jungman, and G. Jonkmans, Phys. Rev. Lett. 112, 202501 (2014).

[52] G. Mention et al., Phys. Rev. D 83, 073006 (2011).

[53] P. Huber, Phys. Rev. C 84, 024617 (2011).

[54] T. Mueller at. al., Phys. Rev. C **83**, 054615 (2011).

[55] RENO, S.-H. Seo, AIP Conf. Proc. 1666, 080002 (2015).

[56] RENO, J. H. Choi et al., Phys. Rev. Lett. 116, 211801 (2016).

[57] D. A. Dwyer and T. J. Langford, Phys. Rev. Lett. 114, 012502 (2015).

[58] J. Kopp, P. A. N. Machado, M. Maltoni, and T. Schwetz, Journal of High Energy Physics 2013, 50 (2013).

[59] Daya Bay, F. P. An et al.,Phys. Rev. Lett. 118,no.9,099902(2017).

[60] Double Chooz, Y. Abe et al., JHEP 01, 163 (2016).

[61] T. Mueller at. al., Phys. Rev. C 83, 054615 (2011).

[62] P. Huber, Phys. Rev. C 84, 024617 (2011).

[63] T. Hagner *et al.*, Astropart. Phys. **14**, 33 (2000).

[64] National Nuclear Data Centre, Brook Haven National Laboratory, http://www.nndc.bnl.gov/sg21/nucl/indc- nds-440.pdf (2013).

[65] P. Vogel and J. Beacom, Phys. Rev. D 60, 053003 (1999).

[66] M. Freund, P. Huber and M. Lindner, Nucl. Phys. B**615**, 331-357 (2001).

[67] G. L. Fogli, L. Lisi, A. Marrone, D. Montanino, and A. Palazzo, Phys. Rev. D **66**, 053010 (2002).

[68] F. P. An et al. (Daya Bay Collaboration), Phys. Rev. D 95, 072006 (2017).

[69] Y. Abe et al. (Double Chooz Collaboration), J. High Energy Phys. 02 (2015) 074.

[70] K. Abe et al. (T2K Collaboration), Phys. Rev. D 96, 092006 (2017); K. Abe et al. (T2K Collaboration), Phys. Rev. Lett. 118, 151801 (2017).

[71] P. Adamson et al. (MINOS Collaboration), Phys. Rev. Lett. 112, 191801 (2014).

[72] C. Patrignani et al. (Particle Data Group), Chin. Phys. C, 40, 100001 (2016).

국문초록

Precise Measurement of Reactor Antineutrino Oscillation Parameters and Fuel-dependent Variation of Antineutrino Yield and Spectrum

이동하
물리천문학부 물리학전공
서울대학교 대학원

The reactor experiment for neutrino oscillation (RENO) 는 2011년 8월부터 영광 원자력발전소 근처에 위치한 두개의 동일한 검출기를 사용하여 전자 반중성미자의 데이터를 받기 시작했다. 대략 2,200일의 데이터를 사용하여, 근거리에서는 850 666 원거리에서는 103 212 개의 중성미자 이벤트 후보를 골라내었으며, 그 중 근거리에서는 2.0%, 원거리에서는 4.7%의 비율으로 백그라운드가 포함되어있다. 5MeV 부근에서 측정된 중성미자의 선행이벤트 스펙트럼과 최신의 이론을 사용하여 예측한 선행 이벤트 스펙트럼에 차이가 있는 것을 발견하였다. 원거리와 근거리의 비율을 기준으로 분석하여 거리와 중성미자의 에너지에 따라 중성미자가 사라지는 것을 확인하였고, 그 에너지 스펙트럼과 양으로부터 $\sin^2 2\theta_{13} = 0.0896 \pm 0.0048(\text{stat.}) \pm 0.0047(\text{syst.})$ and $|\Delta m^2_{ee}| = [2.68 \pm 0.12(\text{stat.}) \pm 0.07(\text{syst.})] \times 10^{-3}$ eV^2 를 측정하였다. 한편, 6개 원자로가 작동하는 사이클의 기간이 서로 조금씩 달라 원자로의 연료인 ^{235}U, ^{238}U, ^{239}Pu 그리고 ^{235}Pu의 비율이 계속적으로 변하고 있으며, 이를 통하여 연료 비율에 따라 IBD 생산량의 변화를 살펴보았다. 이로부터 ^{235}U 에 대한 IBD 생산량 $(6.15 \pm 0.19) \times 10^{43}$ cm^2/fission, ^{239}Pu 에 대한 IBD 생산량 $(4.18 \pm 0.26) \times 10^{43}$ cm^2/fission, 그리고 전체 IBD 생산량 $(5.84 \pm 0.13) \times 10^{43}$ cm^2/fission 을 측정하였다. 이러한 측정으로부터, 4가지 연료의 베타 붕괴로부터 발생하는 중성미자의 스펙트럼이 서로 같지 않음을 6.6 σ로서 확인하고 있다.측정된 각 4가지 연료의 IBD 생산량중 ^{235}U의 경우가 이론으로부터 예상된 것에 비해 가장 많이 적게 나타나고 있다. 따라서 4가지 연료중 ^{235}U의 IBD 생산량을 다시 계산하는 것이 원자로 반중성미자의 변칙을 가장 잘 해결할 수 있을 것이다. 또한, 5MeV 부근에서 측정된 중성미자 이벤트의 스펙트럼과 이론으로부터 예상한 스펙트럼의 차이가 원자로 내부의 ^{235}U의 비율과도 상관관계가 있는 것을 확인하였다.